ABSTRACT

Title of Dissertation: **Airborne Characterization of Regional Aerosol Origins and Optical Properties**

Brett F. Taubman, Doctor of Philosophy, 2004

Dissertation Directed By: **Professor Russell R. Dickerson, Department of Meteorology**

The ubiquity of air pollution in the Mid-Atlantic and northeastern U.S. is a major concern for human and ecological health as well as the climate. Between February 2001 and February 2004, 160 flights on a light aircraft outfitted for atmospheric research were conducted over the region to characterize the factors that lead to severe air pollution episodes and how the pollutants impact the radiation budget. One salient discovery was that the chemistry and physics of multi-day haze and ozone episodes over the Mid-Atlantic and northeastern U.S. may be accurately represented by a two-reservoir system composed of the planetary boundary layer (PBL) and the lower free troposphere (LFT). Primary pollutants are typically emitted in the PBL, where they are subject to greater humidification effects and surface deposition. Pollutants in the LFT are not subject to direct deposition and photochemical processes are accelerated, which appears to play a larger role in particle growth processes than relative humidity. Measurements of a smoke plume from Canadian forest fires showed that the plume was separated from the underlying

layer by a morning subsidence inversion. Absorption of solar radiation within the optically thick plume nearly equaled the total amount attenuated at the surface, creating a feedback loop that sustained the vertical stability and protracted the lifetime of the plume. Satellite reflectances were used to calculate the optical depth of the smoke plume with two sets of inputs; AERONET retrieved optical properties and optical properties measured aboard the aircraft. The optical depths calculated using the AERONET optical properties were the lowest, while retrievals using the in-situ values were 22-43% larger, due to greater absorption measured in-situ. Radiative forcings calculated with the in-situ optical properties matched surface and TOA measurements more closely than those calculated with the AERONET retrievals. Measurements made downwind of power plants during the North American electrical blackout showed reductions in SO_2 (>90%), O_3 (~50%), and light scattered by particles (~70%). These observations indicate the central role power plants play in regional air quality. Finally, statistical analyses of all flights point to the dominance of photochemical and meteorological processes in determining aerosol optical properties.

AIRBORNE CHARACTERIZATION OF REGIONAL AEROSOL ORIGINS AND OPTICAL PROPERTIES

By

Brett F. Taubman

Dissertation submitted to the Faculty of the Graduate School of the
University of Maryland, College Park, in partial fulfillment
of the requirements for the degree of
Doctor of Philosophy
2004

Advisory Committee:
Professor Russell R. Dickerson, Chair
Professor Neil V. Blough
Res. Assoc. Prof. Bruce G. Doddridge
Professor Robert Hudson
Professor Alice C. Mignerey
Professor John M. Ondov

Dedication

To Julie, Sam, and Matthew for your love, support, and above all, your patience.

Acknowledgements

Funding for this work was provided by the Maryland Department of Environment (MDE), the Mid-Atlantic and Northeast – Visibility Union (MANE-VU), and the US Department of Energy's Atmospheric Radiation Measurement (ARM) program, grant DEFG0201ER63166. I gratefully acknowledge the NOAA Air Resources Laboratory (ARL) for the provision of the HYSPLIT transport and dispersion model and/or READY website (http://www.arl.noaa.gov/ready.html) used in this publication. The author would like to thank the Center for Ocean-Land-Atmosphere Studies (COLA), Institute of Global Environment and Society, Calverton, MD for the use of Grid Analysis and Display System (GrADS). I am eternally grateful to the AERONET team and to Paul Ricchiazzi and the SBDART code. Finally, a special thanks for their support and contributions goes to George "Tad" Aburn, George Allen, Bryan Bloomer, Pedro Bueno, Kevin Civerolo, Tom Downs, Jennifer Hains, Daniel Kirk-Davidoff, Al Leston, Zanqhing Li, Lackson Marufu, Charles Piety, Rich Poirot, Matt Seybold, Gopal Sistla, Jeff Stehr, Jeff Underhill, and Brian Vant-Hull.

Table of Contents

List of Tables

List of Figures

Chapter 1: Introduction

1.1. Background

Air pollution impacts human health, global climate, and the environment (McClellan, 2002, Gent *et al*., 2003, USEPA, 2003(b), IPCC, 2001). However, the current scientific understanding of trace gas pollution is greater than for aerosols (IPCC, 2001). Trace gases and aerosols may both have deleterious effects on human health and agriculture, but the impacts on the climate are largely competing. Many trace gases have a warming effect, and have thus been classified as greenhouse gases. Conversely, aerosols have a net cooling effect (IPCC, 2001). Trace gases often have lifetimes that are quite long and, therefore, have global consequences. Aerosols, on the other hand, are generally thought to have lifetimes on the order of one week, due to precipitation cycles, and as a result may be limited to a regional scale. Nevertheless, aerosols have been found in areas of the globe that were hitherto thought to be pristine with no regional emission sources, such as the Arctic (e.g., Rosen *et al*., 1981). Discoveries such as this reinforce the fact that our current understanding of aerosol chemistry, physics, and overall impacts is rudimentary at best.

Surface observations over the last several decades seem to indicate a contradiction in solar heating and surface temperatures. Namely, solar heating has decreased while surface temperatures have increased (Liepert *et al*., 2004). Index trends and modeling studies show that the increasing temperatures, at least in North

America, are unlikely the result of natural climate variation (Karoly *et al*., 2003). The competing effects of greenhouse species and the direct and indirect effects of atmospheric aerosols explain the apparent paradox. Contrary to the effect of greenhouse gases, the net effect of atmospheric aerosols, either directly or through cloud interactions, is to cool the climate by reducing solar radiation at the surface. Specifically, anthropogenic aerosols either directly reflect incoming solar radiation or enhance cloud reflectivity by increasing the number concentration of cloud droplets. The indirect effect accounts for no small portion of the total radiative forcing either. The globally averaged radiative forcing of the aerosol direct effect over the ocean, as determined by satellite observations, was estimated to be –0.4 W m^{-2}, while the aerosol indirect effect was found to be –0.6 to –1.2 W m^{-2} (Sekiguchi *et al*., 2003). However, a lot of uncertainty remains as to an accurate net forcing value.

Sulfate-dominated aerosols are primarily responsible for the direct and indirect cooling effects attributed to aerosols in general. Much of the climate forcing uncertainty stems from a lack of understanding of humidification effects on sulfate aerosols as well as mixing processes with other chemical species. Black carbon (BC), the primary absorbing compound in particulate matter (PM), warms the atmosphere and may in fact be the second most important greenhouse species after CO_2 (excluding water vapor) (Jacobson, 2001). The type and degree of mixing of BC with sulfate particles is one of the processes that generates a large portion of the climate forcing uncertainty (Haywood and Boucher, 2000; Jacobson, 2000; Jacobson, 2001; Chung and Seinfeld, 2002; Lesins *et al*., 2002).

1.1.1. Chemistry

Ozone (O_3) formation in the troposphere occurs in the presence of carbon-containing species (represented here with the simplest atmospheric carbon-containing species, CO), NO_x ($NO + NO_2$), and sunlight via the following reaction pathway:

$$CO + OH\ (+O_2) \rightarrow CO_2 + HO_2$$

$$HO_2 + NO \rightarrow NO_2 + OH$$

$$NO_2 + h\nu \rightarrow NO + O$$

$$O + O_2 + M \rightarrow O_3 + M$$

$$O_3 + h\nu \rightarrow O_2 + O(^1D)$$

$$O(^1D) + H_2O \rightarrow 2OH$$

where $h\nu$ represents a photon and M is a third body needed to stabilize the O_3 molecule (typically either N_2 or O_2). Ozone may subsequently regenerate NO_2 through reaction with NO:

$$O_3 + NO \rightarrow O_2 + NO_2$$

Thus, concentrations of O_3 are highly dependent upon NO_x concentrations (Crutzen, 1971). When the sun goes down and NO_2 cannot be photolyzed, O_3 is no longer produced. Ozone captured in the stable nocturnal boundary layer is then destroyed through reaction with NO or surface deposition. The lifetime of this O_3 is several hours. When O_3 remains in the free troposphere, however, it is no longer subject to deposition and its lifetime may be as long as several weeks.

The chemical and optical properties of transported pollutants may be very different from those locally emitted. Air pollution originating in the Midwest is dominated by power plant emissions, with high levels of SO_2 (but not CO) that lead

to secondary aerosol formation and a highly scattering, sulfate-dominated haze (Malm, 1992). Sulfates are formed in the gas phase by means of the following reactions:

$$OH + SO_2 + M \rightarrow HOSO_2 + M$$

$$HOSO_2 + O_2 + M \rightarrow HO_2 + SO_3 + M$$

$$SO_3 + H_2O \rightarrow\rightarrow H_2SO_4$$

and in the aqueous phase through reaction with hydrogen peroxide:

$$SO_2 + H_2O_2 \rightarrow H_2SO_4.$$

Under cloud free conditions, the lifetime of SO_2 is dependent upon the gas phase reaction with the OH radical and dry deposition. At typical atmospheric concentrations of OH, the lifetime of SO_2 is roughly one week. The dry deposition velocity of SO_2 is ~1 cm s^{-1}, so in a 1 km deep boundary layer, the lifetime due to dry deposition is only ~1 d. When SO_2 is transported out of the boundary layer, however, dry deposition is no longer a factor.

Mobile sources, predominant in urban centers in the eastern U.S., emit significantly more black carbon (BC) and CO than stationary point sources (Chen *et al.*, 2001). Black carbon results from biomass burning or the incomplete combustion of fossil fuels and is graphitic in nature, but is generally found as an amalgam with organic matter as well. The lifetime of CO is on the order of several weeks and it is therefore considered a fairly stable tracer species, whereas the lifetime of BC, as with other particulate species, is thought to depend on the frequency of precipitation.

1.1.1. Meteorology

Variability in the concentrations of fine particulate matter ($PM_{2.5}$, particles with aerodynamic diameters $\leq 2.5\mu m$) and O_3 in the lower atmosphere is controlled by local and regional emissions, chemistry, meteorology, and dynamics. When emissions are held relatively constant, however, the meteorology and dynamics assume a major role in determining air quality. The daytime mixed layer is known to be a reservoir of local emissions and regionally transported emissions that are entrained as it deepens (Berkowitz and Shaw, 1997; Banta *et al*., 1998; Luke *et al*., 1998; Ryan *et al*., 1998; Zhang and Rao, 1999; Baumann *et al*., 2000; Fast *et al*., 2002). The lower free troposphere (LFT), roughly defined here as the narrow layer just above the planetary boundary layer (PBL), may also act as a reservoir of photochemically aged air parcels that are not subject to deposition, particularly during multi-day stagnation events (Taubman *et al*., 2004(a)).

The synoptic meteorology associated with O_3 episodes over the eastern U.S. has been investigated in a number of studies (Vukovich, 1995; Zelenka, 1997; Ryan *et al*., 1998; Zhang *et al*., 1998; Kleinman *et al*., 2000; Seaman and Michelson, 2000; Sistla *et al*., 2001; Vukovich, 2002; Rao *et al*., 2003) and is reasonably well understood. Regional high O_3 events often occur when the Bermuda high strengthens and extends west into the eastern U.S. Subsidence east of the ridge induces clear skies, high temperatures, atmospheric stability, and stagnant winds. These factors enhance photochemistry and inhibit vertical mixing, thereby contributing to increased local concentrations of O_3. Circulation around the ridge results in westerly transport of O_3 and O_3 precursors from the Midwest to the eastern U.S., where they combine

with local emissions. In the eastern U.S., hazy conditions often occur during periods of high O_3, but not always (Chen, 2002). The meteorological conditions that support high concentrations of regional $PM_{2.5}$ are not as well characterized as for O_3. However, recent studies have shown that transport of $PM_{2.5}$ from the south and west into the region plays a role (Malm, 1992; Chen *et al*., 2002; Civerolo *et al*., 2003).

Two meso-scale meteorological phenomena often associated with air pollution events in the eastern U.S. are the Appalachian lee trough (APLT) and the nocturnal low-level jet (LLJ). The synoptic flow typical during these events is orthogonal to the Appalachian mountain range. As the air descends over the eastern ridge of the mountains it is adiabatically heated, creating a column of hot air. In response to the increased buoyancy of the air parcel, surface pressures drop and a mesoscale trough forms (Seaman and Michelson, 2000). To conserve absolute vorticity, the winds turn cyclonically across the trough. The APLT is associated with approximately 70% of the high O_3 episodes in the Mid-Atlantic (Pagnotti, 1987).

The LLJ in this region occurs between approximately 00:00 and 06:00 EST and is a south-southwesterly wind maximum in the residual layer, generally observed between ~300-1000 m. The wind speeds are typically ~10-20 m s^{-1} and are greater than those in the underlying nocturnal boundary layer and those just above it. The nocturnal boundary layer provides a low friction surface over which the jet can travel. This phenomenon also seems to be orographically derived, possibly resulting from the differential heating and pressure gradients associated with sloping terrain (e.g., Parish *et al*., 1988). Pollutant transport via the LLJ is disproportionately important during periods of stagnation when geostrophic winds are light.

1.1.2. Contributions from Biomass Burning

Biomass burning can have significant impacts on regional air quality and the radiative balance of the earth. Large amounts of trace gases, including CO, NO_x, and O_3, are typically associated with biomass combustion plumes (Evans *et al*., 1977; Crutzen *et al*., 1979; Stith *et al*., 1981; Delmas, 1982; Crutzen and Andreae, 1990; Andreae and Merlet, 2001). O_3 is photochemically produced downwind of fires in the presence of NO_x, NMHCs (non-methane hydrocarbons), CO, and UV light (Evans *et al*., 1977; Stith *et al*., 1981; McKeen *et al*., 2002). Combustion temperatures generated from biomass burning are not high enough to fix atmospheric nitrogen; rather the reactive nitrogen generated from biomass burning results from the nitrogen content of the species burned (Andreae and Merlet, 2001). Most of the species also contain S, but little SO_2 is normally observed downwind of biomass burning (Stith *et al*., 1981).

Particles generated from burning vegetation are dominated by organic carbon (OC) and BC (Crutzen and Andreae, 1990; Martins *et al*., 1998) that reduce the flux at the surface by scattering and absorbing solar radiation (Penner *et al*., 1992; Hobbs *et al*., 1997; Remer *et al*., 1998; Eck *et al*., 1998; Li, 1998; Li and Kou, 1998). This is in contrast to sulfate particles, prevalent over the eastern U.S., that predominantly scatter solar radiation and cool both the atmosphere and the surface (Charlson *et al*., 1991; Ramanathan *et al*., 2001). The degree of absorptivity of carbonaceous smoke particles depends largely on fuel type (dictated by region and vegetation), age of the particles, and the phase of burning (i.e., flaming vs. smoldering) (Dubovik *et al*., 2001). Emissions from North American boreal forest fires have been shown to be

less absorptive than those of African savannah and South American cerrado fires and commensurate with those of Amazonian forest fires (Dubovik *et al*., 2001). This is largely due to a protracted smoldering phase in forest fires that produces less absorptive particles. Chemical and physical transformations may, however, occur downwind of the source. In an aged plume, particle coagulation, gas-to-particle conversion, heterogeneous reactions, and cloud processing influence the trace gas concentrations and the size distribution and optical properties of the smoke particles (Reid *et al*., 1998(a); Reid *et al*., 1999, Wong and Li, 2002). Near source and downwind *in-situ* measurements are thus necessary to provide constraints on remote sensing retrieval algorithms as well as for validations of numerical based model simulations.

The scattering Ångström exponent, α, a measure of the wavelength (λ) dependence of the scattering coefficient, is inversely related to particle size, and thereby provides information on the source and age of the observed particles:

$$\alpha = \frac{-\log(\sigma_{sp\lambda 1} / \sigma_{sp\lambda 2})}{\log(\lambda_1 / \lambda_2)} \tag{1}$$

The single-scattering albedo (ω_o) is the ratio of particle scattering (represented by the scattering coefficient, σ_{sp}) to total extinction due to particle scattering and absorption (represented by the absorption coefficient, σ_{ap}), and represents the probability that a photon encountering the particle will be scattered:

$$\omega_o = \frac{\sigma_{sp}}{(\sigma_{sp} + \sigma_{ap})} \tag{2}$$

Smoke particles reportedly become less absorptive with age (Reid *et al*., 1998(a)). In optically thick smoke plumes, small changes in ω_o can have profound

impacts on the radiative budget (Reid *et al*., 1999). The energy balance of the surface-atmosphere system is thus altered according to the degree of scattering and absorption (Eck *et al*., 1998). A more absorbing aerosol can heat the atmosphere and cool the surface, generating greater stability in the lower atmosphere and impacting the hydrological cycle (Ramanathan *et al*., 2001). This in turn affects the vertical mixing of the aerosols and potential removal mechanisms (e.g., Park *et al*., 2001).

The direct effect of aerosols upon this energy balance is quantified through calculations of aerosol direct radiative forcing. Top of the atmosphere forcing (ΔF TOA) is a measure of the reflectivity of the atmosphere (after accounting for surface albedo), while surface forcing (ΔF sfc) gives the total attenuation of solar flux at the surface, both driven by aerosols in this case. If the two are equal, then the aerosols are completely scattering. If the attenuation at the surface is greater than the reflected flux at the top of the atmosphere, then the aerosols have absorbed some of the solar radiation. Aerosol direct radiative forcing depends upon the aerosol optical depth (AOD, τ), ω_o, and the asymmetry parameter (g) of the particles. Aerosol optical depth is defined as the extinction coefficient, σ_{ext}, integrated from the surface (sfc) to the top of the atmosphere (TOA):

$$\tau(\lambda, RH) = \int_{sfc}^{TOA} \sigma_{ext}(\lambda, RH)dz \tag{3}$$

The extinction coefficient is the sum of the scattering and absorption coefficients and τ can therefore be represented as the sum of their vertical integrals:

$$\tau(\lambda, RH) = \int_{sfc}^{TOA} \sigma_{sp}(\lambda, RH)dz + \int_{sfc}^{TOA} \sigma_{ap}(\lambda, RH)dz \tag{4}$$

The asymmetry parameter represents the degree of asymmetry of the angular scattering and is defined as:

$$g = \frac{1}{2}\int_0^{\pi} \cos\theta P(\theta)\sin\theta d\theta \quad (5)$$

where θ is the scattering angle and P is the phase function, the scattered intensity at angle θ relative to the incident beam.

1.1.3. Discrepancies Between Remotely Sensed and In-Situ Measurements

Aerosol optical depth is a quantity that is used for column closure studies as well as the calculation of aerosol radiative forcing. In most areas of the western hemisphere, light is primarily scattered by particles. The contribution of particle light absorption to the aerosol optical depth is small. As a result, uncertainties in absorption values are often overlooked. Because of the large contribution of scattering to the aerosol optical depth, a reasonable agreement in scattering values typically leads to a reasonable agreement in optical depth values. However, significant disparities in optical depth or forcing values may arise when there are large discrepancies in absorption values used as inputs to satellite algorithms and in calculations of aerosol radiative forcing, respectively (Vant-Hull *et al.*, 2004).

Absorption measured in-situ is almost invariably lower than that determined through remotely sensed techniques (e.g. sun photometry) (Hegg *et al.*, 1997; Hartley *et al.*, 2000; Dubovik *et al.*, 2001; Taubman *et al.*, 2004(b)). For example, in-situ aircraft measurements of ω_0 during SCAR-B and INDOEX were consistently lower than sun photometer observations (Dubovik *et al.*, 2001; Ramanathan *et al.*, 2001(b)). Better agreement, however, was achieved during the SAFARI campaign (Haywood *et*

al., 2003, Magi *et al*., 2003). In the LACE-98 campaign (Bundke *et al*., 2002) measurement conformity was only achieved after the introduction of a variable liquid layer used to theoretically envelop the carbonaceous core of aged smoke particles.

Whether or not one measurement technique is more accurate than the other, both have inherent advantages and disadvantages. The important advantage of satellites is that they offer global coverage, a necessity when studying climate variability (Kaufman *et al*., 2002). However, satellites, as well as most other passive remote sensing techniques, cannot resolve vertical layers within the column and only retrieve column-averaged properties. Also, while the surface albedo naturally varies, the satellite observational angle is fixed for a particular pixel. These factors preclude the possible retrieval of all of the aerosol optical properties. Rather, one or more of the optical properties are assumed and the rest are derived from the measured reflectances (Kaufman *et al*., 1990; Wang *et al*., 2003).

Sun photometers that measure solar radiance at the surface, such as those used in the AErosol RObotic NETwork (AERONET) (Holben *et al*., 1998), make observations over a large range of scattering angles through a constant aerosol profile to retrieve many column-averaged aerosol optical properties (Dubovik *et al*., 2000). Previous studies that used sun photometers to retrieve certain aerosol optical properties (size distribution, phase function, optical depth) incorporated algorithms with fixed values for the remaining ones (index of refraction, single scattering albedo) (Kaufman *et al*., 1998; Russell *et al*., 1999(b)). Currently, a more sophisticated and exhaustive algorithm is used for sun photometer retrievals that provides a comprehensive suite of estimated optical properties (Dubovik *et al*., 2000; Dubovik *et al*., 2001). A distinct advantage of remote sensing techniques in general is that they

do not physically alter the aerosols measured. However, the veracity of the measurements depends upon the assumptions used in the retrievals (Remer *et al.*, 1997; Dubovik *et al.*, 2000).

Unlike remote sensing techniques, in-situ measurements can resolve the vertical layers within an atmospheric column. However, measurement errors may arise through the physical interaction of the instrument with the measured aerosols (Remer *et al.*, 1997; Bond *et al.*, 1999). A comprehensive laboratory calibration of the PSAP (Particle/Soot Absorption Photometer) showed that when using the integrating plate method to measure absorption, filter interferences are a significant source of error (Bond *et al.*, 1999). Despite the potential problems, both in-situ and sun photometer measurements of aerosol optical properties are currently used in satellite algorithms (Bundke *et al.*, 2002; Kaufman *et al.*, 1998).

The natural variability in biomass burning aerosol optical properties exacerbates the existing discrepancy between in-situ and remote sensing techniques. Biomass burning aerosol optical properties vary depending on the type of vegetation burned, whether the fire is flaming or smoldering, and the age of the particles (Kaufman *et al.*, 1998; Reid *et al.*, 1999; Wong and Li, 2002). Measurements of smoke particles in Brazil showed a range of single scattering albedos at 550 nm (ω_{0550}) of 0.6 to 0.91, depending on the age (Kaufman *et al.*, 1998; Reid *et al.*, 1998(b)). Canadian smoke had ω_{0550} values from 0.70 to 0.98 for similar reasons (Miller and O'Neill, 1997; Li and Kou, 1998). The ω_{0550} from burning pine needles, measured in a controlled environment, varied between 0.66 and 0.97 according the burning mode (smoldering or flaming) (Miller and O'Neill, 1997).

1.1.4. Contributions from Power Plants

Fossil fuel burning power plants are responsible for more than half of the electrical energy production in the U.S., but also ~22% of the NO_x and ~69% of the SO_2 emissions (USEPA, 2003(a)). As detailed above, nitrogen oxides combine with volatile organic compounds (VOCs) in the presence of sunlight to produce O_3, the principal component of photochemical smog. Likewise, SO_2 may be oxidized to produce sulfate (SO_4^{2-}), the primary constituent of $PM_{2.5}$ in the northeastern U.S. (IMPROVE, 2000). In summertime, under high pressure systems with westerly transport, emissions of NO_x and SO_2 in the northeastern U.S. induce severe smog and haze events, primarily comprising O_3 and sulfate-dominated fine particles (Ryan *et al*., 1998, Sistla *et al*., 2001, Taubman *et al*., 2004(a)). Both pollutants have been linked to adverse health effects, degradation of the environment, and global climate change (McClellan, 2002, Gent *et al*., 2003, USEPA, 2003(b), IPCC, 2001).

Despite improvements made to air quality in the U.S. over the past 20 years, approximately 146 million people live in counties where the monitored air in 2002 was deemed unhealthy (USEPA, 2003(a)). Unacceptably high levels of either O_3 or PM or both were the primary reason for the unhealthy classification. Of all the air pollutants routinely monitored, ground level O_3 has been the most challenging to reduce. Some metropolitan areas have shown improvements, but the 8-hour average O_3 levels have increased in many national parks (USEPA, 2003(b)). This is apparently the result of region-specific responses to VOC versus NO_x reductions. In the past 20 years, VOC emissions have decreased by ~40% while NO_x emissions

have decreased by only ~15% (USEPA, 2003(b)). Except for urban centers, which are VOC limited, the majority of the U.S. is NO_x limited (Fiore *et al*., 1998).

The impact of transported point source pollution on regional air quality depends upon emissions, meteorology, and non-linear chemical responses. Thus far, quantification of these impacts has been based on multi-year measurement and modeling studies (Solomon *et al*., 2000) and the results of long-term emissions reduction scenarios (Malm *et al*., 2002). Not until the work reported herein has there been an opportunity to make direct air quality measurements during a large scale-back of one pollution source.

1.2. Overview of the Research

Between February 2001 and February 2004, 160 research flights were conducted to investigate the chemical, meteorological, and dynamical factors that influence regional air pollution episodes in the Mid-Atlantic and northeastern U.S. Most of these flights were performed in the summertime; however, three mini-campaigns were conducted in the winters of 2001, 2003, and 2004. Measurements were made using a light aircraft outfitted for atmospheric research. Details of the experimental methods and sampling platform will be covered in the next chapter. One of the main foci of the research was climatically relevant: an investigation of the optical property characteristics of the aerosols and their impact on the regional radiation budget. Another area of interest was more policy relevant: the source attribution of the pollution through an examination of the chemical and optical characteristics of the pollutants.

1.3. Organization

The next chapter details the experimental methods used for this work, including the sampling platform, trace gas analyzers, and particle instruments. Chapter 3 discusses the formulation of the two-reservoir conceptual model, a new paradigm for describing the chemistry and physics of the lower atmosphere during multi-day air pollution episodes. The two subsequent chapters describe the measurements made of an optically thick smoke plume from Canadian forest fires that was advected over the eastern U.S. in early July 2002. The radiative impacts of the plume are quantified and comparisons are made between the in-situ measurements of aerosol optical properties and AERONET values when used as inputs to a satellite algorithm to calculate optical depth. Chapter 6 describes the measurements made downwind of power plants that were tripped during the North American electrical blackout in August 2003 and the subsequent analyses. Finally, Chapter 7 gives an overview of the statistical analyses of aerosol optical properties over the three-year time period described above during which research flights were conducted. Following the statistical overview is a summary of all the work described herein as well as the climate and policy implications and recommendations for the future.

Chapter 2: Experimental Methods

2.1. Sampling Platform

The sampling platform used for this research was a twin engine Piper Aztec-E PA-23-250 research aircraft (owned and operated by Advanced Helicopter Concepts, Figure 1). The aircraft is outfitted with a suite of trace gas and aerosol instruments, the inlets for which are on the upper fuselage. There is an aft-facing inlet plumbed to the trace gas instruments while a forward facing, isokinetic inlet feeds the aerosol instruments. Due to apparent inlet sampling line impaction losses of particles larger than 1 μ m (diameter), reported measurements are of sub-μ m particles only. A meteorological probe is nestled between these two inlets. Geographic position is measured and stored using a Global Positioning System, GPS (Garmin GPS-90), with 10 s resolution, and verified several times per flight relative to known geographic reference points. Data acquisition for the continuous meteorological and trace gas instruments at 10 s resolution is performed using a Rustrak Ranger II (EIL Instruments Inc., Hunt Valley, MD) data logger. Aerosol data are logged every 10 s on the aircraft PC based system using commercial and custom data acquisition software.

Figure 1. Photograph of the Piper Aztec-E PA-23-250 research aircraft.

2.2. Meteorological Measurements

Temperature and relative humidity (RH) were measured using a thermistor and capacitive thin film, respectively, with a regularly calibrated Rustrak RR2-252 RH probe (EIL Instruments Inc., Hunt Valley, MD). The instrument is capable of 0.5^{o} C temperature precision and 2% humidity precision at a 30 s response time.

2.2.1. Pressure Altitude

Static pressure was measured inside the unpressurized cabin of the aircraft using a Rosemount Model 2008 pressure transducer, capable of 5 mb precision, and calibrated regularly with a laboratory standard. To calculate pressure altitude, the average static pressures before takeoff and after landing as recorded by the pressure transducer are calculated. Altimeter readings reported by the Automated Weather Observation System (AWOS) at the airports are recorded before takeoff and after landing for every flight. The altimeter reading before takeoff is converted to millibars (mb) and subtracted from the average static pressure value before takeoff. The same

procedure is then followed for the altimeter reading and average static pressure value after landing. The two differences are averaged together. The average value is then subtracted from the static pressure values recorded during the flight and the resultant pressures in mb are converted to pressure altitude (*palt*) using the 1976 standard atmosphere equation:

$$palt = 8303.951372 \times \ln(1013.25 / pressure) \quad (6)$$

The altitude of the airport at takeoff is added to the resulting pressure altitudes. Likewise, the altitude of the airport at landing is added to the resulting pressure altitudes. The two sums are then averaged to give the final pressure altitude values. Adding in quadrature the uncertainty from the altimeter readings and the static pressure measurements, the estimated uncertainty of the pressure altitude values is ± 50 m (95% confidence).

2.3. Trace Gas Measurements

2.3.1. Ozone

Ozone data were acquired with a commercial instrument based on the principle that O_3 absorbs UV light at 254 nm (Thermo Environmental, TEI Model 49, Franklin, MA). The amount of absorption is directly related to the O_3 mixing ratio as described by the Beer-Lambert Law:

$$\frac{I}{I_o} = e^{-axc} \quad (7)$$

where:

a = molecular absorption coefficient, 308 cm^{-1} (STP)

x = path length, 38 cm

c = O_3 mixing ratio (ppbv)

I = UV light intensity with O_3 (sample gas)

I_o = UV light intensity without O_3 (reference gas)

The sample is drawn into the inlet and split into two streams (Figure 2). One of the streams is passed through an O_3 scrubber to become the reference gas (I_o) and continues on to the reference solenoid valve. The other gas stream (I) goes to the sample solenoid valve. The solenoid valves alternate the flow of sample and reference streams to the two cells, A and B, every 10 s. The UV light intensity is measured in each cell by detectors A and B. The difference between the sample and reference cells is the O_3 mixing ratio. This instrument is routinely compared to an in-house primary O_3 calibrator (TEI Model 49PS) and is capable of 1 ppb precision for 10 s data.

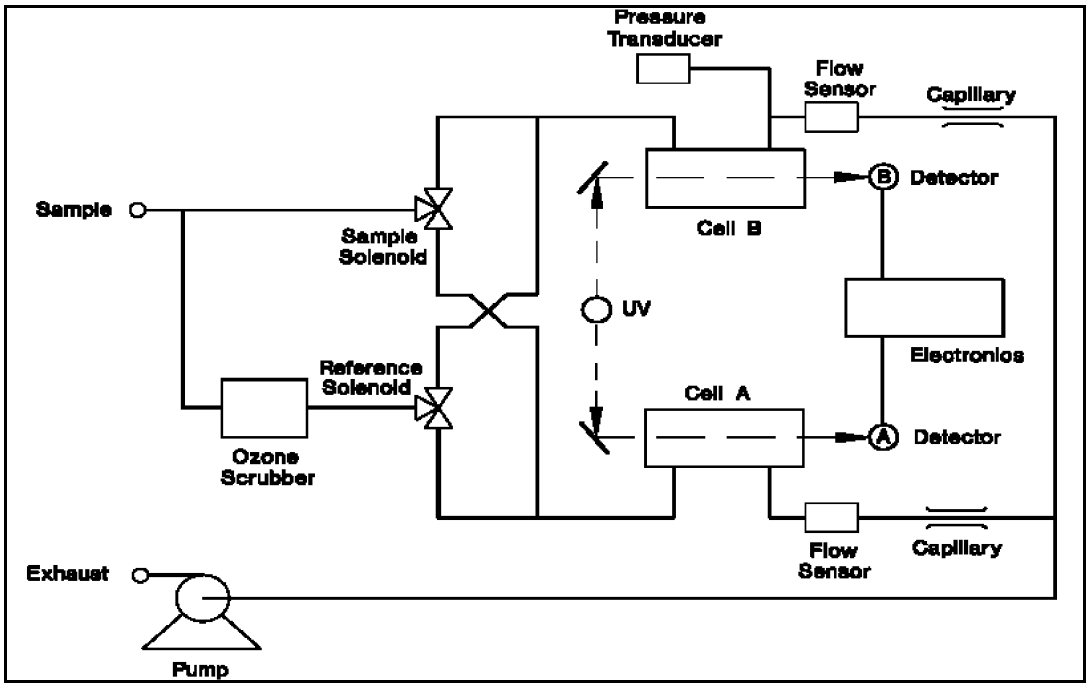

Figure 2. Schematic of the TEI model 49.

2.3.2. Carbon Monoxide

For observations of CO, a high-performance, modified (Dickerson and Delany, 1988) commercial (TEI Model 48) non-dispersive infrared gas filter correlation analyzer was used. The instrument operates on the principle that CO absorbs IR at 4.6 μm . The sample gas stream is drawn into the instrument and flows through the optical bench (see Figure 3). Infrared radiation is chopped, passed through gas filters alternating between CO and N_2, and then directed through a bandpass interference filter to the optical bench where it is absorbed by the sample gas. The remaining radiation exits the optical bench and falls on the detector. The CO gas filter fully absorbs the IR so that there is no further attenuation by the sample gas, thereby creating the reference beam. The N_2 does not absorb the IR, thus allowing absorption by CO in the sample cell. Alternating between the two gas filters effects a modulation of the chopped detector signal. Any interference by other gases is precluded by the fact that modulation of the detector signal occurs equally for the measure and reference beams. Thus, the amplitude of the signal is directly related to the concentration of CO in the sample gas.

The instrument is calibrated regularly using CO working standards (1.9 ppmv CO in nitrogen), in turn referenced to a National Institute of Standards and Technology (NIST) Standard Reference Material (1677c 9970 ppbv CO in nitrogen, certified; NIST, Gaithersburg, Maryland). This instrument is capable of ~2-5% precision determined for a 1-min mean of 10 s data. The CO instrument has

undergone formal international calibrations (Novelli et al., 1998) under a WMO protocol (Doddridge, 1995).

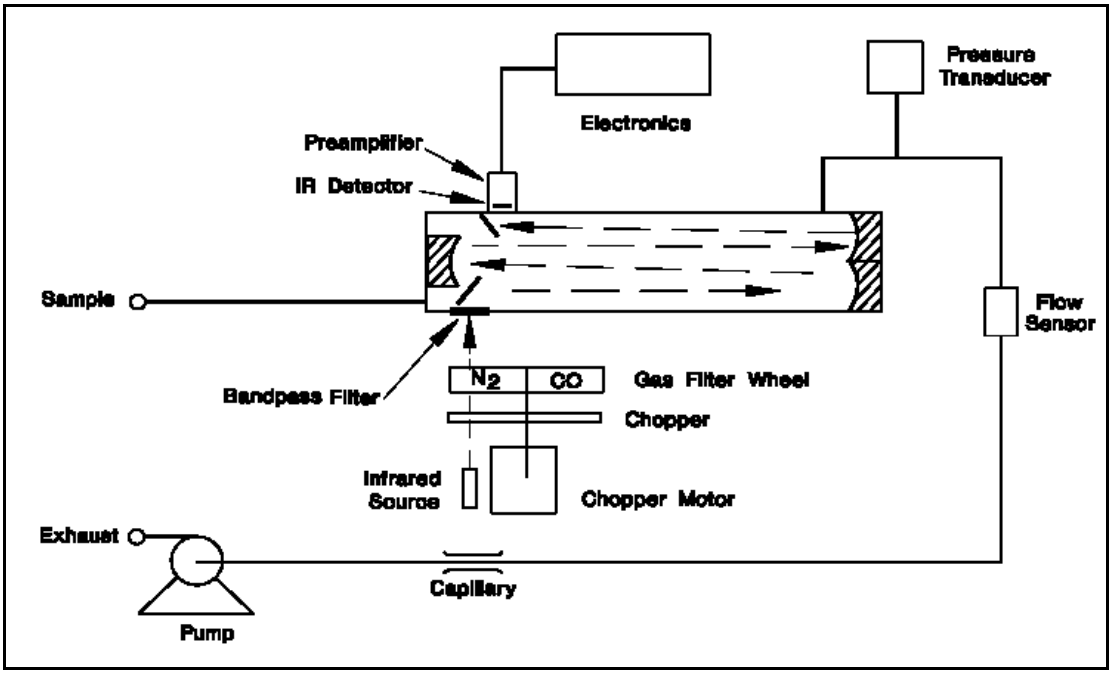

Figure 3. Schematic of the TEI model 48.

2.3.3. Sulfur Dioxide

A modified, commercial, pulsed-fluorescence detector (TEI Model 43C, see Figure 4) is used for measurements of ambient SO_2 (Luke, 1997). This instrument is based on the principle that SO_2 absorbs a pulsed UV light source in the 190 – 230 nm range and is promoted to an excited state. The excited molecule may then decay back to the ground state through one of three pathways: fluorescence, quenching, or dissociation.

Fluorescence:

$SO_2 + h\nu_1 \rightarrow SO_2^* \xrightarrow{k_f} SO_2 + h\nu_2$

Quenching:

$SO_2 + h\nu_1 \rightarrow SO_2^* + M \xrightarrow{k_q} SO_2 + M^*$

Dissociation:

$SO_2 + h\nu_1 \rightarrow SO_2^* \xrightarrow{k_d} SO + O$

where:

$h\nu_1$ = a photon of light at absorption frequency (1)

$h\nu_2$ = a photon of light at a different frequency of fluorescence (2)

M = any molecule available in the ambient air

k_f, k_q, k_d = the rate constants of the respective processes

Considering the above processes, an expression may be derived to represent the fluorescent intensity at the detector:

$$F = \frac{Gk_f I_o[1 - e^{-[ax(SO_2)]}]}{k_f + k_d + k_q[M]} \tag{8}$$

In this equation, G is a geometric factor related to the design of the fluorescent chamber, a is the absorption coefficient of SO_2 and x is the path length. However, when the SO_2 concentration is relatively low and the path length is short, the expression may be simplified to:

$$F = \frac{Gk_f I_o ax(SO_2)}{k_f + k_d + k_q[M]} \tag{9}$$

This expression can then be simplified further because k_f, k_q, and k_d remain mostly constant over a wide range of temperatures and background atmospheres. The

intensity of the impingent light (I_o) is also constant as are the geometric factor and path length. The equation may then be rewritten as a direct proportionality:

$$F = K(SO_2) \tag{10}$$

Thus, the fluorescent radiation that reaches the detector is directly proportional to the SO_2 concentration.

Based upon this principle of operation, the sample air is drawn into the instrument and directed through a hydrocarbon "kicker" (Figure 4). Many interferents, most notably aromatic hydrocarbons, mimic the fluorescent activity of SO_2. The "kicker" removes hydrocarbons from the sample by forcing the molecules to permeate the tube wall. The unaffected SO_2 then enters the fluorescence chamber where it is excited by pulsed UV light that has been wavelength selected by the mirror assembly. As the excited SO_2 molecules decay, the bandpass filter only allows the emitted radiation to reach the photomultiplier tube. In this way, the concentration of trace levels of ambient SO_2 is measured. The instrument has a detection limit of ~140 pptv (S:N=1:1 for $\pm 2\sigma$ noise) for a 1-min mean of 10 s data and is calibrated regularly using SO_2 working standards.

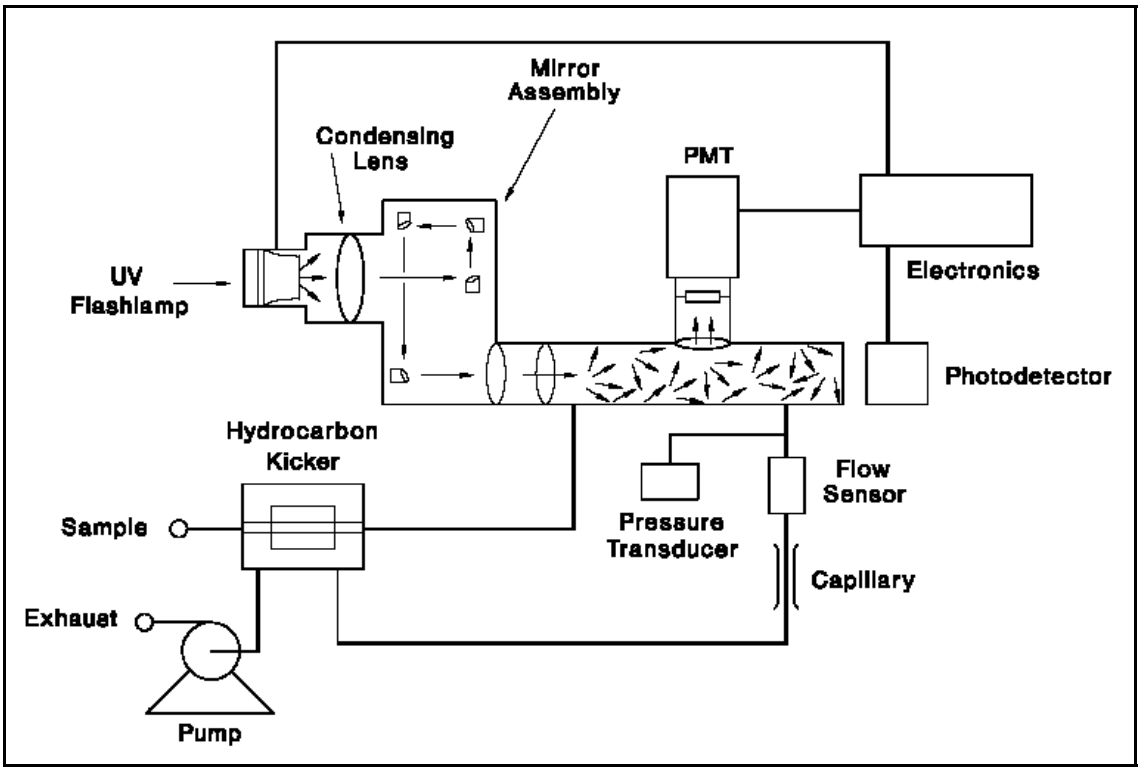

Figure 4. Schematic of the TEI model 43.

2.4. Aerosol Measurements

2.4.1. PSAP

Particle light absorption is measured using a Particle/Soot Absorption Photometer (PSAP, Radiance Research, Seattle, WA). The operational principle is based on the integrating plate technique whereby the intensity of 565 nm light is measured after passing through a filter subjected to ambient aerosol deposition. The transmissivity of the filter is related to the light absorption coefficient of the particles according to Beers Law:

$$A = \ln(I_o/I) \tag{11}$$

where:

A = the absorbance

I_o = the original intensity of impingent light

I = the intensity of transmitted light

The absorption coefficient of the particles (σ_{ap}) can be calculated according to the volume of sample air during the specified averaging time:

$$\sigma_{ap} = (A/V)\ln(I_o/I) \quad (12)$$

where:

A = the area of the sample spot (varies according to the instrument)

V = volume of the air sampled in the averaging period

I_o = the average filter transmittance for averaging period, j

I = the average filter transmittance for averaging period, j + 1

The absorption coefficient is corrected for filter nonlinearity such that:

$$\sigma_{ap,\,corr} = \sigma_{ap} f(Tr) \quad (13)$$

In this equation, *f(Tr)* is a transfer function specific to filter loading of Pallflex filters. The particles are filtered out of the sample stream when it passes through the sample filter. The remaining stream (reference stream) is then passed through a reference filter (Figure 5). The reference filter, which is adjacent to the sample filter, measures the constancy of the LED light source (Figure 6).

The detection limit (95% confidence level) for S:N=1 is 0.9×10^{-6} m^{-1} (Anderson *et al*., 1999, Bond *et al*., 1999) when 1-min measurement averages are used. Further corrections to absorption values were made for differences in flow rate (as measured by the instrument and an electronic bubble flow meter) and spot size, instrumental variation, noise, and exaggerations of absorption due to scattering and

non-scattering influences (Bond *et al.*, 1999). The estimated instrumental uncertainty for the absorption values is 25% with 95% confidence.

Variations in RH have been shown to cause measurement inaccuracies in the PSAP (Anderson *et al*., 2002), which operates under ambient conditions. For this reason, the commercial instrument was modified at the University of Miami. There, a heater and insulator were added to the optical bench portion of the PSAP so that the sample air would be dried before absorption measurements were made. In theory, this should have removed the uncertainty caused by variations in the RH, but introduced new uncertainty in converting dry absorption measurements to ambient conditions. However, the modification was ineffective; a RH dependence in the absorption measurements was still apparent after the modification was made.

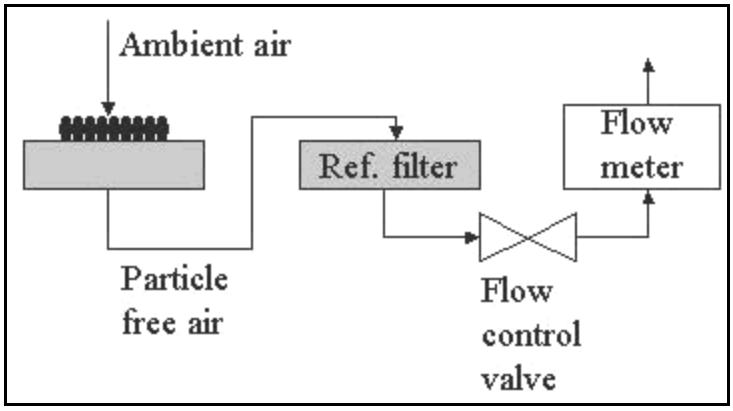

Figure 5. Flow diagram of the PSAP showing the sample filter (left) and reference filter (right).

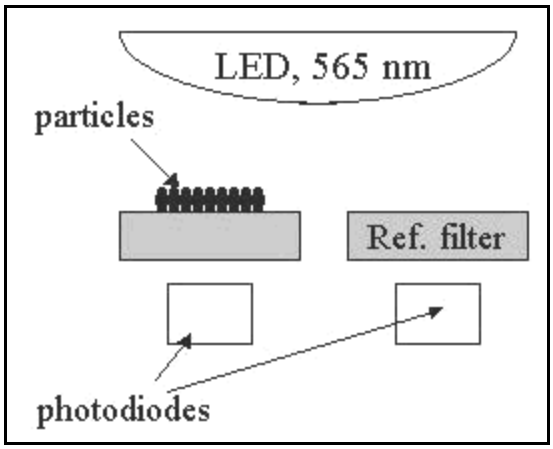

Figure 6. Schematic showing light absorption by the sample filter (left) and reference filter (right).

2.4.2. Nephelometer

Particle light scattering is quantified using an integrating nephelometer (TSI Model 3563) that measures the particle scattering coefficient (σ_{sp}) at 450, 550, and 700 nm after correcting for light scattered by the walls of the measurement chamber, the sample gas, and any electronic noise (Anderson *et al.*, 1996) (Figure 7). Total scattering is measured by integrating the scattered light over an angular range of 7 – 170°. Backscatter may also be measured through the use of the backscatter shutter, which adjusts the integrated range to 90 – 170°.

The instrument operates based on principles described by the Beer-Lambert Law:

$$\frac{I}{I_o} = e^{-\sigma_{ext}x} \tag{14}$$

where:

$$\sigma_{ext} = \sigma_{scat} + \sigma_{abs} \tag{15}$$

$$\sigma_{scat} = \sigma_{rg} + \sigma_{sp} \quad (16)$$

$$\sigma_{abs} = \sigma_{ag} + \sigma_{ap} \quad (17)$$

In these equations, σ_{rg} represents Rayleigh scattering by gases, σ_{sp} represents particle scattering, σ_{ag} represents absorption by gases, and σ_{ap} represents particle absorption. The instrument measures σ_{scat} and calculates σ_{sp} by also measuring and then subtracting σ_{rg} from σ_{scat}.

The nephelometer is calibrated with CO_2 and particle-free air, and corrected as necessary. At an averaging time of 5 minutes, detection limits for S:N=2 are: $\sigma_{sp450} = 0.44\times10^{-6}$ m^{-1}, $\sigma_{sp550} = 0.17\times10^{-6}$ m^{-1}, and $\sigma_{sp700} = 0.26\times10^{-6}$ m^{-1}. Corrections were made to the measurements to account for forward scattering angular truncation and nonlambertian distribution of illumination intensity within the nephelometer. A wavelength dependent correction factor (C_{ts}) was calculated assuming a linear relationship between C_{ts} and the scattering Ångström exponent (α), such that $C_{ts} = a + b\ \alpha$, where a and b are constants used for sub-μm particles and $\alpha_{450/550}$, $\alpha_{450/700}$, and $\alpha_{550/700}$ are used for 450, 550, and 700nm, respectively (Anderson and Ogren, 1998). The estimated instrumental uncertainty for values of total scattering is 10% with 95% confidence.

Measurements of light scattering were made after the sample airflow was dried from ambient conditions to an RH of < 20%. This necessitated the estimation of a growth factor, $F(RH)$, to account for hygroscopic particle growth. $F(RH)$ is the ratio of ambient light scattering, $\sigma_{sp}(\lambda, RH)$, to dry light scattering, $\sigma_{sp}(ref)$:

$$F(RH) = \frac{\sigma_{sp}(\lambda, RH)}{\sigma_{sp}(ref)} \tag{18}$$

$F(RH)$ was calculated using the following relationship between particle scattering coefficients at two values of RH:

$$\frac{\sigma_{sp}(\lambda, RH)}{\sigma_{sp}(ref)} = \left(\frac{1 - RH_{amb}}{1 - RH_{ref}}\right)^{-\gamma}, \tag{19}$$

where RH_{amb} is the ambient RH, RH_{ref} is the RH inside the nephelometer, and γ is an empirically derived constant. Parallel nephelometers were not used in this study, so γ had to be estimated. In polluted conditions, such as those on the east coast of the U.S., typical values of γ range from 0.20-0.50. For this research a value of 0.35 was chosen as per Remer *et al.* (1997) because of the similarities in both the sampling platforms and the regions of the studies.

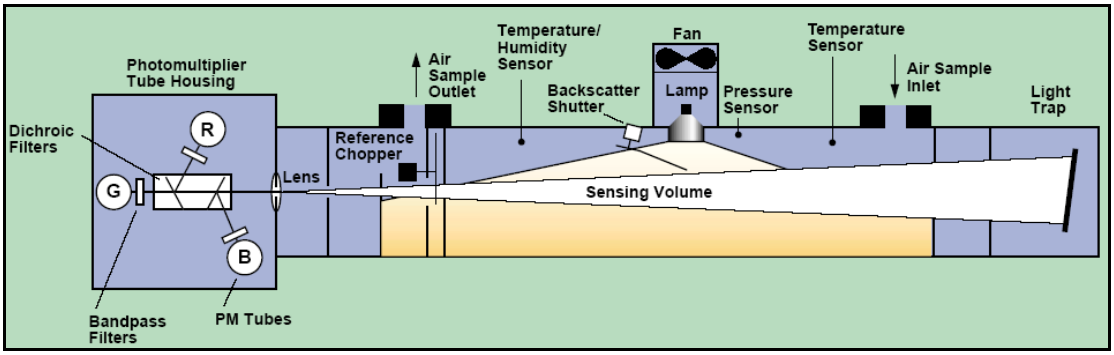

Figure 7. Schematic of the TSI model 3563 three-wavelength integrating nephelometer.

2.4.3. Particle Counts

Information on the total number of particles with optical diameters between 0.01 and 1.0 μm was obtained using a condensation particle counter (TSI Model 3007

CPC) (Figure 8). An internal pump draws the sample air stream through a saturator tube where isopropyl alcohol saturates the sample stream. The air stream then passes through a cooled condenser tube. The alcohol vapor becomes supersaturated and condenses onto any particles larger than 10 nm in diameter. The particles exit the condenser and are passed through a laser. The scattered light is collected and focused onto a photodetector where it is converted to an electrical signal and recorded as a particle count. The frequency of this instrument can be as great as particles s^{-1} and the concentration range is 0 – 100,000 particles cm^{-3}.

Number concentrations for particles with optical diameters between 0.30 and 1.0 μm (nDp) were collected using an optical particle counter (Met One Model 9012). The basic operation of this instrument is the same as the condensation particle counter, but there is no pre-optics condensation process. The internal pump draws the sample stream into the instrument where a laser-diode based optical sensor is used to convert scattered light to numbers of particles in particular size ranges. The pre-specified size ranges were 0.30-0.40 μm, 0.40-0.491 μm, 0.491-0.60 μm, 0.60-0.701 μm, 0.701-0.80 μm, and 0.80~1.0 μm.

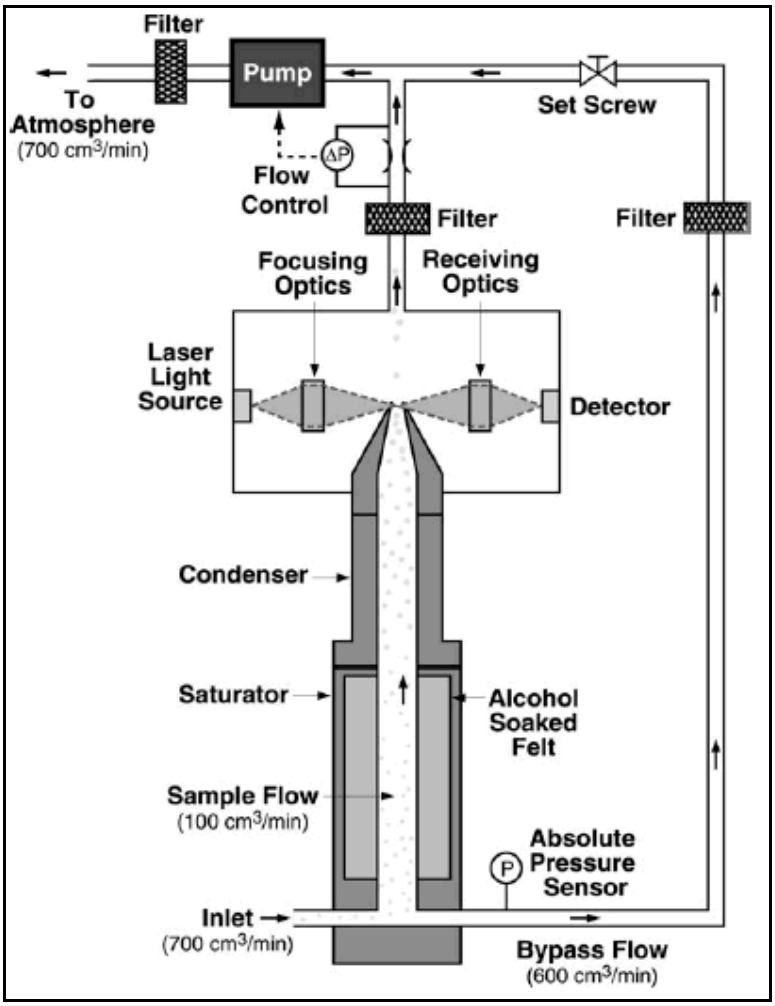

Figure 8. Schematic of the TSI Model 3007 Condensation particle counter.

Chapter 3: The Two-Reservoir Conceptual Model

3.1. Introduction

This chapter investigates the hypothesis that the chemistry and physics of multi-day haze and O_3 episodes over the Mid-Atlantic and northeastern U.S. may be treated as a simple two-reservoir model, comprising the LFT and PBL. Conclusions are based on aircraft measurements made during a constant altitude transect from Manchester, New Hampshire (42.9º N, 71.4º W) to College Park, Maryland (39.0º N, 76.9º W) on August 14, 2002, the last day of a multi-day haze and O_3 episode, and subsequent analyses of air parcel age, source apportionment, and boundary layer chemistry and dynamics.

The flight began in Manchester, NH at 21:45:02 UTC on August 14, 2002 and ended in College Park, MD at 00:30:23 UTC, just after sunset (Figure 9). An altitude of 800 m above mean sea level (MSL) was attained at 21:50:41 UTC and maintained until 00:20:00 UTC. Takeoff and landing are excluded from all time series plots for clarity.

Investigation of the aforementioned hypothesis begins with a brief meteorological analysis of the three-day episode, including new data on the impact of the LLJ on Mid-Atlantic and Northeast haze and O_3 episodes. A statistical analysis is used in order to garner information about source apportionment and air parcel age. Potential temperature (θ) is used as a proxy for altitude above ground level to investigate the chemical and physical signatures of air parcels as they vary with

height. The results described in this chapter are based on work published in the Journal of the Atmospheric Sciences (Taubman *et al*., 2004(a)).

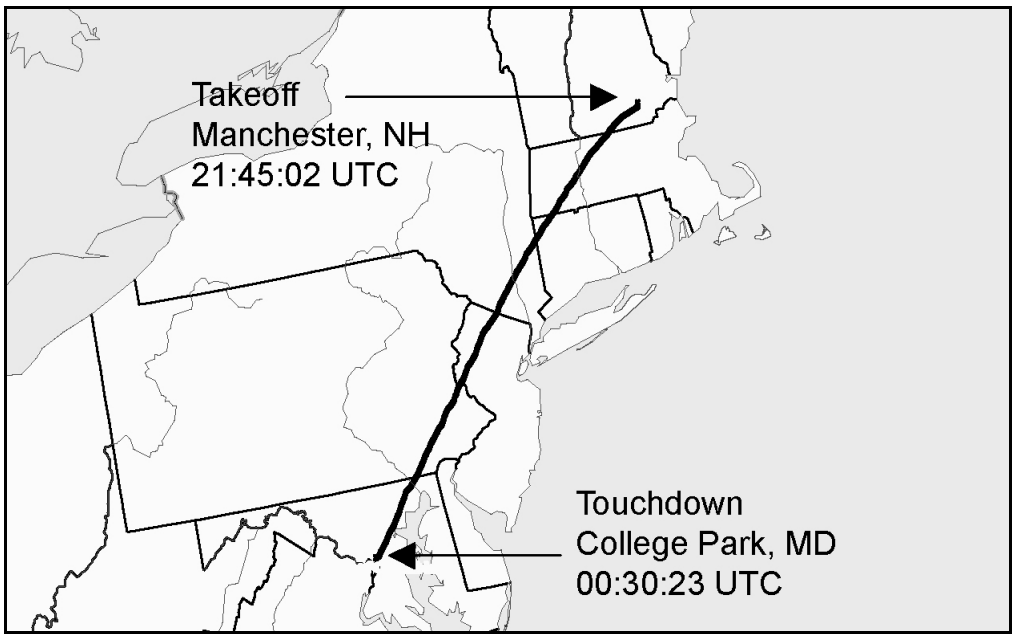

Figure 9. Flight track that began in Manchester, New Hampshire at 21:45:02 UTC and ended in College Park, Maryland at 00:30:23 UTC. Except for initial ascent and final descent, the altitude was constant at 800 m above mean sea level (Taubman *et al.*, 2004(a)).

3.2. Meteorology

On August 10, 2002, a slow moving upper level ridge positioned itself over the Great Lakes while a surface high-pressure system, lying below the region of convergence in the downwind upper level trough, blanketed the eastern seaboard. By August 12, at 850 mb, a trough over the Great Lakes, together with a ridge over the northeastern U.S., created an isobaric gradient normal to an axis lying along the U.S.-Canadian border. Surface analyses on August 12 at 00:00 UTC and 12:00 UTC show a parallel, albeit weaker, isobaric pattern (Figures 10, 11). This general pattern

persisted through the 14th and resulted in prevailing southwesterly winds over the Midwest and Northeast. Stagnant conditions predominated over the Mid-Atlantic throughout the episode. Figures 10 and 11 also indicate the presence of an APLT that augmented southerly flow up the urban corridor. Surface temperatures in the Mid-Atlantic and Northeast rose steadily between the 10th and the 14th.

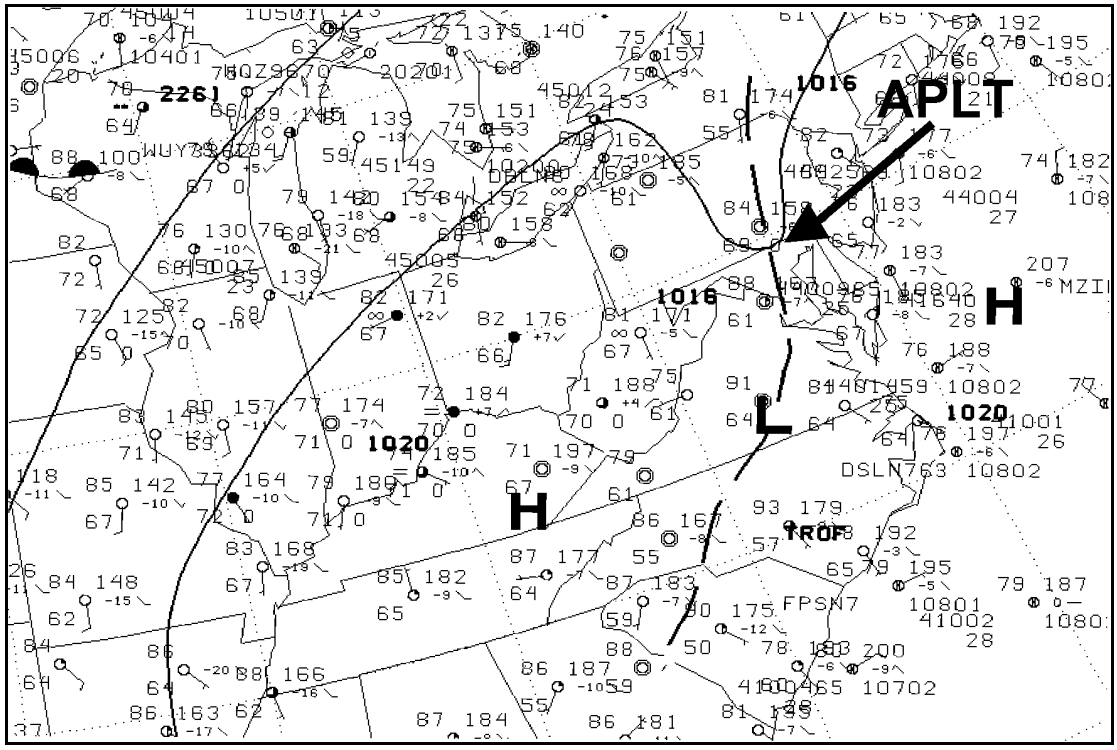

Figure 10. National Center for Environmental Prediction surface analysis for 00:00 UTC 12 August 2002 shows a weak isobaric gradient normal to the U.S.-Canadian border as well as the Appalachian Lee Trough (APLT) (Taubman *et al.*, 2004(a)).

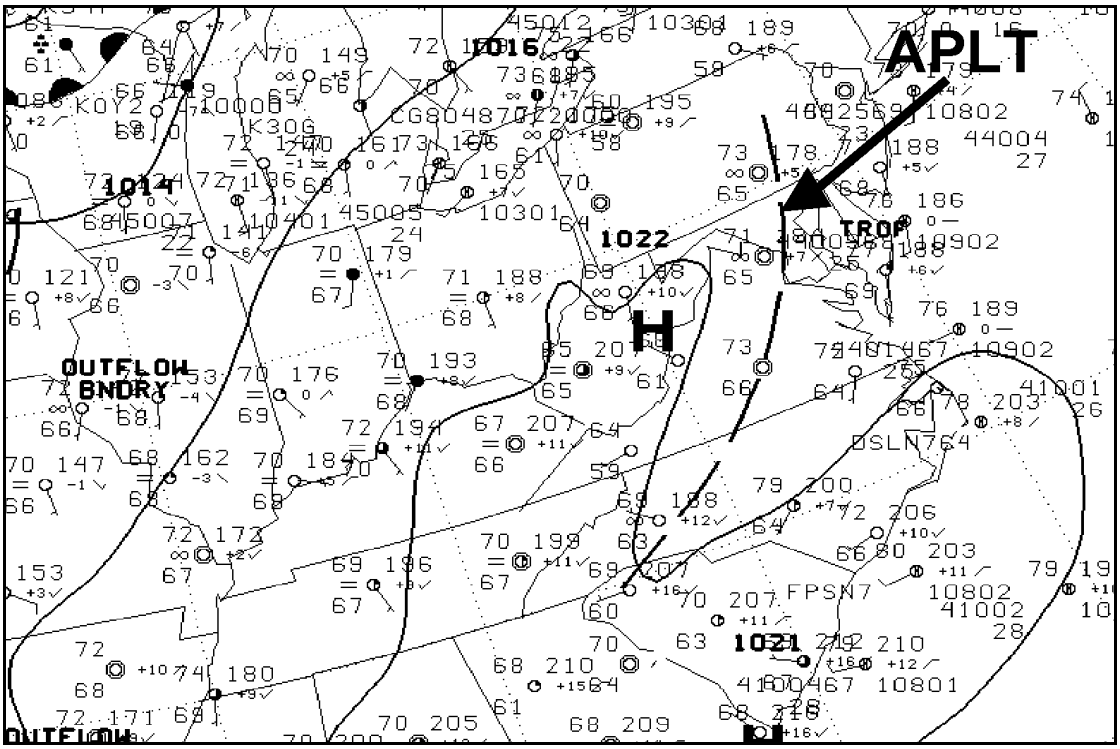

Figure 11. National Center for Environmental Prediction surface analysis for 12:00 UTC 12 August 2002 shows a weak isobaric gradient normal to the U.S.-Canadian border as well as the Appalachian Lee Trough (APLT) (Taubman *et al.*, 2004(a)).

A LLJ was observed every morning between ~01:00 UTC and 07:00 UTC at Ft. Meade, MD from the 11th through the 14th (Figure 12). The wind speed maximum appears to be between ~200 – 800 m AGL, indicating that the nocturnal stable boundary layer was quite shallow, with a maximum depth of only ~200 m AGL. The horizontal extent and magnitude of the jet on the 12th is shown in Figure 13, a time series plot of the Mid-Atlantic and Northeast generated using Rapid Update Cycle-2 (RUC-2) data (Benjamin *et al.*, 1998). The wind vectors in both the observed and analysis data show south-southwesterly flow during times of the jet maximum. At the indicated wind speeds and duration, an air parcel in the LLJ could travel >200 km up

the eastern seaboard overnight to mix with the local air under the jet once the nocturnal inversion eroded and vertical mixing ensued during the daytime.

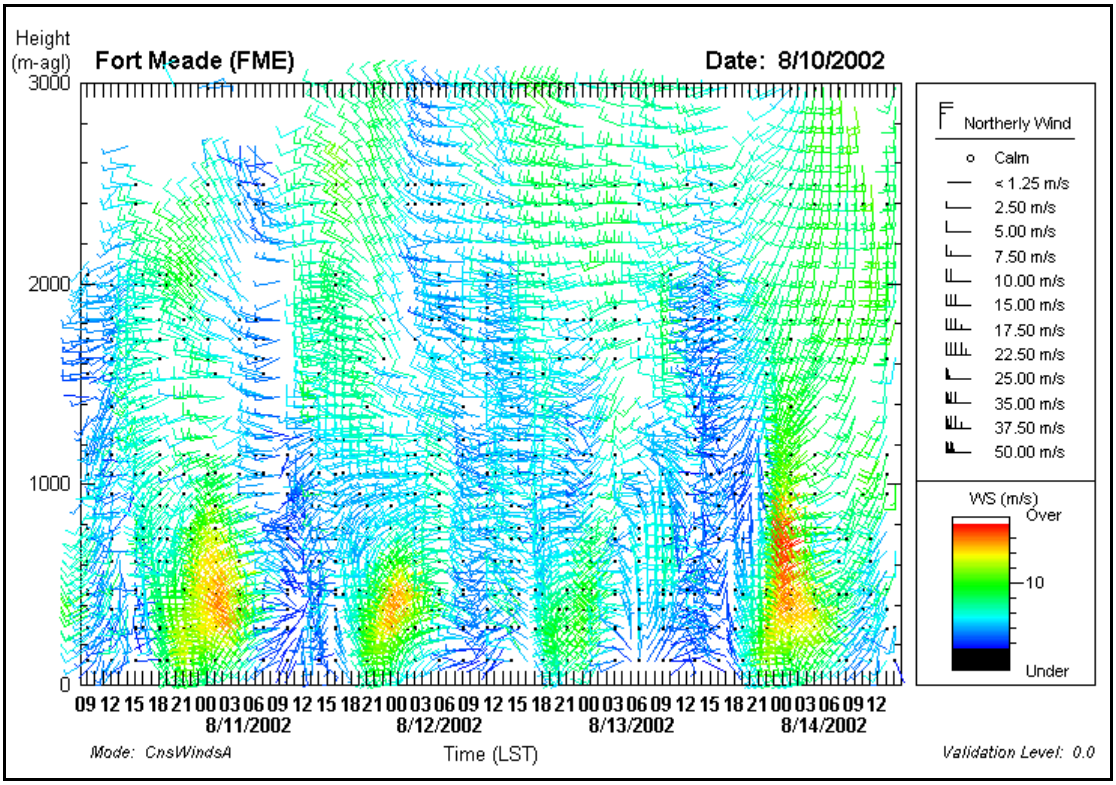

Figure 12. Wind profiler data (30 min average) from Ft. Meade, Maryland from 09:00 LST 10 August to 15:00 LST 14 August 2002 showing south-southwesterly flow in the jet with a maximum between 200 – 800 m AGL (Taubman *et al.*, 2004(a)).

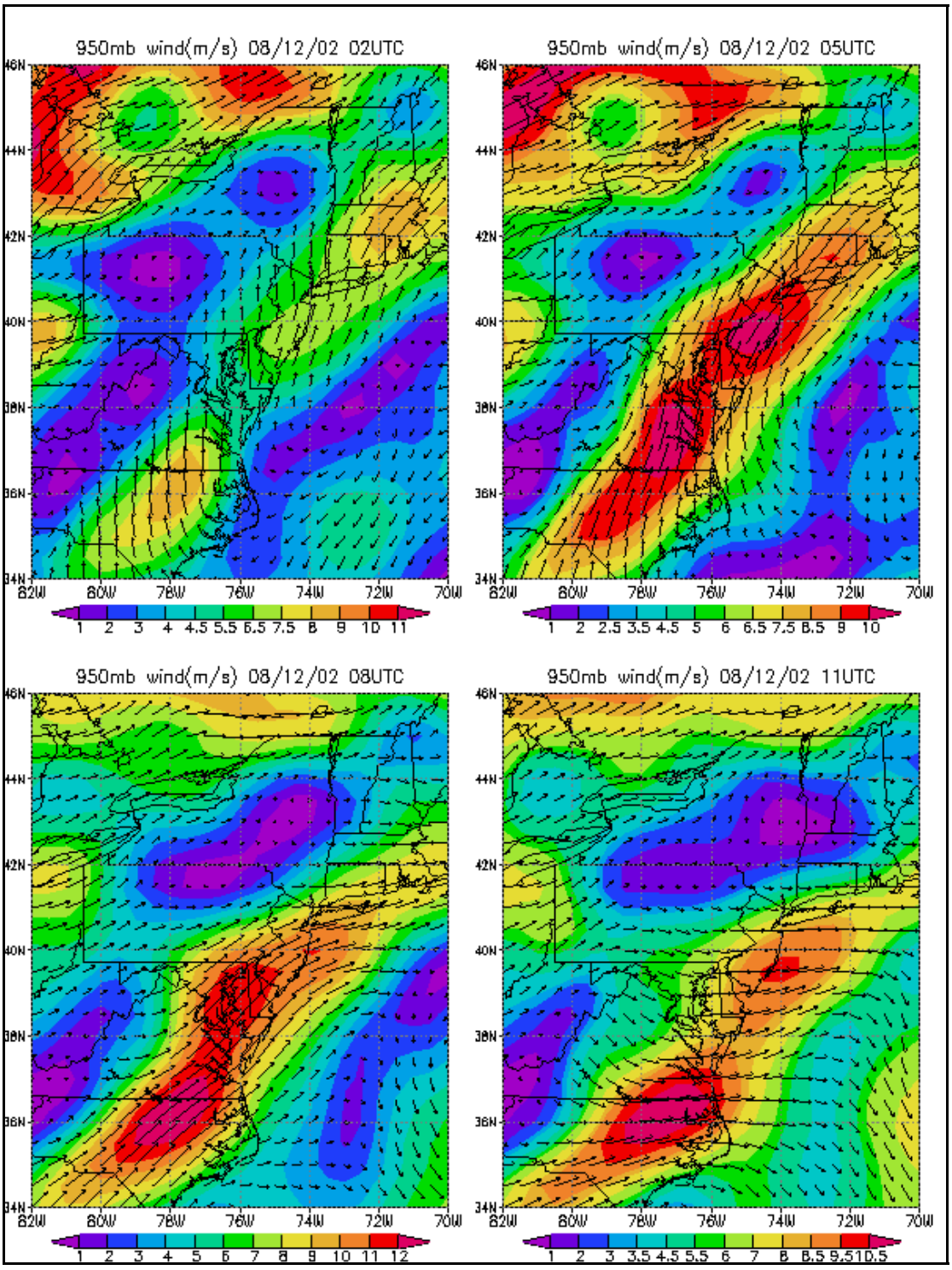

Figure 13. A time series plot of the 950 mb (the approximate altitude of the LLJ) wind speed and direction over the Mid-Atlantic and Northeast from 02:00 to 11:00 UTC 12 August 2002 generated using RUC-2 data (Taubman *et al.*, 2004(a)).

3.3. Observations and Analyses

3.3.1. Trajectory Analysis

A backward trajectory analysis of the entire flight track was performed utilizing the NOAA ARL HYbrid Single-Particle Lagrangian Integrated Trajectory (HYSPLIT) model (Version 4) (Draxler and Rolph, 2003) and Eta Data Assimilation System (EDAS) meteorological fields (with a 3 h temporal resolution). The 72 h model vertical velocity backward trajectories ending at 500, 1000, and 1500 m above ground level (AGL) came primarily from the south-southwest and intersected many of the urban centers in the Mid-Atlantic and Northeastern U.S (e.g., Figure 14). There was little difference in the source regions or transport direction of the parcels analyzed. However, a significant difference was seen in the vertical motions of the air parcels that culminated in southern upstate New York near the Hudson River Valley (Figure 14). A transition from downward vertical motion to upward vertical motion in this area appears to have occurred at ~23:00 UTC.

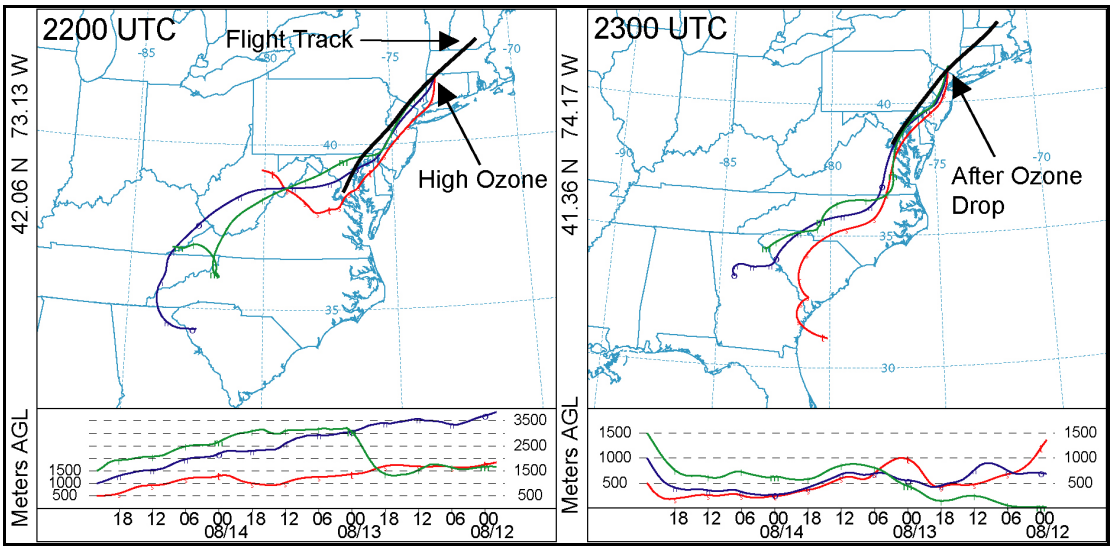

Figure 14. Sample NOAA ARL EDAS model vertical velocity 72 hour backward trajectories for air parcels at 500, 1000, and 1500 m AGL on 14 August 2002 at 42.06° N, 73.13° W, 22:00 UTC (left), where the highest O_3 was measured, and 41.36° N, 74.17° W, 23:00 UTC (right) after a steep decline in O_3 concentration. There is no noticeable distinction in transport direction between the trajectories, but there is a manifest conversion from subsidence (left) to upward vertical motion (right) (Taubman *et al.*, 2004(a)).

3.3.2. Trace Gases

Correlations among the chemical and physical properties observed during the flight allow for insight into source apportionment, photochemical age, and the dynamical structure of the lower atmosphere. To estimate the number of independent air parcels (i.e., the number of degrees of freedom associated with each time series plot), autocorrelation tests were performed that correlated measured variables with themselves over successive time intervals. The threshold for autocorrelation (non-randomness between the two points) was $r > 0.50$ (95% confidence). Any value below this threshold indicated that there was no statistically significant relationship between the points after this time lag, thereby suggesting the presence of a discrete air

parcel. The number of independent air parcels was then calculated from dividing the sampling period by the autocorrelated time lag. Approximately 10 discrete air parcels were positively identified in this manner (the exact value varied slightly according to the variable tested). The statistical significance of each correlation was determined according to the number of degrees of freedom (discrete air parcels) and reported along with the correlation coefficients (Table 1).

Table 1. Correlation coefficients, r, for trace gases, meteorological and dynamic parameters, and particle properties. The number in parenthesis is the p value (the probability that the statistical relationship occurred by random chance) for the regression. If two sets of correlation coefficients and p values are given, the top one is for the regression until 22:56:00 UTC and the bottom is for the period between 22:56:10 and 23:10:00 UTC (Taubman *et al.*, 2004(a)).

	O_3 (ppbv)	CO (ppbv)	σ_{sp450} (m^{-1})	σ_{ap} (Mm^{-1})	$\alpha_{450/700}$
CO (ppbv)	0.70(0.08) -0.84(0.02)				
SO_2 (ppbv)	0.70(0.08) -0.67(0.10)	0.71(0.02)			
σ_{sp450} (m^{-1})	0.90(0.00)				
σ_{sp550} (m^{-1})	0.89(0.00)			0.79(0.03) 0.10(0.87)	
σ_{sp700} (m^{-1})	0.88(0.00)				
nDp (dm^{-3}) 0.30- 0.40 μm	0.76(0.01)			0.50(0.25) -0.45(0.31)	
nDp (dm^{-3}) 0.40-0.49 μm	0.90(0.00)		0.96(0.00)		
TPC (cm^{-3})	0.67(0.10) -0.63(0.13)			0.79(0.00)	
σ_{ap} (Mm^{-1})	0.68(0.09) -0.73(0.16)				
RH (%)					0.82(0.00)
θ (K)	0.56(0.09)				-0.86(0.00)
BC (μg m^{-3})		0.57(0.09)			
ω_b	-0.58(0.17) 0.77(0.04)				

CO and SO_2 were positively correlated throughout the flight and early positive correlations were found between O_3 and CO and O_3 and SO_2 (Table 1, Figure 15), suggestive of a combination of mobile and point source emissions. The initial correlation between O_3 and CO had a regression slope ($\Delta O_3/\Delta CO$) of 0.31 ± 0.04. This value agrees with previous examples of polluted, North American, boundary layer air (Chin *et al.*, 1994, Daum *et al.*, 1996, Dickerson *et al.*, 1995). CO decreased at ~22:40:00 UTC and no longer showed a strong positive correlation with O_3 (Table 1,

Figure 15), whereas SO_2 remained positively correlated with O_3 until O_3 declined at ~22:56:00 UTC (Table 1, Figure 15). This suggests a shift from mixed mobile and point source influences to point source dominated ones.

When the O_3 concentration decreased at ~22:56:00 UTC near the Hudson River Valley, CO and SO_2 concentrations increased and became anti-correlated with O_3 (Table 1, Figure 15). This transition corresponds to the shift in the backward trajectories from downward to upward vertical motion. The increase in CO and SO_2 suggests the influence of mixed sources again, while the sudden decrease in O_3 could be explained by NO_x titration in the middle of a combination mobile and point source plume.

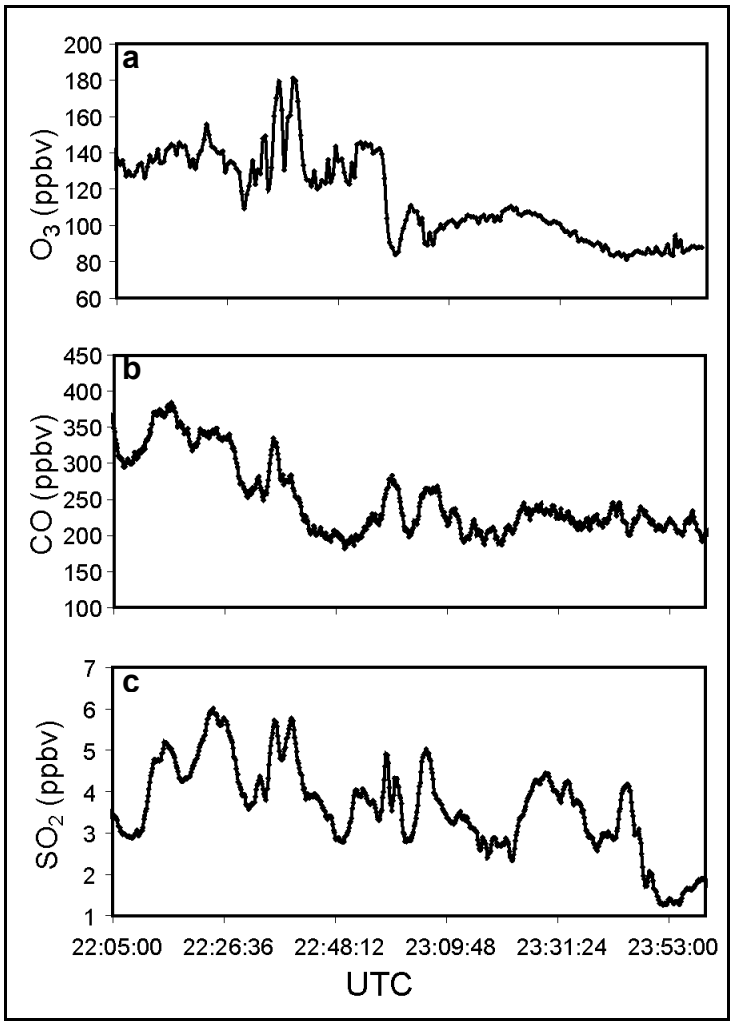

Figure 15. 10 s ozone mixing ratios (a) and running 1 min. mean CO (b) and SO2 (c) mixing ratios measured during the flight (Taubman *et al.*, 2004(a)).

3.3.3. Aerosols

O_3 and nDp (especially particles with diameters between 0.40-0.491 μm), as well as O_3 and σ_{sp}, were positively correlated throughout the entire flight (Table 1, Figures 15, 16). O_3 and total particle counts between 0.01 and 1.0 μm (TPC) along with O_3 and σ_{ap} were initially positively correlated (Table 1, Figures 15, 16). However, these profiles became anti-correlated at ~22:56:00 UTC, when the O_3

concentration rapidly declined (Table 1, Figures 15, 16). Thus, O_3 remained correlated with particles between ~0.30 and 1 μm in diameter, but when the O_3, nDp, and σ_{sp} profiles decreased at ~22:56:00 UTC, there was a significant increase in the number of absorptive particles < 0.30 μm in diameter. This is evidence of primary BC particles emitted from a local, mobile source that had insufficient time to mix with the sulfate-dominated haze of the region. When nDp, σ_{sp} , and σ_{ap} were correlated (before 22:56:00 UTC), greater absorption occurred despite the presence of fewer total sub-micrometer particles. Assuming that the air parcels contained internally mixed BC and sulfate particles at that time, this suggests that the internal mixture was more absorptive than the external one.

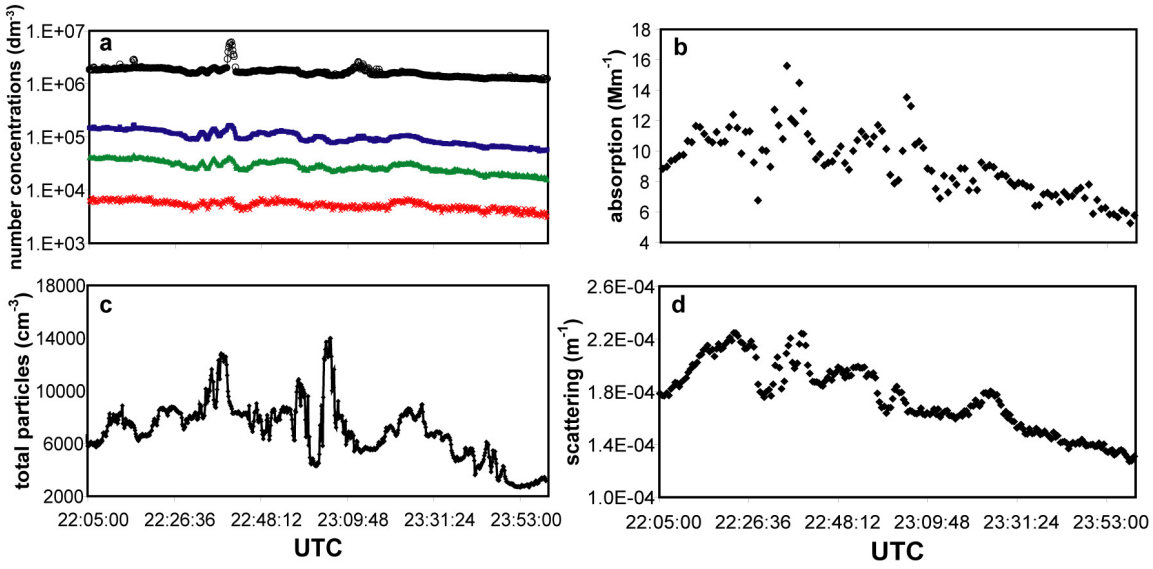

Figure 16. Particle number concentrations measured during the flight (a) for the following size ranges: 0.30-0.40 mm (black), 0.40-0.491 mm (blue), 0.491-0.60 (green), and 0.60-0.701 (red). σ_{ap} corrected to 550 nm (b); total sub-micrometer particle count (c); and σ_{sp} at 550 nm (d) all measured during the flight (Taubman *et al.*, 2004(a)).

The BC concentration was calculated from σ_{ap} assuming BC is the primary absorber in atmospheric aerosols. Despite apparent differences in degrees of mixing, an average mass absorption efficiency of 7 m^2 g^{-1} was assumed in accordance with prior, regional surface and aircraft studies (Novakov *et al.*, 1997; Chen *et al.*, 2001). A regression analysis of BC and CO was performed and a correlation (r = 0.57) was found between the two (Table 1), with a slope of $\Delta BC/\Delta CO = 0.0034 \pm 0.0007$. Chen e*t al.* (2001) found a similar value (0.0034 ± 0.0013) for the annual average at Fort Meade, MD. They scaled this number by the North American CO emissions value to compute a BC emission rate of 0.32 Tg yr^{-1}. The results of this flight support that estimate.

The aerosols measured during the flight were largely scattering. The mean value for ω_o at 550 nm over the entire flight was 0.95 ± 0.01 (see Figure 17), in agreement with previous aircraft observations over the east coast of the U.S. (e.g., Hartley *et al.*, 2000; Hegg *et al.*, 1997) and AERONET observations at NASA Goddard Space Flight Center between 1993 and 2000 (ω_o at 440 and 670 nm equal to 0.98 ± 0.02 and 0.97 ± 0.02, respectively) (Dubovik *et al.*, 2001). Nevertheless, the variations in ω_o were driven by the absorption in this study since σ_{ap} varied by as much as a factor of three, while σ_{sp} varied by less than a factor of two.

Before ~22:56:00 UTC, ω_o was anti-correlated to O_3, while after this time, O_3 and ω_o positively correlated (Table 1). Thus, initially, absorption was highest when the O_3 mixing ratio was highest. Total scattering also peaked at this time, but absorption was relatively stronger, leading to a smaller ω_o. After ~22:56:00 UTC, the greatest absorption was observed with the least O_3. There was a large influx of small,

absorptive particles during this time, and since σ_{sp} dropped off with O_3, ω_o decreased accordingly.

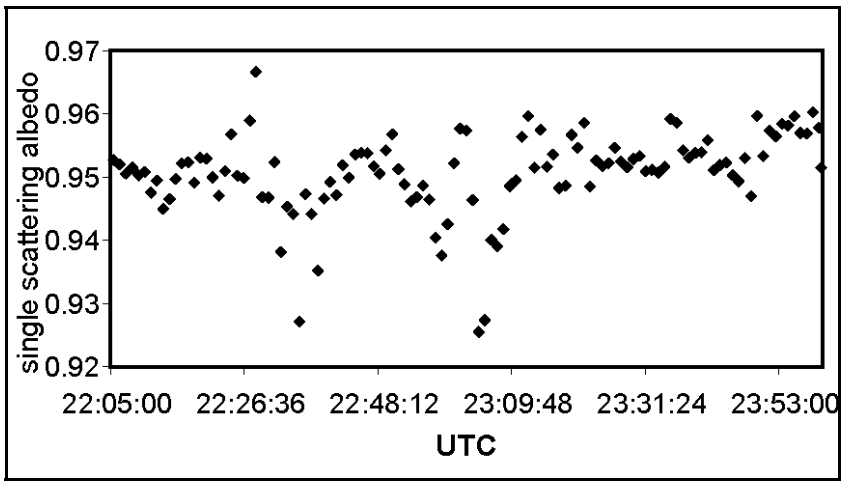

Figure 17. Aerosol single scattering albedo at 550 nm, calculated from flight data. The mean value for the flight was 0.95+0.01 (Taubman *et al.*, 2004(a)).

3.3.4. Thermodynamic Analysis

The flight under investigation was conducted at a constant altitude above mean sea level. Thus, the elevation above the surface increased or decreased according to the local terrain. Because the dynamic structure of the lower atmosphere tends to follow the surface features, the flight continually traversed through different dynamic altitudes. To investigate the dynamical structure of the lower atmosphere and the associated chemistry and physics, the potential temperature (θ) was calculated from the flight measurements of temperature and pressure. Figure 18 shows an inverse relationship between θ, calculated along a portion of the flight path, and the surface elevation, generated using a digital elevation model. This is the

expected result in a stable lower atmosphere, where θ is at a minimum and relatively constant in the daytime mixed layer, with a steep, positive gradient in the interfacial layer, and a smaller positive gradient in the LFT. Thus, as the surface elevation decreases, flight elevation above ground level increases, as does θ if the altitude is at or above the interfacial layer.

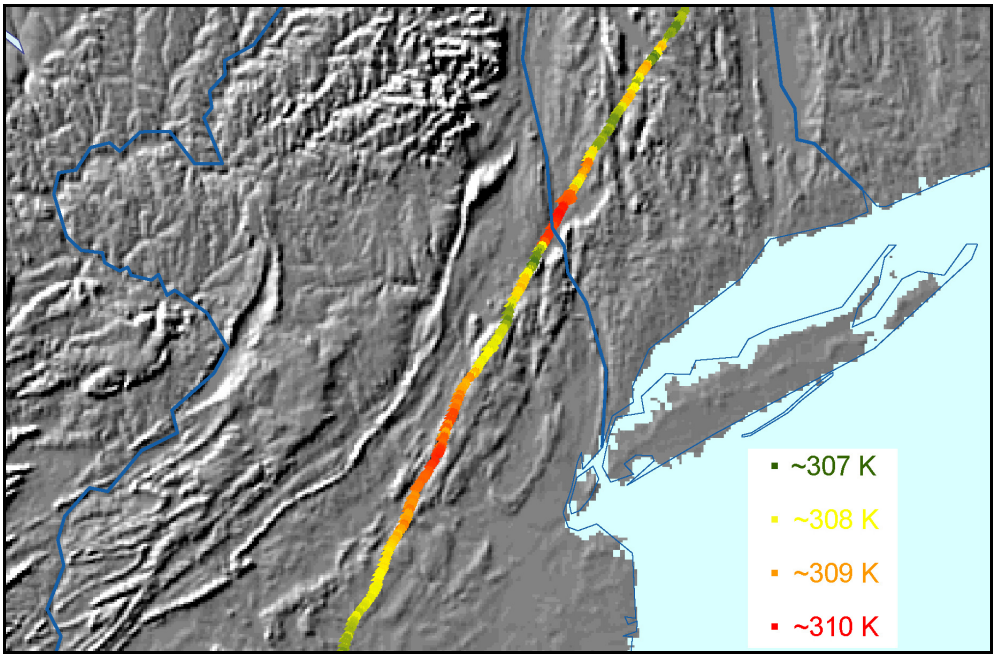

Figure 18. Potential temperature (θ) plotted with color-coded values (provided in the key) along a portion of the flight track. These values are overlaid on a shaded relief digital elevation model of the northeastern U.S. Darker shading signifies lower elevations and lighter shading, higher elevations. The blue lines indicate rivers. The one in the middle is the Hudson River. This region shows the most obvious inverse relationship between θ and surface elevation (Taubman *et al.*, 2004(a)).

It follows, then, that the chemical and physical nature of the atmosphere should vary with altitude, particularly between the PBL and the LFT. To investigate this hypothesis, statistical analyses with θ and representative chemical and physical values were performed. Ozone and θ were positively correlated throughout the flight

(Figure 19a, Table 1). Because θ is constant and at a minimum in the mixed layer, any increase would indicate a transition into the interfacial layer and beyond into the LFT. Likewise, O_3 concentrations should be fairly constant in the mixed layer, and because of the positive correlation with θ, any increases indicate more O_3 in the LFT relative to the PBL. Exceptions to this rule result from the spatially and temporally dynamic nature of the atmosphere and the platform, but the consistency of the correlation supports the argument.

Throughout the flight, α was positively correlated with RH and anti-correlated with θ (Figures 19b,c, Table 1). Within an individual air parcel, α and RH would be expected to anti-correlate because of the covariance of particle size and RH. Thus, the correlation between RH and α was due to the observation of distinct air parcels at discrete altitudes above the surface that contained particles of different sizes and unique optical properties. It can be reasonably assumed that particles in the LFT, where RH was lower and θ was higher, were more aged than those in the PBL. The photochemical processing of these particles would, therefore, be enhanced because of longer lifetimes as well as increased actinic flux in the LFT. This would explain why, despite the lower RH, the particles in the LFT were larger than those in the PBL. Conversely, particles in the PBL, where RH was higher and θ was lower, were relatively fresher and less subject to photochemical processing and hence, were smaller.

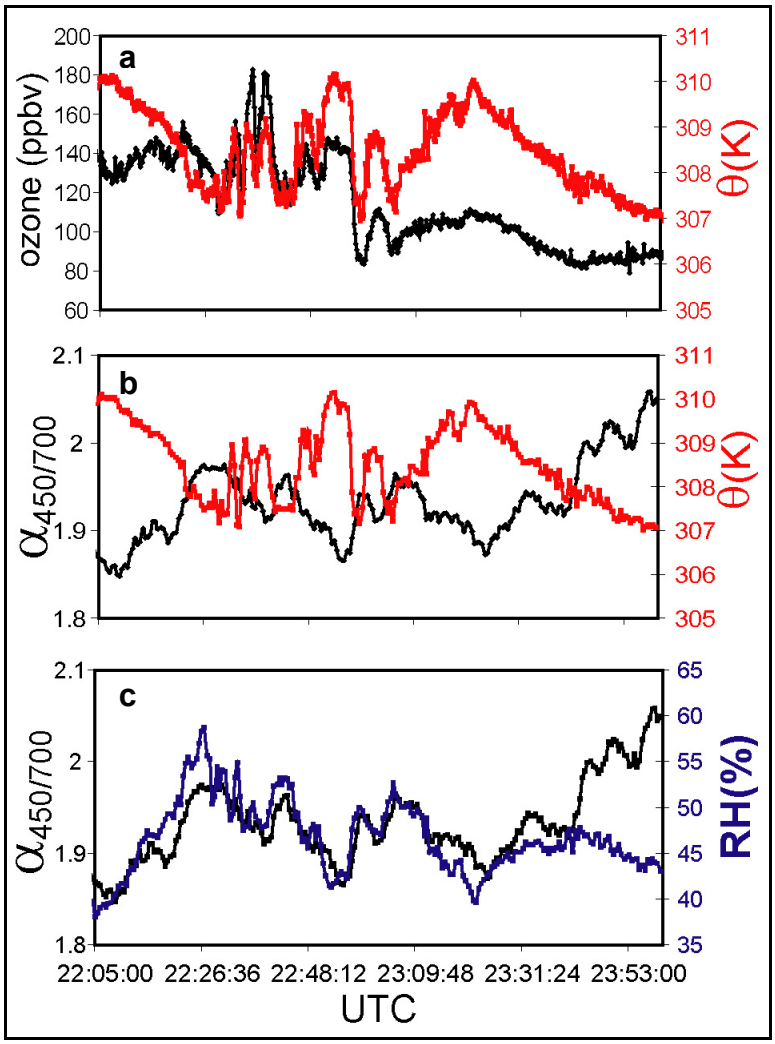

Figure 19. 10 s O_3 mixing ratios (black) recorded during the flight and potential temperature, θ, (red) derived from flight data (a); θ (red) and scattering Ångström exponent, α, (black) calculated from the ratio of total particle scattering, 450/700 (in nm), measured during the flight (b); relative humidity, RH, (blue) and α (black) calculated from flight data (c) (Taubman *et al.*, 2004(a)).

3.4. Discussion

The thermodynamic analysis indicates that the observed chemical and optical properties varied according to altitude, specifically whether the observations were made in the PBL or the LFT. Drier, more aged air parcels were observed in the LFT

where the protracted lower atmospheric stability allowed them to persist for multiple days without being subjected to vertical mixing, dilution, and deposition. These air parcels were more photochemically processed and contained higher concentrations of O_3 and larger particles that scattered and absorbed visible light efficiently. The relatively fresh parcels in the PBL had less O_3 and smaller particles that scattered light less efficiently, but were highly absorptive. Variations in the concentrations of CO and SO_2 seemed to vary less according to altitude *per se*. Rather, the source region and photochemical age of the air parcels in which they resided played more important roles.

The change in vertical winds between the trajectories shown in Figure 4 could be the result of upsloping winds on the windward side of the western ridge of the Hudson River Valley. The associated shift from positive to negative correlations between several species of interest is likely due to observations of the difference between air with more regional characteristics above the LFT to more local air in the PBL. As mentioned before, the absolute accuracy of such a conclusion is questionable because of the spatially and temporally dynamic nature of the study. The fact that the study was performed in the late afternoon, however, reduces the incidence of thermally driven convective eddies. Turbulent eddies would add to the variations in θ, according to the associated heat flux, but would be on a much smaller scale than θ fluctuations due to terrain characteristics.

The current foci of numerical model simulations of severe air pollution episodes are on the composition of the lower atmosphere, including especially the structure of the inversion layer, and the chemical and physical processes that drive the

events. This study provides a characterization of the chemistry and physics that occur during multi-day episodes in the Mid-Atlantic and Northeast that should prove useful in these simulations. The chemical and physical structure of the lower atmosphere could be conceptualized as a simple, two-reservoir model, comprising the PBL and LFT (Figure 20). Of particular importance is the realization that the LFT does not contain clean, background air during these episodes. This not only has direct consequences on model simulations of these episodes, but may have indirect ones as well. Photochemical mechanisms are accelerated in the LFT, but these mechanisms are also operating on air parcels with different chemical and physical characteristics than those in the PBL. Therefore, modeled photochemical mechanisms that work in the PBL would not be appropriate for the LFT. Numerical model simulations of multi-day haze and ozone episodes over the Mid-Atlantic and Northeast therefore must account for the unique chemistry and physics of the two reservoirs. However, future aircraft studies that specifically investigate the small-scale dynamical processes that drive the mixing between the two reservoirs are still necessary. These studies will allow for the more accurate simulation of transfer across the boundary separating the PBL and LFT.

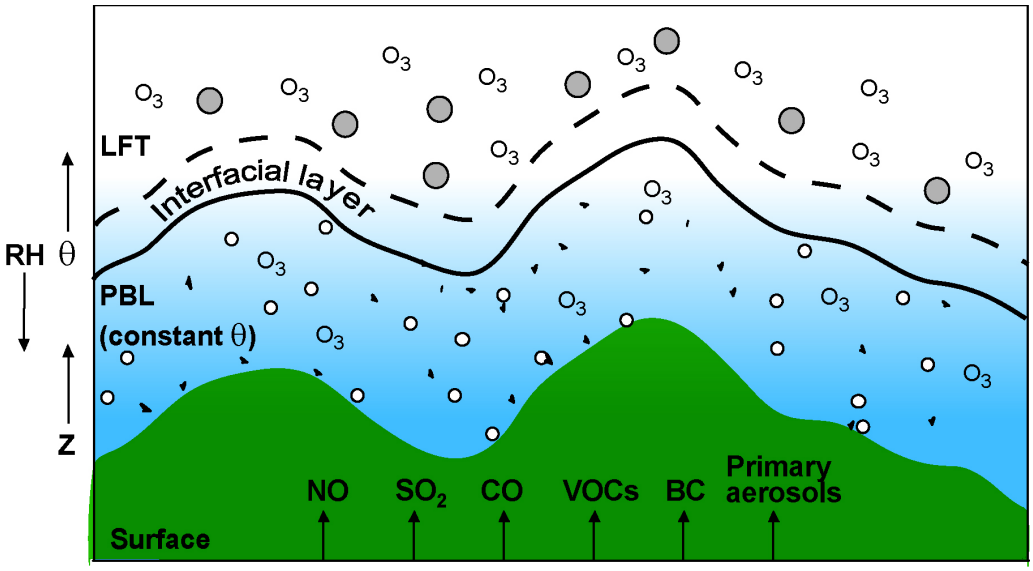

Figure 20. A schematic of the two-reservoir system during the daytime. The vertical and horizontal axes represent altitude and distance, respectively. The shape of the inversion layer that delineates the PBL from the LFT mimics the variations in surface elevation (green). The inversion layer is shown here with an interfacial layer of finite thickness. The upward arrows with the chemical species along the surface represent the injection of emissions into the PBL. The blue to white gradient represents greater RH in the PBL relative to the LFT. Potential temperature (θ) is shown as constant in the mixed layer and increasing with altitude from the interfacial layer. The small white circles and black flecks in the PBL represent sulfate particles and BC particles, respectively. They are shown as an external mixture in the PBL. The larger grey circles in the LFT represent internally mixed sulfate and BC particles. The O_3 represents molecules of ozone. There are more particles in the PBL than the LFT, but more molecules of ozone in the LFT (Taubman *et al.*, 2004(a)).

The observations reported herein may have broader implications as well. Absorbing aerosols heat the atmosphere and alter atmospheric stability (e.g., Park *et al.*, 2001; Menon *et al.*, 2002). During a stagnation event such as this one, when stable layers of air pollution have discrete aerosol optical properties, preexisting atmospheric stability may be augmented if more absorptive aerosol layers are juxtaposed above more scattering layers. This could in turn create a positive feedback loop, inhibiting vertical mixing and dilution and ultimately delaying the

termination of the episode. Such a distribution of aerosol optical properties could also have a significant impact on the solar radiation budget and therefore the accuracy of climate modeling studies.

A specific question regarding absorbing aerosols is the nature and extent of mixing between BC and sulfate particles. Although the aerosols encountered during this study primarily scattered solar radiation, there were manifest fluctuations in their absorptive nature, reflected in the calculated values of ω_o. Two noticeable deviations from the mostly invariant mean value of ω_o were during the periods of highest observed O_3 concentrations (between ~22:30:00 and ~22:40:00 UTC) and lowest observed O_3 concentrations (from ~22:56:00 to ~23:10:00 UTC). During these times, ω_o dropped to a minimum value of ~0.92, with a mean value of 0.94. Given the analytical uncertainty, a value of 0.94 is not statistically different from the overall mean, but does indicate greater relative absorption at these times. During the period of highest O_3, the drop in ω_o may be attributed to two factors: a greater degree of internal mixing between BC and sulfate particles due to the age and photochemical processing of the air parcels in question, and a larger influx of absorptive BC particles due to transport up the eastern seaboard urban corridor. The influence of the APLT and LLJ during this episode redirected the westerly synoptic flow in a more southerly direction during the day and evening, respectively. As a result, air that had been transported from the industrialized Midwest then mixed with the urban plumes of the eastern seaboard.

Another question of great scientific interest involves the mechanism and time scale for particle formation. The strong correlation between O_3 and nDp may provide

evidence for the link between O_3 and secondary organic aerosol formation through the oxidation of hydrocarbons (Andreae and Crutzen, 1997). Greater atmospheric oxidizing potential through increased concentrations of OH and H_2O_2 concomitantly with O_3 would also lead to the production of SO_4^{2-} from SO_2 and thereby secondary aerosol formation. Further explanation for the correlation may lie in the oxidation of SO_2 by dissolved O_3 (Hoffman and Calvert, 1985), but this is unlikely since there were few clouds during the episode and the acidity of Mid-Atlantic and Northeastern aerosols would inhibit such a reaction. The correlation between O_3 and σ_{sp} is likely a secondary result of the O_3 and nDp correlation since the particles with diameters commensurate to visible wavelengths scatter that light most efficiently. Although, highly scattering particles, such as the ones encountered in this study, also increase the flux of diffuse UV radiation and may, therefore, increase the photochemical production of O_3 as well (Dickerson *et al*., 1997), especially in the LFT.

3.5. Summary

The salient discovery of this study is that the chemistry and physics of severe, multi-day haze and ozone episodes over the Mid-Atlantic and northeastern U.S. may be simply and accurately represented by two reservoirs, comprising the PBL and LFT. These conclusions are drawn from observations during a constant altitude flight from Manchester, New Hampshire to College Park, Maryland on August 14, 2002, the last day of a multi-day haze and ozone episode. Most precursor species are injected into the PBL, where surface deposition may occur. When these precursors escape into the LFT, however, deposition is no longer a factor, and chemical lifetimes

are protracted. Photochemical processes are also accelerated in the LFT and air parcels age photochemically with greater rapidity. As a result, more O_3 and larger particles that scattered visible light more efficiently were observed in the LFT than in the PBL. An accurate numerical model simulation of photochemical smog processes over the Mid-Atlantic and Northeast should incorporate the existence of these two reservoirs, and simulate or at least parameterize the role of mixing between them in multi-day smog events.

Chapter 4: Smoke over Haze

4.1. Introduction

In early July of 2002, a pall of smoke, the result of forest fires in Quebec, blanketed the Mid-Atlantic and northeastern U.S. A cutoff upper level low-pressure system centered over Maine, together with a high amplitude ridge to the west, caused long range funneling of northern continental air to the Mid-Atlantic region beginning on July 5, 2002 and continuing through the morning of the 8th (Figure 21). This meridional flow is normally associated with cool, dry, and relatively clean air. However, smoke from forest fires burning in northern Quebec traveled south over 1000 km to cover the Mid-Atlantic and northeastern U.S. Diffluence downstream of the upper level trough caused the plume to fan out over the region. Figure 22 is a Moderate Resolution Imaging Spectroradiometer (MODIS) visible image of the plume and several active fire detections (red dots) on the 7th that shows how the diffluent flow caused such a regional impact.

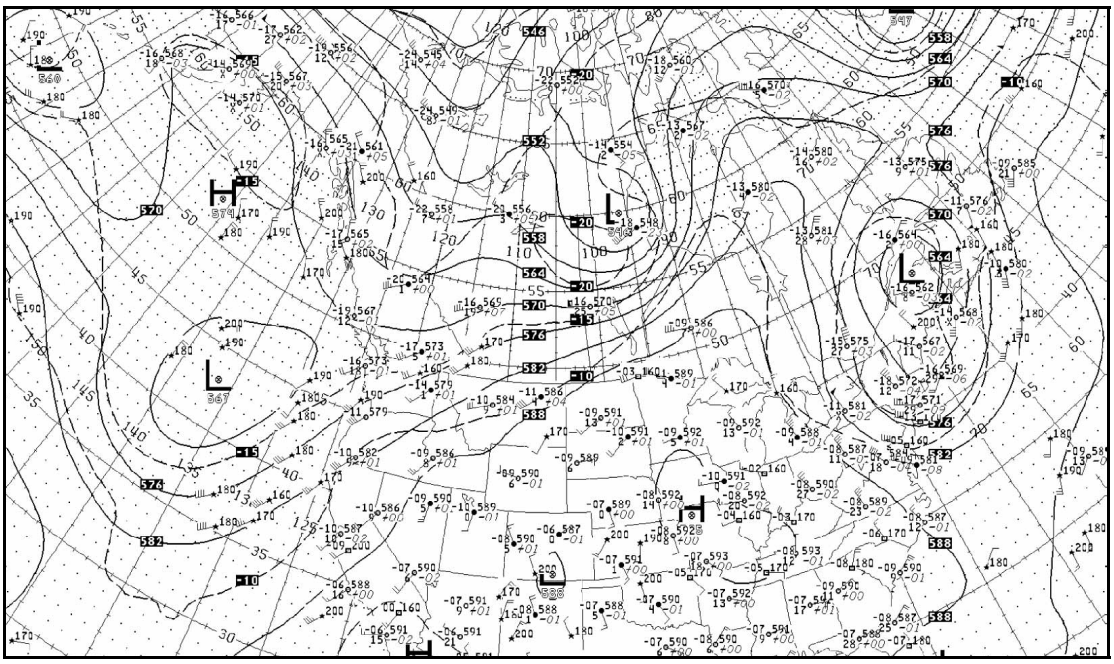

Figure 21. National Center for Environmental Prediction analysis of geopotential height fields at 500 mb for 12:00 UTC 6 July 2002 (adapted from Taubman *et al.*, 2004(b)).

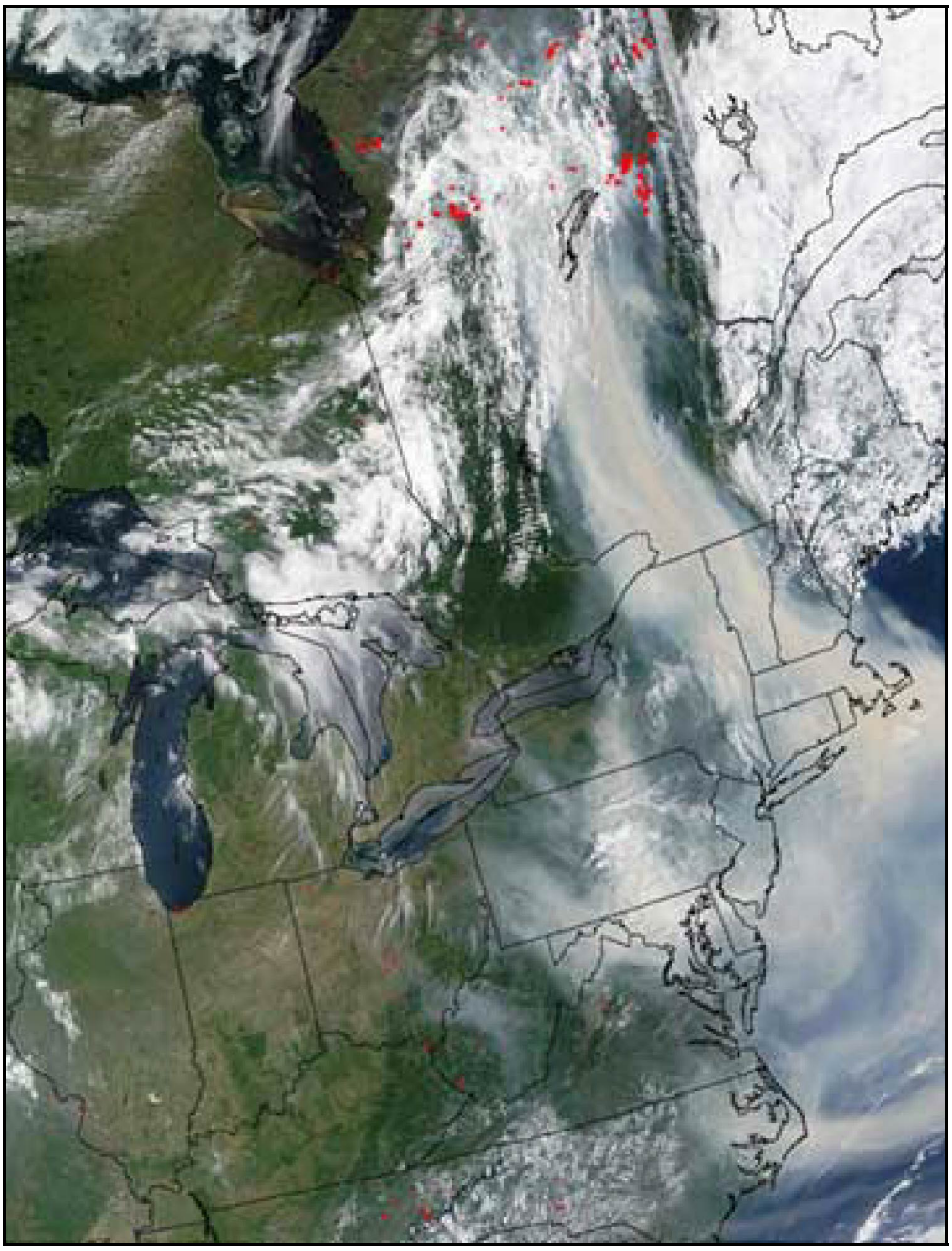

Figure 22. Moderate Resolution Imaging Spectroradiometer (MODIS) visible image from the Terra satellite on 7 July 2002. Active fire detections are shown as red dots east of James Bay. Diffluence downstream of the upper level trough caused the smoke plume to fan out over the eastern U.S. (Taubman *et al.*, 2004(b)).

On July 8, the upper level trough filled and migrated east, resulting in a wind shift to the west. This began to push the plume out over the Atlantic Ocean. By the

9th the majority of the plume was advected offshore. For a more complete analysis of the meteorology associated with this event, go to http://www.atmos.umd.edu/~forecaster/summary_2002.htm

Two research flights, one in the morning and one in the afternoon, were conducted on July 8, 2002 (Figure 23). The dark black circles on the figure indicate ascending or descending fixed location vertical survey spirals performed at ~100 vertical m min^{-1} between ~5 m AGL to ~3 km MSL. The first spiral was made over Luray, Virginia (38.70ºN, 78.48ºW) beginning at ~13:00 UTC. After a short transect to the northeast, the second spiral was performed over Winchester, Virginia (39.15ºN, 78.15ºW) commencing at ~14:00 UTC. The final spiral of the morning, over Cumberland, Maryland (39.60ºN, 78.70ºW) was initiated at ~15:00 UTC. The afternoon spirals were performed over Harford County (Harford), Maryland (39.56ºN, 76.18ºW) and Easton, Maryland (38.80ºN, 76.06ºW) beginning at ~19:00 and 20:00 UTC, respectively. Evidence of the smoke plume was strongest over Luray, Winchester, Harford, and Easton. The spiral over Cumberland showed little evidence of the smoke plume.

Results of aircraft measurements of trace gas and particle concentrations as well as particle optical properties on July 8, 2002 over Maryland and Virginia are reported herein. The AOD, aerosol direct radiative forcing, and heating rates associated with the smoke plume are calculated. This chapter also investigates the impacts that absorptive heating within the plume had on atmospheric stability. The results described in this chapter are based on work published in the Journal of

Geophysical Research (Taubman *et al*., 2004(b)) (reproduced by permission of American Geophysical Union).

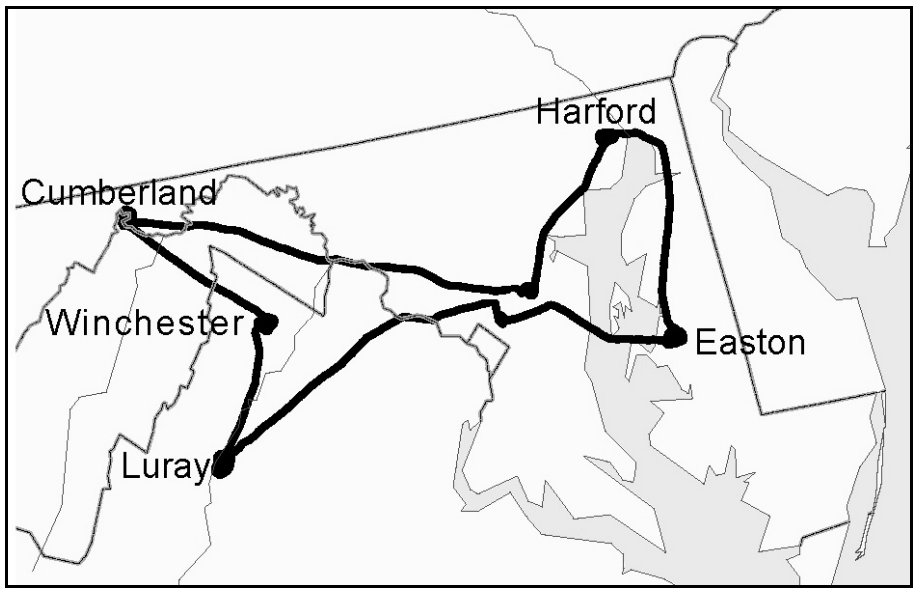

Figure 23. Flight track for 8 July 2002, consisting of a morning and an afternoon flight. Luray, VA (38.70ºN, 78.48ºW), Winchester, VA (39.15ºN, 78.15ºW), and Cumberland, MD (39.60ºN, 78.70ºW) (in that order chronologically) were the locations of the morning flight spirals. Harford, MD (39.56ºN, 76.18ºW) and Easton, MD (38.80ºN, 76.06ºW) (in that order chronologically) were the locations of the afternoon flight spirals (Taubman *et al.*, 2004(b)).

4.2. Results and Discussion

Vertical profiles of the temperature and RH measured over the five locations are given in Figure 24. The three morning profiles (Luray, Winchester, and Cumberland) show a nocturnal radiance inversion around 500 m that erodes by the time of the later profiles. A persistent inversion around 2 km is evident in all of the profiles, delineating the upper limits of the PBL and the dichotomy between the two regimes observed in this study. This particular study investigates the hypothesis that

absorption of solar radiation within the layer between ~2 and 3 km led to the protraction of this temperature inversion, initiated by morning subsidence, through the afternoon.

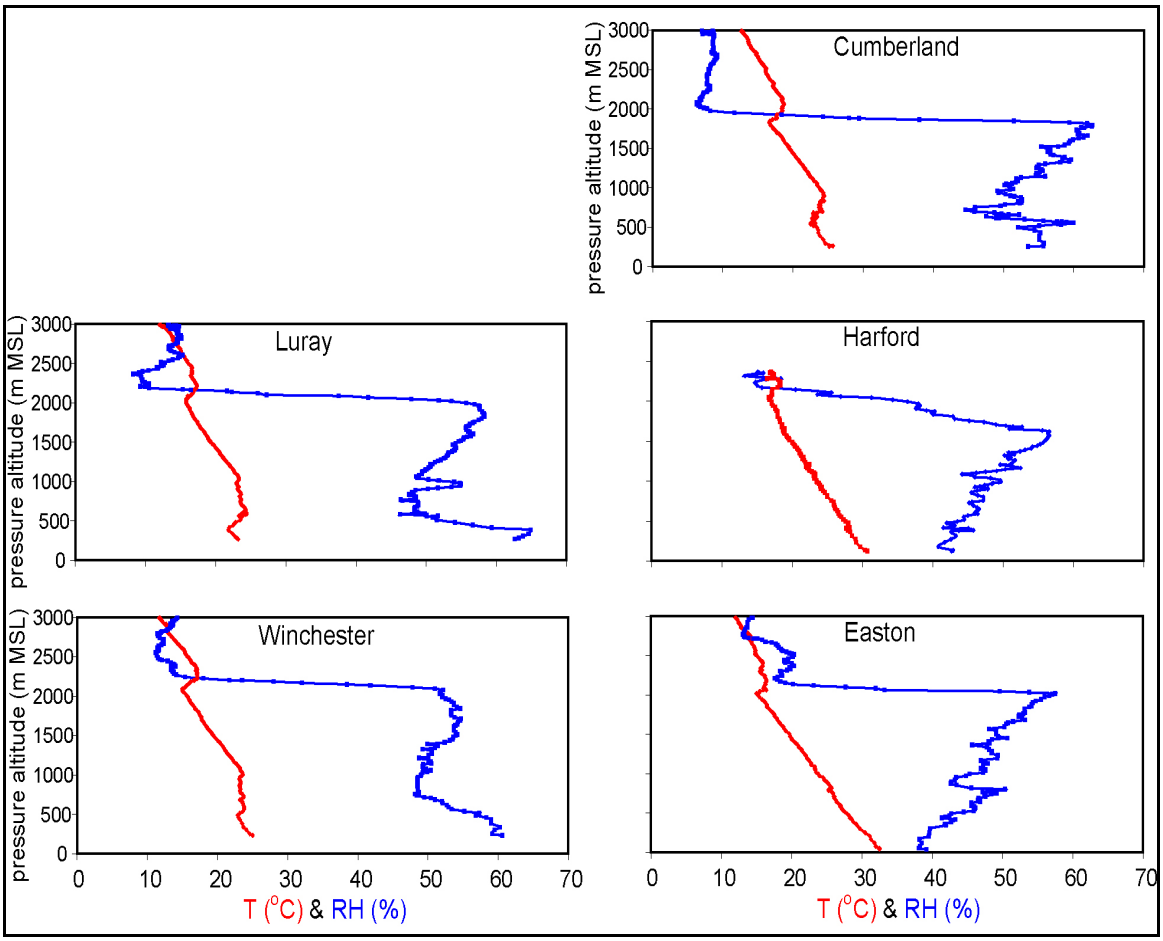

Figure 24. Measured temperature (red) and relative humidity (blue) over Luray, VA, Winchester, VA, Cumberland, MD, Harford, MD, and Easton, MD (adapted from Taubman *et al.*, 2004(b)).

4.2.1. Trajectory Analysis

A backward trajectory analysis utilizing the NOAA Air Resources Laboratory (ARL) HYbrid Single-Particle Lagrangian Integrated Trajectory (HYSPLIT) model

(Version 4) (Draxler and Rolph, 2003) and Eta Data Assimilation System (EDAS) meteorological fields was performed at each of the five locales addressed in this study (Figure 25). The 72-hour model vertical velocity backward trajectories were commenced at altitudes of 1000, 2000, and 3000 m MSL to shed light on observations made within the PBL and the observed free tropospheric pall. The upper-level trajectories all show advection from the north and northwest, indicating that the observations between 2 and 3 km MSL were of the Canadian forest fire smoke. The meteorological and trajectory analyses suggest that air parcels were lifted near the fires and then transported in the lower free troposphere. The lower level trajectories also show northerly advection, however the observations made in this study suggest a vertical separation between PBL air and that in the free troposphere.

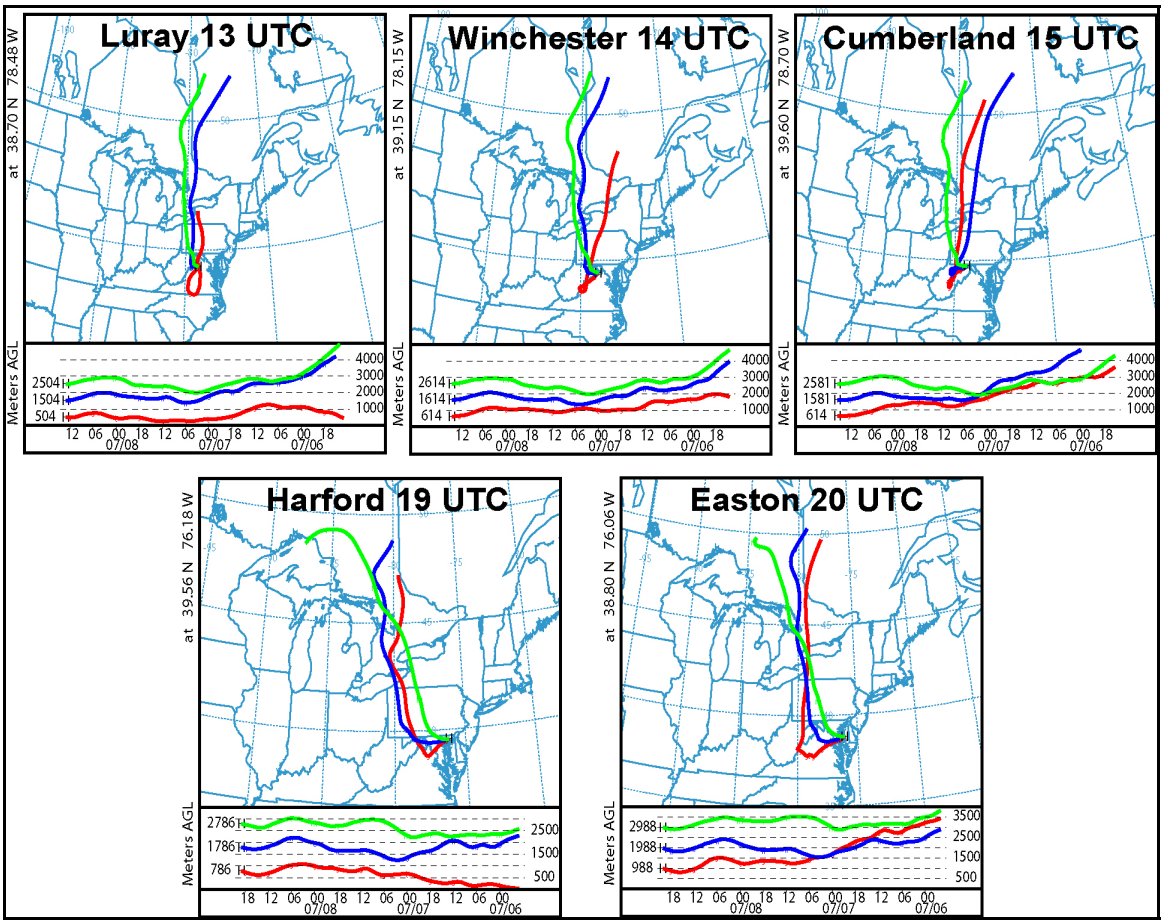

Figure 25. NOAA HYSPLIT 4 ARL EDAS model vertical velocity 72-hour backward trajectories for air parcels at 1000, 2000, and 3000 m MSL on 8 July 2002 over Luray, VA, Winchester, VA, Cumberland, MD, Harford, MD, and Easton, MD (Taubman *et al.*, 2004(b)).

4.2.2. Trace Gases

The mixing ratios for O_3, CO, and SO_2 measured over the five locations are provided in Figures 26, 27, and 28, respectively. Luray, Winchester, Harford, and Easton displayed similar trends: high O_3 and CO mixing ratios between 2 and 3 km with little SO_2 observed within this altitude range. Ozone mixing ratios exceeded 160 ppbv at this altitude and the mixing ratios in the layer aloft consistently exceeded those in the PBL by 40 – 60 ppbv. Carbon monoxide mixing ratios approached 1600

ppbv in the layer aloft, and were upwards of 1000 ppbv greater than those in the PBL. These observations are indicative of a photochemically aged smoke plume. Large amounts of SO_2 were observed near the surface in the three later profiles, including Cumberland. This enhanced SO_2, routinely observed during regular air pollution survey flights conducted in this area (Ryan *et al*., 1998), could be the result of westerly transport from a point source, observed in the later profiles because of the wind shift from the north to the west.

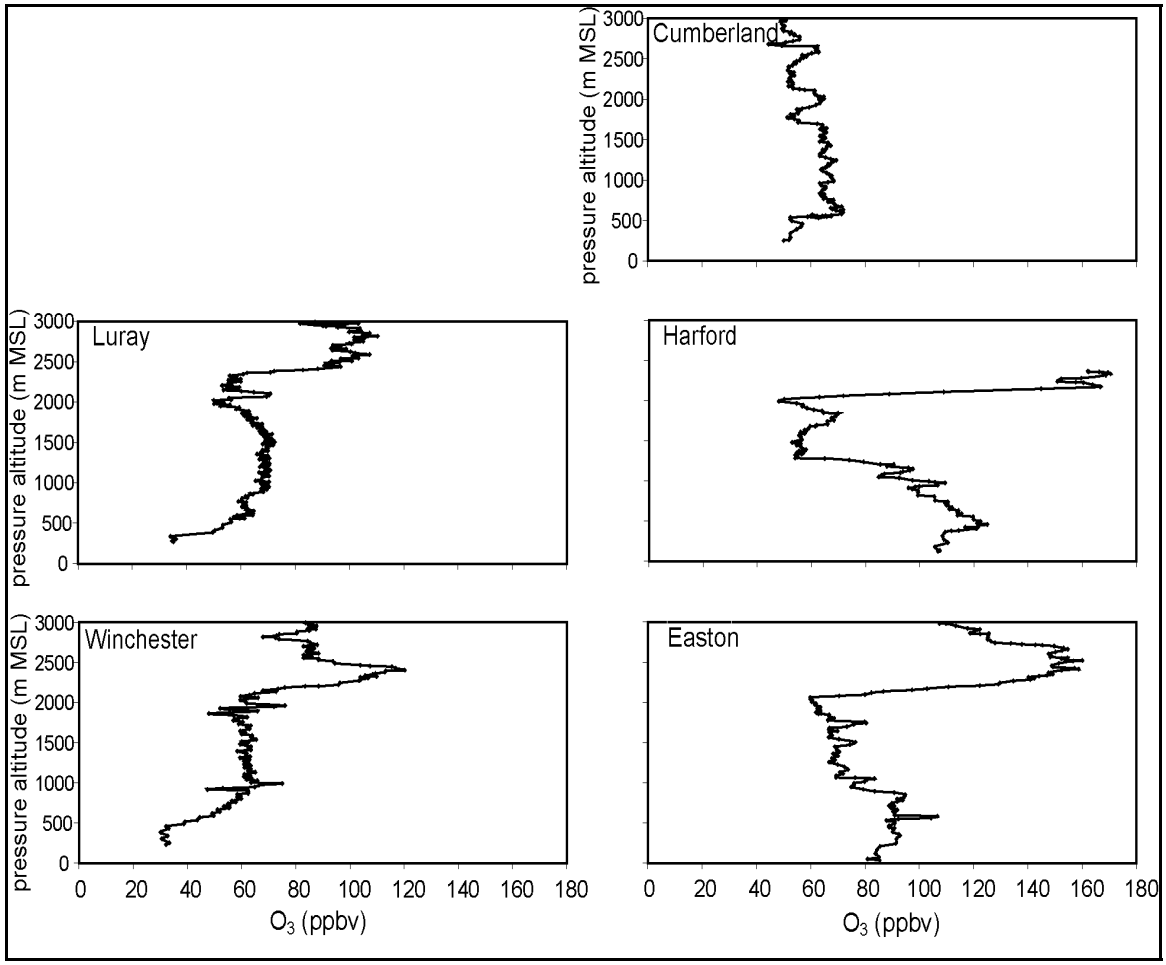

Figure 26. 10-s ozone measured during the vertical survey spirals over Luray, VA, Winchester, VA, Cumberland, MD, Harford, MD, and Easton, MD (adapted from Taubman *et al.*, 2004(b)).

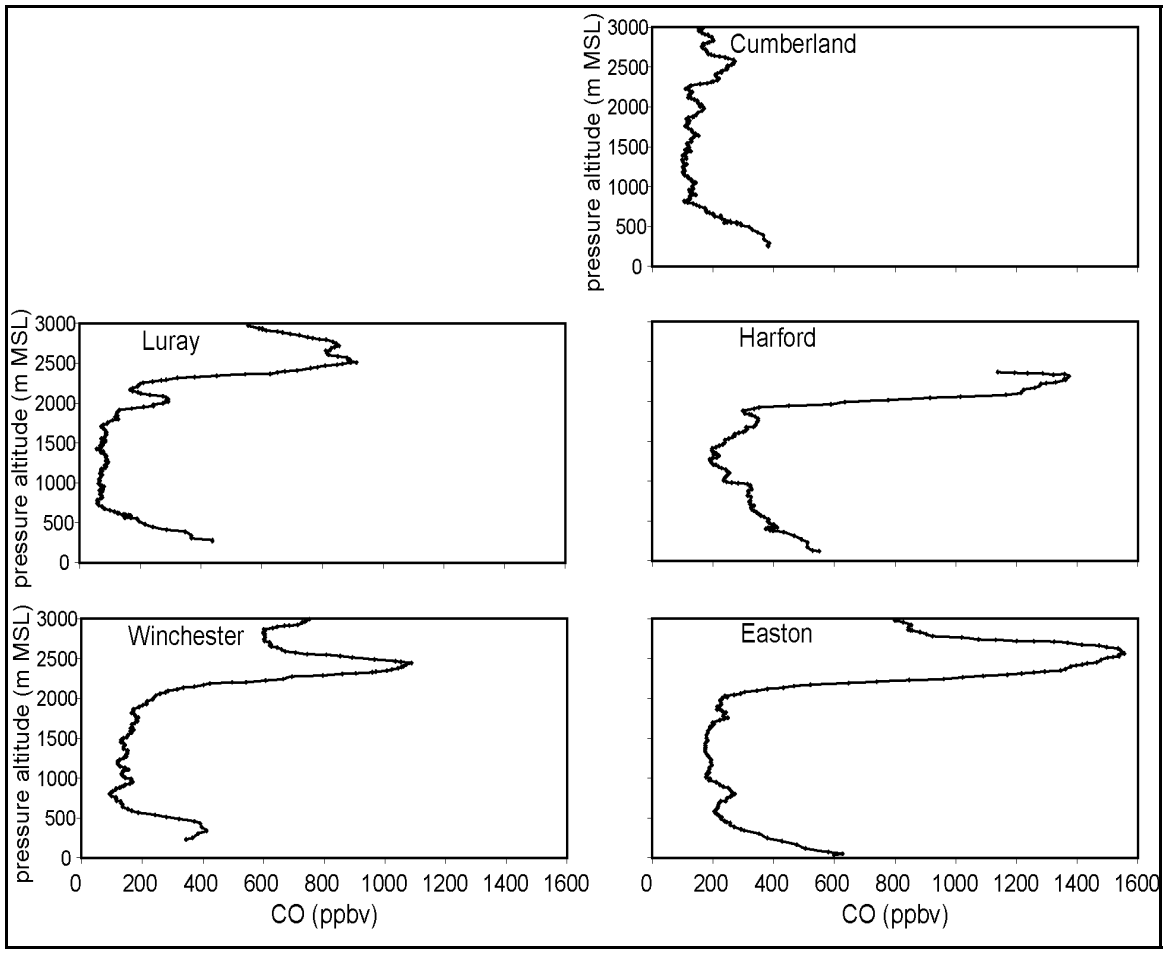

Figure 27. Running 1-min mean CO measured during the vertical survey spirals over Luray, VA, Winchester, VA, Cumberland, MD, Harford, MD, and Easton, MD (adapted from Taubman *et al.*, 2004(b)).

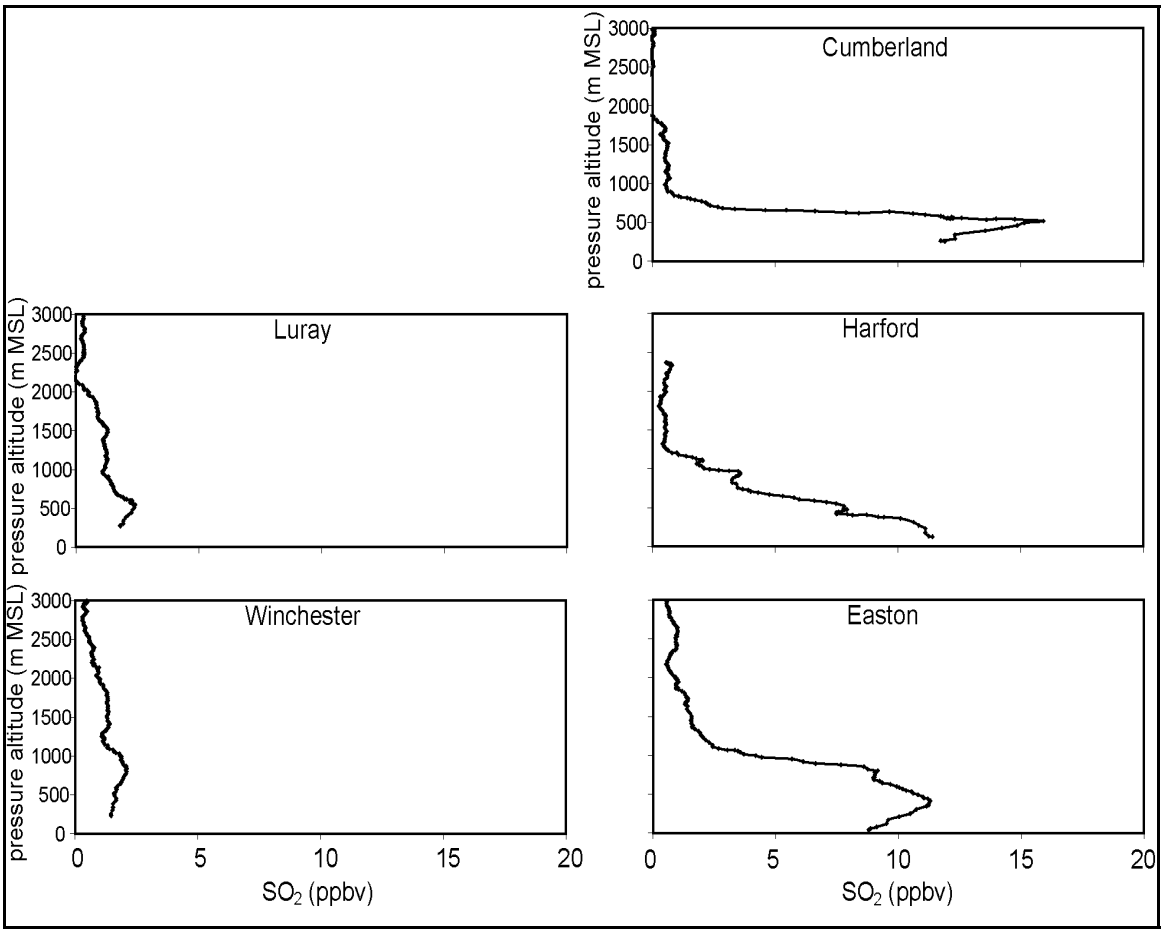

Figure 28. Running 1-min mean SO_2 measured during the vertical survey spirals over Luray, VA, Winchester, VA, Cumberland, MD, Harford, MD, and Easton, MD (adapted from Taubman *et al.*, 2004(b)).

4.2.3. Aerosol Properties

Particle light scattering at 450, 550, and 700 nm, absorption at 550 nm, and particle concentrations in the six accumulation mode size bins over the five locations are provided in Figures 29, 30, and 31, respectively. The absorption values were extrapolated from 565 to 550 nm, based on the assumption that $\sigma_{ap} \propto 1/\lambda$ (Bodhaine, 1995), to calculate the AOD and single-scattering albedo at this wavelength. Methods used to extrapolate measured optical properties across the solar spectrum

will be addressed later in this section. Total scattering at 450, 550, and even at 700 nm over Harford and Easton exceeded 10^{-3} m^{-1} between 2 and 3 km. Particle absorption at 550 nm approached 100 Mm^{-1} in this vertical layer over each location and even surpassed this value at Easton. The greatest numbers of particles were observed in the 0.30 – 0.60 μm diameter range. Particles larger than this may not have been collected efficiently due to inlet line losses. There were at least as many particles in the 0.40 – 0.491 μm range as in the smallest size bin observed over each location (except Cumberland and Harford) at ~2.5 km, roughly the vertical center of the smoke plume. At Luray and Winchester, particles with diameters between 0.491 – 0.60 μm were also as numerous as those in the smallest size bin. These observations are rare in a typical plume of anthropogenic origin. In such cases, the particles with diameters between 0.30 – 0.40 μm are far more numerous than the larger particles, as can be seen in the PBL in the morning profiles.

A large increase in the number of particles between 0.30 – 0.40 μm was seen at roughly 500 m above Cumberland. This increase corresponded to an increase in SO_2 at the same altitude over Cumberland. Despite the fact that similar increases in SO_2 were measured at low altitudes over Harford and Easton, no increase in the number of 0.30 – 0.40 μm particles was observed. The optically thick layer of smoke covering Harford and Easton may have inhibited the photochemical oxidation of SO_2 to SO_4^{2-} and thereby secondary aerosol formation. Over Cumberland, where there was less solar attenuation, gas to particle conversion would not have been hindered. This may have resulted in the observed increase in small particles. Unfortunately, there was no speciation data to confirm this supposition.

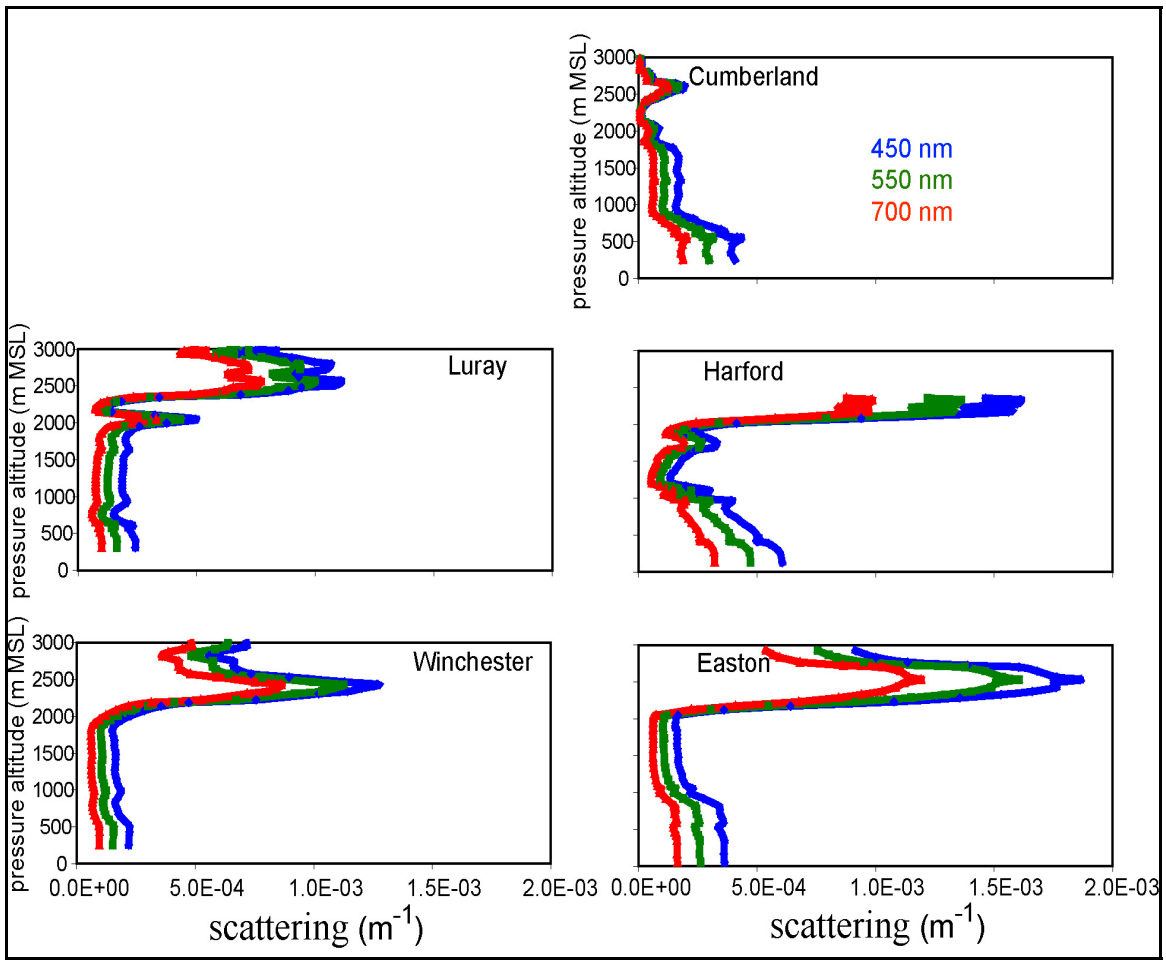

Figure 29. σ_{sp} **at 450 nm (blue), 550 nm (green), and 700 nm (red) measured during the vertical survey spirals over Luray, VA, Winchester, VA, Cumberland, MD, Harford, MD, and Easton, MD (adapted from Taubman *et al.*, 2004(b)).**

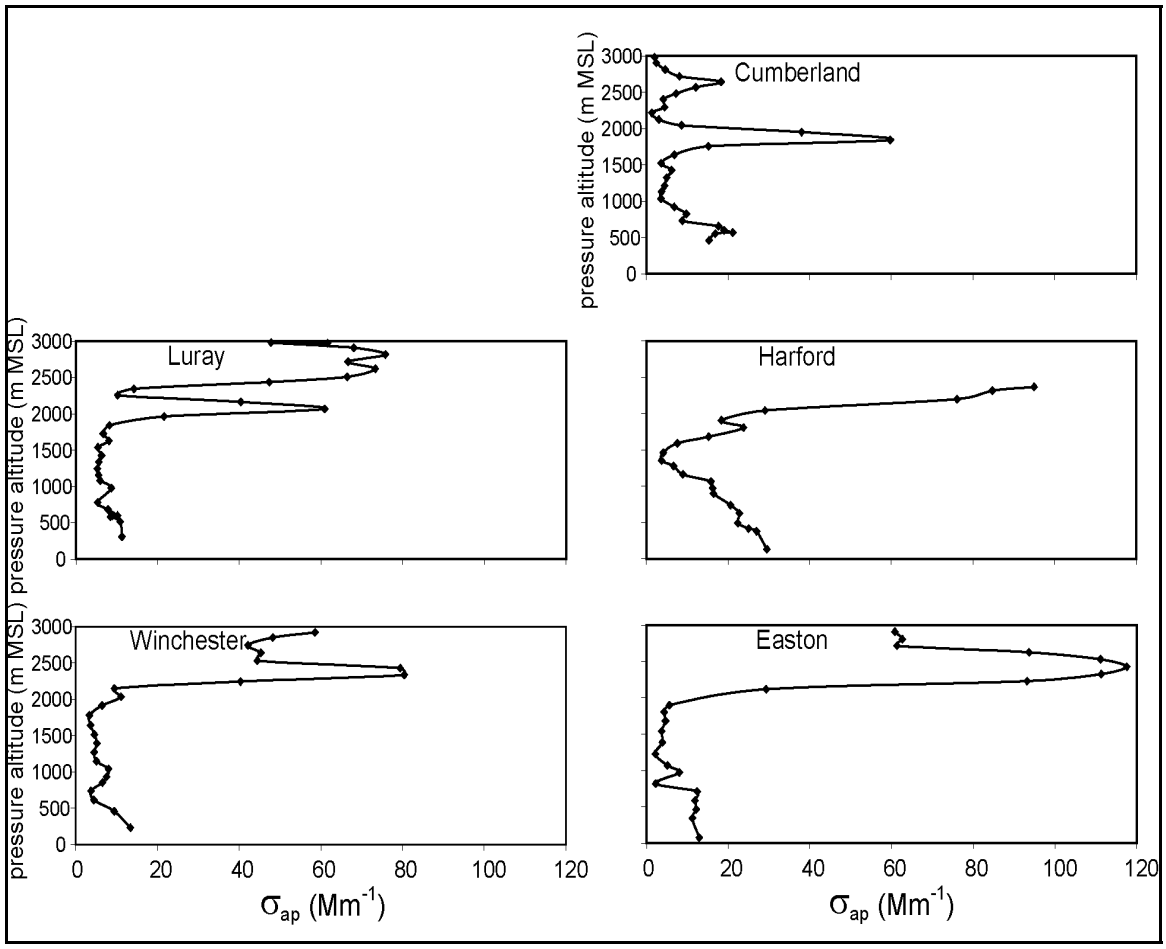

Figure 30. σ_{ap} at 550 nm, extrapolated from σ_{ap} at 565 nm that was measured during the vertical survey spirals over Luray, VA, Winchester, VA, Cumberland, MD, Harford, MD, and Easton, MD (adapted from Taubman *et al.*, 2004(b)).

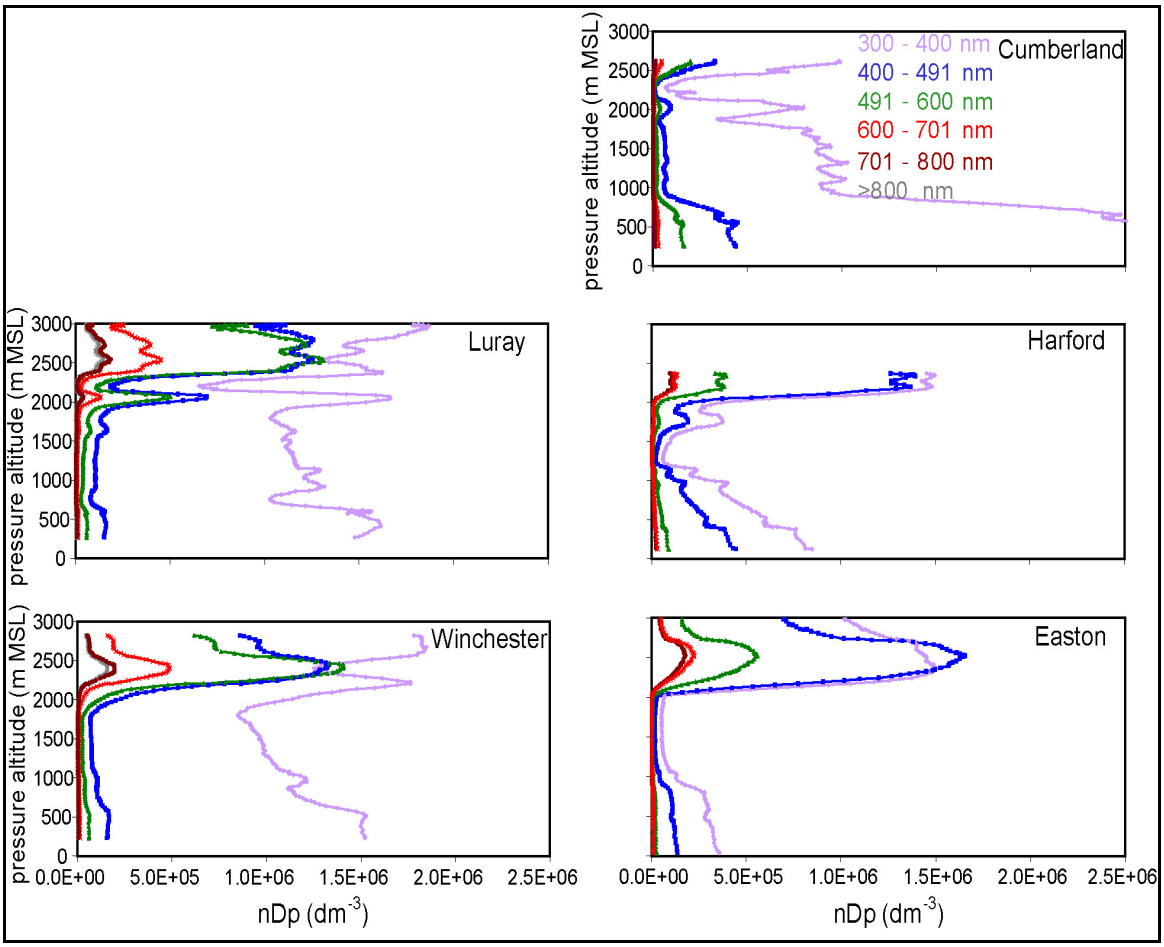

Figure 31. Number of particles in six discrete particle diameter size bins measured during the vertical survey spirals over Luray, VA, Winchester, VA, Cumberland, MD, Harford, MD, and Easton, MD: 0.30-0.40 µm (violet), 0.40-0.491 µm (blue), 0.491-0.60 µm (green), 0.60-0.701 (red), 0.701-0.80 (maroon), 0.80~1.0 µm (gray) (adapted from Taubman *et al.*, 2004(b)).

Calculations of α were made using the following ratios of the total scattering at 450, 550, and 700 nm: 450/550, 450/700, and 550/700. Figure 32 shows $\alpha_{450/700}$ over the five locations. Table 1 gives the average values of α for the smoke layer and the PBL at each location. The average values of α in the PBL are larger than those in the smoke layer, indicating smaller particles in the PBL and larger ones aloft. This is consistent with relatively fresh anthropogenic particles lying below an aged

smoke plume that had traveled over 1000 km (Reid *et al.*, 1998(a)). Even the Cumberland profile, despite showing a weak overall smoke signature, is consistent with this trend.

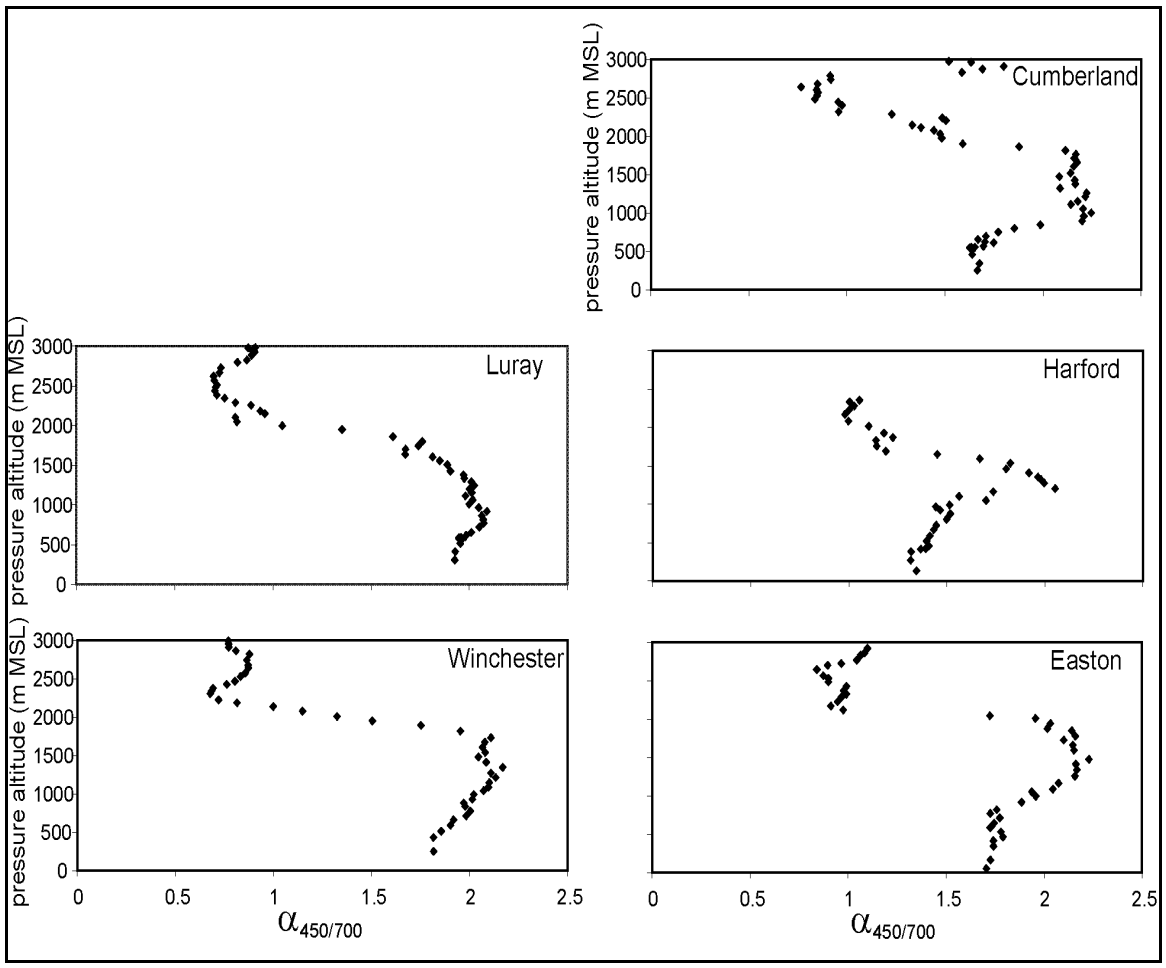

Figure 32. The scattering Ångström exponent, α , (450/700) calculated from flight data measured during the vertical survey spirals over Luray, VA, Winchester, VA, Cumberland, MD, Harford, MD, and Easton, MD (adapted from Taubman *et al.*, 2004(b)).

Table 2. Ångström exponents calculated for the smoke layer and PBL at vertical survey spiral locations during flights on 8 July 2002 (Taubman *et al.*, 2004(b)).

	Smoke $\alpha_{450/550}$	**Smoke** $\alpha_{450/700}$	**Smoke** $\alpha_{550/700}$	**PBL** $\alpha_{450/550}$	**PBL** $\alpha_{450/700}$	**PBL** $\alpha_{550/700}$
Luray	0.57±0.18	0.83±0.15	1.04±0.11	1.84±0.42	1.92±0.38	1.99±0.34
Winchester	0.60±0.44	0.85±0.32	1.05±0.22	1.90±0.34	1.99±0.32	2.06±0.30
Cumberland	1.17±0.64	1.23±0.38	1.29±0.30	1.85±0.26	1.96±0.22	2.05±0.21
Harford	0.87±0.10	1.09±0.09	1.26±0.09	1.45±0.33	1.59±0.30	1.70±0.29
Easton	0.71±0.10	0.97±0.09	1.18±0.09	1.83±0.19	1.94±0.19	2.03±0.16

Uncertainties represent 1 σ deviation about the mean.

Because of the measurement of dry light scattering, σ_{sp} (*ref*), the calculation of AOD had to be modified to account for the difference between σ_{sp} (*ref*) and σ_{sp} (λ, *RH*):

$$\tau(\lambda, RH) = \int_{sfc}^{TOA} \sigma_{sp}(ref) F(RH) dz + \int_{sfc}^{TOA} \sigma_{ap}(\lambda, RH) dz \qquad (20)$$

However, the correction factor, $F(RH)$, was only applied to total scattering measurements made within the PBL. The smoke plume was presumably less hygroscopic than the sulfate dominated anthropogenic aerosols of the Mid-Atlantic U.S. and was observed in the free troposphere, where the RH was already below 20%. The corrections for angular non-idealities, on the other hand, were applied to all of the measurements.

The vertical survey spirals covered roughly the bottom 3 km of the atmosphere, from ~5 m AGL (z_1) to ~3 km MSL (z_2). Because of the small temporal and horizontal spatial scale of the individual spirals, atmospheric homogeneity was assumed in both horizontal composition and time. Based on this assumption, AOD for the vertical column at a single time was calculated. Measurements of extinction (as the sum of scattering and absorption) were made every minute and roughly every

100 m to give approximately 30 measurements per spiral. These extinction measurements were then integrated vertically and the AOD reported herein was calculated as such:

$$\tau(\lambda, RH) = \int_{z_1}^{z_2} \sigma_{sp}(ref) F(RH) dz + \int_{z_1}^{z_2} \sigma_{ap}(\lambda, RH) dz \quad (21)$$

The smoke plume was observed in the lower free troposphere at a minimum altitude of ~2 km MSL and extended somewhat beyond 3 km MSL. Therefore, the entire smoke plume was not accounted for in these calculations. AOD at 550 nm (τ_{550}) is given in Table 3. The uncertainty in these values was calculated by adding in quadrature the uncertainties in the particle scattering and absorption. A 25% uncertainty was assigned to the absorption values according to the instrumental error. A 15% uncertainty was estimated for the scattering values after adding in quadrature the 10% instrumental error and an additional 11% sensitivity to the possible range of γ values in the humidification factor.

Table 3. AOD calculated from ~5 m AGL to ~3 km MSL at 550 nm at vertical survey spiral locations during flights on 8 July 2002 (Taubman *et al.*, 2004(b)).

	Luray	Winchester	Cumberland	*Harford	Easton
τ_{550}	1.01±0.14	0.98±0.14	0.42±0.06	1.05±0.15	1.53±0.21

*AOD only to ~2.5 km MSL

The profiles of ω_o at 550 nm (ω_{o550}) over the five locations are given in Figure 33. The average values of ω_{o550} in the PBL and smoke layer aloft at each location are given in Table 4. The particles in the smoke plume were consistently more absorbing than the particles in the PBL. The mean values in the smoke plume and the PBL at 550 nm were 0.93±0.02 and 0.95±0.01, respectively. Calculation of the mean smoke value excluded Cumberland. A weak smoke signature was observed over this location, and inclusion would bias the calculation toward a value uncharacteristic of the smoke plume measured over the other sites. These ω_{o550} values are consistent with those reported by Dubovik *et al*. (2001) for North American boreal forest fires and at NASA GSFC. The smoke plume values also fall within the range of satellite-based retrieval values for smoke from boreal forest fires (Ferrare *et al*., 1990; Li and Kou, 1998). The uncertainty in ω_o was calculated according to the aforementioned uncertainties in the absorption and scattering values with the following equation:

$$\frac{|\Delta\omega_o|}{\omega_o} = (1-\omega_o)\left\{\left(\frac{\Delta\sigma_{sp}}{\sigma_{sp}}\right)^2 + \left(\frac{\Delta\sigma_{ap}}{\sigma_{ap}}\right)^2\right\}^{1/2} \qquad (22)$$

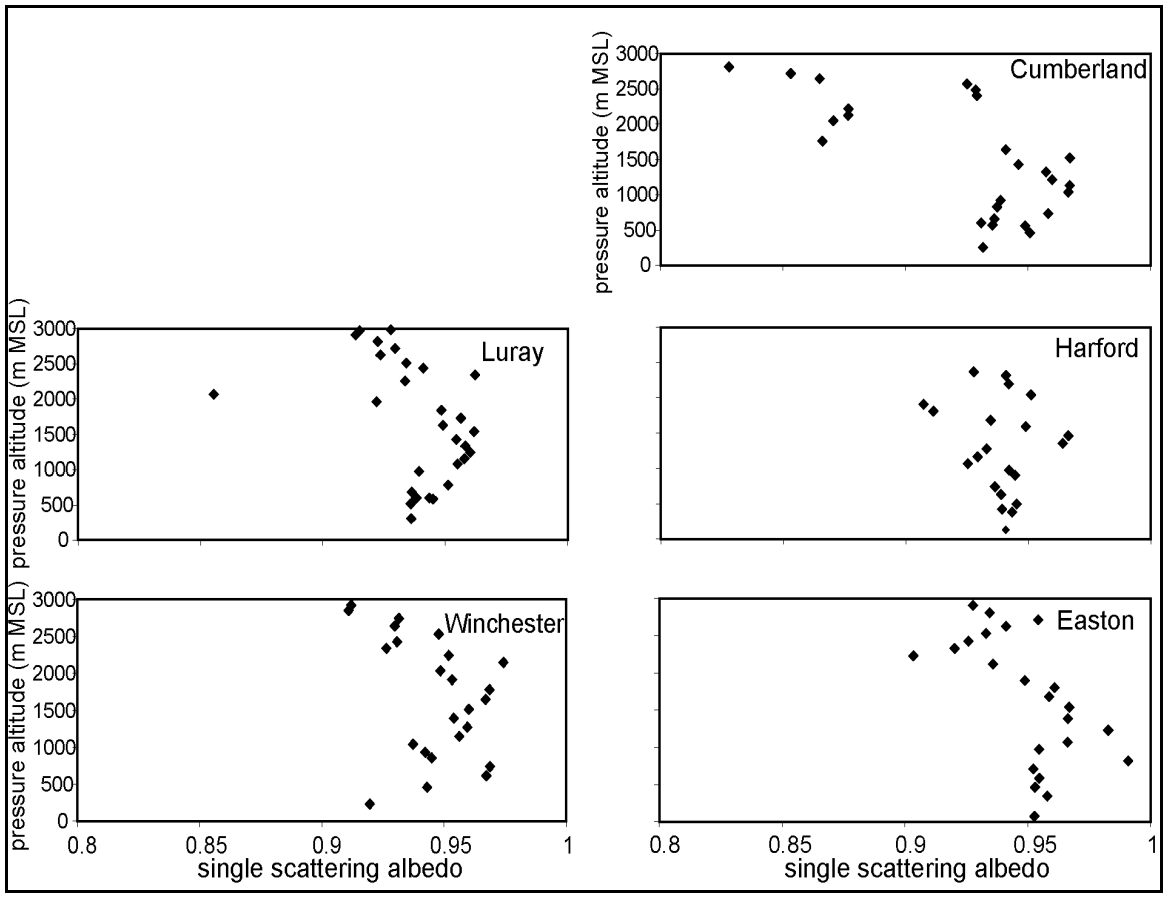

Figure 33. The single-scattering albedo, ω_o , at 550 nm calculated from flight data measured during the vertical survey spirals over Luray, VA, Winchester, VA, Cumberland, MD, Harford, MD, and Easton, MD (adapted from Taubman *et al.*, 2004(b)).

Table 4. Single-scattering albedo at 550 nm calculated for the smoke layer and PBL at vertical survey spiral locations during flights on 8 July 2002 (Taubman *et al.*, 2004(b)).

	Luray	Winchester	Cumberland	Harford	Easton
Smoke ω_{b550}	0.91±0.03	0.93±0.02	0.81±0.06	0.93±0.02	0.93±0.02
PBL ω_{b550}	0.95±0.01	0.95±0.01	0.94±0.02	0.94±0.02	0.96±0.01

The wavelength dependent index of refraction and particle size distribution were necessary to extrapolate optical properties at the measured wavelengths over the solar spectrum using Mie theory (Mishchenko *et al.*, 2002). The real index of refraction at 550 nm was determined assuming the column integrated AERONET (Holben *et al.*, 1998) value at 550 nm (1.56, interpolated from the wavelengths measured) on July 8, 2002 represented a weighted average of two discrete values, one for the PBL plume and one for the smoke plume. The value assigned to the PBL plume was 1.43 according to a 7-year average from NASA GSFC in Greenbelt, MD (Dubovik *et al.*, 2001). A value of 1.58 was therefore assigned to the smoke plume, slightly larger than the column integrated value. This refractive index was then scaled according to the wavelength dependence of the AERONET values. The imaginary index of refraction was calculated assuming absorption was solely the result of particle BC content. The wavelength dependence was then considered to be proportional to that measured for BC (Chang and Charalampopolous, 1990), adjusted so the ω_b value calculated at 550 nm matched the in-situ value.

The measured particle concentrations were over a limited size range. Thus, size distributions were determined using the measured Ångström exponents and the

assumed complex index of refraction at 550 nm. The lognormal distributions were adjusted so that the measured Ångström exponents matched those calculated by Mie theory for adjustable lognormal distributions (Mishchenko *et al*., 2002). Figure 34 shows the lognormal curves of the size distributions for the smoke and PBL layers derived from the Ångström exponents, together with data points from the MET-One measured size distributions as a consistency check. The AERONET retrieval is given for comparison. Though the lognormal curve for the AERONET distribution was based directly on statistics from the data, the volume-weighted curve does not appear to fit the data well. Optical properties (ω_0, phase functions) at other wavelengths were then calculated based on the size distributions and wavelength dependent complex index of refraction.

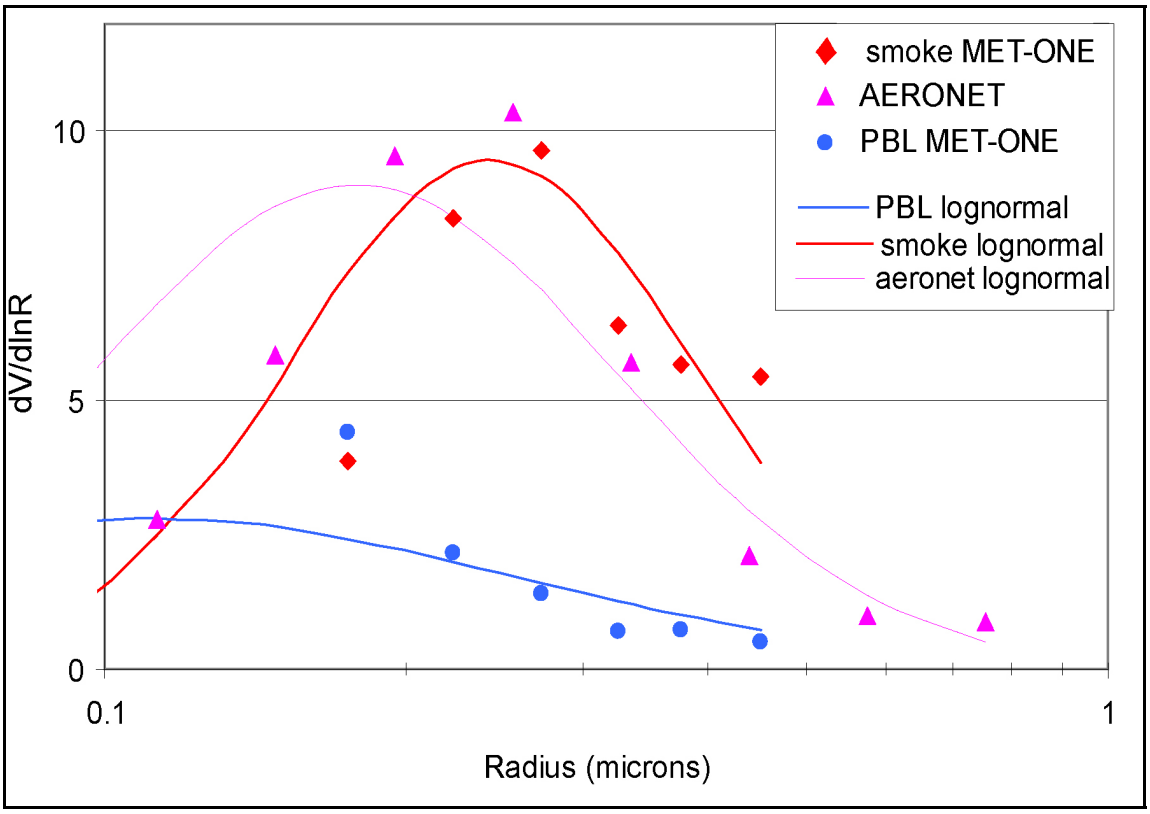

Figure 34. Population per cubic centimeter: Met-One smoke data points (diamonds), Met-One PBL aerosol data points (circles), and AERONET retrievals (triangles). The solid lines are lognormal fits to scattering Ångström exponents from in-situ data. The dotted line is based on statistics from the AERONET retrieval. The amplitude of each lognormal curve was adjusted to fit the points (adapted from Vant-Hull *et al.*, 2004).

4.2.4. Aerosol Direct Radiative Forcing

The clear sky aerosol direct radiative forcing (ΔF) at each location was calculated using the Santa Barbara DISORT Radiative Transfer (SBDART) code (Ricchiazzi *et al.*, 1998). AOD is proportional to the sum of the scattering and absorption cross sections calculated from Mie theory, allowing measured values to be extrapolated to any wavelength. The calculated values of AOD and ω_0 at 0.30, 0.40, 0.55, 0.70, 1.0, 2.0, and 3.0 μm in ~100 m vertical layers from roughly the surface to

3 km (depending on the vertical survey spiral at each location) were used as inputs to the code. Measured temperature, pressure, water vapor, and O_3 values were also input for the lowest 3 km. Surface albedo between $0.47\,\mu m - 2.1\,\mu m$ was taken from the MODIS land team 8 d surface reflectance product (Vermote and Vermuelen, 1999), derived from satellite measurements during a low aerosol period 2-3 weeks after this study. Outside of this wavelength range, CERES (Clouds and the Earth's Radiant Energy System) mixed vegetation albedos were used (Charlock *et al*., 2002). These values were chosen because of consistency with the MODIS land team surface reflectance at the specified sites.

ΔF TOA, ΔF sfc, and atmospheric absorption (Atmos) were calculated at each location. To determine the effects of the smoke layer at each location, the program was run with the smoke layer intact and after removal of the layer. The difference between the two sets of outputs was the direct effect of the smoke plume (Table 5). The PBL forcing was compared to a zero aerosol background and was, therefore, not the anthropogenic forcing. Since no background was assumed, a more accurate value for the smoke forcing was obtained. Because the smoke signature was weak at Cumberland and the majority of the plume was not measured at Harford, the values reported for these locations are not necessarily representative of the situation being described.

Table 5. ΔF TOA, ΔF sfc, and Atmos calculated with the PBL and smoke layers (Total forcing), with just the PBL layer (PBL), and the difference between the two (Smoke) at vertical survey spiral locations during flights on 8 July 2002 (Taubman *et al.*, 2004(b)).

	Total forcing			**PBL**			**Smoke**		
	ΔF TOA Wm^{-2}	Atmos Wm^{-2}	ΔF sfc Wm^{-2}	ΔF TOA Wm^{-2}	Atmos Wm^{-2}	ΔF sfc Wm^{-2}	ΔF TOA Wm^{-2}	Atmos Wm^{-2}	ΔF sfc Wm^{-2}
Luray	-47±7	115± 17	-162± 24	-26±4	30±5	-56± 8	-21±3	85± 13	-106± 16
Winchester	-50±8	108± 16	-168± 25	-20±3	23±3	-43± 6	-30±5	85± 13	-115± 17
Cumberland	-25±4	57± 9	-82± 12	-27±4	36±5	-63± 9	2±1	21± 3	-19± 3
Harford	-42±6	124± 19	-166± 25	-31±5	57±9	-88± 13	-11±2	67± 10	-78± 12
Easton	-57±9	167± 25	-224± 34	-29±4	29±4	-58± 9	-28±4	138± 21	-166± 25

Sources of error in the values calculated using the radiative transfer code resulted from uncertainties in the AOD at 550 nm and the extrapolation to other wavelengths using Mie theory. The AOD at 550 nm was found to be linearly proportional with the calculated forcing values, and the uncertainty in the forcing values was therefore assumed to be proportional to the uncertainty in AOD. The extrapolation uncertainty was calculated using sensitivity tests in which the real index of refraction was varied by 0.04 (a value greater than the AERONET uncertainty of 0.03) (Dubovik *et al.*, 2000) and the Ångström exponents used to calculate the size distributions were varied by one standard deviation. These sources of error were then added in quadrature to give the uncertainties listed in Table 5.

Calculations of the effect of the smoke plume indicated that the forcing at the TOA was small relative to the surface forcing. The values for atmospheric absorption were, therefore, nearly equal to the attenuation at the surface. This indicates that

multiple scattering of solar radiation within the optically thick plume typically ended in photon absorption. The fact that the smoke overlaid more scattering, smaller particles also increased the absorption within the smoke layer. The net effect was to cool the surface and heat the air aloft, thereby increasing the vertical stability of the lower atmosphere.

To quantify this effect, the calculated heating rates at each spiral location were integrated from sunrise to the time of observation. These values were then used to generate vertical heating profiles. Observed temperature profiles from the surface to ~2 km (below the temperature inversion) were extrapolated to 3 km to provide a temperature profile that did not include the observed inversion. The extrapolated temperature profiles were then subtracted from the measured temperature profiles. The resulting temperature difference was compared to the integrated heating profiles to determine the impact of the absorptive heating on the observed temperature profiles (Figure 35).

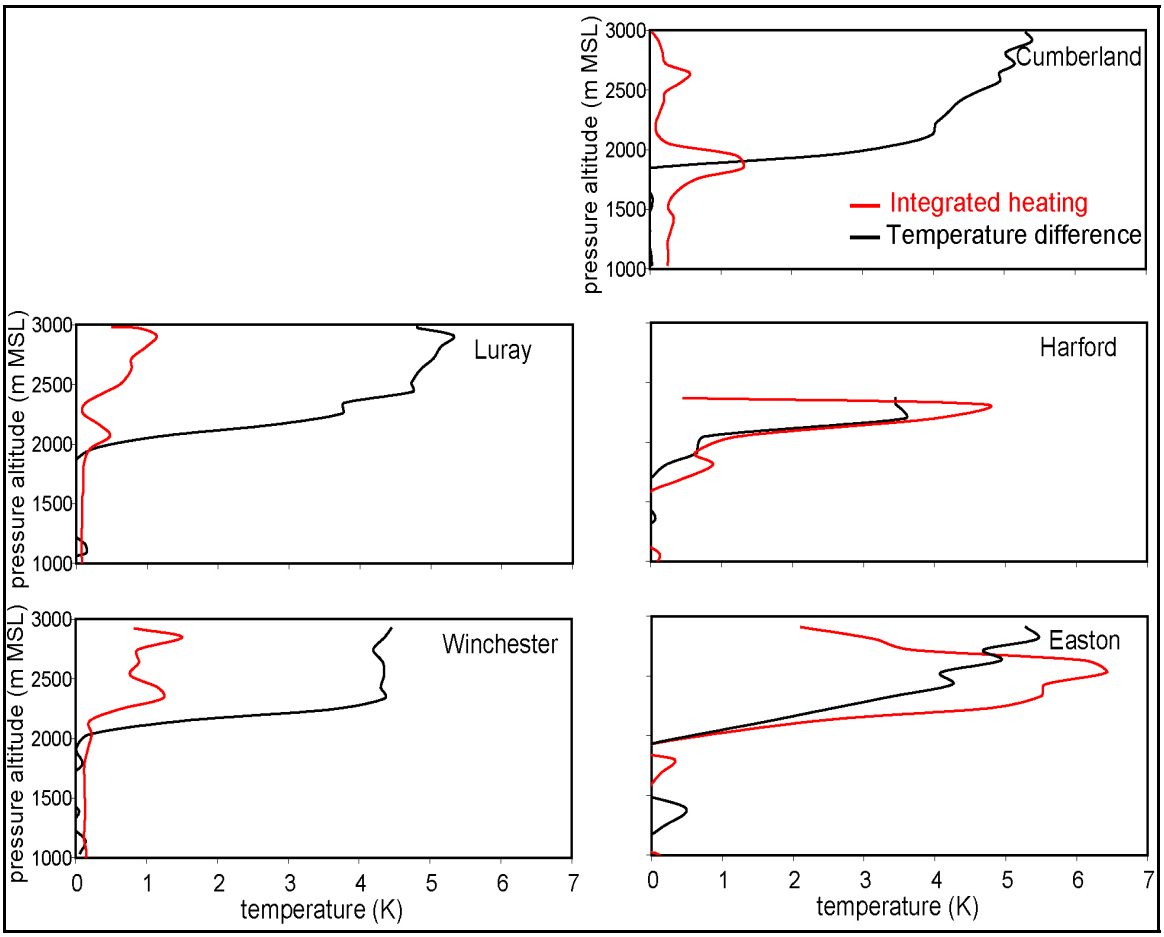

Figure 35. The temperature differences between the temperature measured during the vertical survey spirals over Luray, VA, Winchester, VA, Cumberland, MD, Harford, MD, and Easton, MD and temperature profiles extrapolated from 2 to 3 km as if there were no temperature inversions are shown with the black lines. The integrated heating profiles calculated with the radiative transfer code and integrated from sunrise to the time of each observation spiral are given with the red lines (adapted from Taubman *et al.*, 2004(b)).

The integrated heating for the morning profiles underestimated the observed temperature difference while the afternoon profiles overestimated the amount of heating. The spatially and temporally dynamic nature of the smoke plume would naturally affect the accuracy of this calculation. However, there was also more smoke above the highest measurements made in the aircraft, which was unaccounted

for in the heating rate calculations. Solar attenuation from this unaccounted for smoke would reduce the calculated absorption, and thereby the heating rates, at lower altitudes. This would decrease the amplitude and width of the resulting heating rate profiles. Although these explanations could account for the discrepancy in the afternoon profiles, heating in the smoke layer did not seem to account for the morning inversion.

Figure 36 is the NOAA ARL EDAS meteogram of pressure vertical velocity from 900 – 700 mb, which shows weak subsidence on the morning of the 8th. Hence, adiabatic heating of the descending air may have initially capped the mixed layer and positioned the smoke plume in a thin layer just above it, where heating of the absorptive smoke layer strengthened the inversion. The meteogram shows negative vertical velocity beginning at ~15:00 UTC, indicating upward vertical motion. If the modeled vertical velocity was correct, the subsidence inversion should have dissipated by the afternoon. However, the measured temperature showed an inversion after 20:00 UTC. Thus, the initial subsidence inversion may have acted to sequester the smoke in a thin enough layer above the PBL where it heated the layer and stabilized the atmosphere enough to create a positive feedback loop for its own sequestration. This prevented vertical mixing and dilution and ultimately increased the regional impact of the plume.

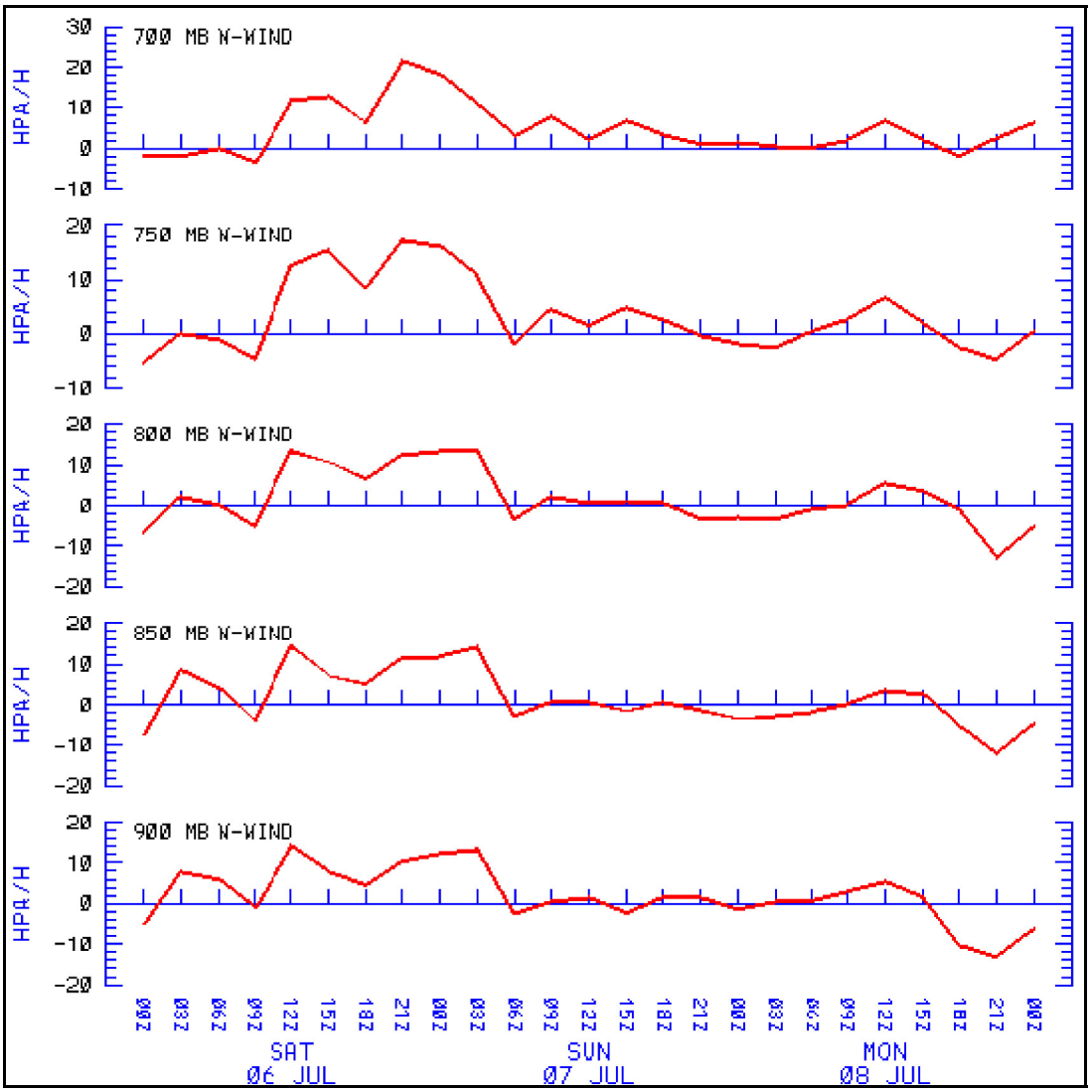

Figure 36. NOAA ARL EDAS meteogram of the pressure vertical velocity at 39.18ºN, 76.67ºW for 6 July – 8 July 2002. The morning of the 8th shows downward vertical motion. By the afternoon of the 8th, there is upward vertical motion (Taubman *et al.*, 2004(b)).

4.3. Summary

Measurements were made of trace gas and particle concentrations as well as particle optical properties associated with the smoke plume advected ~1500 km to the Mid-Atlantic from the Quebec forest fires. Large increases in CO and O_3 mixing

ratios, total particle scattering and absorption, as well as in the number of particles with optical diameters between 0.30 ~1.0 μm were observed between ~2 and 3 km. However, very little SO_2 (less than 0.1% of the CO) was observed at this altitude.

The more absorptive smoke particles had a mean single-scattering albedo value of 0.93±0.02 at 550 nm while the underlying PBL particles had a mean value of 0.95±0.01 at 550 nm. The scattering Ångström exponents of the larger, aged smoke particles were between 0.83±0.15 and 1.23±0.38 while the smaller, PBL particles had values between 1.59±0.30 and 1.99±0.32 for $\alpha_{450/700}$. Calculated Aerosol Optical Depths (550 nm) from just above the surface to ~3 km ranged from 0.42±0.06 above Cumberland to 1.53±0.21 above Easton.

Clear sky aerosol direct radiative forcing was calculated at each location using the SBDART code. Absorption of solar radiation within the smoke plume nearly equaled that which was attenuated at the surface, acting to cool the surface and heat the air aloft. Due to a morning subsidence inversion, the smoke plume was positioned in a thin layer above the PBL between ~2 and 3 km. The heating of this layer was concentrated enough to maintain the temperature inversion through the afternoon. This created a positive feedback loop that prevented vertical mixing and dilution, thereby protracting the lifetime of the plume and the regional radiative impacts.

Chapter 5: Regional Forcing and Uncertainty Analysis

5.1. Introduction

This chapter details the calculation of the regional radiative forcing from the Canadian forest fire smoke plume investigated in the previous chapter and examines the uncertainty involved in measurements of aerosol optical properties when used as inputs to satellite retrieval algorithms. AERONET and aircraft in-situ measurements were made on July 8, 2002 when the plume traversed Maryland and Virginia. The two independent measurements of aerosol optical properties were used as inputs to a standard satellite algorithm to calculate the aerosol optical depth. The optical depth was extrapolated across the solar spectrum to estimate the broadband, regional radiative forcing due to the optically thick smoke plume. Column closure was evaluated by comparing the calculated values of optical depth and radiative forcing at the TOA and surface with measurements from space using CERES and at the surface with SURFRAD (SURFace RADiation network of radiometers) and ISIS (Integrated Surface Irradiance Study). A comprehensive uncertainty analysis of the retrieved smoke optical depth and radiative forcing is detailed, including the possible reasons for disparity between the two measurement techniques.

The results described in this chapter are based on work that I co-authored, in press in the Journal of Geophysical Research (Vant-Hull *et al*., 2004) (reproduced by permission of American Geophysical Union). Brian Vant-Hull, the first author, performed the radiative forcing calculations and used the standard satellite algorithm,

while I collected and analyzed the in situ data and assisted in all other calculations and analyses.

5.2. Results

5.2.1. In-situ Measurements

The sampling platform used to acquire the in-situ data for this study, flight track, and meteorology during the event were detailed in the previous chapter. Two atmospheric layers with discrete aerosol properties were observed in the study. The aerosols within the PBL (surface to ~2 km) were of local origin, stemming from fossil fuel combustion emissions. The LFT, between ~2 and 3 km, was dominated by smoke that was transported from the Canadian forest fires. The larger, more absorptive smoke particles were sequestered in this thin layer by a subsidence inversion. Radiative heating of the smoke protracted the thermal inversion, thereby preventing the vertical mixing and dilution of the plume (Taubman *et al*., 2004(b)). The distinct aerosol characteristics of the two layers allowed for their independent treatment in subsequent calculations.

Observations over Cumberland, MD showed a weak smoke signature in the LFT and inconsistent aerosol properties within the PBL as compared to the other sites. Therefore, the data from this location were excluded from calculations of layer averages.

5.2.2. AERONET Measurements

AERONET is an automated network of ground-based sun photometers that measure the direct solar irradiance at eight wavelengths (340, 380, 440, 500, 670, 870, 940 and 1020 nm) as well as the sky radiance at four wavelengths (440, 670, 870, and 1020 nm). After accounting for attenuation due to Rayleigh scattering and absorption by O_3 and trace gas pollutants, optical depth at each of the wavelengths, $\tau(\lambda)$, is calculated from extinction of the direct solar beam according to the Beer-Bouguer Law:

$$K(\lambda)\downarrow_{dir} = K(\lambda)_{\infty} e^{-\tau(\lambda)} \tag{23}$$

where:

$K(\lambda)\downarrow_{dir}$ = the wavelength dependent direct beam flux at the surface

$K(\lambda)_{\infty}$ = the wavelength dependant solar radiation at the TOA.

By observing sky radiance over many scattering angles through a constant aerosol profile, particle size distributions and phase functions are retrieved.

Three AERONET sites coincided geographically with the aircraft measurements: The GSFC site in Greenbelt, MD (39.02ºN, 76.87ºW), the Smithsonian Environmental Research Center (SERC) site located on the edge of the Chesapeake Bay in Edgewater, MD (38.88°N, 76.50°W), and the Maryland Science Center (MDSC) site located in downtown Baltimore in the inner harbor (39.27°N, 76.62°W). The observed optical depths at all three of the AERONET sites on July 8, 2002 were fairly high; values representative of an optically thick smoke plume. Values at the GSFC site varied between 1.3 and 2.2, the SERC site fluctuated

between 1.8 and 2.2, while the MDSC site recorded optical depths ranging from 1.3 to 1.8 for the day.

In contrast to the optically thick values in the LFT, aircraft measurements in the PBL indicated a regional average value of 0.34 ± 0.10 (the uncertainty represents the variability about this mean value). Because the smoke layer values were roughly five times greater, the AERONET retrievals were probably dominated by the smoke optical properties. However, the PBL aerosol was closer to the instrument and would still exert an influence. Table 6 compares aerosol properties retrieved at the GSFC AERONET site with those measured in-situ aboard the aircraft on July 8, 2002. As mentioned earlier, the aircraft inlet system was unable to collect coarse mode aerosols. According to the AERONET almucantar retrievals, however, the coarse mode only accounted for ~3% of the total optical depth at 550 nm. There are two AERONET asymmetry parameter values given in Table 6. The first one, g = 0.65, is the value provided by AERONET. The second one, g = 0.62, was calculated using Mie theory and the retrieved index of refraction and size distribution (Mishchenko *et al.*, 2002). The satellite retrieved optical depth (see section 5.2.3) was virtually identical whether using the Mie theory phase function (corresponding to the lower asymmetry parameter) or the Henyey-Greenstein phase function (with the larger asymmetry parameter). To be consistent, the Mie theory calculated values were used in the study. The ω_0 and asymmetry parameter values retrieved from the MDSC site were higher than the GSFC values, perhaps due to the propinquity to the water. Whatever the reason, the MDSC values were not considered representative of the entire plume and were excluded from the analysis. The SERC site retrieved only

optical depth. Thus, the AERONET ω_0 and asymmetry parameter values used in this study came solely from the GSFC site.

The column averaged AERONET ω_0 value on July 8, 2002, interpolated to 550 nm (ω_{0550}), was 0.964. The GSFC climatological value (from 1993-2000) of ω_{0550} is $\sim 0.98 \pm 0.02$ (Dubovik *et al*., 2001). It was assumed that this climatological value is representative of the regional, fossil fuel combustion-dominated PBL aerosols. The ω_0 retrieval on July 8, 2002, on the other hand, must have been a weighted column average of PBL fossil fuel combustion and LFT smoke aerosols. Because the smoke layer had approximately five times the optical thickness as the underlying layer, the smoke ω_{0550} value would have been ~0.962. This value, however, is nearly equivalent to the column averaged value of 0.964. Therefore, the column averaged value was used to represent the particles in the smoke layer.

Table 6. Averaged aerosol parameters for the three optical models. Wavelength dependent quantities are given for 550 nm. AERONET values represent a total column average, interpolated to 550 nm, with algorithm uncertainties given for ω_0. Instrumental (but not statistical) uncertainties are given for the aircraft values of ω_0. The uncertainties for g are a composite of instrumental uncertainties and assumptions made in calculating the index of refraction (Vant-Hull *et al.*, 2004).

	Effective radius r_e	variance $\delta(\ln r)$	Refractive index (n+ik)	single scattering albedo ω_0	asymmetry parameter g
AERONET GSFC	0.15 μm	0.61	1.56 + 0.0067i	0.964 ± .03	0.65/0.62
Aircraft smoke	0.22 μm	0.46	1.58 + 0.015i	0.930 ± .02	0.66 ± .04
Aircraft PBL	0.08 μm	0.86	1.43 + 0.006i	0.949 ± .02	0.62 ± .04

5.2.3. Satellite Retrieval of Optical Depth

The in-situ measurements at the four spiral locations (excluding Cumberland, MD) and the retrievals from the three AERONET sites were mostly invariant about the respective mean values, given instrumental and statistical uncertainties. The mean values were therefore considered to be representative of the region defined by Figure 37. Given the synoptic scale of the meteorological system during this event (see Figure 21), the region was extended to include the SurfRad site as well.

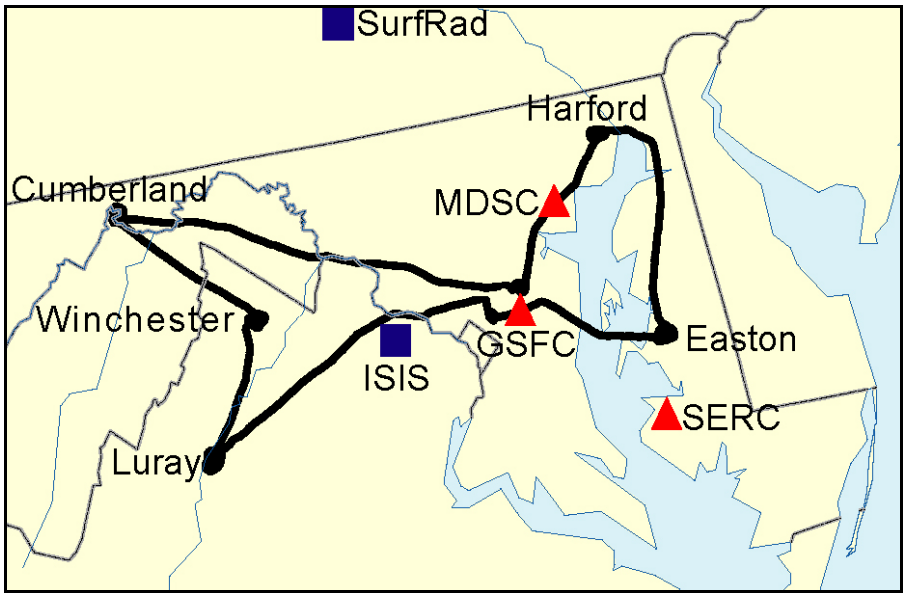

Figure 37. Flight track and locations of measurement spirals on July 8, 2002. The AERONET sites are indicated by red triangles, the SurfRad and ISIS sites by blue squares (adapted from Vant-Hull *et al.*, 2004).

A two-layer system with discrete optical properties in each layer was assumed. The PBL, defined here as the altitude range between the surface and 2 km, made up the bottom layer of the system, while the LFT, between 2 and 3 km, was the upper layer (Figure 38). The aerosol properties within the PBL were assumed to be fixed. The values used were the regional averages (as measured by the aircraft or calculated from measured values) of optical depth (0.34 ± 0.10), ω_{0550} (0.95 ± 0.01), and asymmetry parameter (0.62). The ω_{0550} and asymmetry parameter values used within the smoke layer were either the regional average aircraft values ($\omega_{0550} = 0.93 \pm 0.02$, g = 0.66) or the values derived from the AERONET retrievals ($\omega_{0550} = 0.964$, g = 0.62). To retrieve optical depth using the satellite algorithm, the PBL aerosol optical depth was assumed to be invariant, while the smoke optical depth was varied until the calculated and measured radiances at the TOA were equal.

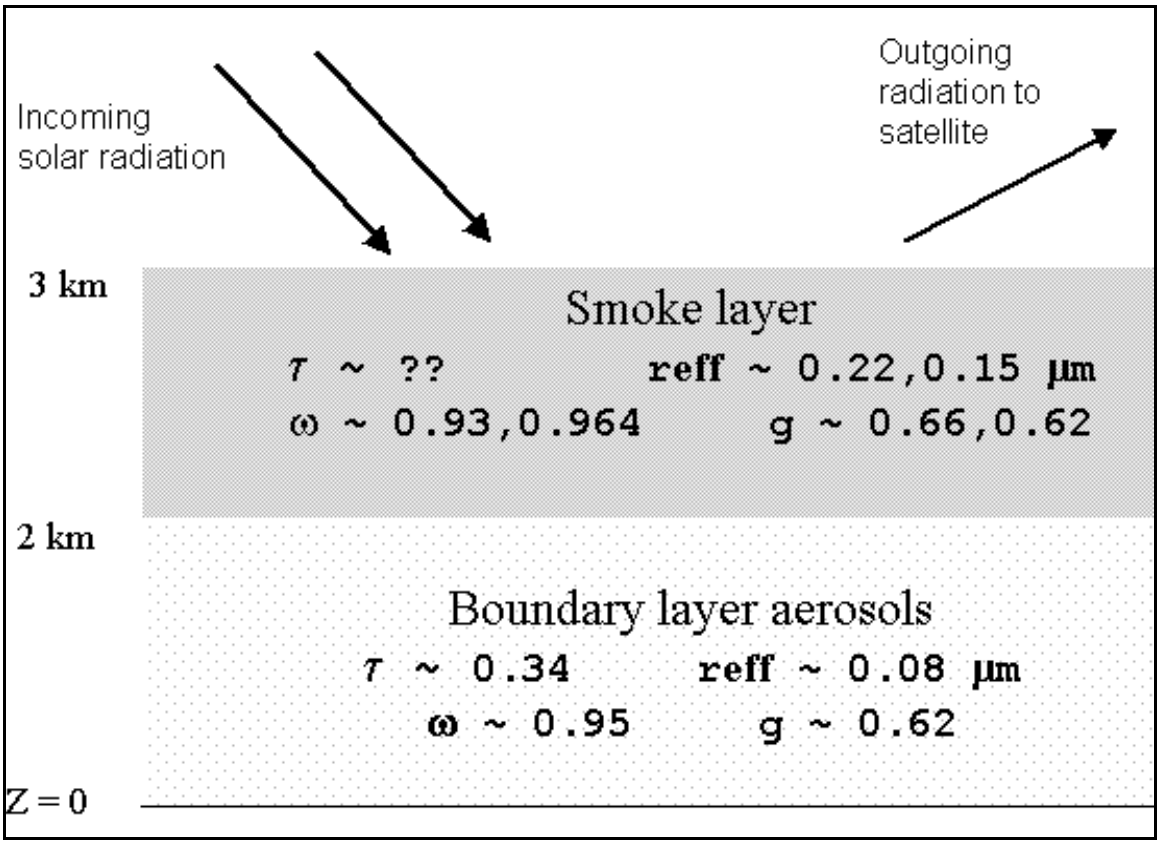

Figure 38. Two layer model in which the smoke layer optical depth was adjusted until the outgoing radiance matched that observed by satellite. The smoke parameters came either from the aircraft in-situ measurements or from AERONET, respectively (adapted from Vant-Hull *et al*., 2004).

TOA radiances at 550 nm (5 km resolution) were measured from the MODIS instrument during the Terra overpass from 1540 to 1545 UTC. The pixels under review were cloud screened to ensure that there was no interference from clouds. Distinguishing between smoke and clouds in the visible wavelengths can be difficult. However, cloud droplet diameters are commensurate to near IR wavelengths while smoke particle diameters are in the sub-micrometer range. Thus, reflectivity in the near IR may be used to distinguish between the two (Kaufman *et al*., 1990(b)). Cloud screening in this manner indicated that the area under review was cloud free.

The satellite retrieved optical depth was calculated from two primary optical models: one employing the AERONET column average values, and one utilizing the layered structure measured by the aircraft, with disparate properties in each layer (Table 7). Two mixed models were also used to retrieve the optical depth. Both mixed models used a layered system, with the PBL layer and different combinations of aircraft and AERONET ω_0 and phase function values in the smoke layer (Table 7). The satellite retrievals of optical depth were compared to the AERONET measurements of optical depth (interpolated from 440 and 670 nm to 550 nm as well interpolated in time to match the satellite overpass) at each of the three sites within the study region (Table 7). The interpolations added estimated uncertainties of ± 0.02 to the algorithm uncertainty for the AERONET observations (Holben, 1998). To make the comparison, the data from four satellite pixels that fell within a 0.1° box centered on each sun photometer were averaged. Some of the data over SERC were rejected due to abnormally high surface reflectance over the Chesapeake Bay.

Table 7. Comparison of aerosol optical depth retrievals. The first three rows show the satellite retrieved optical depth added to the assumed optical depth of the PBL aerosol, the fourth row is a satellite retrieval of the total aerosol column based on AERONET derived properties. The source of the optical parameters used as inputs are listed on the left. Uncertainties denote the variation in retrieved values from surrounding pixels only, and do not reflect instrument or algorithm errors. The fifth row lists the optical depths observed by AERONET interpolated to the time of the satellite overpass, with instrumental and interpolation uncertainties included. The last two rows list the MODIS retrieval with the smoke model used in the western U.S., and the operational retrieval, with algorithmic uncertainties included (Vant-Hull *et al*., 2004).

Single Scattering Albedo	Scattering Phase Functions	GSFC (4 pixels)	SERC (3 pixels)	MDSC (4 pixels)
In-situ + PBL	In-situ + PBL	2.25 ± .10	2.18 ± .26	1.92 ± .08
AERONET + PBL	In-situ + PBL	1.71 ± .07	1.67 ± .21	1.46 ± .06
AERONET+ PBL	AERONET+ PBL	1.55 ± .06	1.51 ± .19	1.33 ± .05
Pure AERONET	Pure AERONET	1.54 ± .06	1.50 ± .19	1.31 ± .05
AERONET Observations		*1.68 ± .04*	*1.79 ± .03*	*1.34 ± .04*
MODIS standard smoke model		*2.02 ± .45*	*1.93 ± .44*	- - -
MODIS operational Eastern US model		1.*69 ± .39*	*1.64 ± .38*	- - -

Satellite retrievals of optical depth using the aircraft optical properties were the highest (Figure 39a), while those using the AERONET optical properties were the lowest (Figure 39b). The mixed models generated optical depths between the two extremes and identified the sensitivity of the satellite retrievals to variations in absorption values and size distributions. Figure 39c shows the optical depth ratio when using in-situ versus AERONET optical properties. The optical depth calculated with the in-situ optical properties was roughly 30% higher than the optical depth calculated with the AERONET optical properties, due mainly to the disparity in ω_0

values between the two models. However, a 30% disparity in optical depth values is inconsistent with a 3.5% divergence in ω_0. This apparent contradiction is explained by multiple scattering effects in optically thick media (Bohren, 1987). Specifically, despite the high probability that each individual encounter leads to a scattering event (dictated by the high ω_0 value), multiple scattering creates greater opportunities for photon absorption. As a result, when optical depths are large, the TOA reflectance becomes a nonlinear function of the single scattering albedo (Wong and Li, 2002).

The MODIS retrieval is given to provide a comparison to an operational satellite algorithm (Figure 39d). MODIS optical depth was retrieved using the smoke model for western U.S. biomass burning and the eastern U.S. operational retrieval with the cloud screening function deactivated (Table 7). Figure 39d shows the retrieval using the eastern U.S. algorithm. The values of ω_0 (0.96) and g (0.66) used in the MODIS retrieval algorithm were nearly identical to the AERONET values. Consequently, the optical depth generated by the MODIS retrieval was very similar to the value determined by AERONET (Figure 39b).

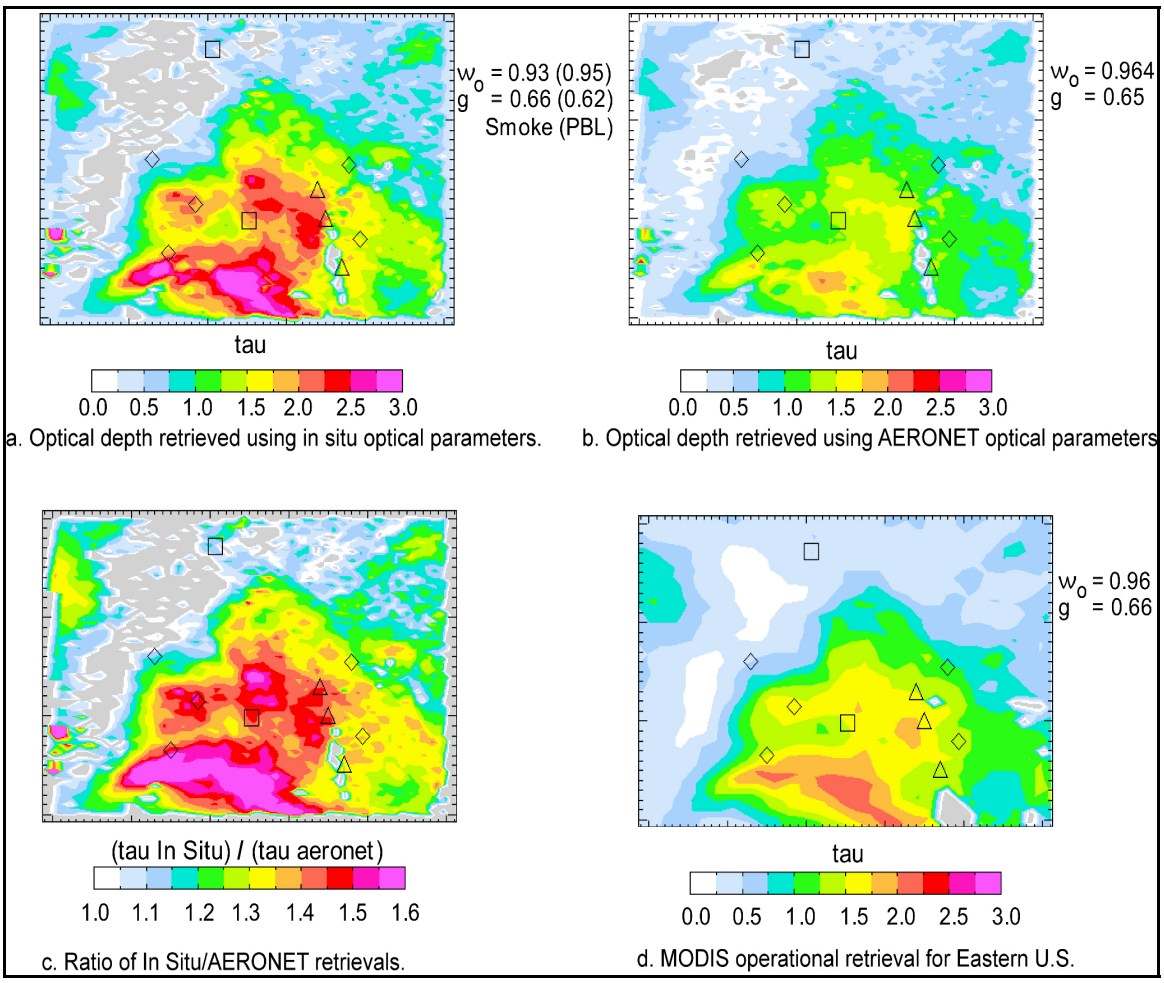

Figure 39. Comparison of optical depth retrievals via satellite. Diamonds show the locations of aircraft spirals, triangles denote AERONET locations, and squares indicate surface radiometer sites. The color scale ranges from 1 to 3. The panels show optical depth retrieved using in-situ optical parameters (a), optical depth retrieved using AERONET optical parameters (b), the ratio of In-situ/AERONET retrievals (c), and the MODIS operational retrieval for the Eastern U.S. (d) (Vant-Hull *et al.*, 2004).

There were portions of the region in which the optical depth retrieval was performed where the calculated reflectance was greater than that measured by the satellite. The areas where this occurred are denoted by the gray color in Figure 39. The large area in the northwestern corner of Figure 39a indicates vicinities lying

outside of the smoke plume where the optical depth must have been lower than the assumed regional average of 0.34. Cumberland, MD is seen to lie right on the edge of this region, confirming that this locale was mostly devoid of smoke at the time of observation. The small gray areas between the two southernmost AERONET sites represent portions of the Chesapeake Bay where the surface reflectance product generated artificially large values. The cloud-screening function in the algorithm may be responsible for any of the other scattered gray areas.

As mentioned earlier, the veracity of satellite retrievals of optical depth are dependent upon the accuracy of the assumed aerosol optical properties used as inputs to the retrieval algorithm. This comparison exhibits the range of possible retrieval values when using different optical properties as inputs. Some of the optical depth retrievals were nearly twice as large when using in-situ measurements of optical properties as compared to retrievals using AERONET optical properties. Because it is unknown which values are the correct ones, the range of retrieval values represents the uncertainty surrounding satellite retrievals of optical depth.

5.2.4. Aerosol Radiative Forcings

The regional aerosol radiative forcings were calculated using the satellite retrievals of optical depth together with the in-situ and AERONET aerosol optical properties. To test column closure of the aerosol optical properties, the radiative forcing calculations were compared to surface broadband flux measurements taken by the Pennsylvania SurfRad and Virginia ISIS radiometers as well as TOA fluxes measured by the CERES satellite radiometer. All radiative forcing calculations were

performed with the SBDART code (Ricchiazi *et al*., 1998), using the LOWTRAN-7 solar spectrum and sixteen streams.

The SurfRad and ISIS surface forcing measurements (clear sky spectrally integrated flux minus spectrally integrated flux with smoke) were compared to the forcing calculations using the four aforementioned optical models (Table 8). Some of the data were interpolated temporally to coincide with the satellite overpass. The SurfRad site was largely smoke-free (see Figure 39, Table 8). Conversely, the ISIS site was enshrouded in smoke (see Figure 39, Table 8). Nevertheless, for both situations, the value calculated using the aircraft in-situ optical properties came closest to the surface measurements. The calculated value was ~10% less than the value measured at the SurfRad site, and ~20% greater than the measured value at the ISIS site (Table 8). The radiative forcing values calculated with the AERONET optical properties, on the other hand, were significantly less than the measured values. Specifically, the calculated values were roughly 50% and 33% lower than the values measured at the SurfRad and ISIS sites, respectively.

Table 8. Broadband surface radiative forcing at the two radiometer sites. The top four rows are calculations based on satellite retrievals of optical depth whereas the bottom row gives the actual measurements. Uncertainties indicate spatial variation between pixels surrounding the site for the satellite retrievals and temporal interpolation uncertainty for radiometers (adapted from Vant-Hull *et al*., 2004).

Single scattering albedo	Scattering phase functions	SurfRad 1541 Z		ISIS 1541 Z	
		Tau	Forcing (W/m^2)	Tau	Forcing (W/m^2)
In-situ + PBL	In-situ + PBL	$0.57 \pm .12$	-102 ± 19	$1.93 \pm .09$	-297 ± 11
AERONET + PBL	In-situ + PBL	$0.53 \pm .09$	-87 ± 12	$1.47 \pm .04$	-193 ± 4
AERONET + PBL	AERONET+ PBL	$0.51 \pm .08$	-88 ± 12	$1.33 \pm .03$	-188 ± 3
Pure AERONET	Pure AERONET	$0.45 \pm .12$	-58 ± 17	$1.32 \pm .03$	-166 ± 3
Measured Forcing			***-113*** $\pm$ *11*		***-246*** $\pm$ *8*

The greater optical depths generated with the in-situ optical properties were largely the reason for the larger surface forcings calculated with the in-situ values. The lower forcing values calculated with the AERONET optical properties are more difficult to justify. Using only the fine-mode aerosol retrievals may be partly to blame. Larger particles account for greater percentages of the optical depth as the wavelength increases to become commensurate with the particle diameter. However, coarse mode aerosols only accounted for 10% of the AERONET retrievals of optical depth at $1.02\,\mu m$. Even if the radiative forcing at longer wavelengths were due primarily to coarse mode aerosols, these wavelengths only account for a small portion of the overall forcing. Rather, the lower radiative forcing values are probably the result of the narrow AERONET size distribution within the region of greatest solar intensity. Broadband radiative forcing is calculated by integrating the forcing at each wavelength. Aerosols with a narrow size distribution are only spectrally active over a

narrow range of wavelengths. Conversely, aerosols with broader size distributions (e.g., the aircraft in-situ derived size distribution) are spectrally active across a greater wavelength range and result in a larger broadband radiative forcing.

The CERES instrument, on the same Earth Observing System (EOS) satellite as MODIS, measures both solar-reflected and Earth-emitted radiation. The CERES team uses an ERBE-like (Earth Radiation Budget Experiment) inversion of measured radiance to calculate instantaneous TOA flux (Green and Robbins, 1997). This process uses angular dependence models (ADMs) that account for the anisotropy of the radiation field due to geotype (e.g., ocean, land, snow, desert, coast) and cloud cover. The CERES TOA flux was compared to the TOA flux calculated with the in-situ and AERONET optical properties (Figure 40). The calculated TOA fluxes are both larger than the flux retrieved by CERES, although the flux calculated with the in-situ optical properties is closer to the CERES value. This is despite the fact that the optical depth retrieved using the AERONET optical properties was lower than that retrieved with the in-situ values. Thus, the larger flux calculated with the AERONET optical properties must be due entirely to the aerosol optical properties. The smaller, more scattering particles scattered more light in the backward direction, thereby increasing the calculated TOA flux. The measured and calculated flux values were also used to estimate TOA forcing. Figure 41 shows the forcing at the TOA, the surface, and within the atmosphere calculated using the in-situ and AERONET optical properties. The fluxes measured at the surface and the TOA were all closer to the fluxes calculated with the in-situ optical properties. Therefore, the aerosol radiative forcing calculated with the in-situ values may be more accurate.

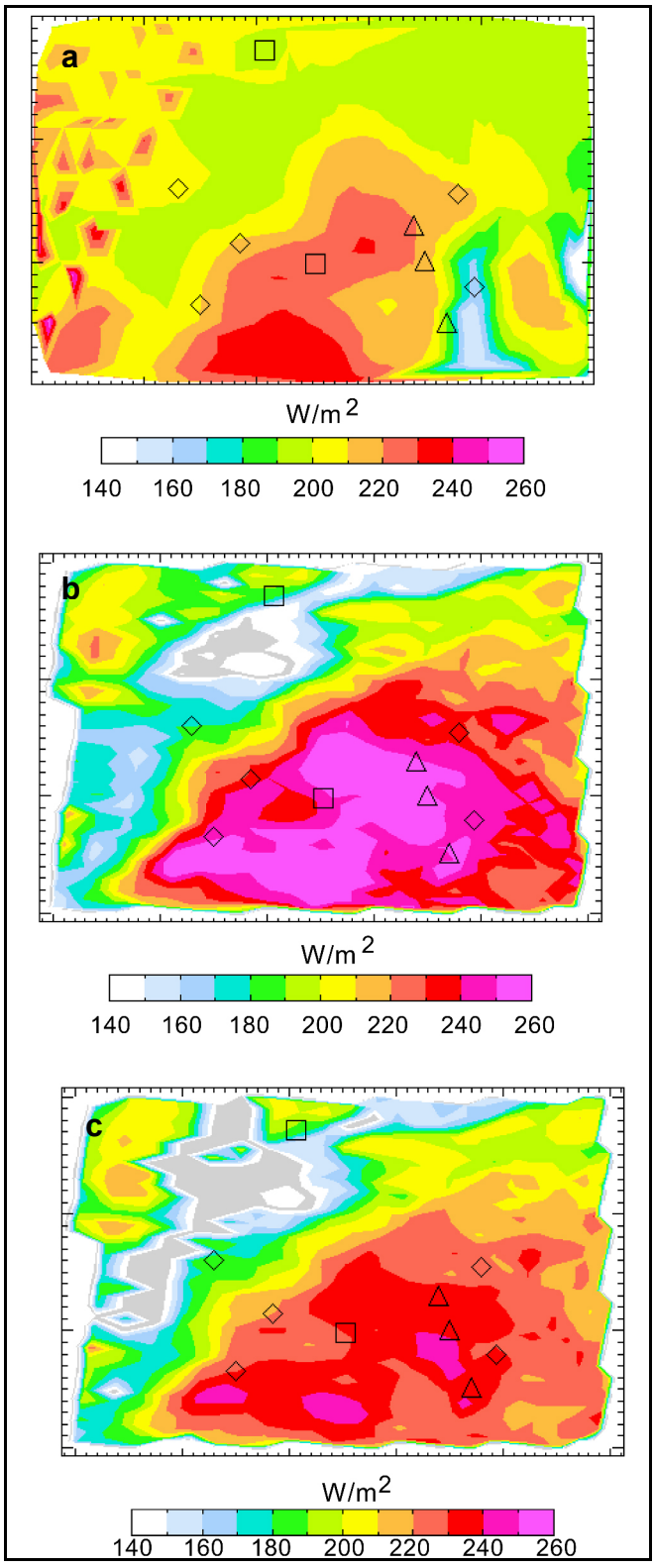

Figure 40. Comparisons of TOA flux measurements to calculations from the two primary optical models. For symbol definitions see figure 39. The gray areas are undefined data. The three panels indicate: TOA flux retrieved by CERES

(a), TOA flux calculated from the AERONET model (b), and TOA flux calculated from the in-situ model (c) (Vant-Hull *et al.*, 2004).

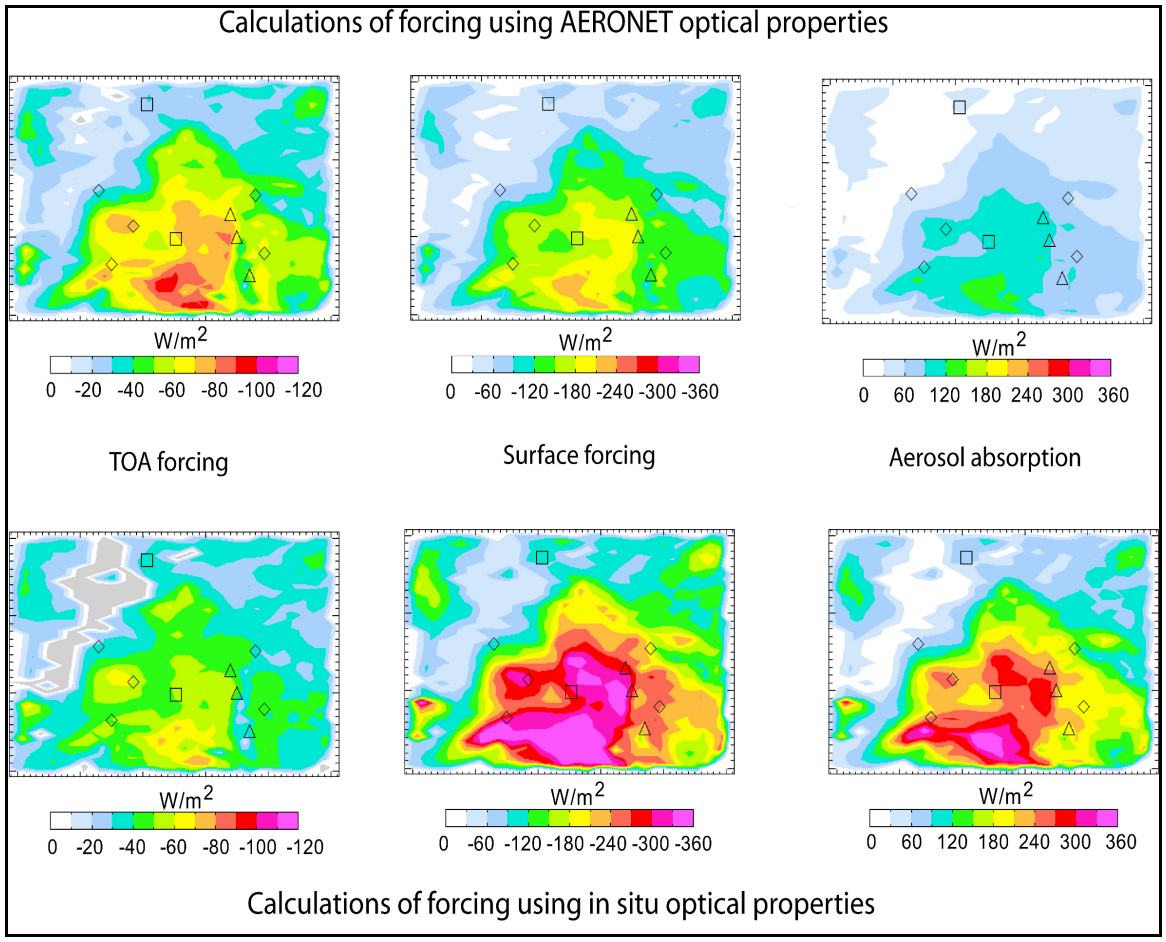

Figure 41. Radiative forcing maps calculated from the optical depth retrievals and optical models. The top row is based on AERONET, the bottom row is based on in-situ data. For symbol definitions see figure 39. Gray areas are undefined data. The color scale ranges from 0 - 120 W/m^2 for TOA forcing, 0 - 360 W/m^2 for the absorption and surface forcing (Vant-Hull *et al.*, 2004).

5.2.5. Uncertainty in Optical Depth Retrievals

When the TOA reflectance is fixed, minor fluctuations in the single scattering albedo produce large, contrary changes in the satellite derived optical depth (Figure 42). The curve may be roughly described by the following relationship:

$$\Delta\tau \approx -(5\tau^{5/2})\Delta\omega_o \qquad (24)$$

Thus, for an optical depth, τ = 2, a small decrease in the single scattering albedo of 0.01 would increase the optical depth by ~0.28 or 14%.

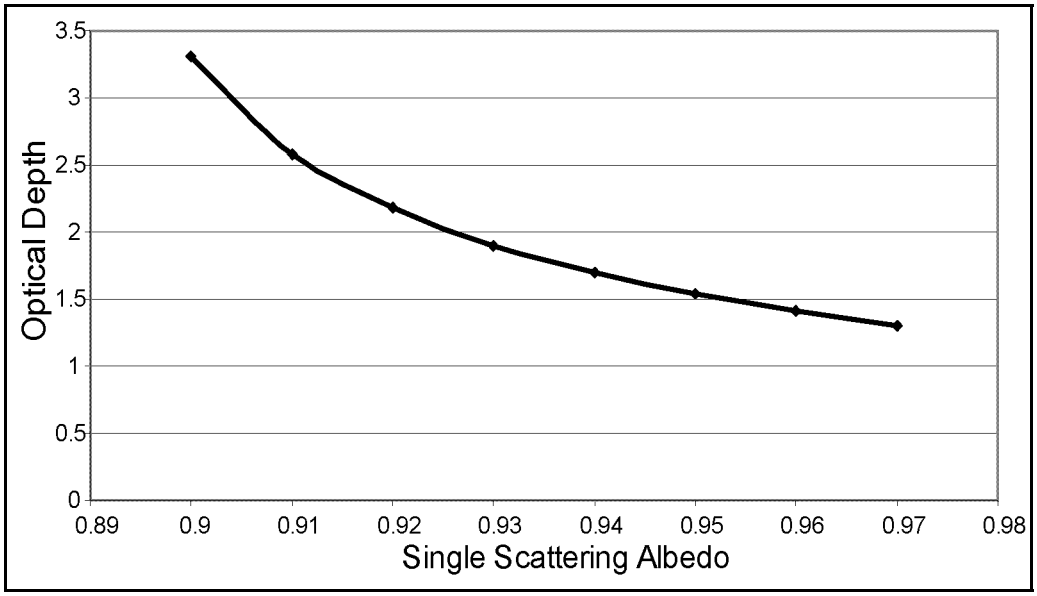

Figure 42. Retrieved optical depth as a function of single scattering albedo for a fixed TOA radiance (Vant-Hull *et al*., 2004).

When the measured radiance is fixed, changes in the surface albedo produce contrary changes in the retrieved optical depth. To test the sensitivity of the retrieved optical depth to the surface albedo, a point was selected in the middle of the study area as representative of the typical sun-satellite geometry used in the retrievals. Figure 43 shows "isorads", or lines of constant radiance, in 5 W m^{-2} increments. The slopes of the isorads decrease with increasing optical depths. This indicates that the optical depth becomes less sensitive to the surface reflectance as it becomes larger. At an optical depth close to 2 (reasonable with regard to this study), an uncertainty in

surface reflectance of ± 0.02 (typical for mid-latitude, summertime, mixed vegetation land cover) would create an optical depth uncertainty of ± 0.1. This would be, for example, approximately a 5% uncertainty for the optical depths retrieved over the AERONET sites.

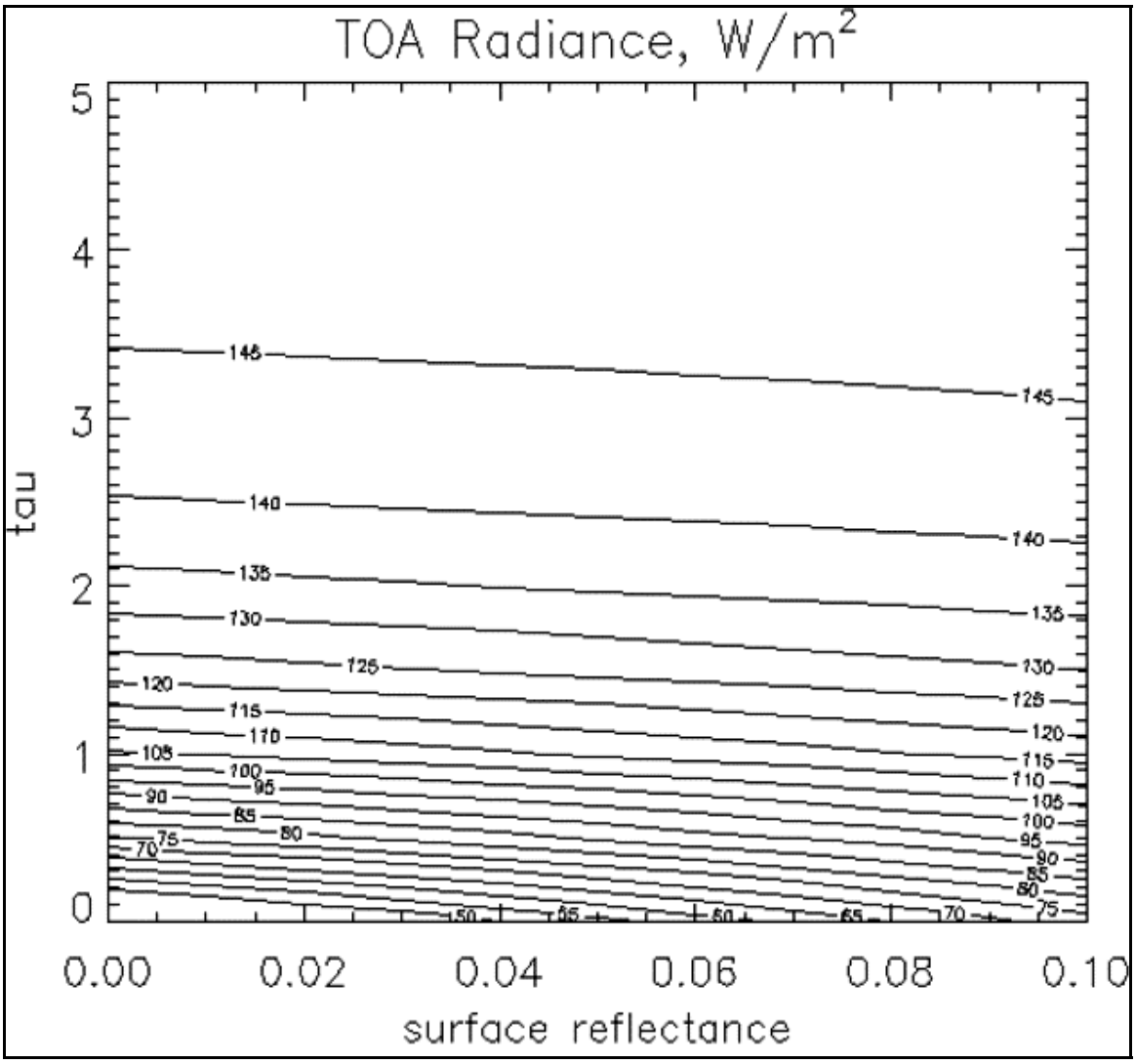

Figure 43. Satellite observed radiance (contours) as a function of optical depth and surface reflectance (Vant-Hull *et al*., 2004).

The measured scattering Ångström exponents ($\alpha_{450/550}$ and $\alpha_{550/700}$) were used to calculate the phase functions. For the purpose of this study, the scattering Ångström exponents were assumed to vary no more than one standard deviation about the mean values. A sensitivity analysis was performed to determine the effect of these possible fluctuations on the retrieved optical depth. The results are given in Table 9. The asymmetry parameters are also shown to provide a measure of the impact of the perturbations on calculated optical properties. The optical properties were affected less by the absolute values of the Ångström exponents than by the distance between the values. Thus, when the two Ångström exponents were altered by one standard deviation about their respective mean values, but in opposite directions, the optical depth changed by ~20% (see the last two rows, Table 9).

Table 9. Retrieved optical depth of smoke as a function of the scattering phase functions derived from scattering Ångström exponents measured in-situ. Note that optical depth does not include PBL (Vant-Hull *et al.*, 2004).

	Angstrom Exponents	g	Tau GSFC
"average"	$\alpha_{450/550} + 0$, $\alpha_{550/700} + 0$	**0.662**	**1.90**
"high"	$\alpha_{450/550}$ + s.d., $\alpha_{550/700}$ + s.d.	0.656	1.87
"low"	$\alpha_{450/550}$ - s.d., $\alpha_{550/700}$ - s.d.	0.667	1.94
"tight"	$\alpha_{450/550}$ + s.d., $\alpha_{550/700}$ - s.d.	0.638	1.60
"wide"	$\alpha_{450/550}$ - s.d., $\alpha_{550/700}$ + s.d.	0.691	2.33

The calculated phase functions (and hence the optical depth) are also impacted by the real part of the complex index of refraction. The retrieval is mostly invariant when $1.54 < n < 1.62$. When the real index of refraction falls below this range, however, the impacts to the retrieved optical depth become substantial. AERONET reports an uncertainty in real index of refraction values of ± 0.03 (Dubovik *et al.*, 2000). An estimated real index of refraction value of 1.58 ± 0.03 for this study falls within the above stable range, making the contribution to retrieved optical depth uncertainty minimal.

The PBL aerosol optical depth was fixed at 0.34 ± 0.1 (the regional average determined by the aircraft profiles, with the uncertainty representing the variation about the mean value) to isolate the radiative impacts of the smoke. However, the optical depth, in reality, must have varied across the study area at the time of satellite overpass. As a result, the retrieved smoke optical depth must counterbalance the unaccounted for variance in the PBL. The uncertainty of the PBL aerosol (0.1) was therefore added to the uncertainty of the retrieved optical depth in the smoke layer.

When all of the individual uncertainties, including the instrumental uncertainty with scattering and absorption measurements addressed in chapter 2, were added in quadrature, a total uncertainty of $\pm 22\%$ for satellite retrieved optical depths close to 2 resulted. An uncertainty of this magnitude accounts for the assortment of values calculated with the different optical models. Therefore, given the current instrumental uncertainties, the in-situ and AERONET optical properties used in this study may be said to be equivalent.

5.2.6. Uncertainty in Forcing Calculations

Calculations of surface forcing are sensitive to the retrieved optical depth values. In fact, for the optical depth values reported in this study, multiple scattering effects did not play a dominant role and the surface forcing was proportional to the optical depth. The relationship between uncertainties in the optical depth and single scattering albedo is described in equation 24. For an uncertainty in ω_0 of ± 0.02 (the approximate instrumental uncertainties for the range of single scattering albedo values measured during this study), the optical depth uncertainties at the SurfRad and ISIS sites would be 0.5% and 16%, respectively. Equivalent uncertainties in the surface forcing values at these two sites would then be expected.

As mentioned before, the optical depth over multiple wavelengths is affected by the size distribution, the calculation of which is affected by the real part of the index of refraction. Within the aforementioned stable range of real index of refraction values, the effect on surface forcing values was minimal, but once this threshold was breached, the effect was quite large (Table 10). The SurfRad site is not given because the optical depth there was too low to show significant effects. The

width of the size distribution is also inversely related to the numerical distance between scattering Ångström exponents. However, changes to the size distribution may not result in concomitant variations in the retrieved optical depth at a single wavelength and broadband TOA forcing. In fact, altering the size distribution may even create an inverse impact on optical depth at 550 nm and TOA forcing (Table 10). The forcing values represent the integrated forcing over many wavelengths and the impacts felt at a single wavelength may not reflect the overall variability.

The uncertainties in the optical depth and size distribution were added in quadrature and the overall uncertainties in the calculated surface forcing values at the SurfRad and ISIS sites were determined to be ~6% and ~19%, respectively. These uncertainties account for the disparity between the measured values and the values calculated with the in-situ optical properties, but not for the values calculated with the AERONET optical properties. Because it was measured by satellite, the TOA forcing was determined for the entire region. However, the spectral variability of the surface reflectance is complicated to estimate. Not to mention the fact that the uncertainties associated with the aerosol characteristics alone contributed ~11% to the total uncertainty. Regardless, the TOA forcing calculated with the in-situ data matched the CERES values (within uncertainty ranges), while the TOA forcing calculated with the AERONET optical properties did not.

Table 10. Effects of varying the scattering Ångström exponents and real index of refraction on retrieved radiative forcing. Refer to table 9 for the explanation of the types of variations in the two values. The PBL aerosol layer was not varied (adapted from Vant-Hull *et al*., 2004).

	Tau (550 nm) ISIS (Sterling, VA)	Surface Forcing (Watts/m^2)	TOA Forcing (Watts/m^2)
Average properties: Total	**1.93**	**-297**	**-50**
PBL	**0.34**	**-64**	**-25**
Ångström exponent variations			
"tight"	1.66	-279	-54
"wide"	2.28	-324	-44
"low"	1.96	-299	-49
"high"	1.90	-295	-51
Index of refraction variations			
n = 1.50	2.45	-345	-43
n = 1.54	1.97	-299	-49
n = 1.62	1.92	-298	-50

5.3. Discussion

In-situ measurements of aerosol optical properties used as inputs to a satellite algorithm generated greater optical depth values than when AERONET derived optical properties were used. Because the optical depth was large, due to the thick pall of smoke, the absorption, though relatively small compared to the scattering, played a more vital role in the retrieval. Further, the radiative forcing calculated at the surface and TOA did not correlate with the retrieved optical depth.

The single scattering albedo was the primary source of uncertainty in the satellite retrieval of optical depth. The difference between the AERONET derived single scattering albedo and that measured in-situ cannot be attributed to the column averaged retrieval performed by AERONET. The values were equivalent given the

statistical and instrumental uncertainties; however, the difference between the two had a large impact on the radiative calculations that were based upon them.

The in-situ ω_{0550} value of 0.93, as compared to the AERONET value of 0.964, indicates that either the in-situ absorption was twice as large or the in-situ scattering was twice as small as the AERONET value. This disparity also arises in an evaluation of the GSFC AERONET climatological average ω_{0550} value of 0.975 (Dubovik *et al*., 2001) and the in-situ measurement value of 0.95 (Hartley *et al*., 2000). The notion that in-situ scattering measurements are responsible for the discrepancy of ω_{0550} values is unlikely. Scattering typically (this study included) makes up more than 90% of the total extinction by particles. Multiple column closure studies have demonstrated conformity in optical depth values (the vertically integrated extinction by particles) measured in-situ by aircraft and using sun photometer retrievals (Hegg *et al*., 1997; Remer *et al*., 1997; Russell *et al*., 1999; Ross *et al*., 1998; Kato *et al*., 2000; Fiebig *et al*., 2003; Haywood *et al*., 2003; Magi *et al*., 2003). Considering the large scattering/absorption ratio seen in these studies, the scattering values must also have agreed.

The above studies set the bar for conformity at values within 20% and a few percent for the optical depth and ω_0 , respectively. When column closure tests are based upon the optical depth, little information is gained in regards to the absorption, which is relatively small compared to the scattering, and could vary considerably while having little impact on the optical depth and ω_0 . It is imperative, however, when dealing with optically thick plumes such as the one encountered in this study, to achieve greater confidence in ω_0 values. The MODIS retrieval uncertainty is given

as $\pm(0.2\tau + .05)$ (Kaufman and Tanre, 1998), or 35% for an optical depth of 1.5. That seems quite large until one realizes that, according to the results of this study, if the uncertainty in ω_{o550} was ± 0.03, the uncertainty for an optical depth of 1.5 would surpass that quoted for the MODIS retrieval (see Figure 42 and equation 24).

There was a consistent difference in the measured optical properties as observed by the two platforms used for this study. Smoke optical properties have been observed to change as the optical depth of the plume changed (Remer *et al*., 1998; Dubovik *et al*., 2001; Wong and Li, 2002). However, there was no spatial trend observed in either the aircraft or the AERONET measurements of the smoke optical properties. Therefore, the offset cannot be attributed to a compositional difference in the smoke particles observed by the two platforms.

The absorption, then, must be the reason behind the discrepancy between the two measurement platforms. The PSAP is a simple and widely used instrument for measuring in-situ particle absorption, particularly on aircraft platforms (Hegg *et al*., 1997; Reid *et al*., 1998(b); Hartley *et al*., 2000; Taubman *et al*., 2004(a); Taubman *et al*., 2004(b)). Nevertheless, it is a filter based measurement technique that naturally introduces measurement error. The laboratory calibration on which the corrections to the PSAP values in this study and most others since 1999 were based (Bond *et al*., 1999) used a single, solid, standard absorptive hydrocarbon aerosol. However, different particles react differently to variability in heating and humidity as well as to filter interactions. For example, the recommended corrections to account for scattering effects were based solely on the calibration aerosol (n = 1.67 at 550 nm), but different aerosols would cause different scattering effects depending on the

ambient aerosol index of refraction. Because scattering is so dominant relative to absorption, this is not an insignificant source of uncertainty either. Also, many particles are largely liquid and, therefore, may deform when collected on the filter. The calibration was based upon a non-deformable solid aerosol, whereas aged smoke particles (such as the ones observed in this study) are thought to be a solid core enveloped by liquid (Bundke *et al*., 2002).

The radiative forcing values calculated with the in-situ optical properties were closer to the SURFRAD, ISIS, and CERES measurements than those calculated using the AERONET optical properties. In apparent contradiction to these results is the fact that the satellite retrieved optical depth using the AERONET optical properties was closer to observed values than when the in-situ values were used as inputs. The AERONET area-weighted size distribution consisted of an incomplete multimodal distribution. The effective radius used in the radiative calculations was based on an area-weighted average, although it was difficult to estimate a value for the incomplete multimodal distribution, a potential source of error. The multiple assumptions and steps necessary to complete the radiative forcing calculations may have introduced a systematic bias that favored the higher optical depths generated with the in-situ values. Further, the conversion of CERES radiance measurements to TOA flux is based on multiple assumptions of radiation anisotopries due to different surface characteristics and cloud cover, creating uncertainties that are challenging to quantify. Despite the uncertainty surrounding the calculations, the results of this study suggest that optical depth values at a single wavelength may not correspond to radiative forcing values that are integrated over the entire solar spectrum.

5.4. Summary

The optical depth of the smoke plume from Canadian forest fires was calculated using satellite reflectances as well as AERONET retrieved and in-situ aircraft measured optical properties. Different combinations of the AERONET and in-situ values were also used. The optical depths calculated using the pure AERONET optical properties were the lowest, while the retrievals using pure in-situ values were the highest. The larger optical depths retrieved using the in-situ optical properties were due to the fact that the in-situ measurement of absorption was twice as large as that derived by AERONET. However, given the algorithmic, instrumental, and statistical uncertainties of the results, the retrieved values of optical depth could be said to be equivalent.

The broadband radiative forcings at the surface and TOA were calculated using the satellite retrieved optical depth at a single wavelength by extrapolating the value across the solar spectrum according to the particle size distributions. Forcings calculated using the in-situ optical properties matched surface and TOA measurements more closely than those determined using the AERONET optical properties. This is in apparent contradiction with the fact that optical depth retrievals using AERONET optical properties matched the AERONET observations more closely than the retrievals using the in-situ optical properties and merits further investigation.

Measuring absorption by particles in the atmosphere is a relatively new focus in the aerosol community. Despite Herculean efforts, achieving consistency between

disparate measurement techniques has proven a formidable challenge. Satellites provide the most spatially efficacious means of observing aerosols, but the accuracy of their retrievals depends upon the veracity of the aerosol optical properties used as inputs. Calculations of radiative forcing are even more involved than optical depth retrievals and are, thereby, more prone to inaccuracy. This phenomenon is demonstrated by the fact that the optical properties measured in-situ and by AERONET and the retrieved optical depths calculated with these two inputs were equivalent, given instrumental uncertainty, but the radiative forcing values based on these inputs diverged considerably. The disparities between the two measurement platforms observed in this study were exacerbated by the optical thickness of the smoke plume. Because typical aerosol loading is considerably lower than that observed in this study, this issue has garnered little interest in the past.

Chapter 6: The Blackout

6.1. Introduction

The August 14, 2003 electrical blackout was the largest in North American history. It affected roughly 50 million people in a 24,000 km^2 area that stretched from New York through Connecticut, Massachusetts, and Vermont to Ottawa and Toronto, Canada west to Detroit, Michigan, and south through Ohio, Pennsylvania, and New Jersey. Within minutes after 16:00 EST on August 14, 2003, 21 power plants were tripped in the United States. In all, over 100 power plants were significantly scaled back for varying amounts of time, ranging from hours to days. Figure 44 shows a nighttime satellite view of the evening prior to the blackout, August 13. Figure 45 shows the same view on the evening of the blackout, August 14. Note the loss of evening illumination throughout most of the northeastern U.S. and southeastern Canada. Power was gradually restored to the region over the next several days.

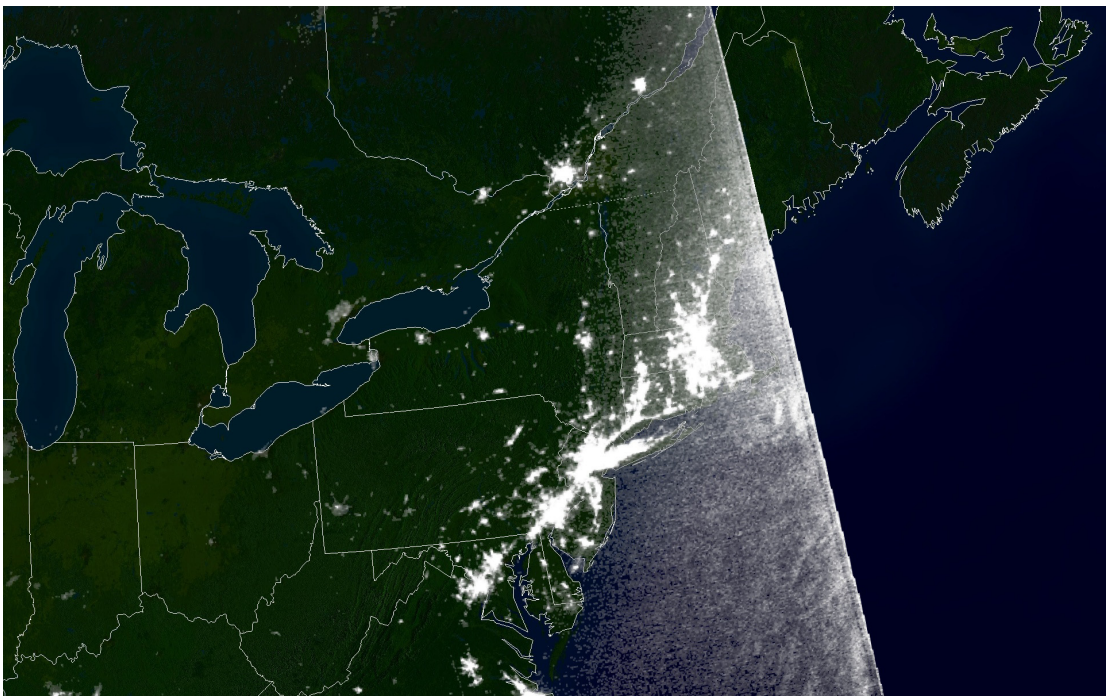

Figure 44. Satellite image of the northeastern US taken Aug. 13, 2003, at 21:21 EDT (NOAA processed the data from the Defense Meteorological Satellite Program).

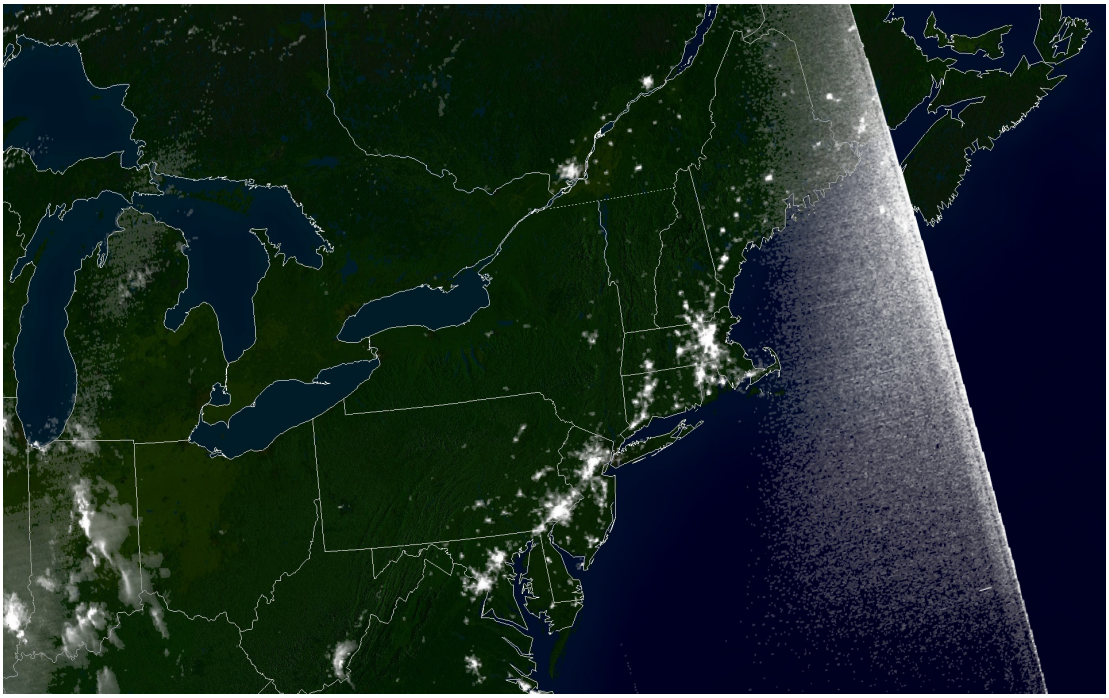

Figure 45. Satellite image of the northeastern US taken Aug. 14, 2003, at 21:03 EDT (NOAA processed the data from the Defense Meteorological Satellite Program).

Airborne measurements were made over Maryland and Virginia (outside the blackout area) and Pennsylvania (downwind of the blackout area) on August 15, 2003, ~24 h into the blackout. The data were compared to those from the previous summer in the same locations and under similar meteorological conditions when upwind power plants were operating normally. Emissions data were examined in conjunction with back trajectories to determine the contribution of power plants to the observed air quality. The results enabled the quantification of the impact of reduced SO_2 and NO_x emissions, with all other factors held relatively constant, on air quality in the northeastern U.S. The results described in this chapter are based on work that I co-authored, published in Geophysical Research Letters (Marufu *et al*., 2004) (reproduced by permission of American Geophysical Union). I was the mission

scientist aboard the flights used in this study. I also performed most of the subsequent analyses and contributed extensively to the written manuscript.

6.2. Results and Discussion

Two flights were conducted on August 15, 2003. During the first flight, three vertical survey spirals (surface - 3 km) were performed over Luray (38.70ºN, 78.48ºW) and Winchester (39.15ºN, 78.15ºW) in Virginia and Cumberland, Maryland (39.60ºN, 78.70ºW) at ~14:00, 15:00, and 15:30 UTC, respectively. Two spirals were performed over Selinsgrove, Pennsylvania (40.82ºN, 76.86ºW) at ~19:00 and 20:00 UTC during the second flight.

The morning spirals (outside the blackout region) revealed trace gas mixing ratios and particle properties typical of those routinely observed on previous flights (Dickerson *et al*., 1995; Ryan *et al*., 1998; Taubman *et al*., 2004(a)). Observations over Luray, for example, showed maxima in SO_2 and O_3 mixing ratios in a thin layer at ~1 km MSL (Figures 46a,b). A corresponding peak in particle light scattering was also seen at this altitude; but scattering values increased again below 500 m MSL (Figure 46c), corresponding to a maximum in CO (Figure 46d). These observations indicate a stable nocturnal boundary layer with a maximum depth of 500 m MSL. Above this altitude, NO_x and SO_2 from power plants produced O_3 and SO_4^{2-}, respectively, which were transported in the residual layer. Below 500 m, the pollution was most likely of local origin. Particles observed in the nocturnal boundary layer may have been largely organics, the products of vehicle exhaust and

home heating and cooking, which can scatter visible light efficiently (Malm *et al*., 1994).

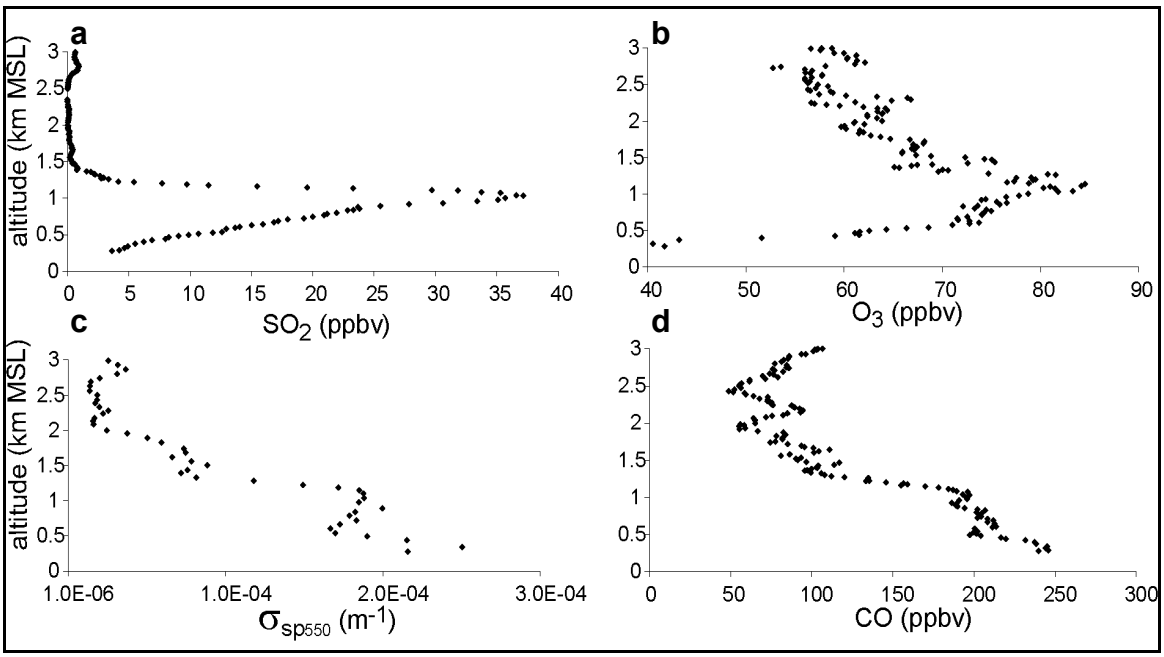

Figure 46. Running 1 min mean SO_2 mixing ratios (a); 10 s O_3 mixing ratios (b); particle light scattering at 550 nm (c); and running 1 min mean CO mixing ratios (d) over Luray, Virginia (outside blackout area) at 1500 UTC (10:00 LST) 15 Aug, 2003 (Marufu *et al*., 2004).

Observations from the afternoon flight were different. Spirals over Selinsgrove, Pennsylvania revealed very little O_3, SO_2, and PM relative to the morning flight and areas to the south (Figures 47a-c). CO concentrations were within 0.5 σ of the 1992 median August and September values over Baltimore, Maryland and vicinity (Dickerson *et al*., 1995), and remained fairly constant throughout the afternoon, apparently only varying with altitude (Figure 47d). Linear regressions between O_3 and SO_2 measured during the flight showed that O_3 over Selinsgrove was not correlated with SO_2 ($r = -0.13$), while it was elsewhere ($r = 0.80$) (Figures 48a,b).

The observations over Selinsgrove are consistent with reductions in power plant emissions but no corresponding changes in vehicle emissions.

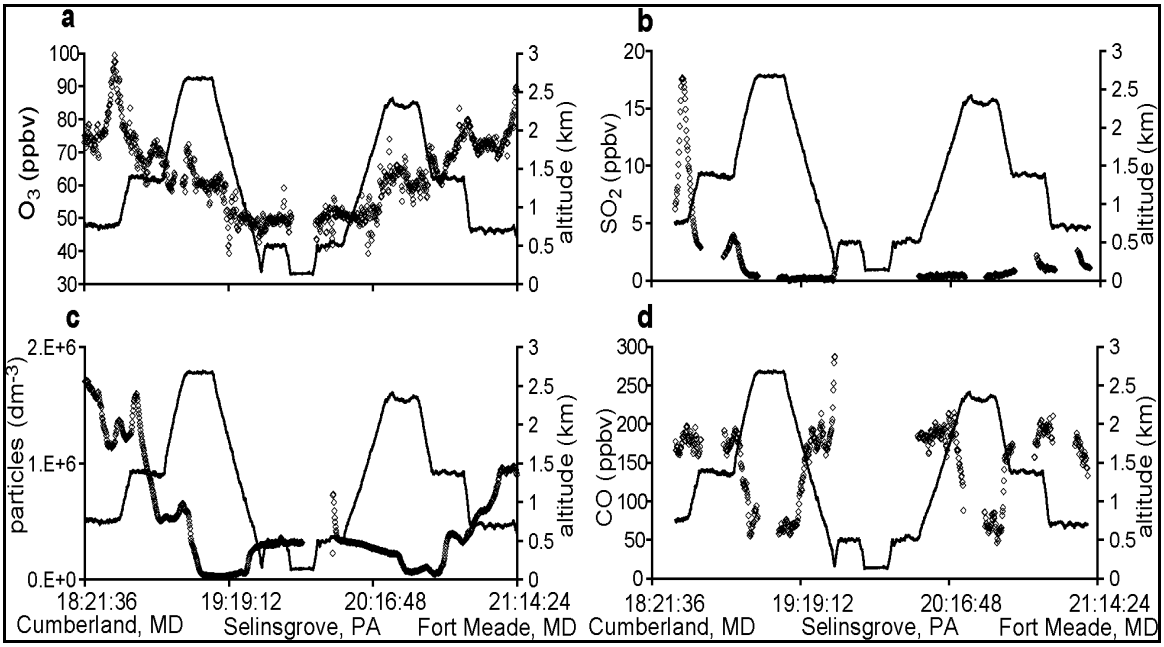

Figure 47. Second flight on August 15, 2003 showing altitude (solid black lines), time (UTC), as well as takeoff, landing and spiral locations. Open diamonds represent 10 s O_3 mixing ratios (a); running 1 min mean SO_2 mixing ratios (b); sub-micrometer particle counts (c); and running 1 min mean CO mixing ratios (d) (Marufu *et al.*, 2004).

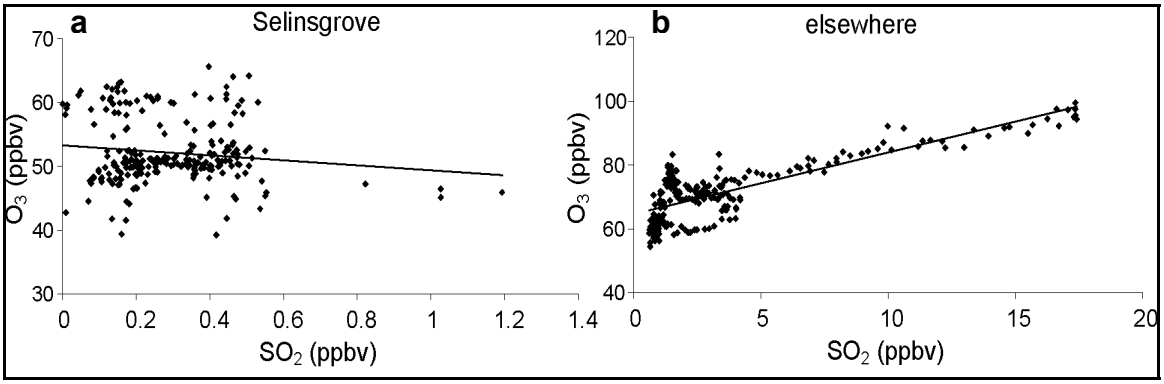

Figure 48. Linear regressions of SO_2 and O_3 over Selinsgrove, PA (r = -0.13) (a) and elsewhere (r = 0.80) (b) during the second flight on August 15, 2003.

To investigate whether the improvement in air quality over Selinsgrove was due to reductions in upwind power plant emissions, 24 h backward trajectories were run from Selinsgrove at 500, 1500, and 2500 m AGL using the NOAA ARL HYbrid Single-Particle Lagrangian Integrated Trajectory (HYSPLIT) model (Version 4) (Draxler and Rolph, 2003) and EDAS meteorological fields (Figure 49a). A 100 km wide swath was then assigned to the trajectory paths to account for uncertainties. Hourly NO_x and SO_2 emissions data (USEPA, 2003, Personal Communication) for U.S. power plants falling within the swaths were integrated over the 24 h period preceding the measurements (Table 11), thus enabling a comparison between the upwind emissions data and the wind trajectory analysis. A large source of uncertainty in this approach is the lack of emissions data from Canada.

Table 11. 24 h integrated SO_2 and NO_x emissions from upwind power plants that fell within back trajectory source regions for Selinsgrove on 15 Aug, 2003 and 4 Aug, 2002 (normal day), and Cumberland on 15 Aug, 2003(outside blackout area). Also shown are percentage emissions reductions upwind of Selinsgrove on 15 Aug, 2003 relative to 4 Aug, 2002 and Cumberland on 15 Aug, 2003 (Marufu *et al*., 2004).

	Selinsgrove 15 Aug, 2003	**Selinsgrove 4 Aug, 2002**	**Cumberland 15 Aug, 2003**	**Emissions reduction upwind of Selinsgrove on 15 Aug, 2003 relative to:**	
	Blackout Day	*Normal Day*	*Blackout Day*	*Selinsgrove on 4 Aug, 2002*	*Cumberland on 15 Aug, 2003*
SO_2 tons/day	2424.1	7227.9	7033.9	66 %	66%
NO_x tons/day	309.2	1565.0	1219.9	80%	75%

The same back trajectory and emissions procedure was followed for Selinsgrove, PA on August 4, 2002 (prior to blackout) and Cumberland, MD on August 15, 2003 (out of blackout area) to provide a comparison with emissions from power plants that were operating normally. On August 4, 2002, the synoptic meteorological patterns over Selinsgrove were similar to those on August 15, 2003. Regional mean surface temperatures were ~33^{o}C on both days, winds and relative humidity were similar (Figure 49b), and both days were mostly cloud free but for some high clouds. Also, downwelling flux measured by the SurfRad site in central Pennsylvania revealed little difference between the two days. This analysis yielded large differences in upwind power plant emissions (Table 11). SO_2 and NO_x emissions upwind of Selinsgrove on August 15, 2003 were reduced to 34% and 20% of normal and to 34% and 25% of that observed upwind of Cumberland, respectively (Table 11).

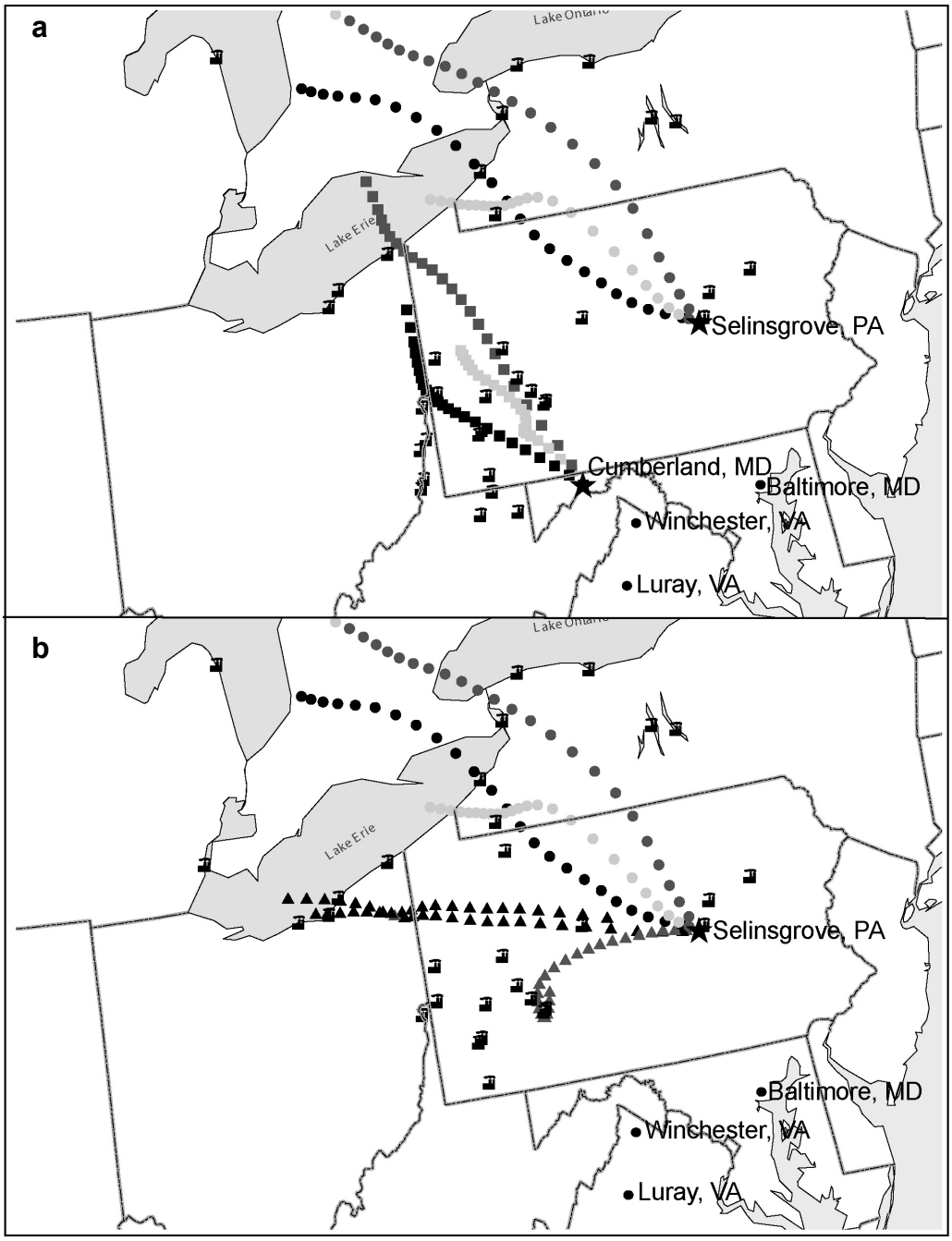

Figure 49. Map of northeastern U.S. showing modeled back trajectories (24 h) from Cumberland, MD and Selinsgrove, PA on 15 Aug, 2003 at 1500 and 2000 UTC, respectively (a); and Selinsgrove, PA on 15 Aug, 2003 (circles) and on 4 Aug, 2002 (triangles) at 2000 and 2100 UTC, respectively (b). Light gray represents 0-500 m, dark gray 500-1500 m, and black 1500-2500 m AGL. Icons represent power plants that fall within trajectory buffers regardless of size or extent of down scaling during the blackout (Marufu *et al*., 2004).

The impact of this emissions disparity on downwind air quality is illustrated in Figure 50. Sulfur dioxide, O_3, and light scattered by particles measured over Selinsgrove in 2003 were reduced by >90%, ~50%, and ~70%, respectively, relative to 2002 observations (Figures 50a-c). Defining visual range as the 98% extinction point, the reduction in aerosol extinction corresponds to an increase in visual range of > 40 km. The concomitant decreases in SO_2 and particle light scattering suggest that improvements in visibility resulted directly from reduced power plant SO_2 emissions. Reductions in O_3, apparently the result of decreased NO_x emissions, were greatest near the surface (~38 ppbv) and fell off at higher altitudes where large-scale processes play a more dominant role in the O_3 budget. As with CO concentrations, however, light absorption by particles shows a less dramatic difference (Figure 50d). In fact, absorption was higher in 2003 than in 2002, suggesting little or no reduction in mobile emissions during the blackout relative to typical values. The single scattering albedo was 0.95 on the normal day, but fell to 0.85 during the blackout because of the reduced scattering. Electricity generation produces very little CO or absorbing aerosols; instead, they are mainly emitted by mobile sources that continued to operate during the blackout. No discernible changes in road vehicular traffic activity could be observed near or upwind of the study area during the blackout (Szekeres, 2004).

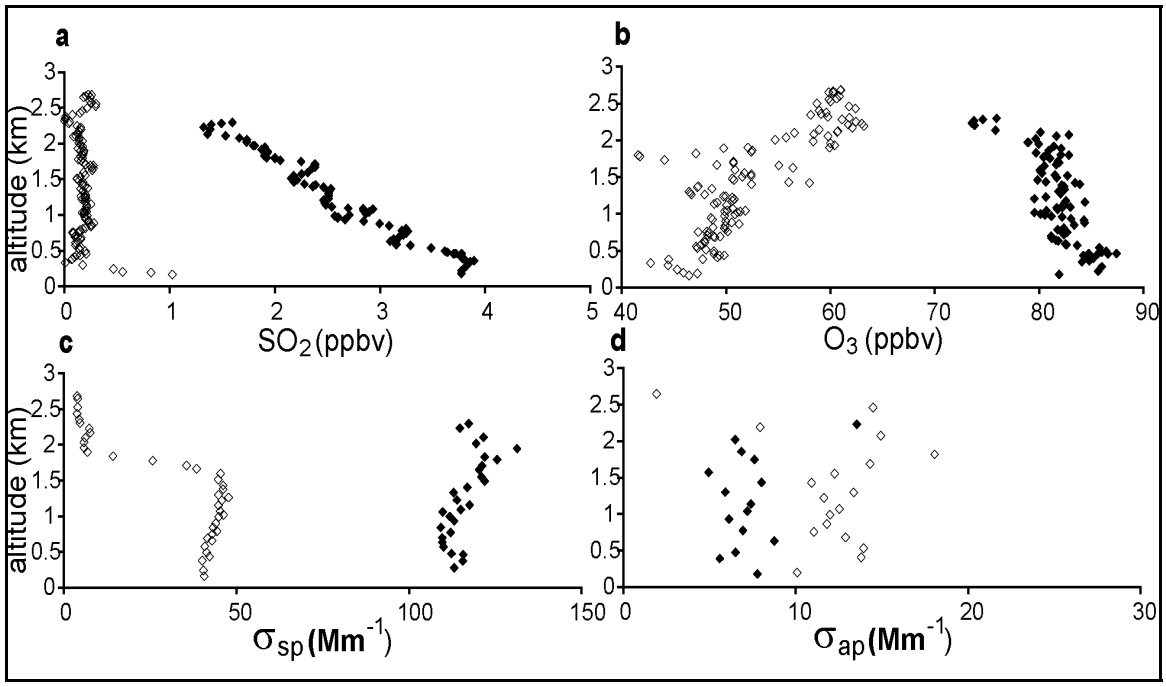

Figure 50. Comparison of running 1 min mean SO_2 mixing ratios (a); 10 s O_3 mixing ratios (b); particle light scattering at 550 nm (c); and particle light absorption at 565 nm (d) measured on 15 Aug, 2003 (open diamonds) and 4 Aug, 2002 (filled diamonds) over Selinsgrove, Pennsylvania (Marufu *et al.*, 2004).

Twenty-four hour forward trajectories using the NOAA ARL HYSPLIT model (Version 4) (Draxler and Rolph, 2003) and EDAS meteorological fields run from Selinsgrove at 21:00 UTC from 500, 1500, and 2500 m AGL reach Baltimore, Philadelphia, and New York, depending on the altitude (Figure 51). Based on these results, the improvement in air quality depicted in Figure 50 was likely experienced over several major eastern cities. This is corroborated by the fact that O_3 concentrations in the Baltimore non-attainment area were forecasted to be 115 ppbv but reached only 80 ppbv (Maryland Department of Environment, 2003). Because the median and RMS forecast errors are 10 and 22 ppbv, respectively, the bulk of this overestimation has been attributed to the reduction in power plant emissions.

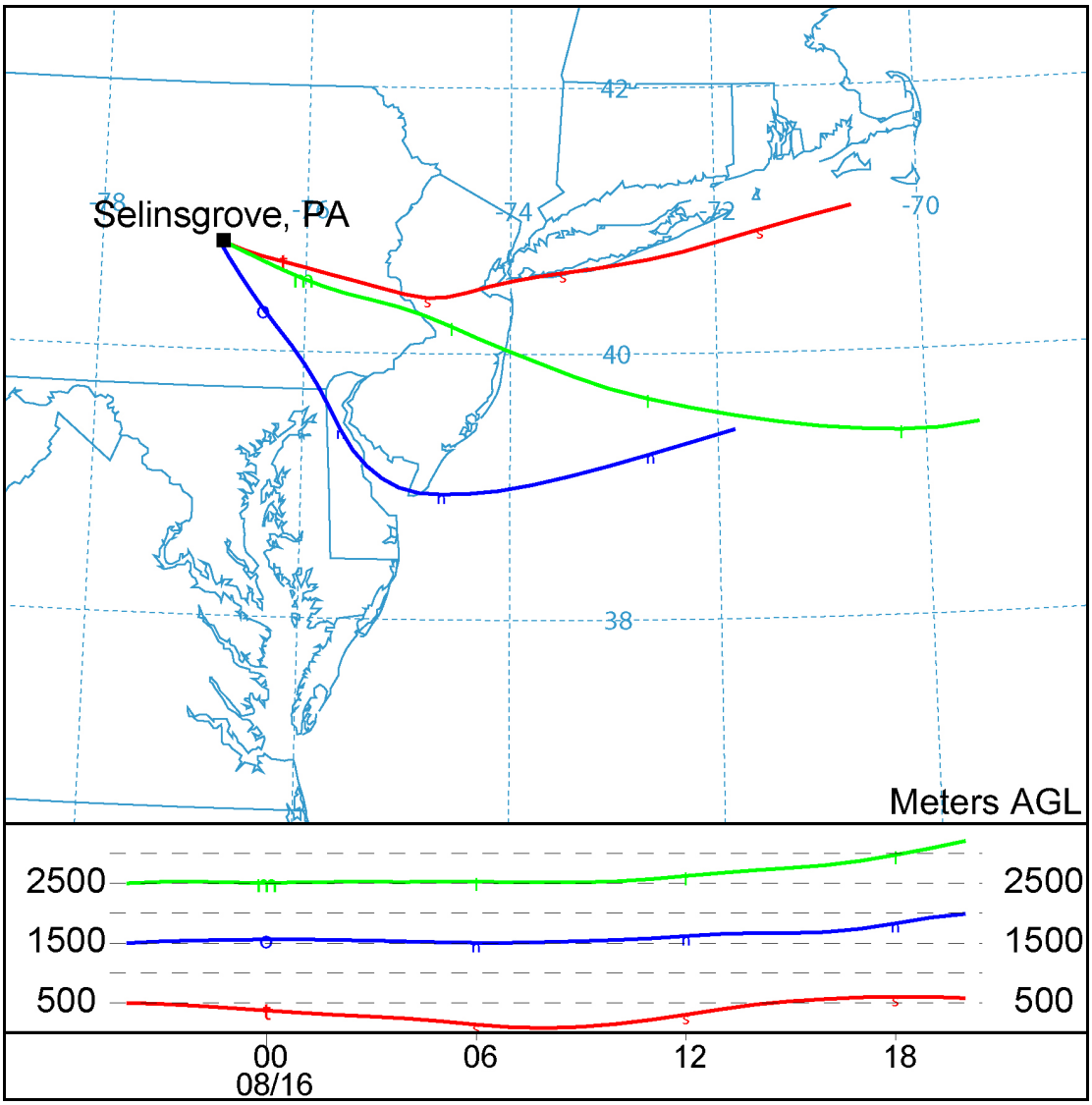

Figure 51. 24 h forward trajectories using the NOAA ARL HYSPLIT model (Version 4) and EDAS meteorological fields run from Selinsgrove, PA at 21:00 UTC 15 August 2003 from 500, 1500, and 2500 m AGL traverse Baltimore, Philadelphia, and New York.

6.3. Summary

Airborne measurements over central Pennsylvania on August 15, 2003, ~24 hours into one of the largest electrical blackouts in North American history, showed large reductions in SO_2 (>90%), O_3 (~50%), and light scattered by particles (~70%) relative to observations over western Maryland earlier in the day and over the same

location the year before. This translated into a reduction in low level O_3 of ~38 ppbv and an improvement in visual range of > 40 km. Forward trajectories show that these improvements in air quality benefited much of the eastern U.S. Carbon monoxide and particle light absorption values did not change much, however, suggesting that mobile emissions were largely unaffected during the blackout. Reported power plant SO_2 and NO_x emissions upwind of central Pennsylvania on August 15, 2003 were 34% and 20% of normal, respectively. Thus, the decreases in SO_2, O_3, and particle light scattering appear to be predominantly due to reductions in power plant emissions hundreds of km upwind of the study area. The observed reductions exceed expectation based on estimated relative contribution of power plants to these pollutants and their precursors (NO_x ~22%, SO_2 ~69%, and PM ~ 8%) (USEPA, 2003(a)). This apparent paradox may be the result of an underestimation of emissions from power plants, inaccurate representation of power plant effluent in emissions models, or unaccounted for atmospheric chemical reaction(s). These unique observations will provide a valuable resource for determining whether air quality models can accurately reproduce the contributions of specific pollution sources to regional air quality.

Chapter 7: Overview and Conclusions

7.1. Statistical Overview

The previous chapters highlight investigations of the most interesting events captured while performing the aircraft measurements. However, as described in the introduction, between February 2001 and February 2004, 160 research flights were conducted over the Mid-Atlantic and northeastern U.S. In an attempt to ascertain seasonal or annual trends in the aerosol optical properties measured during the flights, a statistical analysis was undertaken.

For each month during which flights were conducted, the fixed position, vertical survey spirals were grouped according to location and time of day. If more than one spiral per month was performed near the same time (but on a different day) at a given location, the mean, median, standard deviation, minimum and maximum values as well as the 1st and 3rd quartile values were calculated for temperature, relative humidity, O_3, SO_2, CO, σ_{sp} (at 450, 550, and 700 nm), backscatter ratio (at 450, 550, and 700 nm when available), σ_{ap} (corrected to 550 nm), and particle counts (for particles with diameters between 0.01 and 1.0 μm as well as diameters between 0.3 and 1.0 μm). Figure 52 shows the flight tracks for the flights with vertical survey spirals that were analyzed. The stars represent the locations where the vertical survey spirals were performed. The three character codes given at the spiral locations are the airport identifiers. The airport names, latitudes, and longitudes are provided in Appendix 1.

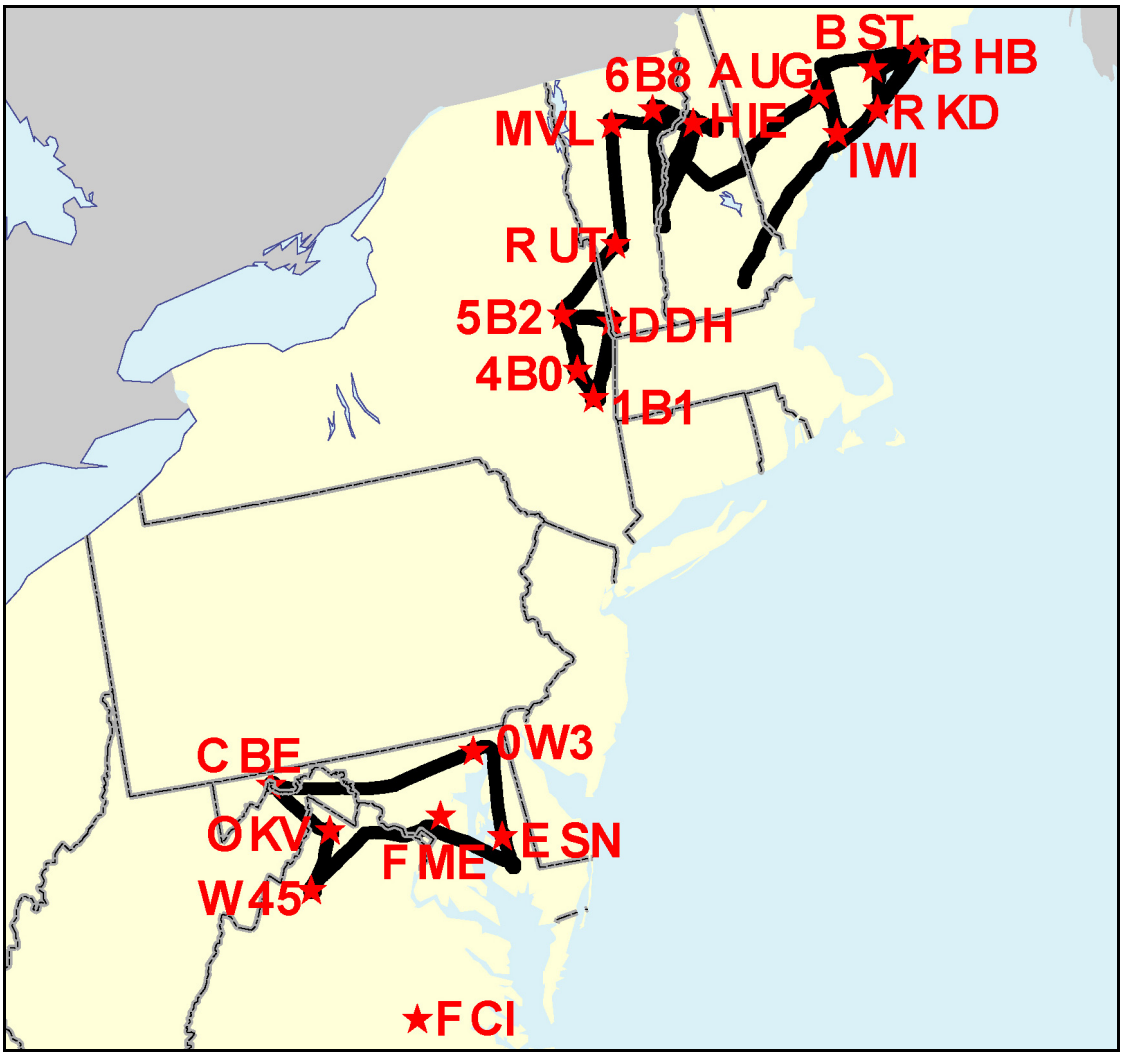

Figure 52. Map of the Mid-Atlantic and northeastern US. Solid black lines denote flight tracks. Red stars show locations of vertical survey spirals with the three character identifiers also given in red.

The statistical data were calculated at 100 m intervals beginning at the surface and culminating at 3 km. Data were collected at different frequencies depending on the instruments and the particular flights. Likewise, as detailed previously, vertical survey spirals were conducted as closely to 100 m min^{-1} as possible, although strict adherence to this rate of climb was sometimes impossible. As a result, there was often more than one value in a 100 m interval. In these cases, the values were

averaged so that only one value was reported for every 100 m. Conversely, there was frequently little or no data collected near the top of the 3 km column, depending on the flight time (morning spirals were typically performed from the surface to 3 km whereas the afternoon flights usually only went to 2.5 km) and the weather conditions (the inlet system and instrumentation are not designed for sampling within clouds). Also, because pressure altitude is calculated as meters above mean sea level, there was often a lack of data near the surface (depending on surface altitude above mean sea level).

Plots of the optical property statistical values are given in Appendix II. The 2001 and 2002 data show the single scattering albedo at 550 nm. The winter 2003 data show the particle counts (for particles with diameters between 0.01 and 1.0 and 0.30 and 1.0 μm) since the PSAP was being modified during that campaign. The subsequent data include these values as well as the asymmetry parameter at 550 nm. The asymmetry parameter data are available due to the use of the backscatter shutter on the nephelometer. By measuring scattering from 90 – 170^{o} (the nephelometer is limited in its scattering angles; data are corrected for this angular truncation, see chapter 2), the backscatter to total scatter ratio was calculated. This ratio was converted to the asymmetry parameter with the equation:

$$g = -2x + 1 \tag{25}$$

where x represents the backscatter to total scatter ratio. The plots shown in Appendix II are the median values with the horizontal error bars representing the 1st and 3rd quartile values.

Seventy-two hour backward wind trajectories at 250 and 1500 m above ground level (AGL) using the NOAA ARL HYSPLIT model (Version 4) (Draxler and Rolph, 2003) and EDAS meteorological fields were run from each spiral location used in the calculation of the statistical data beginning at the times the individual spirals were performed. Therefore, there are twice as many trajectories as there are spirals that went into the calculation of the statistical data (one at 250 m and one at 1500 m above each spiral location for every time a spiral was performed). The 250 m altitude was chosen to characterize the transport path of the air parcels ultimately observed within the daytime mixed layer. The 1500 m altitude was chosen to characterize the transport path of the air parcels observed near the maximum depth of the daytime mixed layer. The seventy-two hour time frame was chosen to illustrate the regional origins of the pollutants. The trajectories that correspond to the statistical data are given in Appendix III. Each point along the trajectories represents an hour in the path of the air parcel. The individual points are color coded according to altitude (color bar shown in the Appendix). The end of each trajectory is labeled with the research flight designation (ymmddflight#) and beginning altitude. Some endpoints are not shown because the trajectory path continues outside the regional area of the plots. While the back trajectories do not provide a quantitative insight into the statistical analysis, they do allow for a qualitative examination of whether the monthly statistical values are representative of specific transport regimes.

7.1.1. Summary of Results

The calculated asymmetry parameters in the summer of 2003 and winter of 2004 (Appendix 2) show a distinct inter-seasonal trend. The values in summer are

larger than those in winter, providing evidence that photochemical processes dominate over RH as the determining factor in particle growth. The larger a particle is relative to the wavelength of impingent radiation, the more it will scatter light in the forward direction. This leads to a smaller backscatter ratio and a higher asymmetry parameter. Relative humidity is generally higher in winter due to the decreased temperatures, but the amount of solar radiation reaching the lower atmosphere is much less than in the summertime. Consequently, the oxidation potential of the atmosphere is increased and photochemical processes are accelerated in the summertime. The primary constituent of $PM_{2.5}$ in the eastern U.S. is SO_4^{2-} (Malm, 1992). Sulfate is largely a secondary pollutant, resulting from the oxidation of SO_2 (see Chapter 1). When the oxidation potential is diminished (as in the wintertime), SO_2 cannot be oxidized as rapidly as in the summertime. When this is the case, less SO_4^{2-} is produced and particle growth decreases. With less SO_4^{2-} available, the RH is irrelevant, as it will only play a role when enough soluble material is readily available. All this, however, is only true assuming that emissions and transport of SO_2 are relatively constant between summer and winter.

Further evidence of photochemical processes playing the dominant role over RH in determining particle growth is the tendency for the asymmetry parameter to increase slightly above the PBL. The PBL in this case was defined as the point where the RH began to rapidly decrease with altitude. Thus, the RH is lower above the PBL than within it. At the same time, however, larger asymmetry parameters mean larger particles that scatter light predominantly in the forward direction. The actinic flux is greater above the PBL and photochemical processes are accelerated. Also, particles

are less subject to deposition and rainout above the PBL and may persist for longer periods, thereby allowing more time for growth. The same phenomenon (larger particles above the PBL than within and photochemical processes playing a dominant role over RH in particle growth processes) was observed through independent analytical techniques and described in detail in Chapter 3.

There are three interesting trends associated with the calculated single scattering albedo values at 550 nm. First, the ω_{0550} values appear to decrease with altitude. Hartley *et al*. (2000) also observed this phenomenon during the TARFOX experiment. Their explanation was twofold: that it was due to decreasing RH with altitude and/or an increase in the relative amounts of carbonaceous to sulfate species with altitude. The first explanation is unlikely given the fact that particle growth seems to be dominated by photochemical processes rather than RH. The latter is the more likely scenario and is corroborated by evidence presented herein. However, the reality may be somewhat more complex.

The statistical analysis showed that scattering tends to decrease with altitude while absorption, although a small fraction of total particle light extinction, remains fairly constant with altitude. Sulfate is the primary light scattering species in $PM_{2.5}$ in the eastern U.S. It is also highly soluble and consequently subject to rain out, a possible reason for the decrease in scattering with altitude. Black carbon is the primary light absorbing species in $PM_{2.5}$. Black carbon is not soluble and would be less subject to rain out prior to mixing. This may explain the constancy of absorption with altitude as well as the decrease in ω_{550} with altitude. It would also support the

hypothesis that the relative amounts of carbonaceous to sulfate species increase with altitude. There are more factors at work though.

In Chapter 3, it was shown that the extent of internal mixing between sulfate-dominated particles and BC particles determines the degree of absorptivity of the resulting mixture. When BC and sulfate-dominated particles were internally mixed, the absorption was greater than the corresponding external mixture. Thus, the increase in absorption with altitude is not solely due to an increase in the relative amounts of carbonaceous species. It is also due to a change in the degree of mixing between predominantly absorbing and predominantly scattering particles with altitude.

The second noticeable trend associated with ω_{0550} (now defined as the extinction weighted column average) is a diurnal increase. Single scattering albedo values at 550 nm were seen to increase in time between the morning and afternoon. This was due primarily to the fact that scattering generally increased over the course of a day while absorption remained largely constant. This finding also supports the predominance of photochemical processes over RH in particle growth. Relative humidity typically decreases diurnally while photochemical processes increase due to increased solar radiation. The oxidation of SO_2 to SO_4^{2-} is the rate limiting step in the particle growth process since the SO_2 must be converted to SO_4^{2-} before RH can play a role. Nonetheless, at the moderate RH values typically encountered during the flights, the rate limiting step also appears to be the dominant one.

The final observable trend in ω_{0550} is a weak seasonal increase, which may possibly follow a photochemical argument similar to the other observable trends.

Absorption remained relatively constant from the beginning of the summer to the end, while scattering increased as the season progressed. Once again, this could be explained through an increase in photochemical processes; this time, however, more as a result of increased temperatures and reaction rates than an increase in actinic flux, which should peak near the summer solstice. Another explanation may lie in increased power consumption (due to increased use of air conditioning), although this is unlikely; SO_2 emissions tend to be relatively constant seasonally and annually.

Another interesting observation in the ω_{0550} data is a decline in the 2003 values as compared to the previous two years (Figure 53). The 2004 winter data are also lower than any of the summer values (including 2003), but unfortunately there are no other winter data with which to compare them. Again, the reason for the decline can be explained by variable scattering values and fairly constant absorption values. Scattering values were lower in 2003 relative to the previous two years while absorption values changed little between the years. The summer of 2003 was considerably cooler and wetter than the previous two summers. The synoptic scale meteorological patterns were often such that a large upper air ridge was positioned over the Great Plains with a low centered over the eastern third of the country. This created large scale funneling of continental polar air from Canada to the Mid-Atlantic and Northeast, bringing with it cooler, more pristine conditions. There is very little industry or electricity generation due north of the Mid-Atlantic and Northeast. Most industrial facilities and power plants lie to the west and northwest. Also, recirculation of the air around the Western Atlantic Ridge entrained moisture from the Atlantic Ocean and Gulf of Mexico, which encouraged greater than average precipitation. As

noted before, rain out would reduce the amounts of soluble SO_4^{2-} in the atmosphere. Hydrophobic BC, however, would be largely undisturbed by increased precipitation amounts. Thus, to a large degree the drop in ω_{0550} values in the summer of 2003 can be attributed to the anomalous meteorological patterns. The monthly average ω_{0550} values at the GSFC AERONET site also show a slight decrease in the summer of 2003 relative to the previous two summers (Figure 53). Although these decreases are not statistically significant as the values in question are all within analytical uncertainty. On the other hand, the AERONET and aircraft values do disagree despite analytical uncertainty. The optical depth values measured by the two platforms, however, agree during the summer of 2003 (Figure 54). Given that the scattering makes up ~90% or more of the total extinction, the scattering values most likely agree also. Once again, the absorption values are seen as the reason for the disagreement between the two platforms. Higher absorption measured aboard the aircraft has little effect on optical depth values, but does impact the single-scattering albedo. The same inconsistencies are seen between the two platforms for February 2004 (Figures 53, 54).

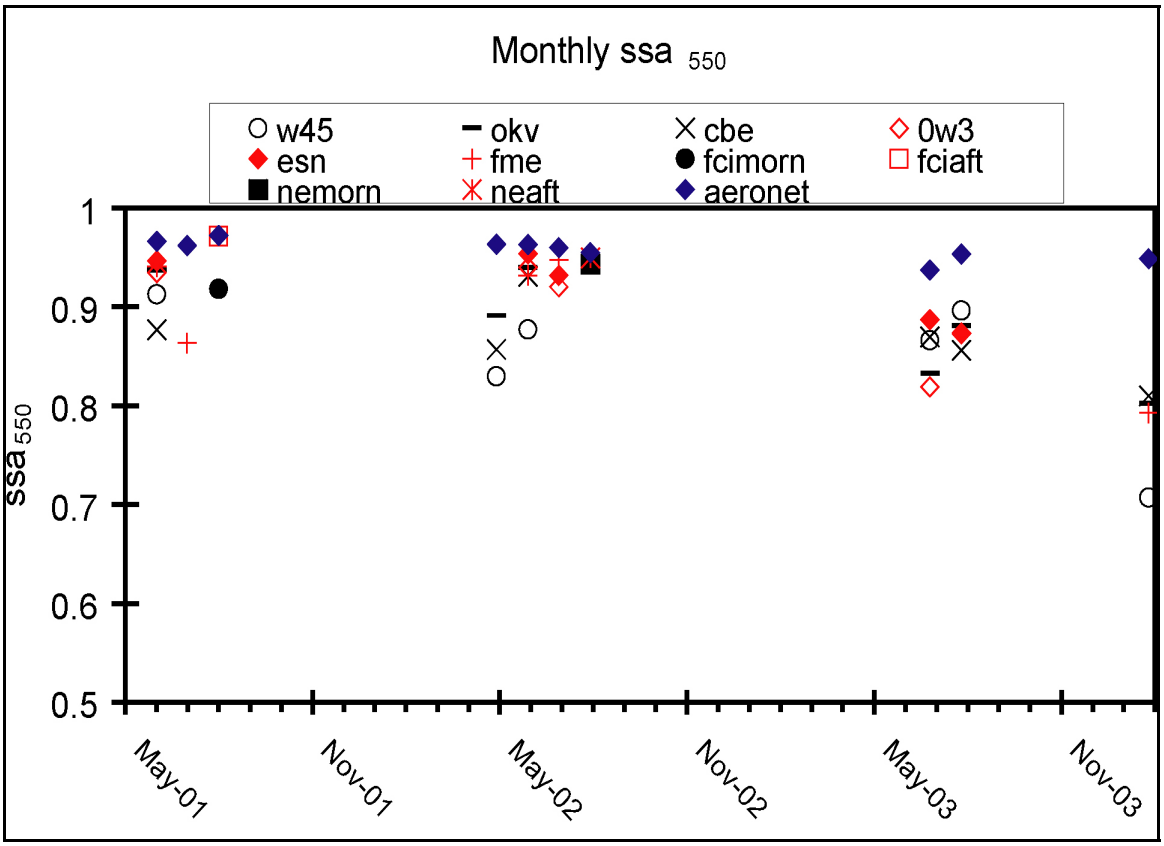

Figure 53. Monthly median single scattering albedo values at 550 nm measured by the aircraft and monthly average values determined by AERONET. The symbols are identified in the key. The aircraft measurement locations are described by the airport identifiers. Fcimorn and fciaft denote the median value from all spirals performed in that particular month over the airport FCI in the morning (fcimorn) and afternoon (fciaft). Nemorn and neaft denote the median values of all flight spirals performed in the Northeast between August 12 and August 14, 2002 in the morning (nemorn) and afternoon (neaft). See Appendix IV.1 for uncertainty estimates.

The statistical data show a general propensity for the scattering values to be perturbed while the absorption values remain largely invariant. Potential problems do exist with the measurement technique used aboard the aircraft that were discussed thoroughly in previous chapters and will not be revisited here other than to say that they may contribute to an overestimation of low absorption values. Also discussed above is the fact that selective rain out of soluble SO_4^{2-} species over insoluble BC

may engender the phenomenon. There is another possibility as well. Sulfate dominated particles are largely secondary pollutants that result from point source emissions of SO_2. By definition, point sources are geographically fixed and happen to be largely concentrated in the Ohio River Valley and to a lesser degree the Great Lakes region. Thus, the impact of this pollution source on the air quality in the eastern U.S. is dependent upon certain meteorological conditions. BC on the other hand is predominantly the product of vehicular emissions and is, therefore, more ubiquitous with respect to geographical variations. The impact of these emissions would not be as dependent upon meteorological conditions.

The August 2002 data were analyzed in a different manner from the rest of the data. All the flights that went into the analysis for this month were part of a multi-day campaign in the northeastern U.S. during a sustained haze episode in that region. Chapter 3 describes the study based on measurements made during the transect between New Hampshire to Maryland on the last day of the campaign. Rather than grouping spirals conducted over the same locations, as per the other months, all morning spirals during the three-day campaign were grouped together for statistical analysis. The same was done for the afternoon spirals. This was performed to investigate the regional nature of the pollution episode and, specifically, the hypothesis that optical property values should be mostly invariant both spatially and temporally. The results exceeded expectations.

The winds were mainly from the west during the campaign and only shifted to the southwest toward the end of the campaign (Appendix III.22-27). Thus, most of the emissions that were transported to the measurement locations were from power

plants in the Great Lakes region. There is not a lot of vehicular activity in the area of the study or in the transport paths of the trajectories compared to the large metropolitan areas in the Mid-Atlantic and Northeast. As a result, scattering values were relatively high and absorption values were average to low (Appendix II.9). The consistency of the values (denoted by the small error bars on the plots) points to the regional nature of the episode and the impact of transported pollutants on the regional air quality. Further corroboration of the regional nature of the episode is seen in the comparison of average GSFC AERONET optical depth and single scattering albedo values for the days of the episode to values calculated from flight measurements (Figures 53, 54). The similarity of both the optical depth and single scattering albedo values as observed by the disparate sampling platforms hundreds of km away argues against the likelihood of this being coincidental. Interestingly, though, while the aircraft values of single scattering albedo were relatively high (presumably due to the predominance of sulfates and lack of soot), the AERONET values were low (within uncertainty ranges though) compared to climatological data (Dubovik *et al*., 2001). Even so, accounting for the analytical uncertainty of both sets of measurements, the aircraft values agree with the AERONET climatological values. This does not explain, however, the lower values observed by AERONET during this period. Given the synoptic scale of the episode, westerly and southwesterly winds would traverse the Ohio River Valley and areas to the south before reaching the GSFC site. These areas have some of the highest concentrations of elemental carbon according to the Interagency Monitoring of Protected Visual Environments (IMPROVE) network of surface observation stations (Malm *et al*., 2004). The relatively large

concentrations of absorptive particles would explain the lower single-scattering albedos observed by AERONET during this period.

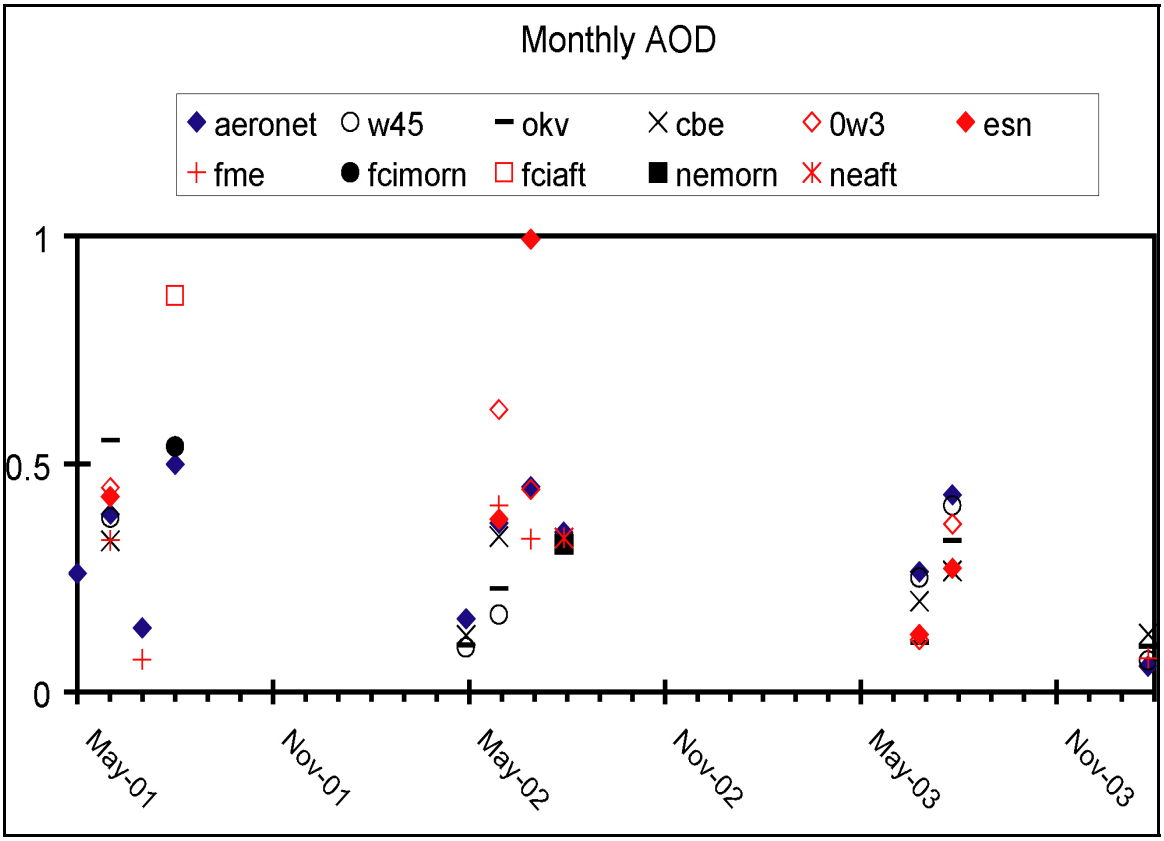

Figure 54. Monthly median values of aerosol optical depth at 550 nm calculated from aircraft measurements of extinction and monthly averages as determined by AERONET. See Figure 53 for an explanation of the symbology. See Appendix IV.2 for uncertainty estimates.

There are some general conclusions that may be drawn from the wind trajectory analyses. Namely, wind speed and direction seem to have an impact on the aerosol optical properties observed over the eastern U.S. As noted earlier, the largest effect is seen in the scattering values. Absorption values, once again, were largely unperturbed by the wind speed and direction. As a result, the variability in the single-

scattering albedo was mainly due to the variability in scattering values. Also, because scattering makes up ~90% or more of the extinction, changes in aerosol optical depth were the result of fluctuations in scattering values. This finding would hold true under most circumstances given the typical ratio of scattering to absorption. Winds from the west and northwest brought the highest scattering aerosols and thus, the highest single-scattering albedo and optical depth values. Areas to the west and northwest of the eastern U.S. are dominated by coal-fired power plants, the likely explanation for this occurrence. Southerly winds brought slightly lower scattering values and as a result, the single-scattering albedo and optical depth values were lower as well. Areas to the south lack the power plants of the Midwest, but biogenic emissions of organic species are much higher. Particles dominated by organics also scatter light efficiently (Malm *et al*., 1994). Winds from the north, where there is little in the way of pollution sources or biogenic emissions, were associated with lower scattering values and, therefore, single-scattering albedo and optical depth values. Wind speed also affected these values though. Higher wind speeds, translated into longer trajectories, were always associated with lower scattering and even absorption values. Greater dispersion of pollution does not allow it to accumulate in one spot. Thus, when wind speeds were greater, the optical depth declined, whereas the single-scattering albedo was largely unaffected since scattering and absorption were equally impacted.

Particle number data are unavailable until the winter of 2003 and so only the data will from that point on will be discussed. There is little difference seen in the number of total sub-micrometer particles ($0.01 - 1.0\,\mu m$) in the boundary layer

between the summer and winter data (Appendix II). There are, however, fewer accumulation mode particles ($0.3 - 1.0\,\mu m$) in the boundary layer in the winters of 2003 and 2004 as compared to the summer of 2003. There appears to be as many primary particles in the boundary layer during the winter as there are in the summer. The difference, then, is in the formation of secondary particles between the seasons. This provides further evidence that photochemical processes play the predominant role in particle growth. If there are roughly the same amounts of primary particles in the boundary layer regardless of the season, the difference in haze episodes stems largely from the photochemical processes that drive them. However, this conclusion presupposes equivalent amounts of particles that are subject to photochemical processes (i.e., SO_2 or organics) during both seasons. The requisite meteorology must therefore be present to transport the emissions of primary photochemically active species.

There is also a general decline seen in summertime and wintertime of particle numbers with altitude. However, the decline in the wintertime occurs at much lower altitudes than in the summertime. This is due to the decreased surface heating during the wintertime. Surface heating drives the vertical mixing of air parcels. In the wintertime, vertical mixing is decreased and particles are seldom able to reach the lower free troposphere.

Comparisons between in-situ aircraft measurements and AERONET observations have already been discussed in detail. Therefore, the only further comment will be a substantiation of previous comparisons through the statistical analyses. When the monthly average AERONET values of optical depth and single-

scattering albedo (both interpolated to 550 nm) were compared to the monthly median values calculated using aircraft measurements, the optical depth values agreed nicely while the AERONET values of single-scattering albedo were consistently higher (Figures 53, 54). Once again, because scattering makes up ~90% or more of the total extinction, this shows that the scattering values are most likely in agreement, while the absorption values measured aboard the aircraft are significantly higher than those determined by AERONET.

7.2. Conclusions

7.2.1. Summary

Chapter 3 details the investigation that led to the inception of the two reservoir conceptual model, the theory that the chemistry and physics of multi-day haze and ozone episodes over the Mid-Atlantic and northeastern U.S. may be accurately represented by two reservoirs, the PBL and LFT. Measurements were made during a constant altitude flight at the maximum height of the PBL from New Hampshire to Maryland on the last day of a multi-day haze and ozone episode in early August 2002. Precursor species are typically emitted in the PBL, where they are subject to surface deposition. When these precursors reach the LFT, however, deposition is no longer a factor, and their lifetimes are protracted. The acceleration of photochemical processes in the LFT causes air parcels to undergo chemical changes more rapidly. As a result, there were greater concentrations of O_3 and larger particles that scattered (and absorbed) visible light more efficiently in the LFT than in the PBL.

Chapters 4 and 5 describe the measurements and subsequent analyses of the smoke plume from Canadian forest fires that was advected over the eastern U.S. Observations of the smoke plume were made aboard the aircraft on July 8, 2002. On this day, the smoke was contained in a layer between 2 and 3 km and distinct from the local haze pollution below. Large O_3 and CO mixing ratios were found in the smoke layer together with many sub-micrometer particles that scattered and absorbed the solar radiation efficiently. The smoke particles had a mean single-scattering albedo value of 0.93±0.02 at 550 nm while the underlying PBL particles had a mean value of 0.95±0.01 at 550 nm. The scattering Ångström exponents of the larger, aged smoke particles were between 0.83±0.15 and 1.23±0.38 while the smaller, PBL particles had values between 1.59±0.30 and 1.99±0.32 for $\alpha_{450/700}$. Calculated Aerosol Optical Depths (550 nm) from just above the surface to ~3 km ranged from 0.42±0.06 to 1.53±0.21 depending on the location.

According to radiative transfer calculations, absorption of solar radiation within the smoke plume nearly equaled the total amount attenuated at the surface. This demonstrates a cooling at the surface coupled with a warming of the air aloft. A morning subsidence inversion was posited as the cause of the delineation of the smoke from the underlying layer. Solar heating of the smoke layer then maintained the temperature inversion through the afternoon. This is an example of a positive feedback loop that prevented vertical mixing and dilution, thereby protracting the lifetime of the plume and the regional radiative impacts.

Satellite reflectances were used to calculate the optical depth of the smoke plume with two sets of inputs, AERONET retrieved optical properties and in-situ

aircraft measured optical properties. Different combinations of AERONET and in-situ measured optical properties were also used to retrieve the optical depth. The optical depths calculated using the pure AERONET optical properties were the lowest, while retrievals using the pure in-situ values produced optical depths 22-43% larger, due to the lower reflectivity (greater absorption) of the measured aerosol. In fact, the in-situ measurement of absorption was twice as large as that derived by AERONET. Even so, the optical depth retrievals using the different inputs were equivalent given the total uncertainty of the results.

To calculate broadband regional radiative forcings, the optical depth values (550 nm) were extrapolated across the entire solar spectrum according to the particle size distributions. The radiative forcing at the surface and TOA calculated using the in-situ optical properties came closer to surface and TOA measurements than those calculated with the AERONET optical properties.

Finally, Chapter 6 details airborne measurements made over central Pennsylvania on August 15, 2003, ~24 hours into the largest electrical blackout in North American history. The observations included large reductions in SO_2 (>90%), O_3 (~50%), and light scattered by particles (~70%) relative to observations over western Maryland earlier in the day and over the same location (central Pennsylvania) the year before. Ground level O_3 dropped by ~38 ppbv and visibility improved by >40 km. Carbon monoxide and absorption values were unaffected by the blackout. Forward trajectories illustrate that the cleaner air resulting from the blackout benefited much of the eastern U.S., including Philadelphia, New York, and Baltimore.

Reported power plant SO_2 and NO_x emissions upwind of central Pennsylvania on August 15, 2003 were 34% and 20% of normal, respectively. The decreases in SO_2, O_3, and particle light scattering appear to be mainly due to reduced power plant emissions hundreds of km upwind of the study area, an observation that exceeds expectations based on the estimated relative contributions of power plants to these pollutants and their precursors (NO_x ~22%, SO_2 ~69% and PM ~ 8%) (USEPA, 2003(a)). This apparent inconsistency may be the result of an underestimation of power plant emissions, inaccurate representation of power plant effluent in emissions models, or unaccounted for atmospheric chemical reactions. These unique observations will provide a valuable resource for determining whether air quality models can accurately reproduce the contributions of specific pollution sources to regional air quality.

7.2.2. Policy Implications

The 2003 North American electrical blackout provided a unique opportunity to enhance our understanding of the complex interplay of factors contributing to air pollution in the Mid-Atlantic and northeastern U.S. Transport of point source pollution over hundreds of kilometers, particularly into large urban areas, makes it difficult to quantify the effects power plants have on regional air quality. Measurements made during the blackout are likely inimitable because of the suddenness and magnitude of the scale back. A multiplicity of power plants was tripped while all other variables, atmospheric and chemical, were held relatively constant. The blackout also rendered inoperable many surface stations in the region normally capable of making measurements of such a phenomenon. Likewise, high

clouds prevented satellites from contributing much data to the investigation. As a result, the aircraft measurements were a valuable source of data for this unique event.

The regulation of electrical generation facilities and adoption of sound environmental policies that benefit the consumer without deleterious effects to the producer are contentious issues. Determining the direct impact of power plant emissions on regional pollution levels aids in the formulation of effective mitigation strategies. The evidence from the aircraft measurements shows that power plants may play a more dominant role in regional air quality than previously suspected. In fact, the observed reductions in air pollutants exceed expectations based on the estimated relative contributions of power plants to these pollutants and their precursors (see section 7.2.1). Regardless, the results from the blackout study should aid in parameterizing future modeling studies that investigate the impact of power plants and other pollution sources on regional air quality as well as guide in the formulation of future mitigation strategies.

The regulation of power generation facilities and air pollution is not just a North American problem. These issues have global import. In fact, Asian NO_x emissions surpassed those in North America and Europe in the last decade and will most likely continue to do so for the foreseeable future (Akimoto, 2003). International initiatives to mitigate global air pollution are not only necessary but call for involvement from both developed and developing countries.

7.2.3. Climate Implications

The two-reservoir conceptual model provides a characterization of the chemistry and physics that occur during multi-day air pollution episodes in the Mid-

Atlantic and Northeast. The existence of a layer aloft comprising large, absorptive particles and high concentrations of O_3 is a product of the vertical stability of these multi-day episodes. An accurate numerical model simulation of photochemical smog processes over the Mid-Atlantic and Northeast should incorporate the existence of these two reservoirs, and simulate or at least parameterize the role of mixing between them in multi-day smog events.

The smoke plume from Canadian forest fires allowed for the characterization of the optical properties and radiative impacts of a boreal forest fire plume that had been transported over 1000 km. The results of this study further our understanding of the chemical transformations of transported smoke particles and the role absorbing aerosols play in the global climate. The presence of a discrete, optically thick, absorptive layer of smoke overlying a more scattering plume provided a rare opportunity to quantify the climatic impacts of this type of vertical stratification. The results also reinforce the importance of in-situ aircraft measurements of aerosol optical properties. Remote sensing platforms that collect column-integrated aerosol optical properties cannot provide the requisite vertical information for the investigation of the climatic impacts of stratified layers of aerosols with different radiative properties.

A common theme that reoccurred throughout this research was the presence of an absorptive aerosol layer overlying a more scattering one. The presence of such a layer may have profound impacts on the global climate. Despite the fact that the absorptive layer was optically thin the majority of the time (except during the forest fire smoke plume), the underlying scattering layer would exacerbate the absorptive

nature of the layer aloft. Because of multiple scattering effects, each photon would have a greater probability of being absorbed than if the absorptive layer existed independently. Plus, because the scattering layer lies below the absorptive one, the reflectivity of this layer is diminished. If this phenomenon of an absorptive layer overlying a scattering layer is as ubiquitous as this study suggests (which is reasonable considering the meteorological and chemical explanations put forward in this chapter), then it may serve to decrease the modeled estimates of the net global cooling effects of scattering aerosols and increase estimates of the net warming effects of absorbing aerosols that are based on column-averaged and surface measurements.

7.3. Recommendations

Aerosol optical depth, the vertically integrated sum of aerosol light scattering and absorption, is a quantity that is used for column closure studies and the calculation of aerosol radiative forcing. In most areas of the western hemisphere, light is primarily scattered by particles. The contribution of particle light absorption to the aerosol optical depth is small. As a result, uncertainties in absorption values are often overlooked. Because of the large contribution of scattering to the aerosol optical depth, a reasonable agreement in scattering values typically leads to a reasonable agreement in optical depth values. However, radiative forcing calculations are more complex than optical depth retrievals and are more prone to inaccuracy. This particular phenomenon was demonstrated in Chapter 5, where optical depth retrievals using two sets of inputs were equivalent to within uncertainty,

but the radiative forcing values based upon the two inputs were significantly different.

The degree of particle absorption as well as the vertical distribution of absorptive particles can have profound impacts on the energy balance of the surface-atmosphere system, the stability of the lower atmosphere, the hydrological cycle, and ultimately the global climate. Therefore, it is imperative that the experimental community improves the uncertainty surrounding the quantification of particle light absorption. Absorption measured in-situ is consistently lower than that determined through remotely sensed techniques (e.g. sun photometry). Also, while there are readily available instruments for measuring particle light scattering at multiple wavelengths, very few exist for the measurement of absorption at multiple wavelengths. Thus, to extrapolate absorption measurements to wavelengths other than those measured, one must rely on laboratory measurements of the refractive indices of light absorbing species that may be quite different than the observed ambient species. Similarly, the calibrations of field deployable particle light absorption measuring instruments have been largely based on laboratory measurements of standardized light absorbing spherical particles. Increasing the accuracy of particle light absorption measurements and decreasing the uncertainty range of such measurements would be extremely beneficial to both satellite retrievals of atmospheric aerosols and numerical model simulations of climate change.

One area of concern that has recently garnered the attention of the experimental community is the need for a validation, calibration, and standardization process for particle inlets on instrumented aircraft. Because of the spatial and

temporal variability of atmospheric particles, remote sensing, especially by satellites, provides the most efficacious means of observation. However, remotes sensors cannot directly measure the particle optical and physical properties, and must rely on certain assumptions. In-situ measurements are thereby required as a means of validation. Aircraft measurements in particular supply the requisite vertical distribution information. The accuracy of these measurements, however, is limited by knowledge of the particle inlet system sampling efficiency. The efficiency is impacted by the positioning of the inlet relative to the aircraft boundary layer, the isokineticity of the inlet, diffusional loss of small particles, and sedimentation, inertial losses, and turbulent deposition of larger particles. The chemical composition and size distributions of the particles may also be affected by direct or indirect heating of the sample. Currently available low-turbulence inlets that prevent the loss of large particles are only suitable for large aircraft because of space and power requirements. We are currently working on the design of an efficient aerosol inlet system for light aircraft that may allow for the measurement of super-micrometer particles. The new inlet, if successful, would greatly enhance the ability of the scientific community to accurately characterize the chemical and optical properties of aerosol columns on a regular basis.

Appendix I

Spiral	Airport	Town	Lat	Long	Elevation (m)
0W3	Harford County	Churchville, MD	39.57ºN	76.20ºW	400
19N	Camden County	Berlin, NJ	39.78ºN	74.95ºW	150
1B1	Columbia County	Hudson, NY	42.29ºN	73.71ºW	197
1N7	Blairstown	Blairstown, NY	40.97ºN	75.00ºW	372
2G2	Jefferson County	Stubenville, OH	40.36ºN	80.70ºW	1194
3G6	Tri-City	Sebring, OH	40.91ºN	81.00ºW	1188
4B0	South Albany	South Bethlehem, NY	42.56ºN	73.83ºW	196
5B2	Saratoga County	Saratoga Springs, NY	43.05ºN	73.86ºW	433
5W5	Triple W	Raleigh, NC	35.62ºN	78.70ºW	244
5W8	Siler City Municipal	Siler City, NC	35.70ºN	79.51ºW	614
6B8	Caledonia County	Lyndonville, VT	44.57ºN	72.02ºW	1188
8G2	Corry-Lawrence	Corry, PA	41.91ºN	79.64ºW	1766
8G6	Harrison County	Cadiz, OH	40.24ºN	81.01ºW	1174
9G1	West Penn/Rock	Tarentum, PA	40.60ºN	79.82ºW	1125

AKQ	Wakefield	Wakefield, VA	36.99ºN	77.00ºW	113
ANP	Lee	Annapolis, MD	38.94ºN	76.57ºW	30
AOO	Altoona Blair County	Altoona, PA	40.30ºN	78.32ºW	1504
AUG	Augusta St.	Augusta, ME	44.32ºN	69.80ºW	352
AXQ	Clarion County	Clarion, PA	41.23ºN	79.44ºW	1458
BHB	Hancock County Bar Harbor	Bar Harbor, ME	44.45ºN	68.36ºW	83
BST	Belfast Municipal	Belfast, ME	44.41ºN	69.01ºW	195
CBE	Cumberland Regional	Cumberland, MD	39.62ºN	78.76ºW	776
CGE	Cambridge Dorchester	Cambridge, MD	38.54ºN	76.03ºW	19
CGS	College Park	College Park, MD	38.98ºN	76.92ºW	50
DDH	William H. Morse State	Bennington, VT	42.89ºN	73.25ºW	826
EHO	Shelby Municipal	Shelby, NC	35.26ºN	81.60ºW	847
ERI	Erie International	Erie, PA	42.08ºN	80.18ºW	733
ESN	Easton Newman	Easton, MD	38.80ºN	76.07ºW	74
EVY	Summit	Middletown, DE	39.52ºN	75.72ºW	45
FCI	Chesterfield County	Richmond, VA	37.41ºN	77.53ºW	237

FDK	Frederick	Frederick, MD	39.42°N	77.37°W	303
FME	Tipton AFB	Fort Meade, MD	39.08ºN	76.76ºW	145
HIE	Mount Washington Regional	Whitefield, NH	43.37ºN	71.54ºW	1074
HMZ	Bedford County	Bedford, PA	40.09ºN	78.51ºW	1161
HNZ	Henderson-Oxford	Henderson, NC	36.36ºN	78.53ºW	527
IDI	Indiana County Jimmy Stewart	Indiana, PA	40.63ºN	79.11ºW	1405
ITH	Tompkins County	Ithaca, NY	42.49ºN	76.46ºW	1099
IWI	Wiscasset	Wiscasset, ME	43.96ºN	69.71ºW	70
JNX	Johnson County	Smithfield, NC	35.54ºN	78.39ºW	165
JQF	Concord Regional	Concord, NC	35.39ºN	80.71ºW	690
LEB	Lebanon Municipal	Lebanon, NH	43.63ºN	72.30ºW	604
LHZ	Franklin County	Louisburg, NC	36.02ºN	78.33ºW	369
LKR	Lancaster County McWhirter County	Lancaster, SC	34.72ºN	80.85ºW	486
LKU	Louisa County Feeman	Louisa, VA	38.01ºN	77.97ºW	493
MHT	Manchester	Manchester, NH	42.93ºN	71.44ºW	242

MRB	Eastern WV Regional Shepherd	Martinsburg, WV	39.40ºN	77.98ºW	557
MRN	Morganton Lenoir	Morganton, NC	35.82ºN	81.61ºW	1270
MVL	Morisville-Stowe State	Morrisville, VT	44.53ºN	72.61ºW	732
N03	Cortland County Chase	Cortland, NY	42.59ºN	76.21ºW	1198
N23	Sidney Municipal	Sidney, NY	42.30ºN	75.42ºW	1027
N27	Bradford County	Towanda, PA	41.74ºN	76.45ºW	730
N38	Grand Canyon State	Wellsboro, PA	41.73ºN	77.40ºW	1899
N70	Pennridge	Perkasie, PA	40.39ºN	75.29ºW	568
N87	Trenton Robbinsville	Robbinsville, NJ	40.21ºN	74.60ºW	119
OFP	Hanover County Municipal	Ashland, VA	37.71ºN	77.44ºW	205
OKV	Winchester Regional	Winchester, VA	39.14ºN	78.14ºW	727
P53	Rostraver	Monongahela, PA	40.21ºN	79.83ºW	1228
PNE	Northeast Philadelphia	Philadelphia, PA	40.08ºN	75.01ºW	121
RKD	Knox County Regional	Rockland, ME	44.53ºN	72.95ºW	787
RUT	Rutland State	Rutland, VT	43.06ºN	69.10ºW	55

SEG	Penn Valley	Selinsgrove, PA	40.82ºN	76.86ºW	450
SVH	Statesville Municipal	Statesville, NC	35.77ºN	80.96ºW	965
THV	York	York, PA	39.92ºN	76.87ºW	480
VUJ	Stanly County	Albemarle, NC	35.42ºN	80.15ºW	609
W00	Freeway	Mitchellville, MD	38.94ºN	76.77ºW	168
W29	Bay Bridge	Stevensville, MD	38.98ºN	76.33ºW	15
W45	Luray Caverns	Luray, VA	38.67ºN	78.50ºW	902
W79	Tappahannock Municipal	Tappahannock, VA	37.93ºN	76.87ºW	31
W81	Crewe Municipal	Crewe, VA	37.18ºN	78.10ºW	420
W96	New Kent County	Quinton, VA	37.50ºN	77.13ºW	123
WVL	Waterville Robert Lafleur	Waterville, ME	44.53ºN	69.68ºW	333

Appendix II

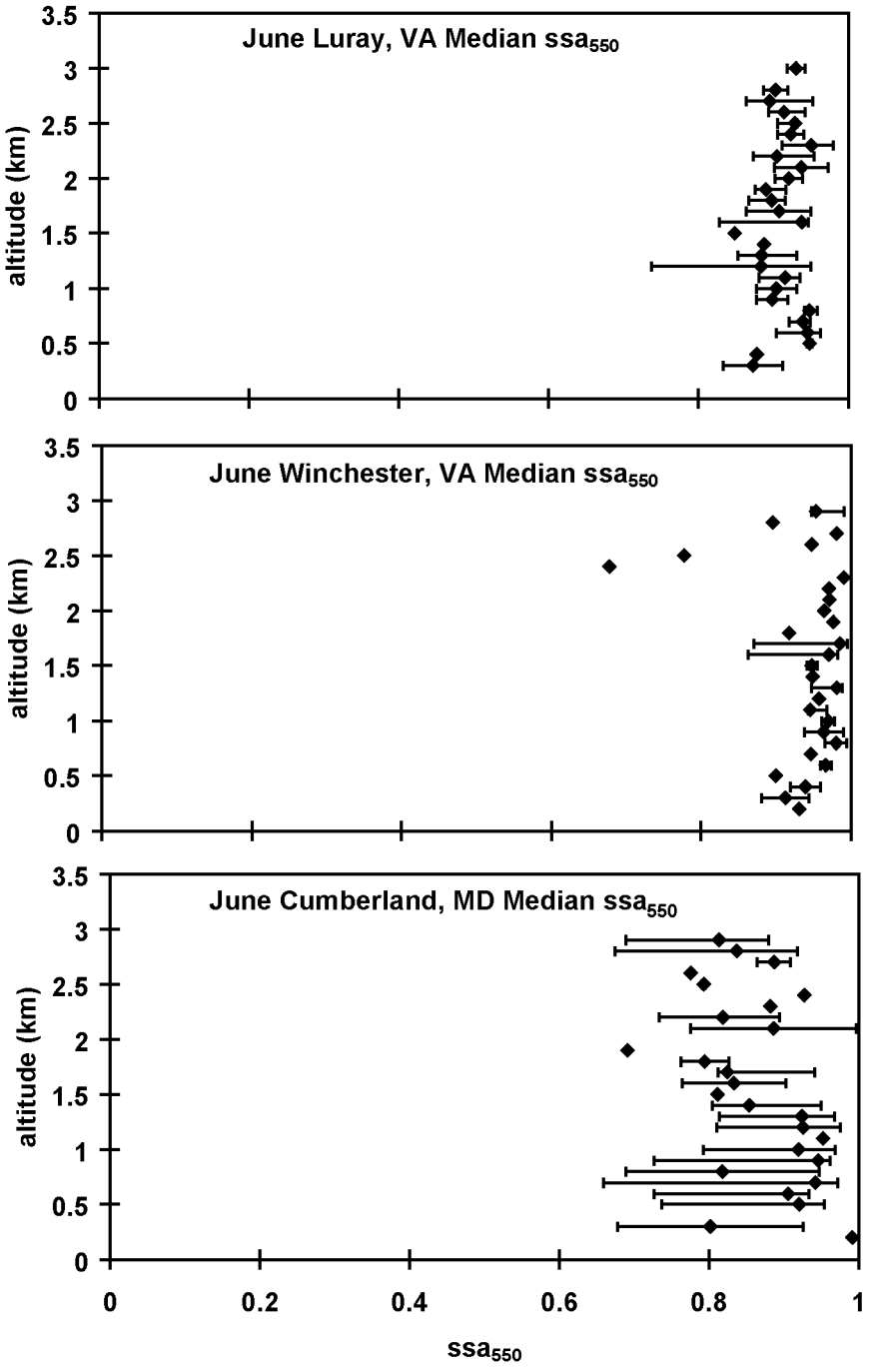

Appendix II.1. June 2001 morning profile median single scattering albedo (550 nm). The error bars represent the 1st and 3rd quartile values.

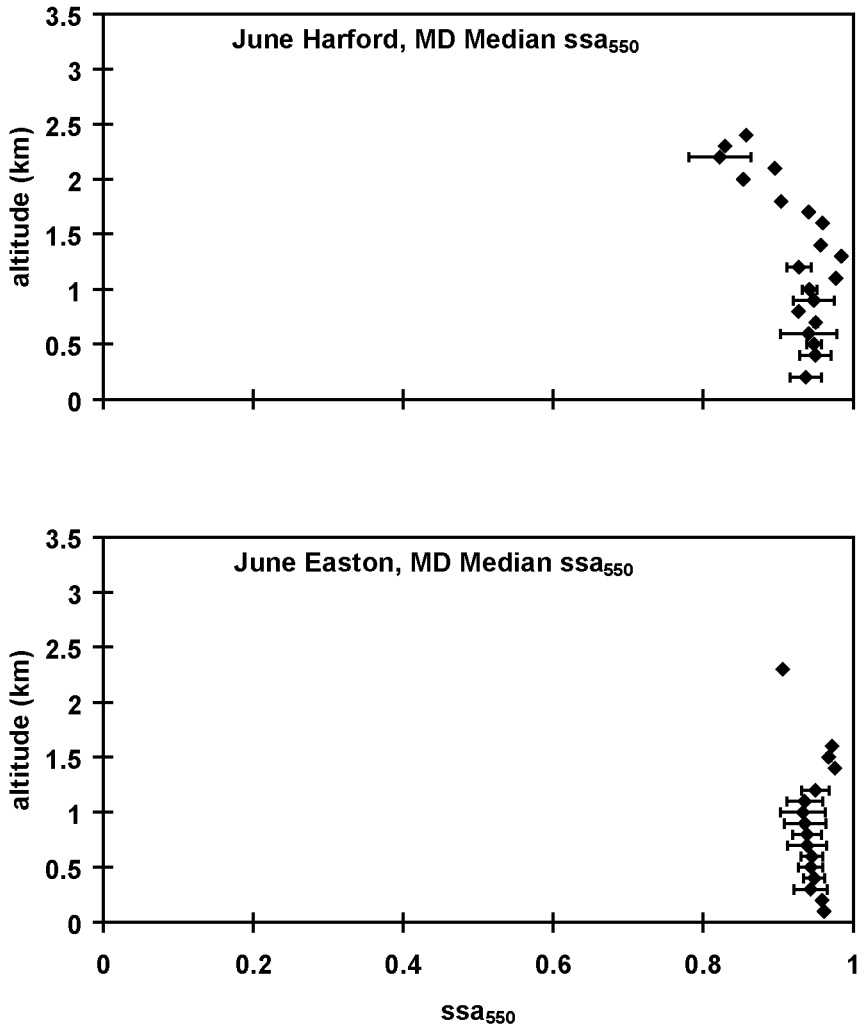

Appendix II.2. June 2001 afternoon profiles median single scattering albedo (550 nm).

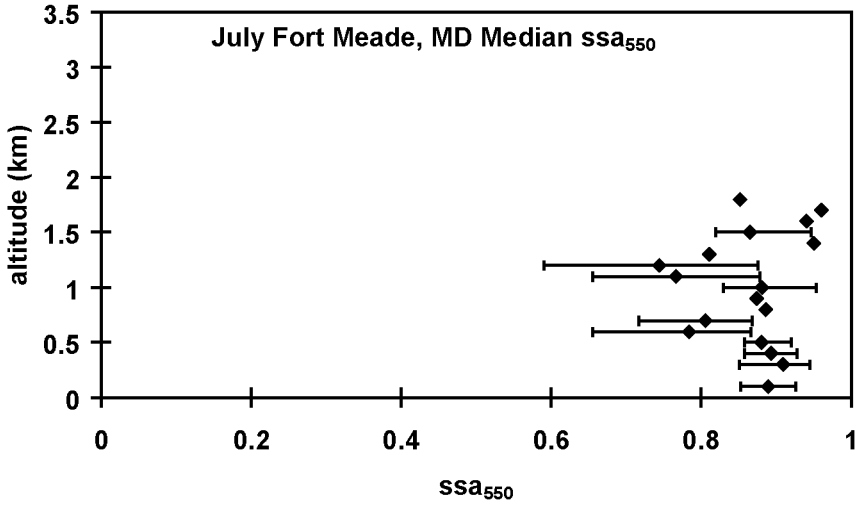

Appendix II.3. July 2001 afternoon profiles median single scattering albedo (550 nm).

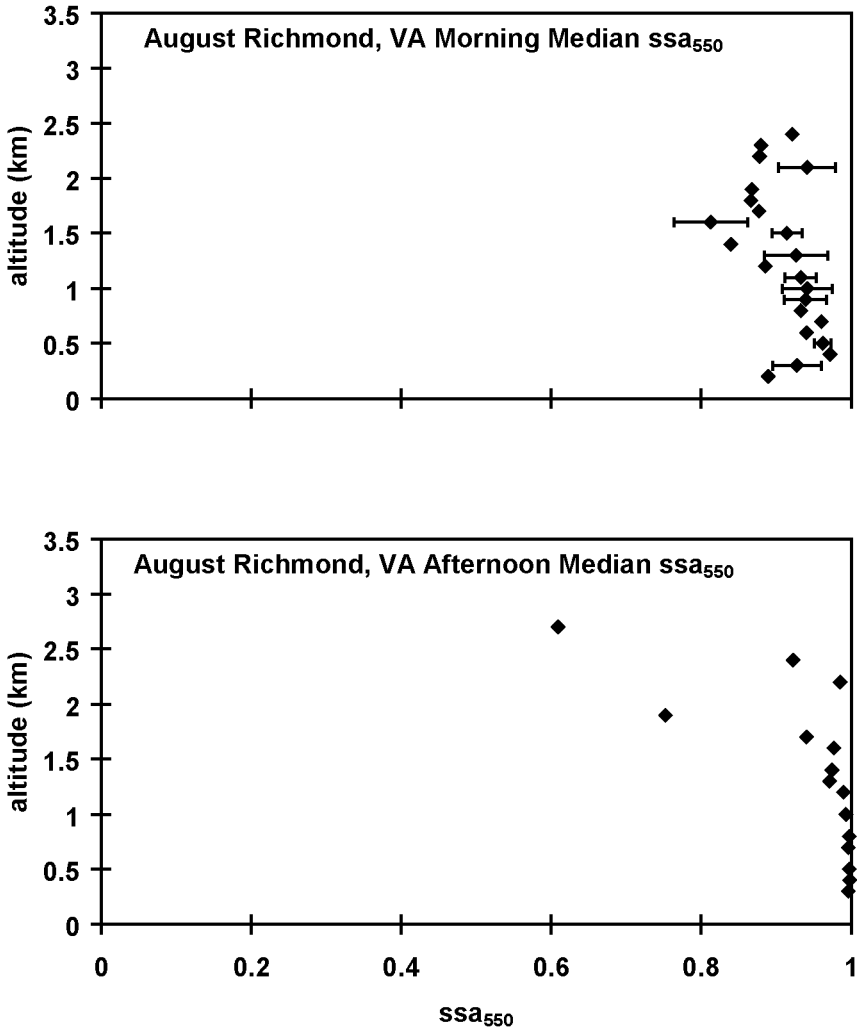

Appendix II.4. August 2001 morning and afternoon profiles median single scattering albedo (550 nm).

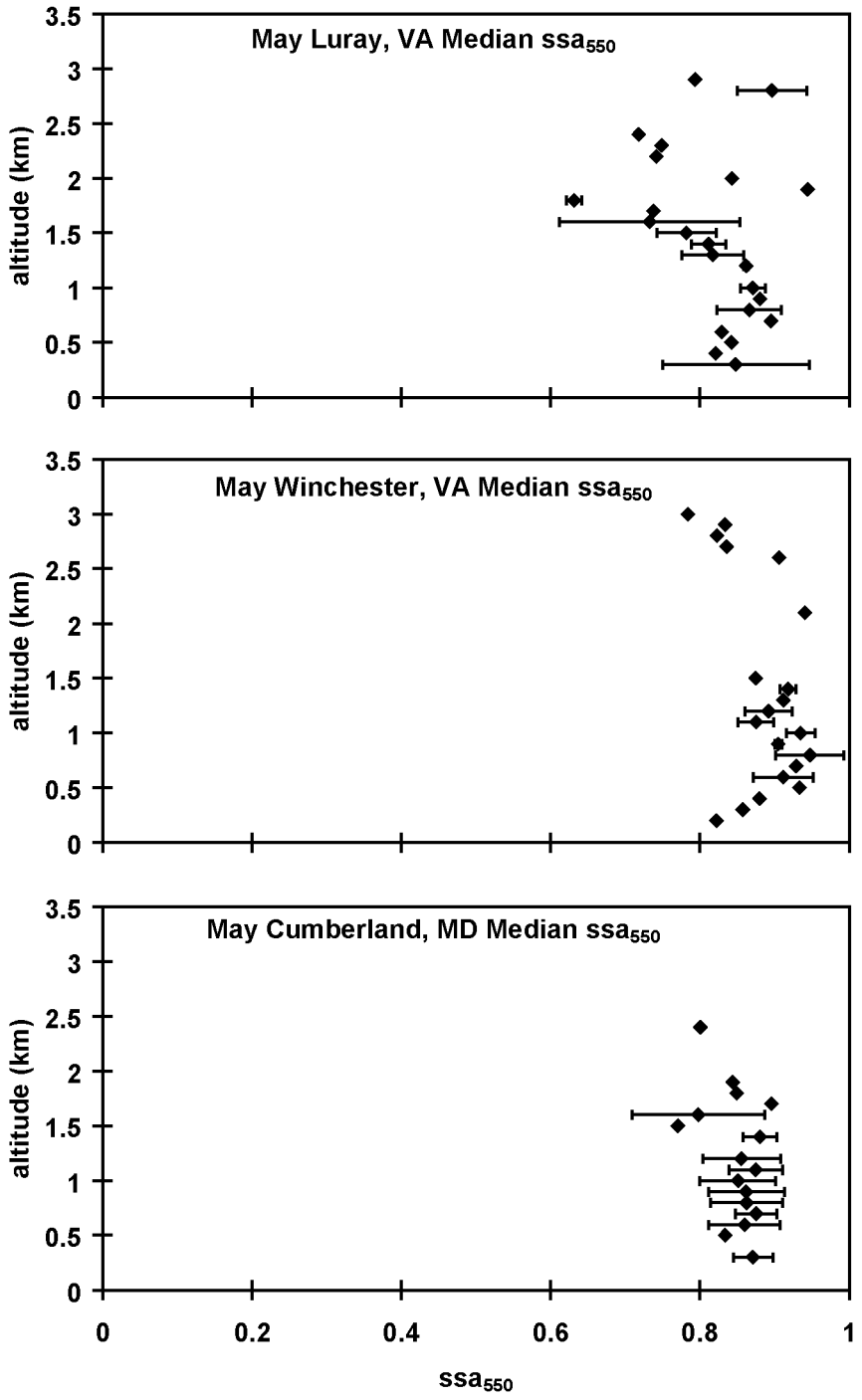

Appendix II.5. May 2002 morning profiles median single scattering albedo (550 nm).

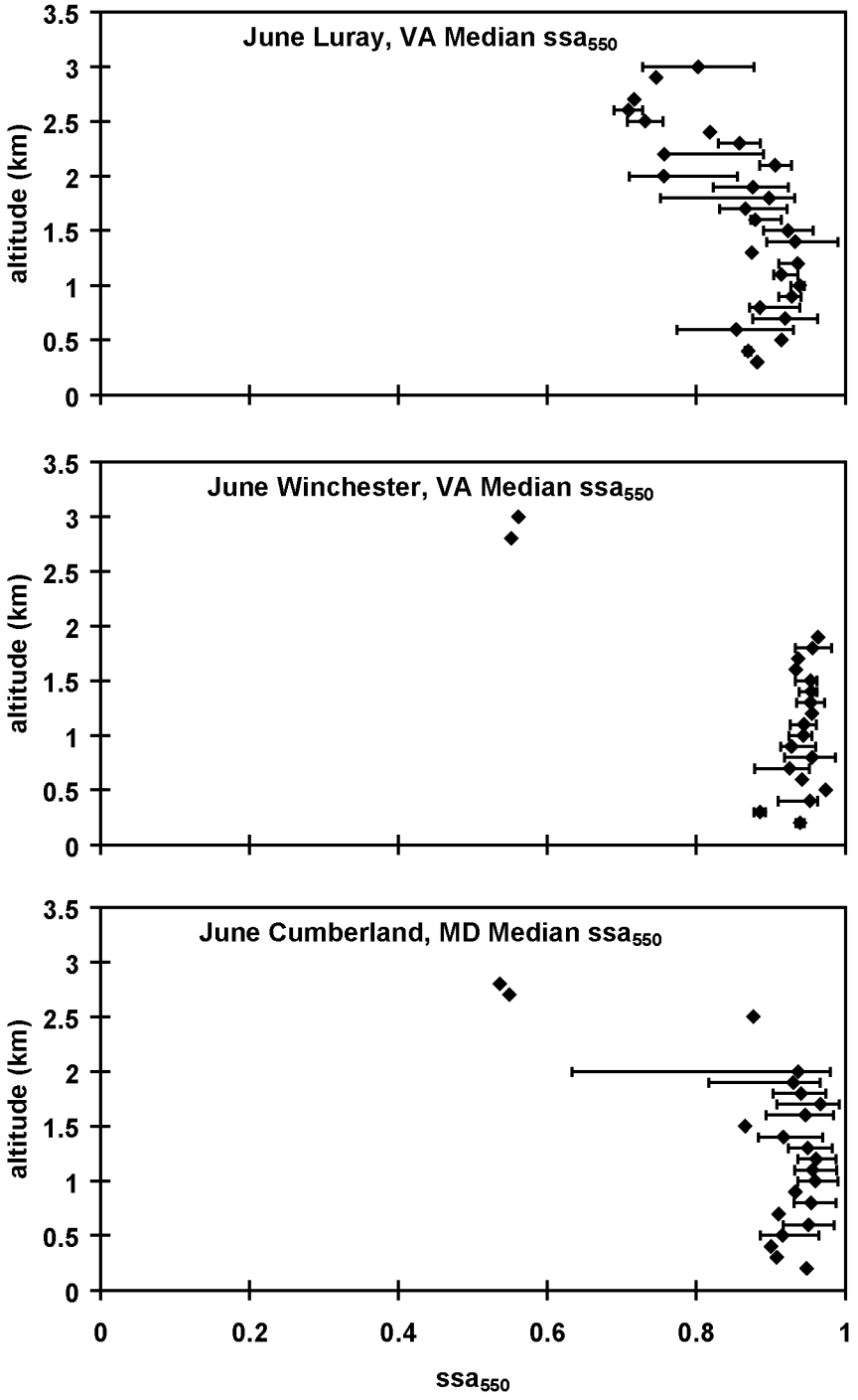

Appendix II.6. June 2002 morning profiles median single scattering albedo (550 nm).

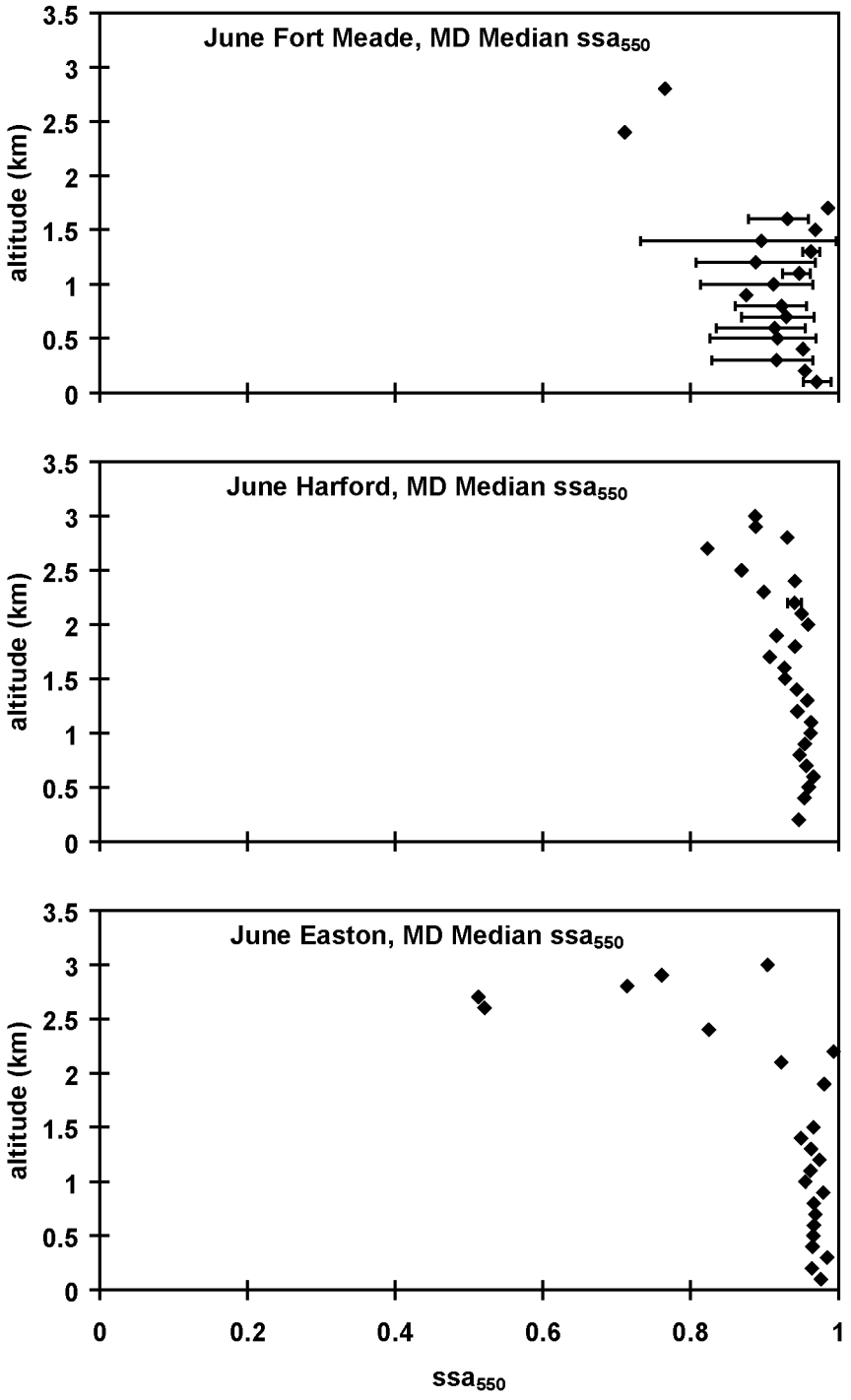

Appendix II.7. June 2002 afternoon profiles median single scattering albedo (550 nm).

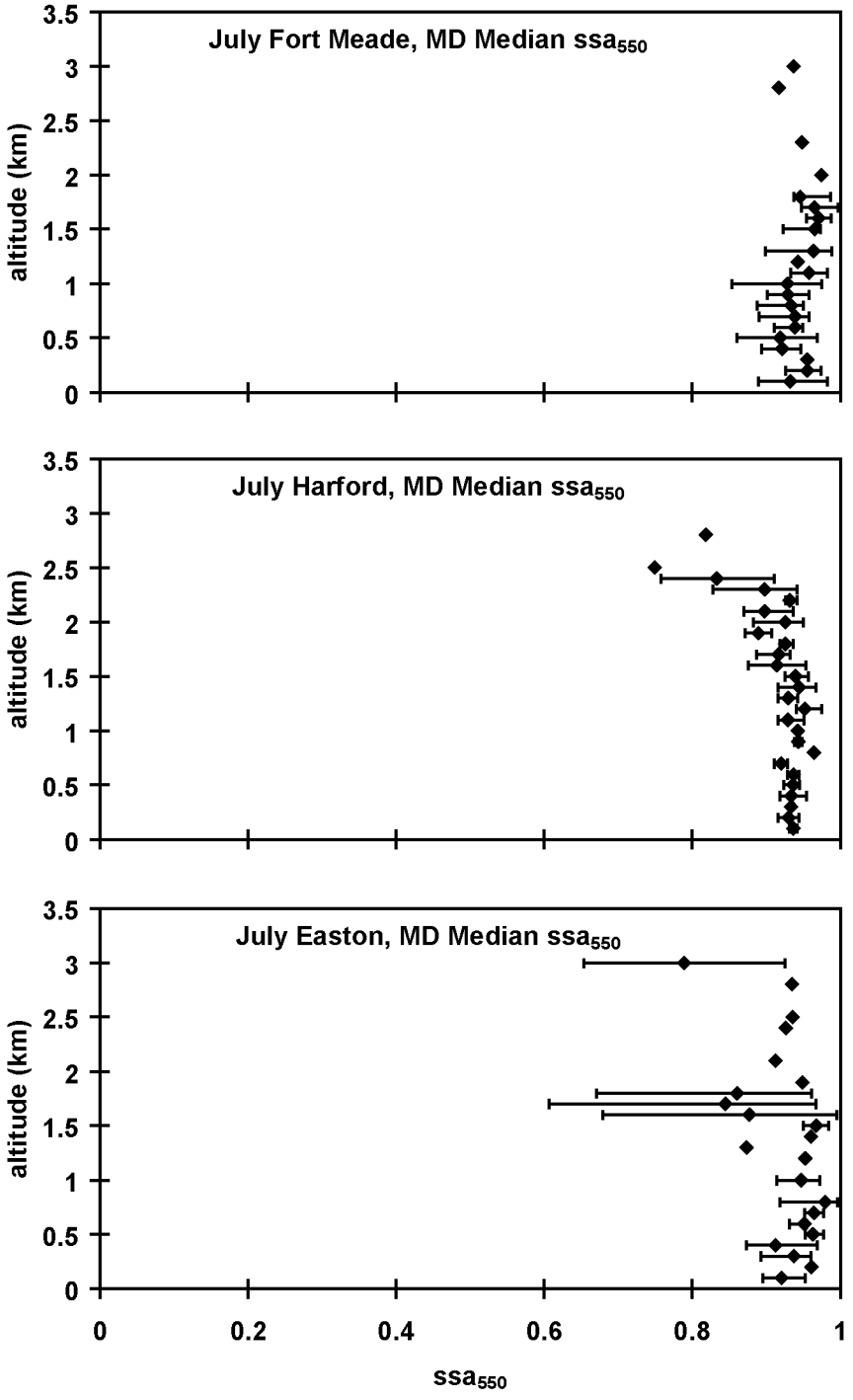

Appendix II.8. July 2002 afternoon profiles median single scattering albedo (550 nm).

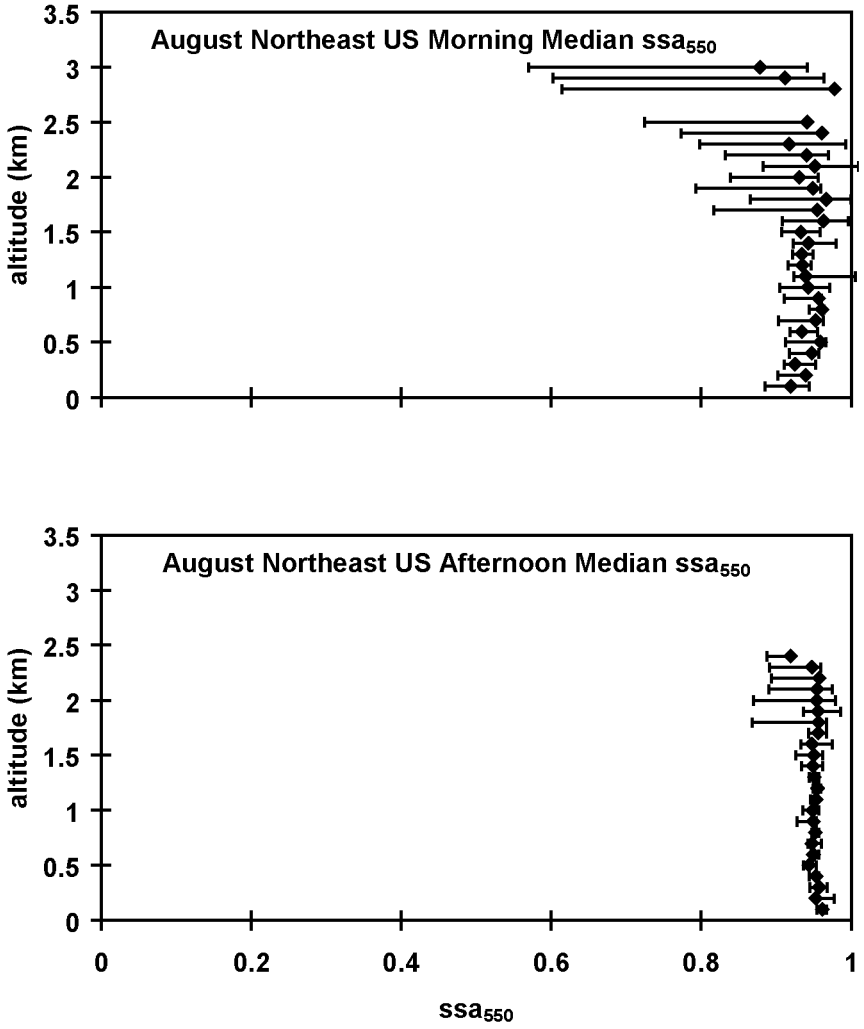

Appendix II.9. August 2002 morning and afternoon profiles over northeastern US median single scattering albedo (550 nm).

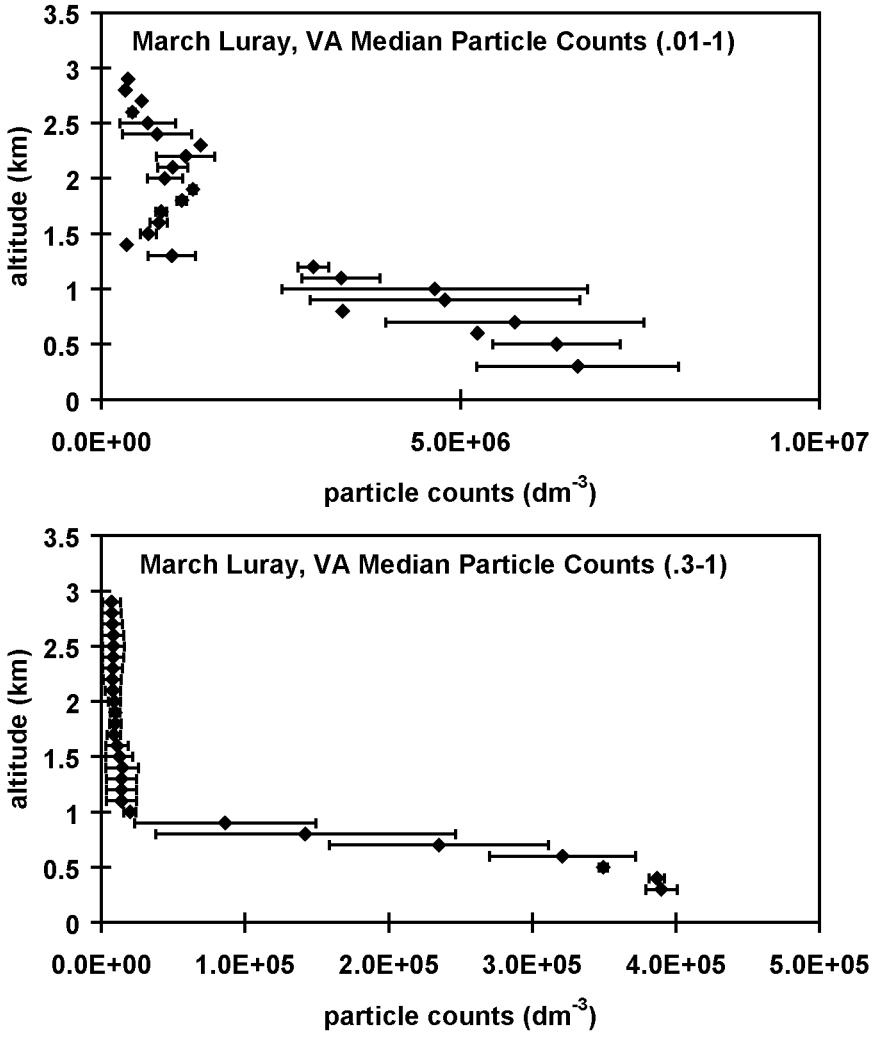

Appendix II.10. March 2003 Luray, VA profiles median particle counts [0.01 - 1 μm (above), 0.3 - 1 μm (below)].

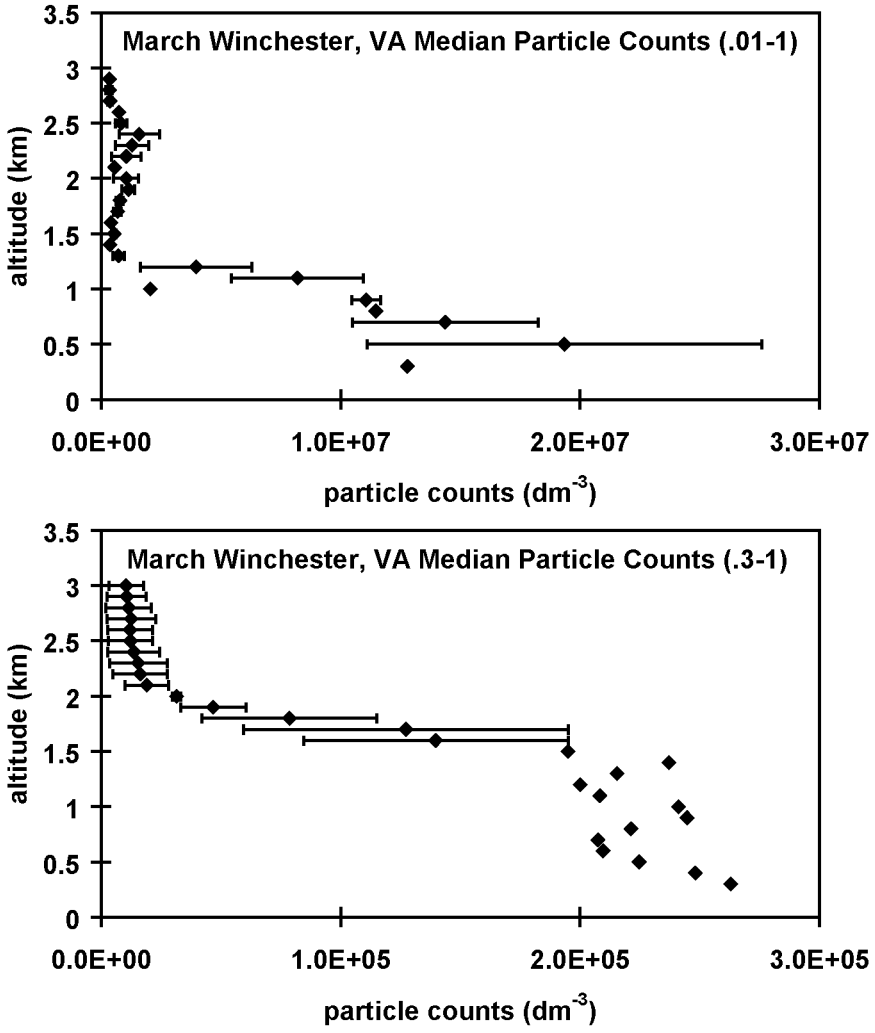

Appendix II.11. March 2003 Winchester, VA profiles median particle counts [0.01 - 1 μm (above), 0.3 - 1 μm (below)].

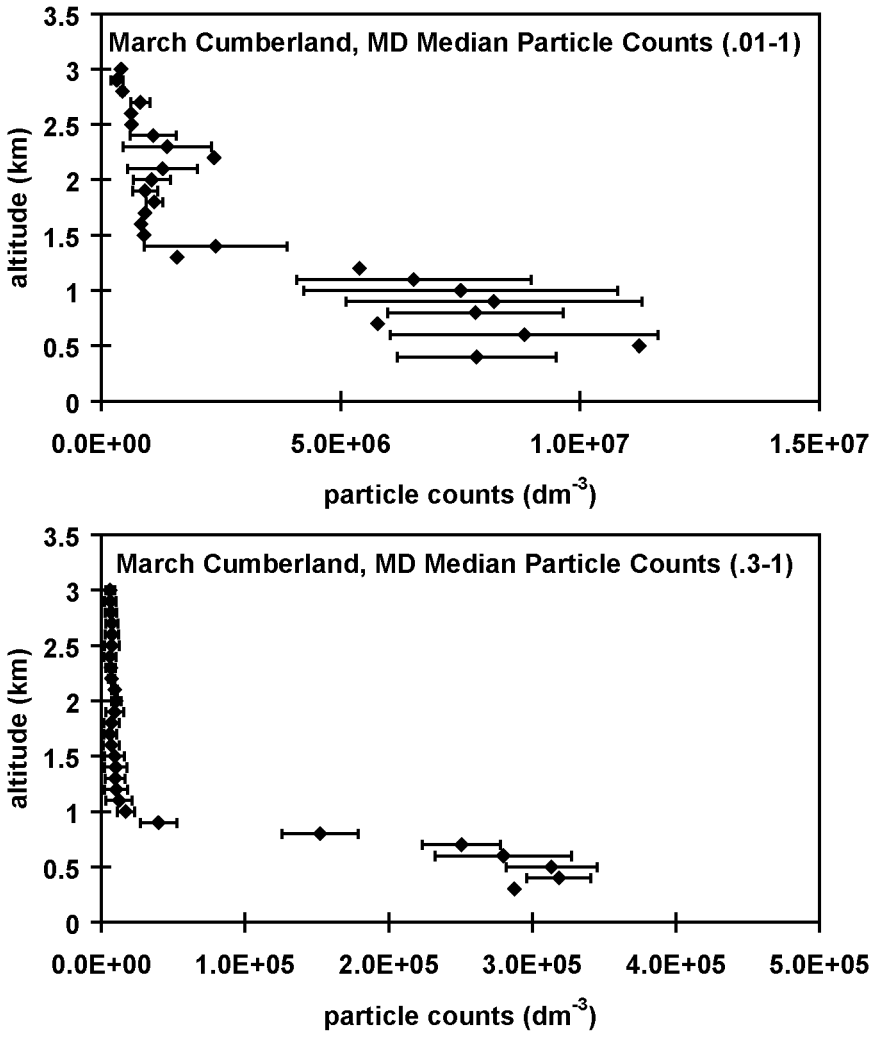

Appendix II.12. March 2003 Cumberland, MD profiles median particle counts [0.01 - 1 μm (above), 0.3 - 1 μm (below)].

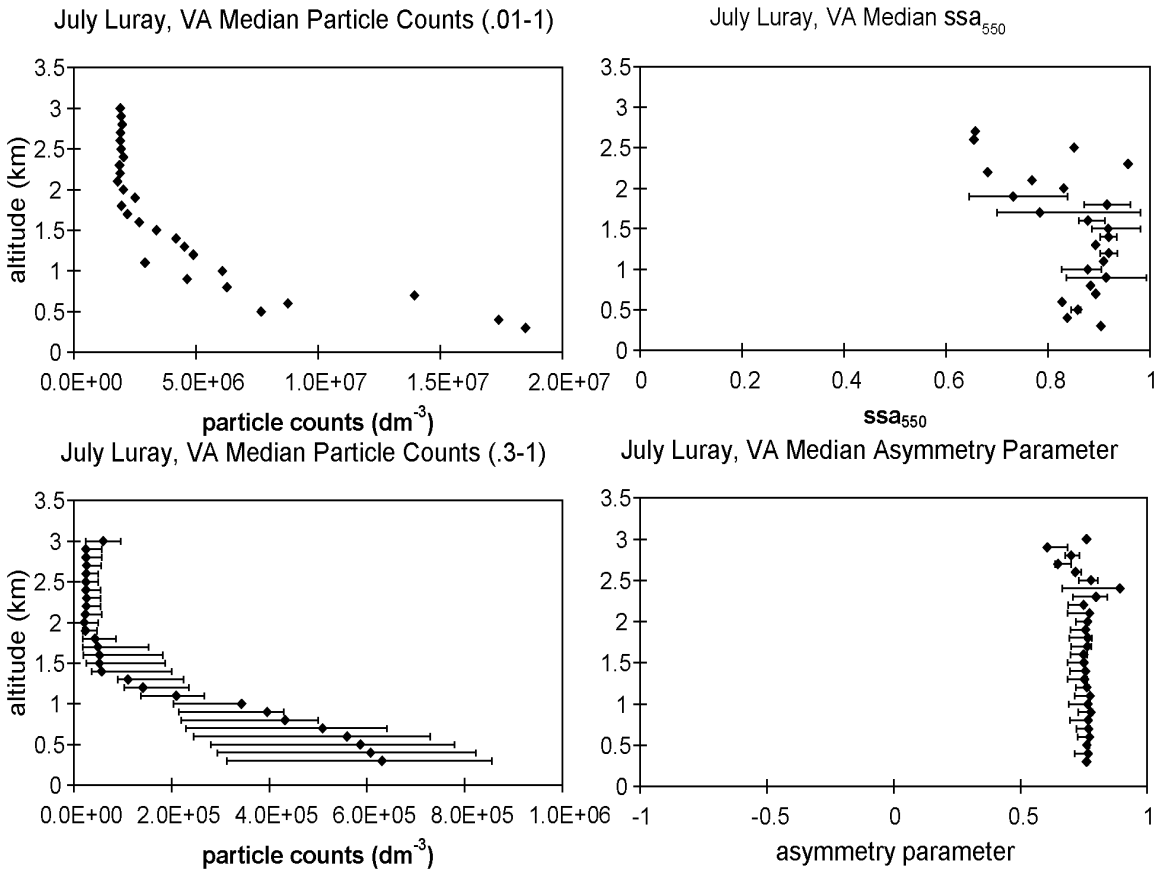

Appendix II.13. July 2003 Luray, VA profiles median particle counts (0.01 - 1 μm and 0.3 - 1 μm), single scattering albedo (550 nm), and asymmetry parameter (550 nm).

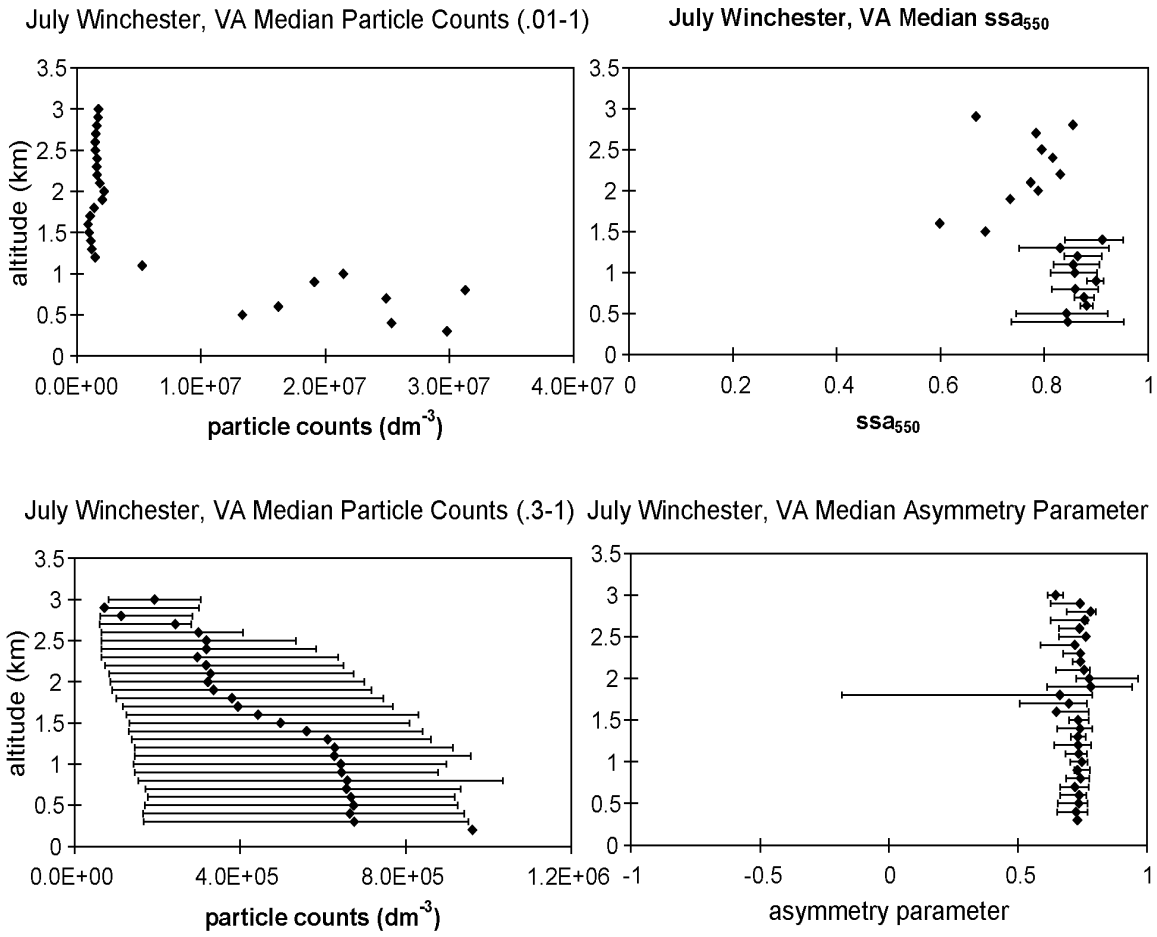

Appendix II.14. July 2003 Winchester, VA profiles median particle counts (0.01 - 1 μm and 0.3 - 1 μm), single scattering albedo (550 nm), and asymmetry parameter (550 nm).

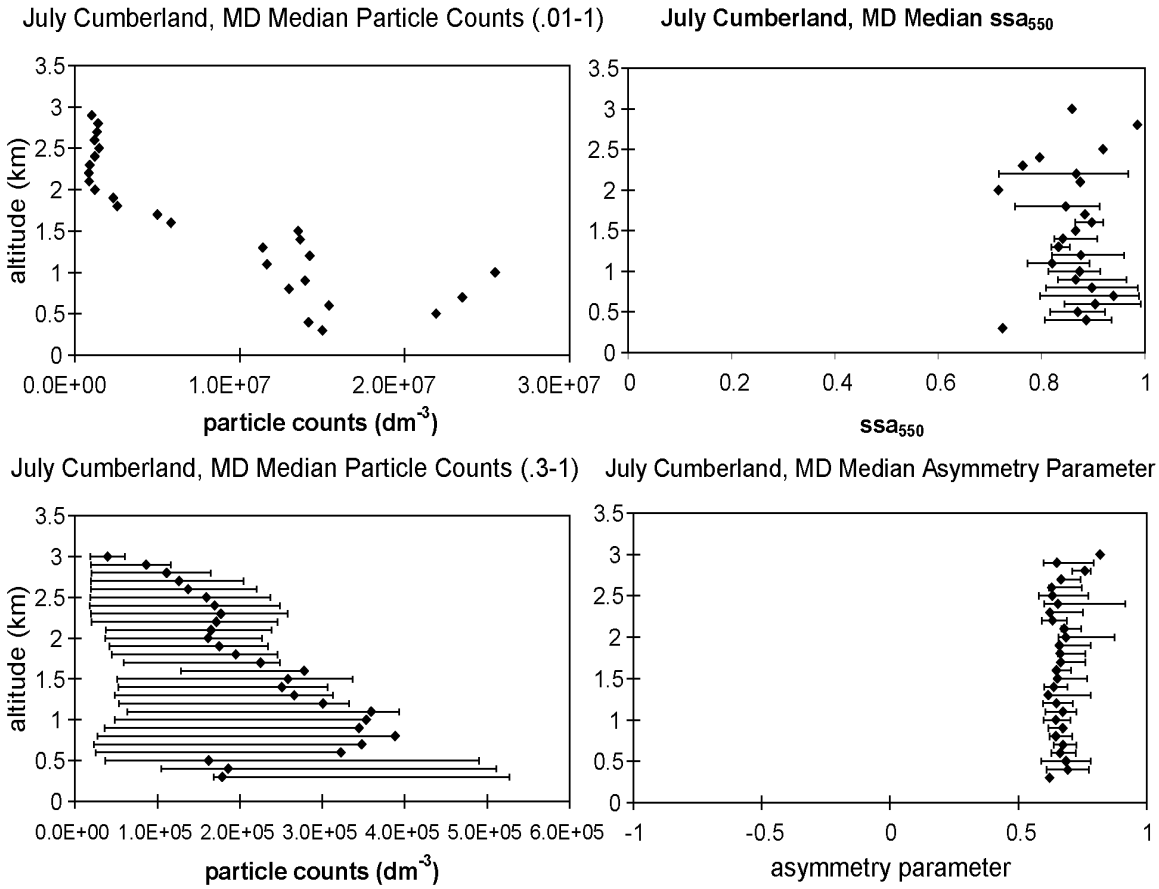

Appendix II.15. July 2003 Cumberland, MD profiles median particle counts (0.01 - 1 μm and 0.3 - 1 μm), single scattering albedo (550 nm), and asymmetry parameter (550 nm).

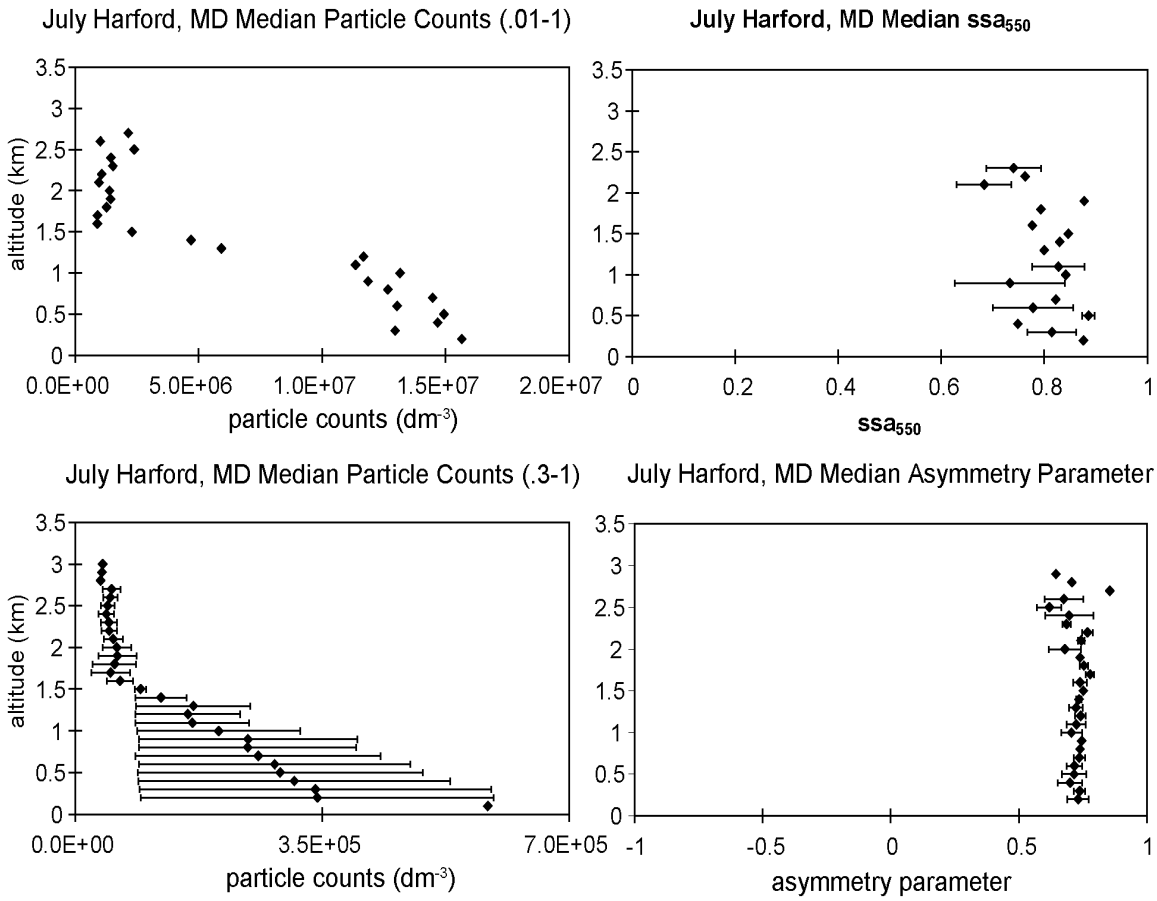

Appendix II.16. July 2003 Harford County, MD profiles median particle counts (0.01 - 1 μm and 0.3 - 1 μm), single scattering albedo (550 nm), and asymmetry parameter (550 nm).

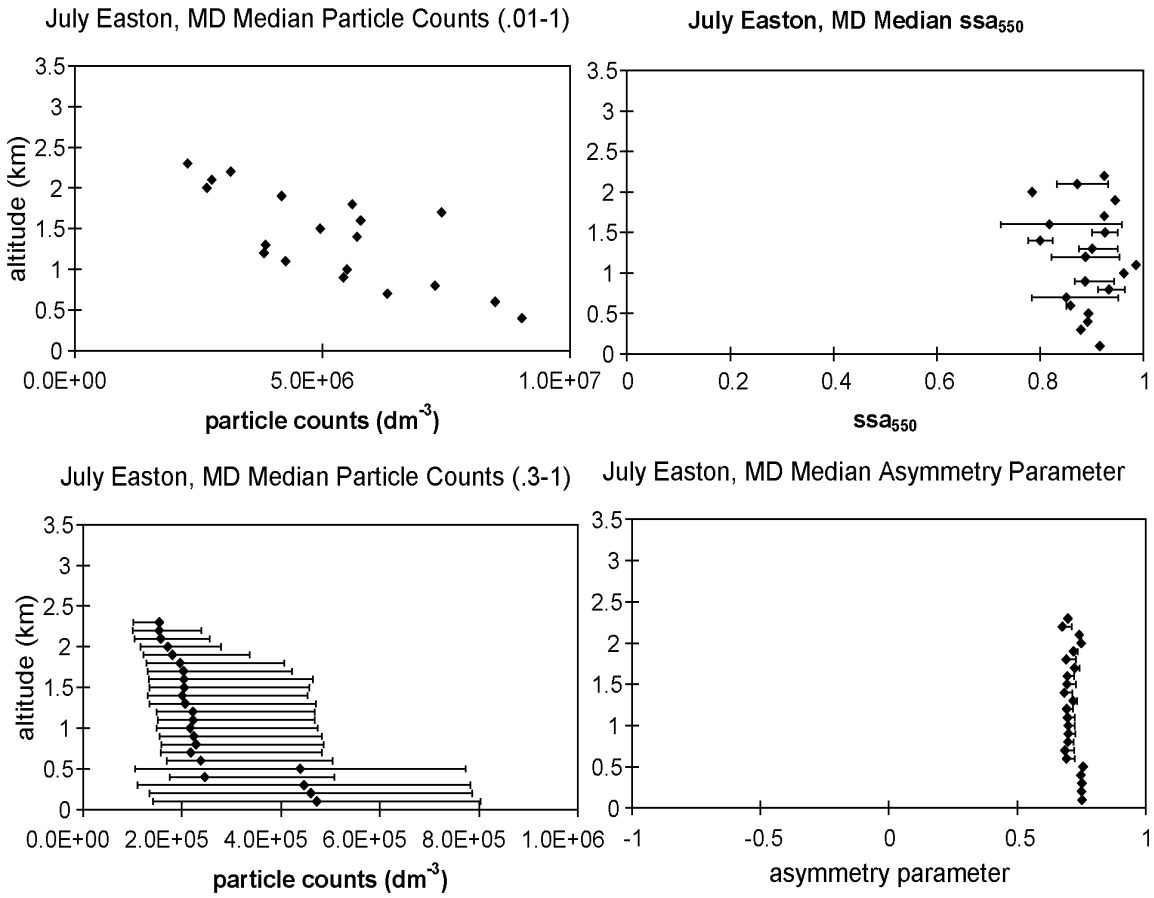

Appendix II.17. July 2003 Easton, MD profiles median particle counts (0.01 - 1 μm and 0.3 - 1 μm), single scattering albedo (550 nm), and asymmetry parameter (550 nm).

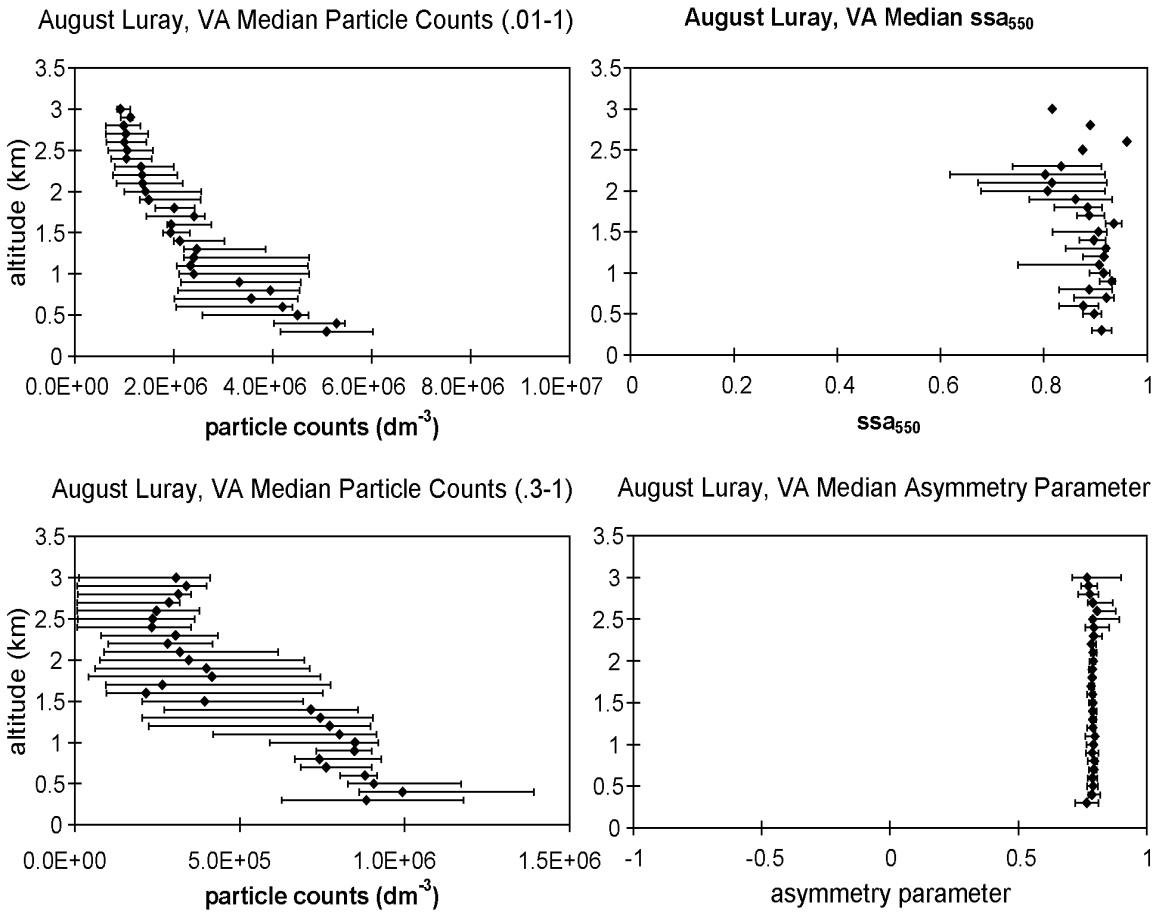

Appendix II.18. August 2003 Luray, VA profiles median particle counts (0.01 - 1 μm and 0.3 - 1 μm), single scattering albedo (550 nm), and asymmetry parameter (550 nm).

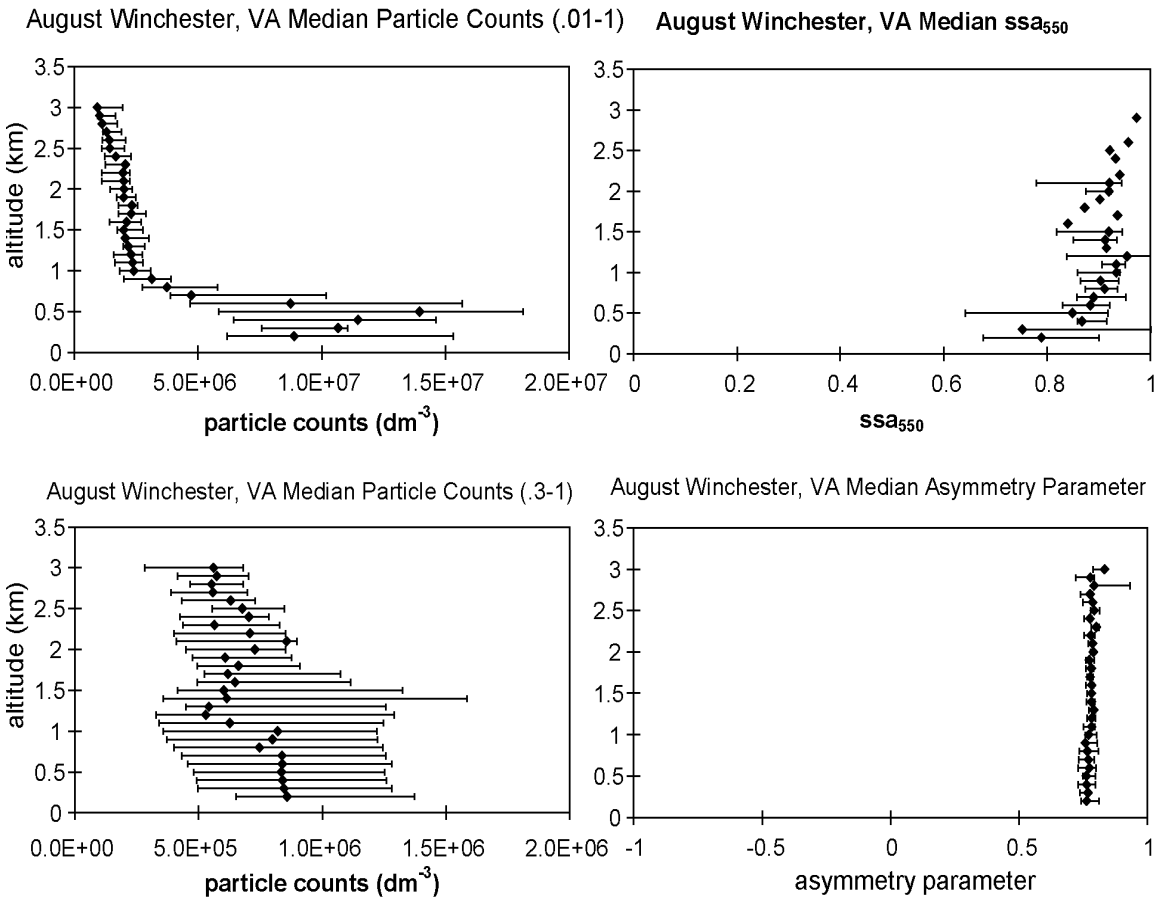

Appendix II.19. August 2003 Winchester, VA profiles median particle counts (0.01 - 1 μm and 0.3 - 1 μm), single scattering albedo (550 nm), and asymmetry parameter (550 nm).

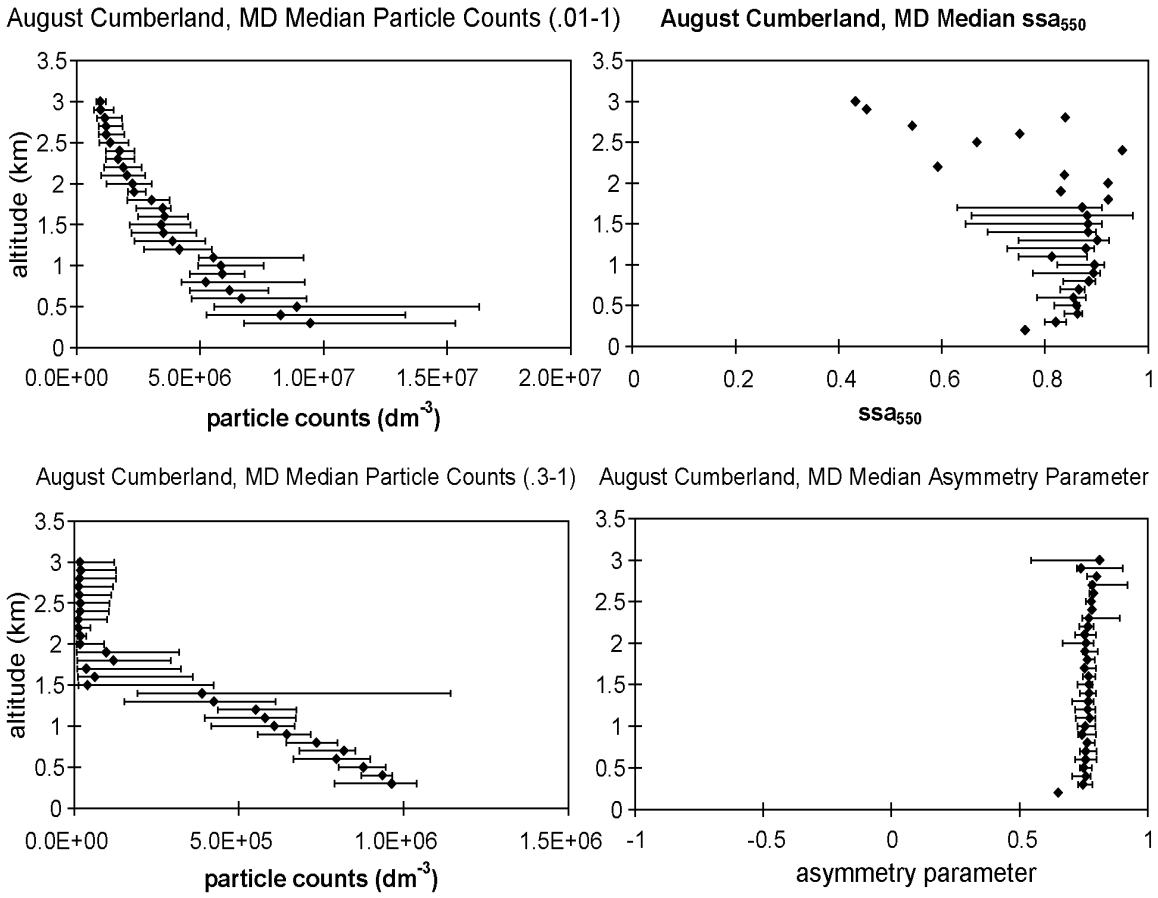

Appendix II.20. August 2003 Cumberland, MD profiles median particle counts (0.01 - 1 μm and 0.3 - 1 μm), single scattering albedo (550 nm), and asymmetry parameter (550 nm).

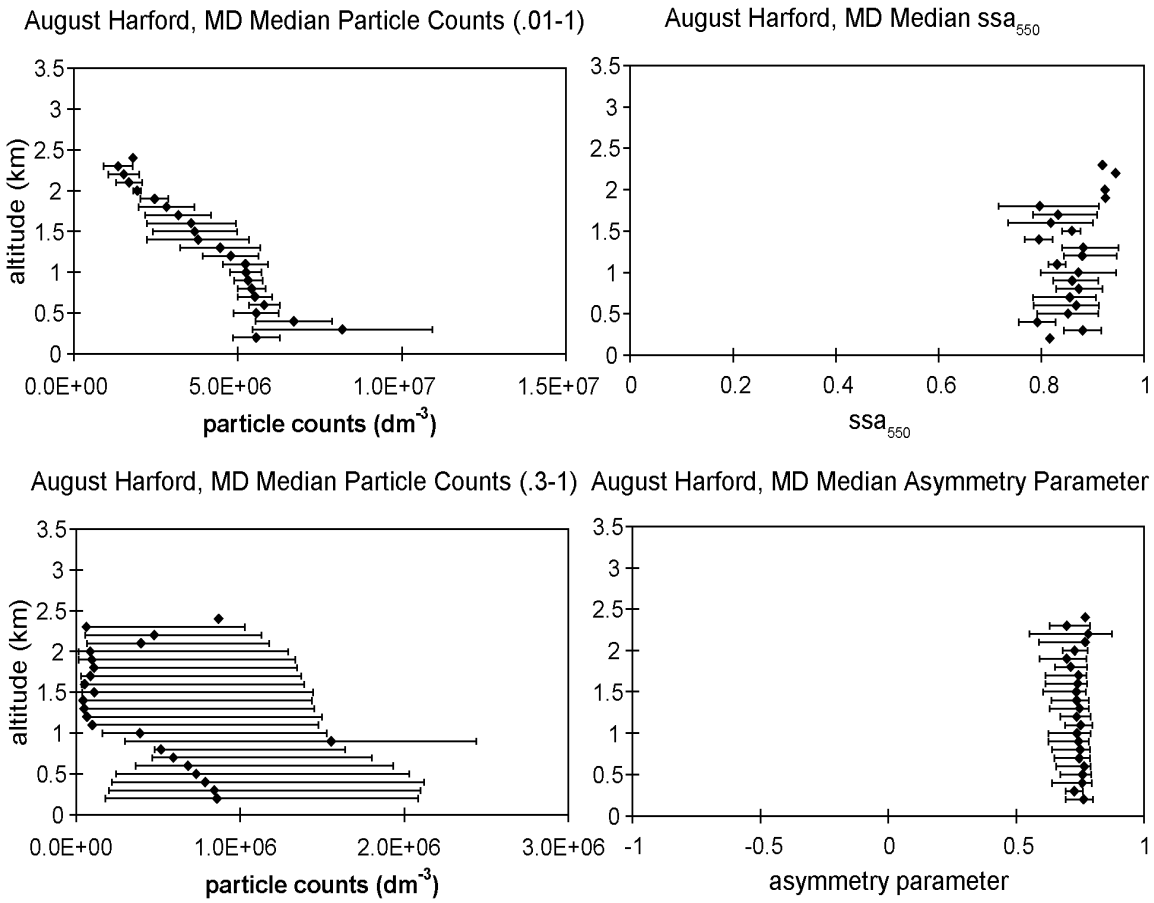

Appendix II.21. August 2003 Harford County, MD profiles median particle counts (0.01 - 1 μm and 0.3 - 1 μm), single scattering albedo (550 nm), and asymmetry parameter (550 nm).

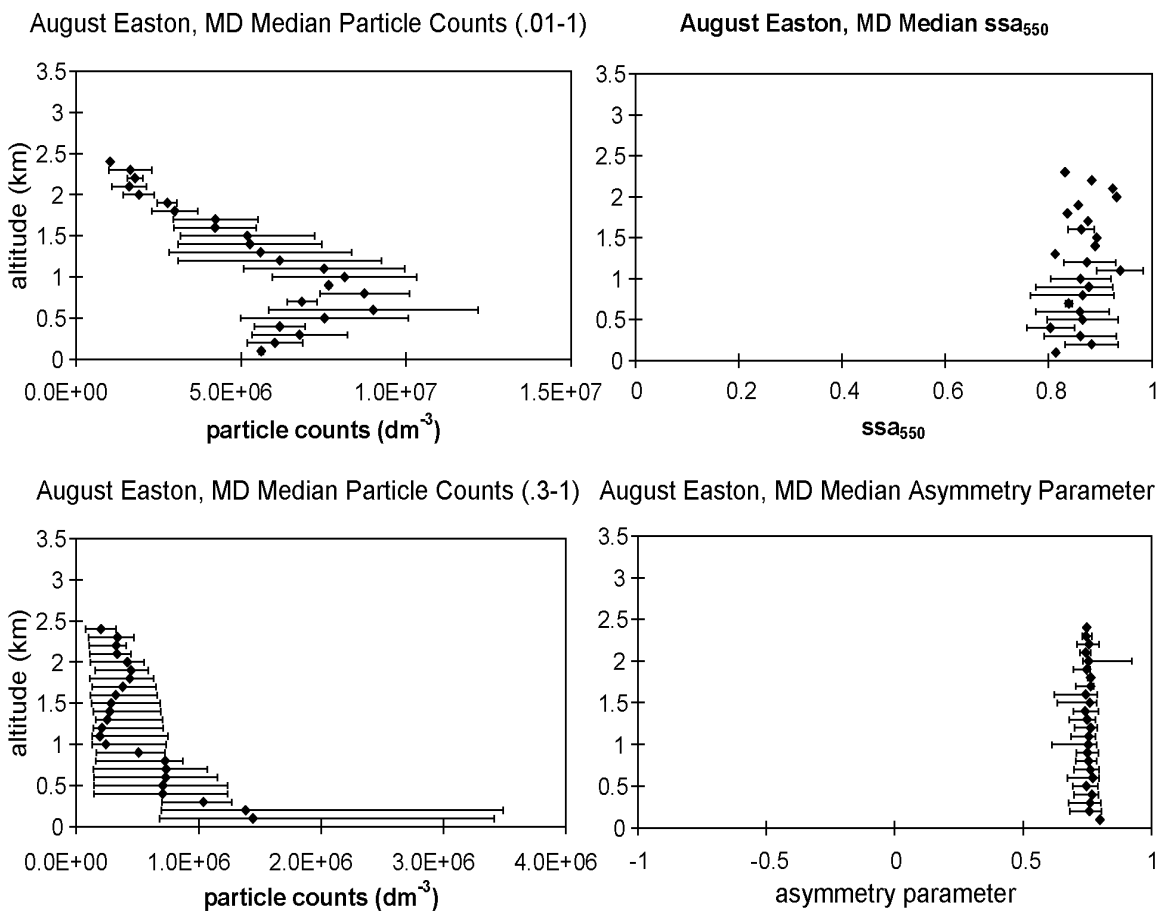

Appendix II.22. August 2003 Easton, MD profiles median particle counts (0.01 - 1 μm and 0.3 - 1 μm), single scattering albedo (550 nm), and asymmetry parameter (550 nm).

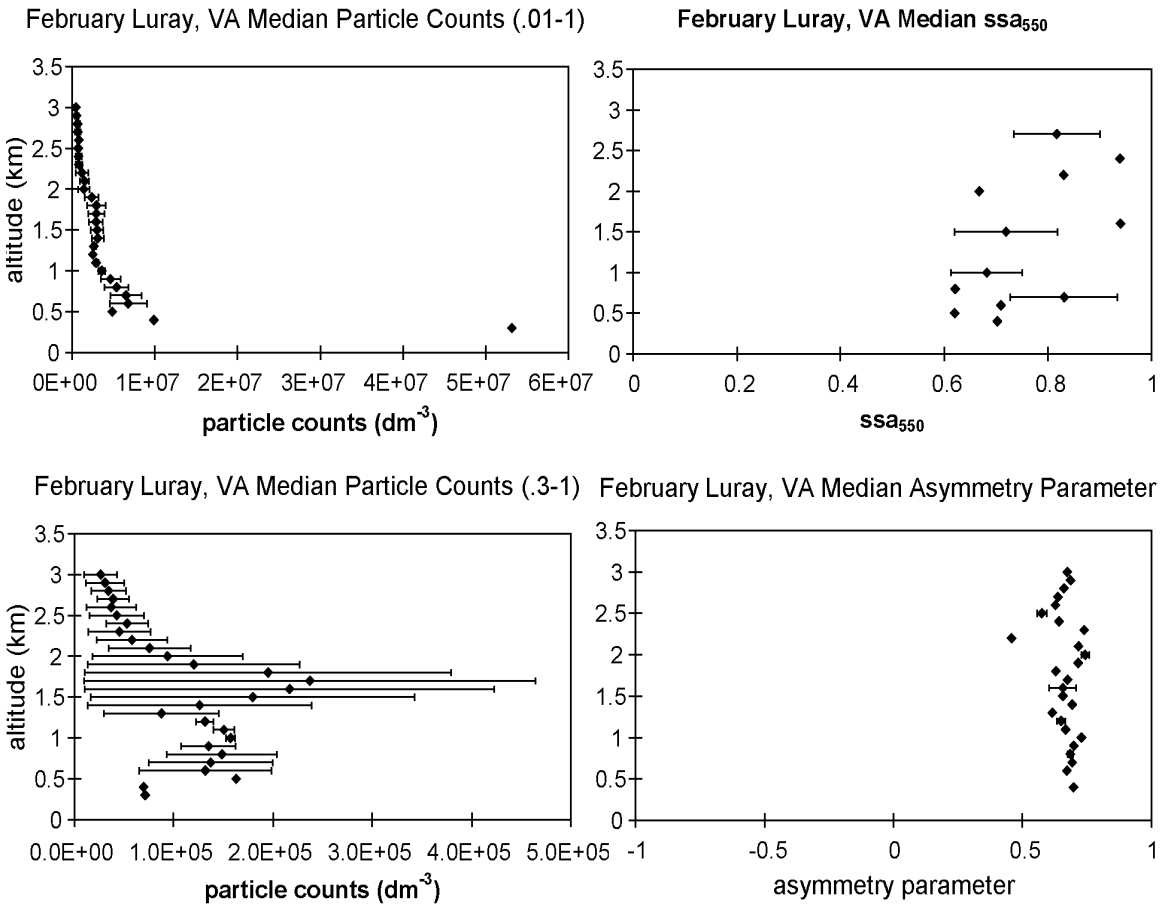

Appendix II.23. February 2004 Luray, VA profiles median particle counts (0.01 - 1 μm and 0.3 - 1 μm), single scattering albedo (550 nm), and asymmetry parameter (550 nm).

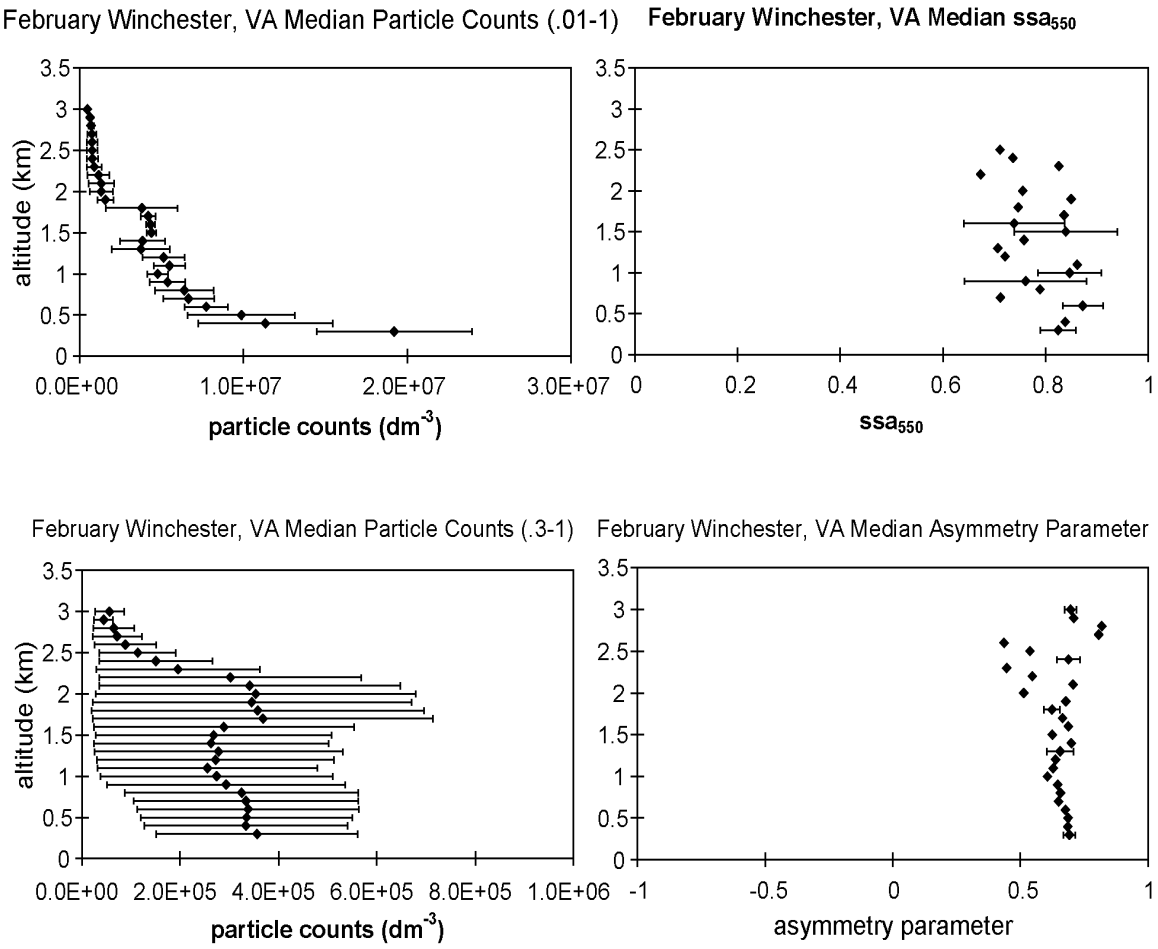

Appendix II.24. February 2004 Winchester, VA profiles median particle counts (0.01 - 1 μm and 0.3 - 1 μm), single scattering albedo (550 nm), and asymmetry parameter (550 nm).

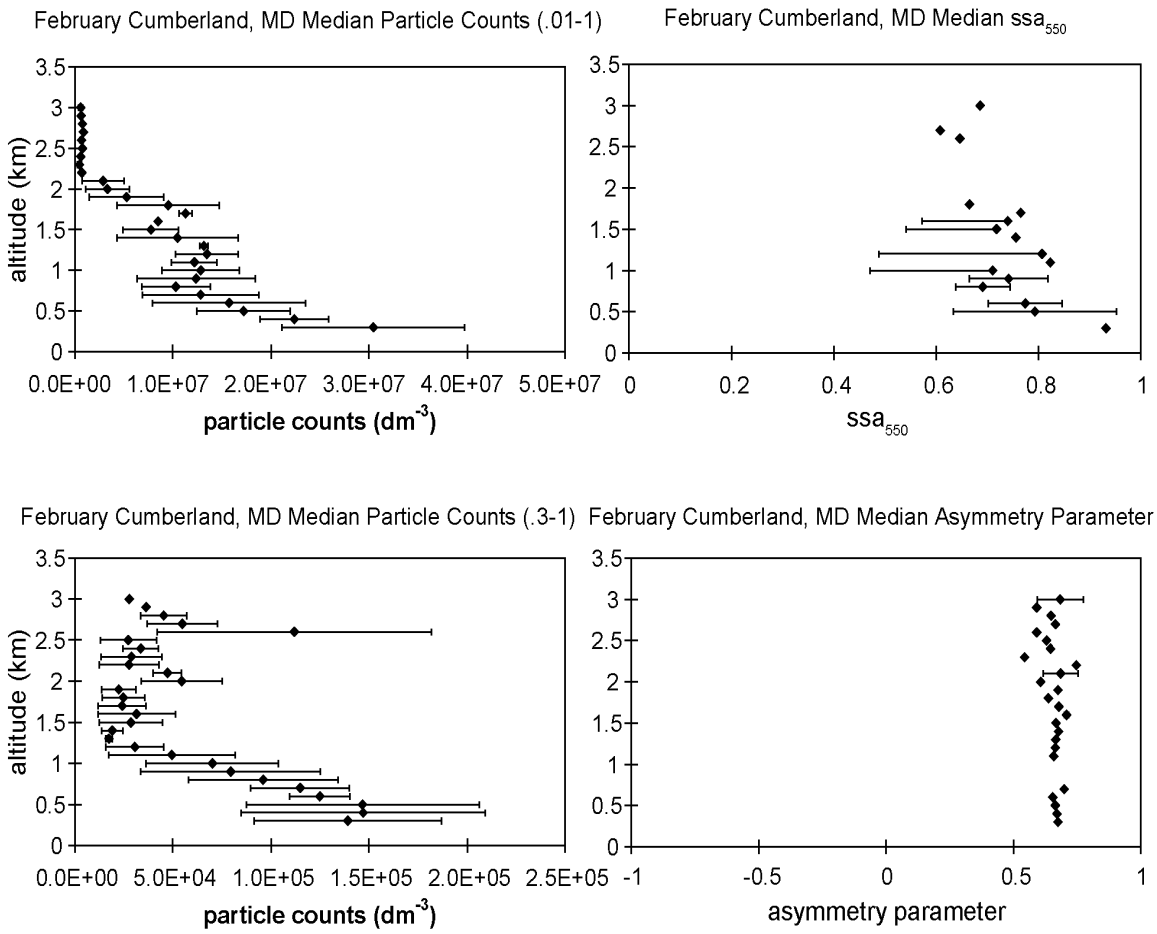

Appendix II.25. February 2004 Cumberland, MD profiles median particle counts (0.01 - 1 μm and 0.3 - 1 μm), single scattering albedo (550 nm), and asymmetry parameter (550 nm).

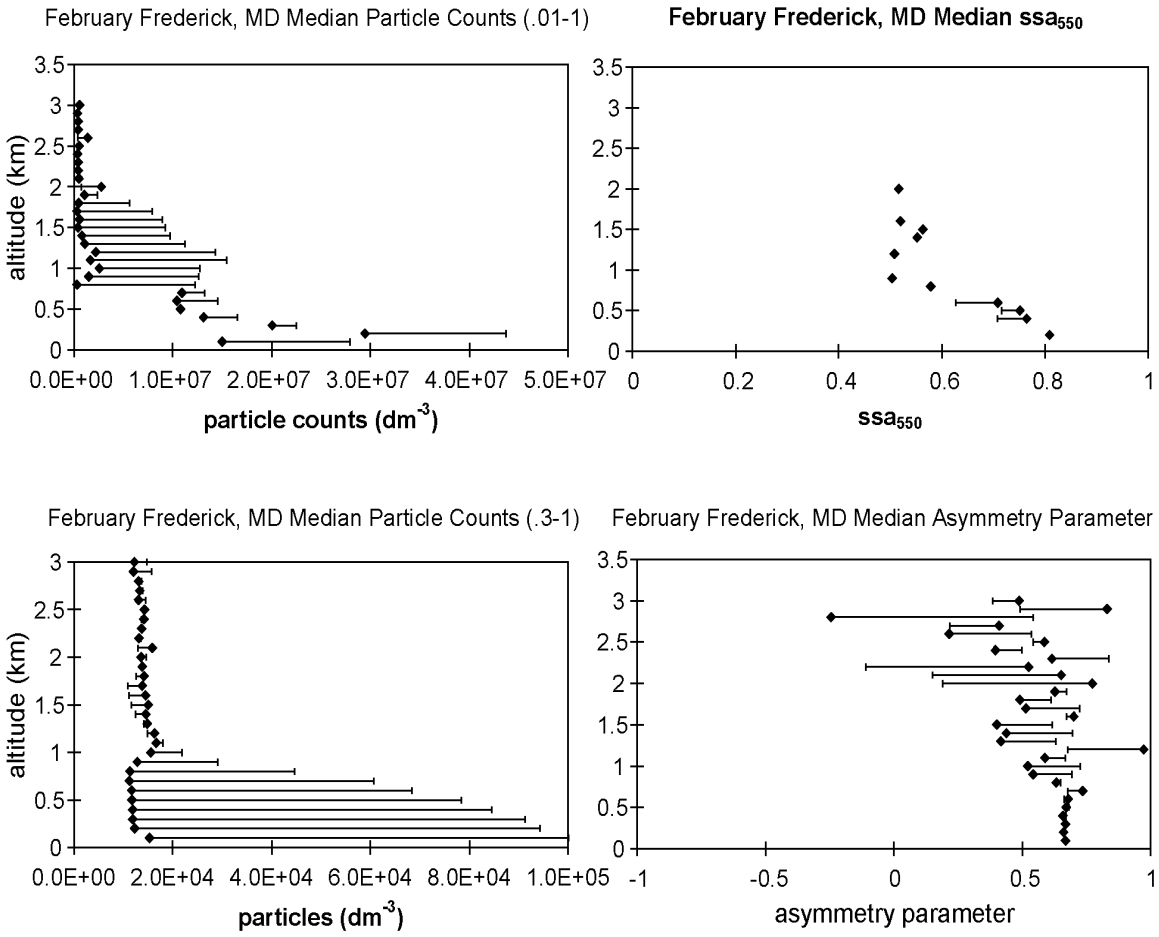

Appendix II.26. February 2004 Frederick, MD profiles median particle counts (0.01 - 1 μm and 0.3 - 1 μm), single scattering albedo (550 nm), and asymmetry parameter (550 nm).

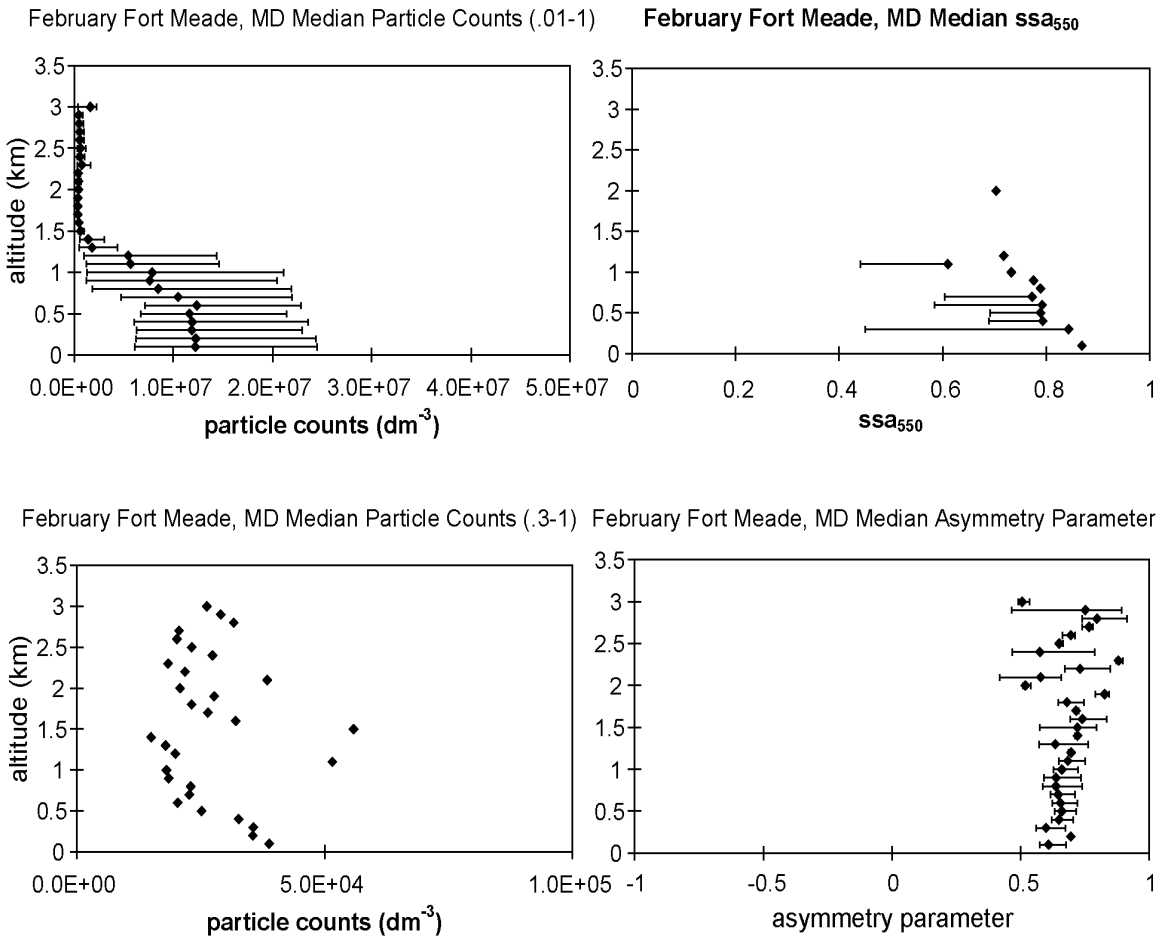

Appendix II.27. February 2004 Fort Meade, MD profiles median particle counts (0.01 - 1 μm and 0.3 - 1 μm), single scattering albedo (550 nm), and asymmetry parameter (550 nm).

Appendix III

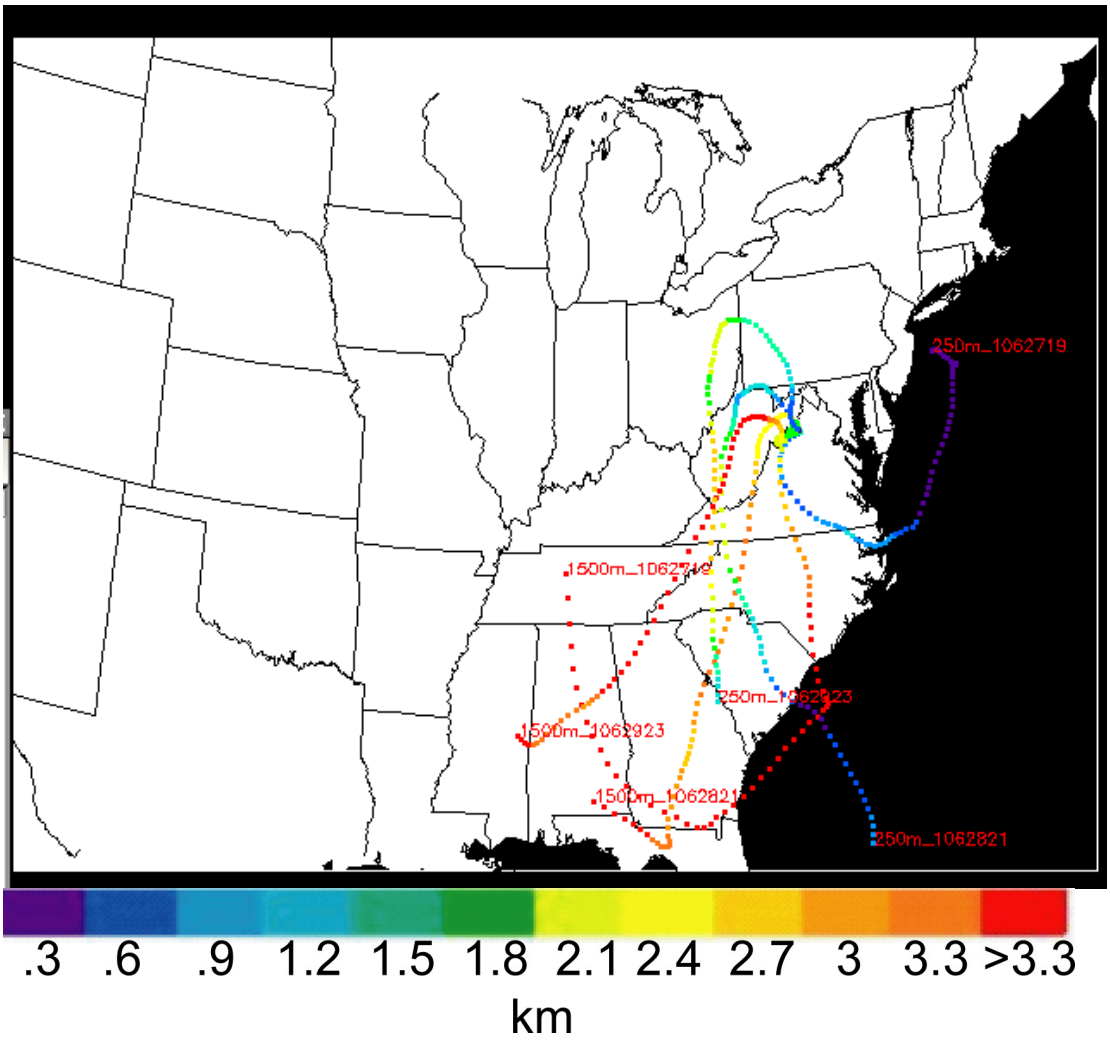

Appendix III.1. June 2001 W45 72 h backward trajectories

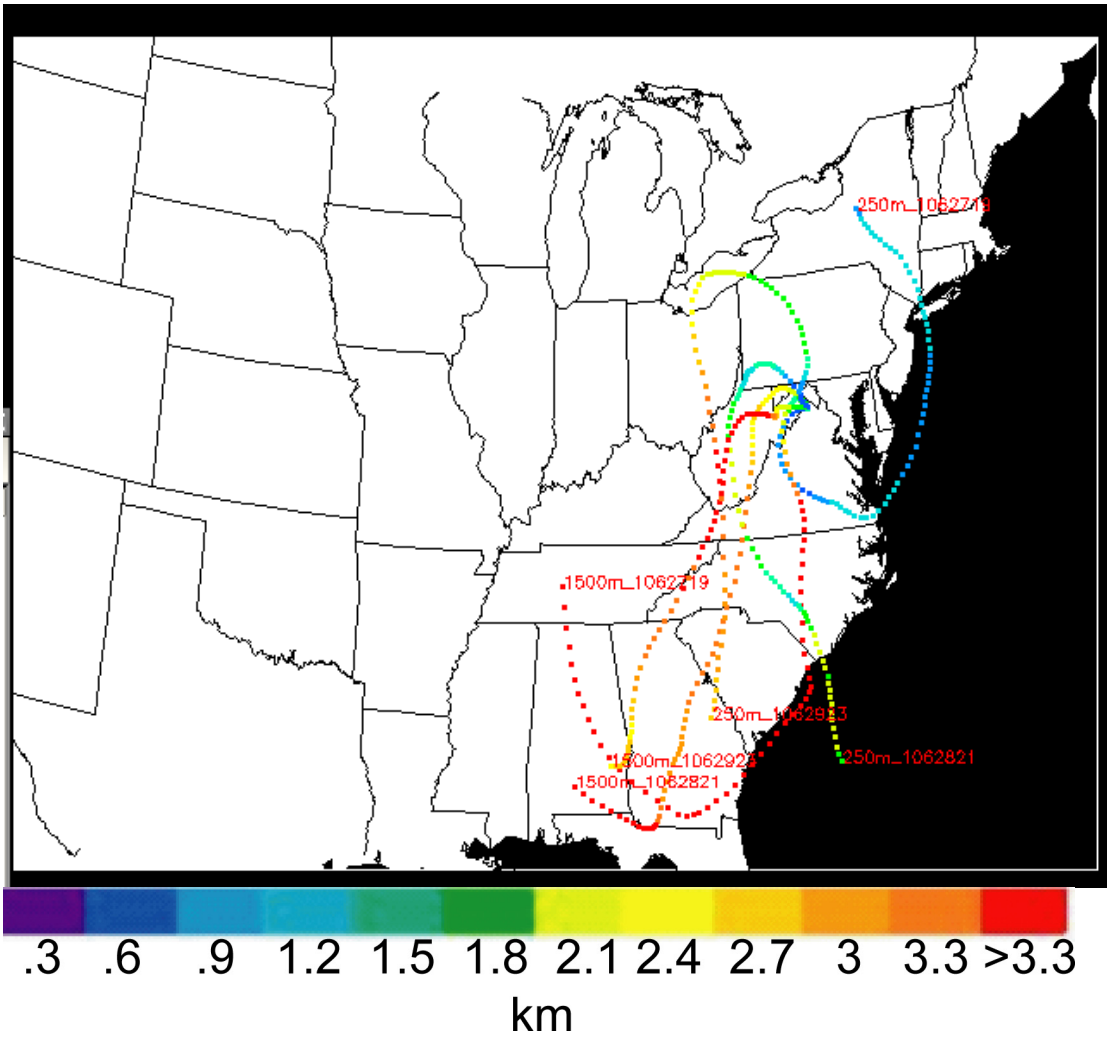

Appendix III.2. June 2001 OKV 72 h backward trajectories

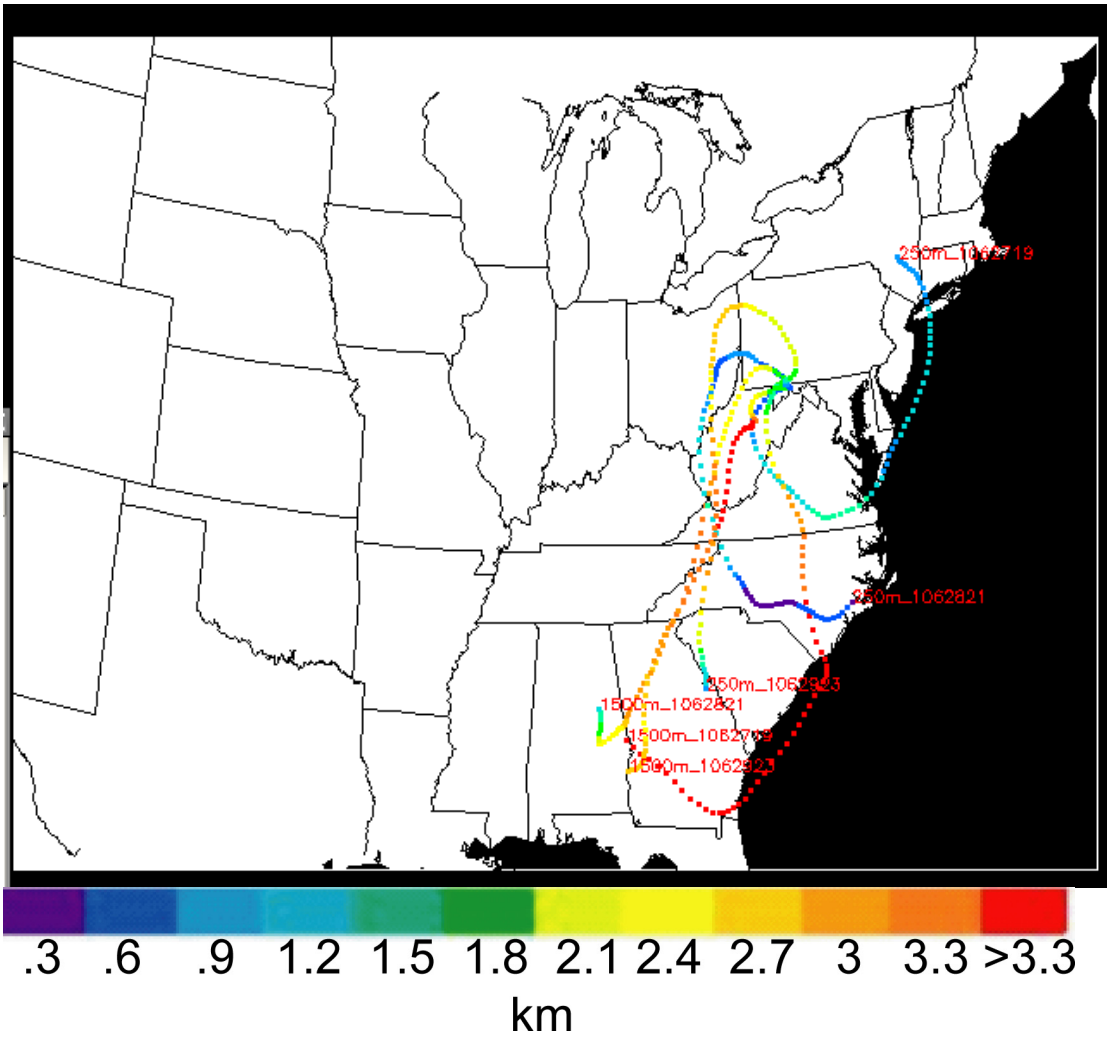

Appendix III.3. June 2001 CBE 72 h backward trajectories

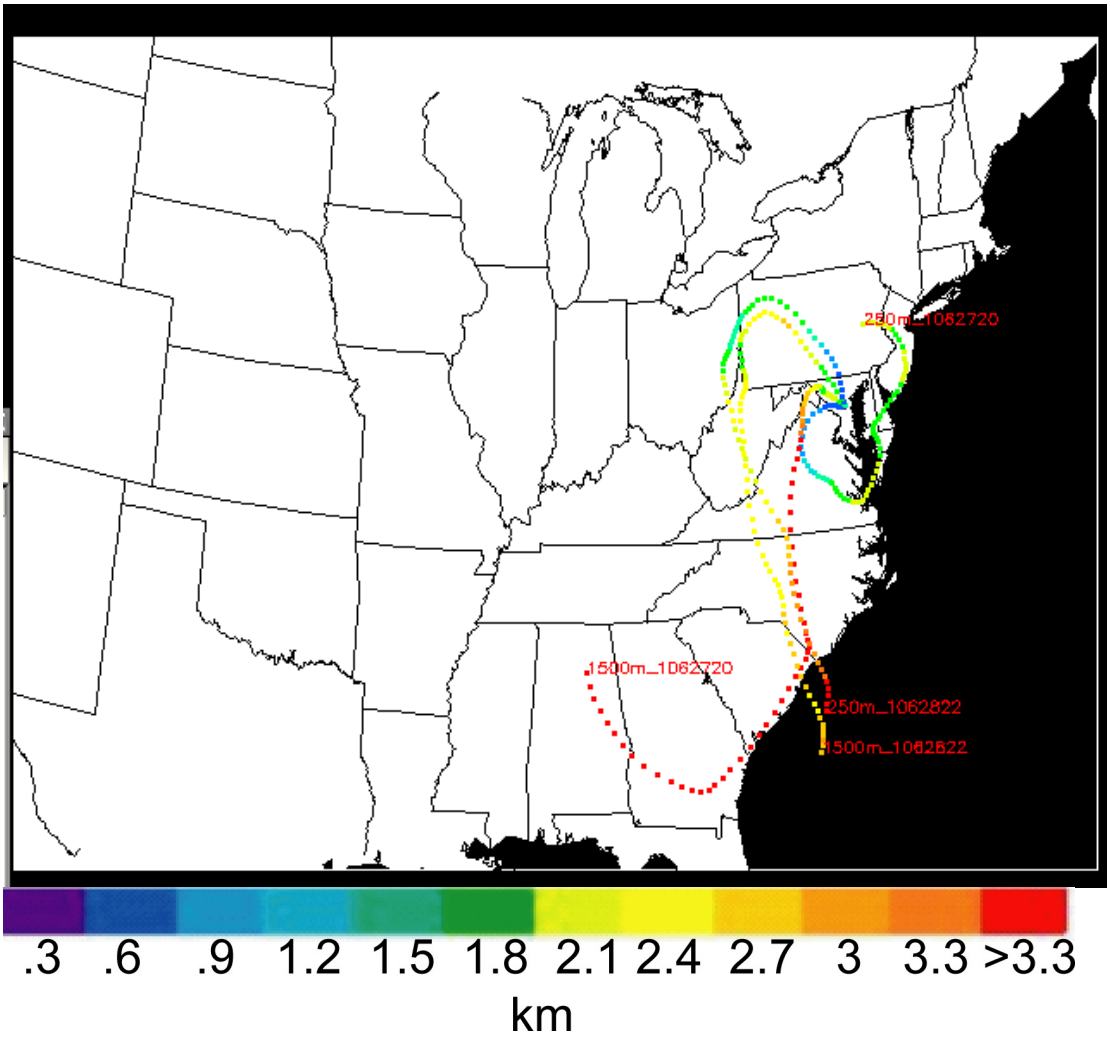

Appendix III.4. June 2001 FME 72 h backward trajectories

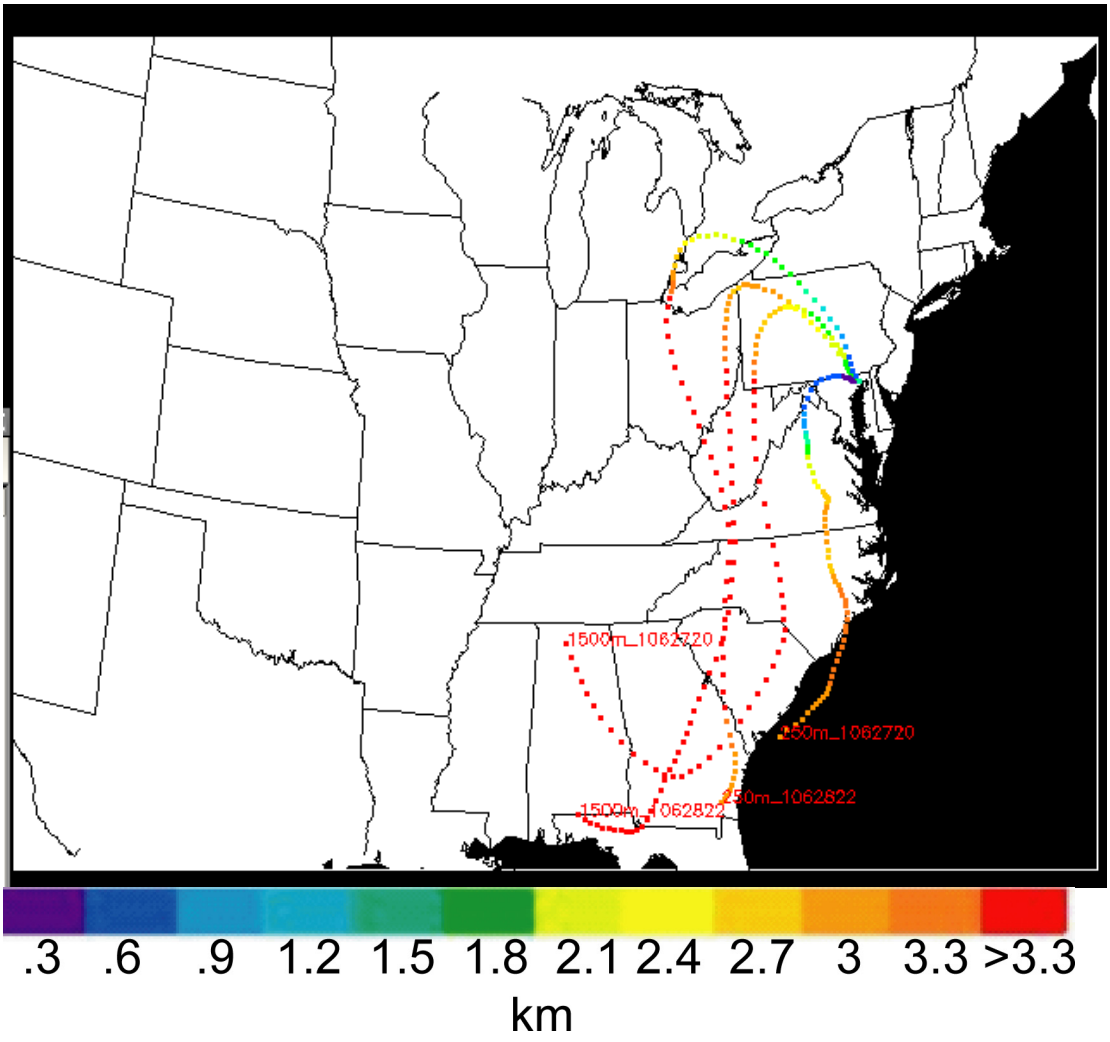

Appendix III.5. June 2001 0W3 72 h backward trajectories

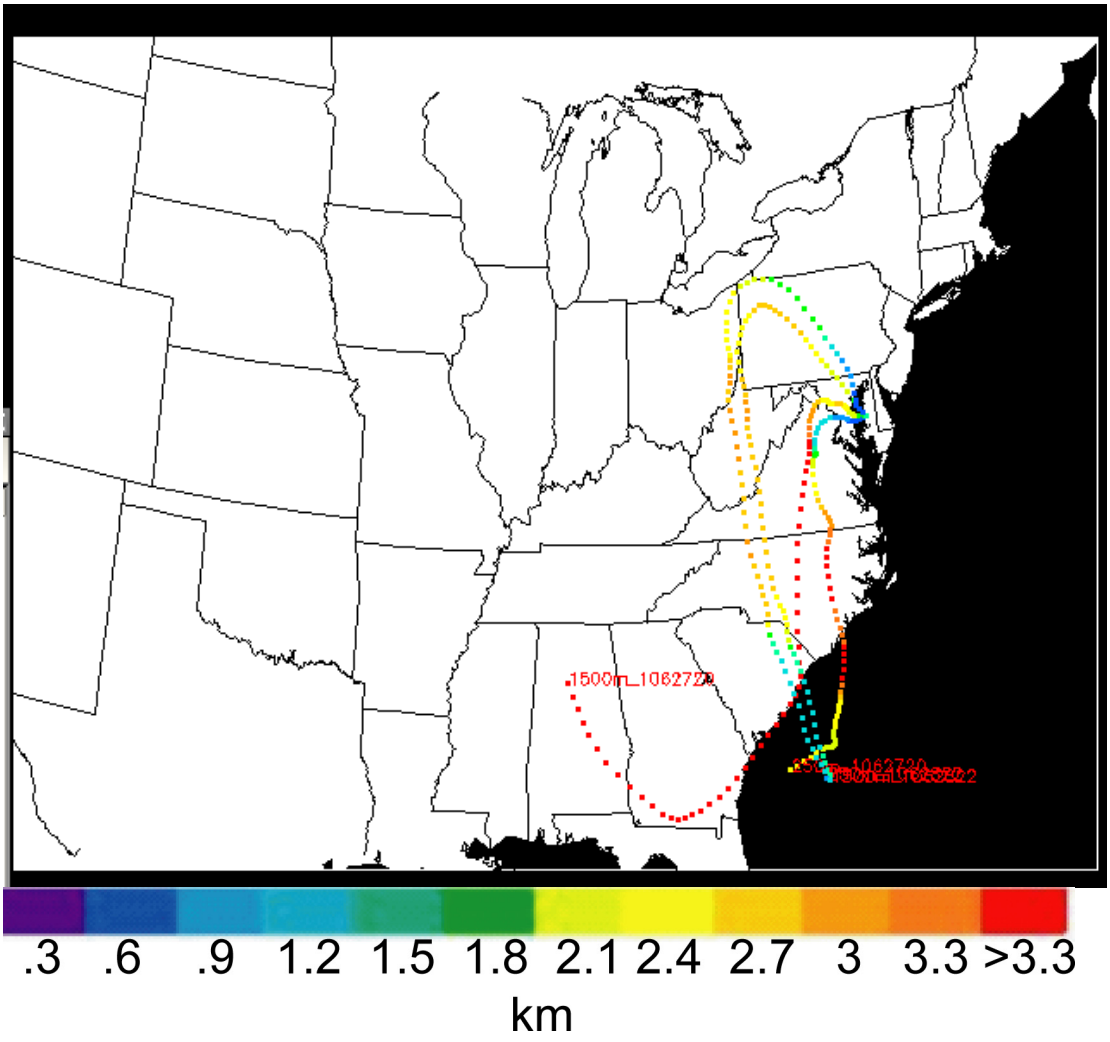

Appendix III.6. June 2001 ESN 72 h backward trajectories

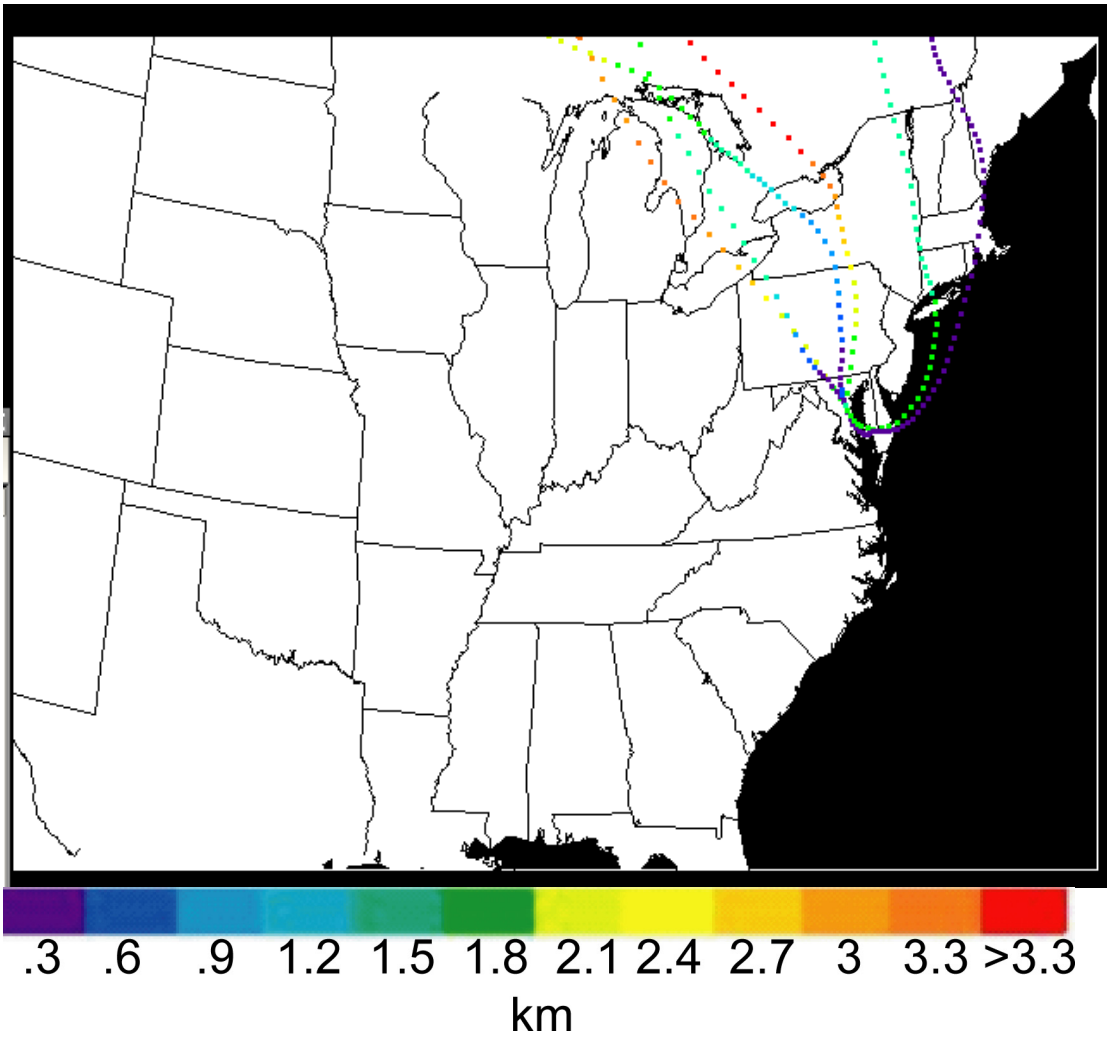

Appendix III.7. July 2001 FME 72 h backward trajectories

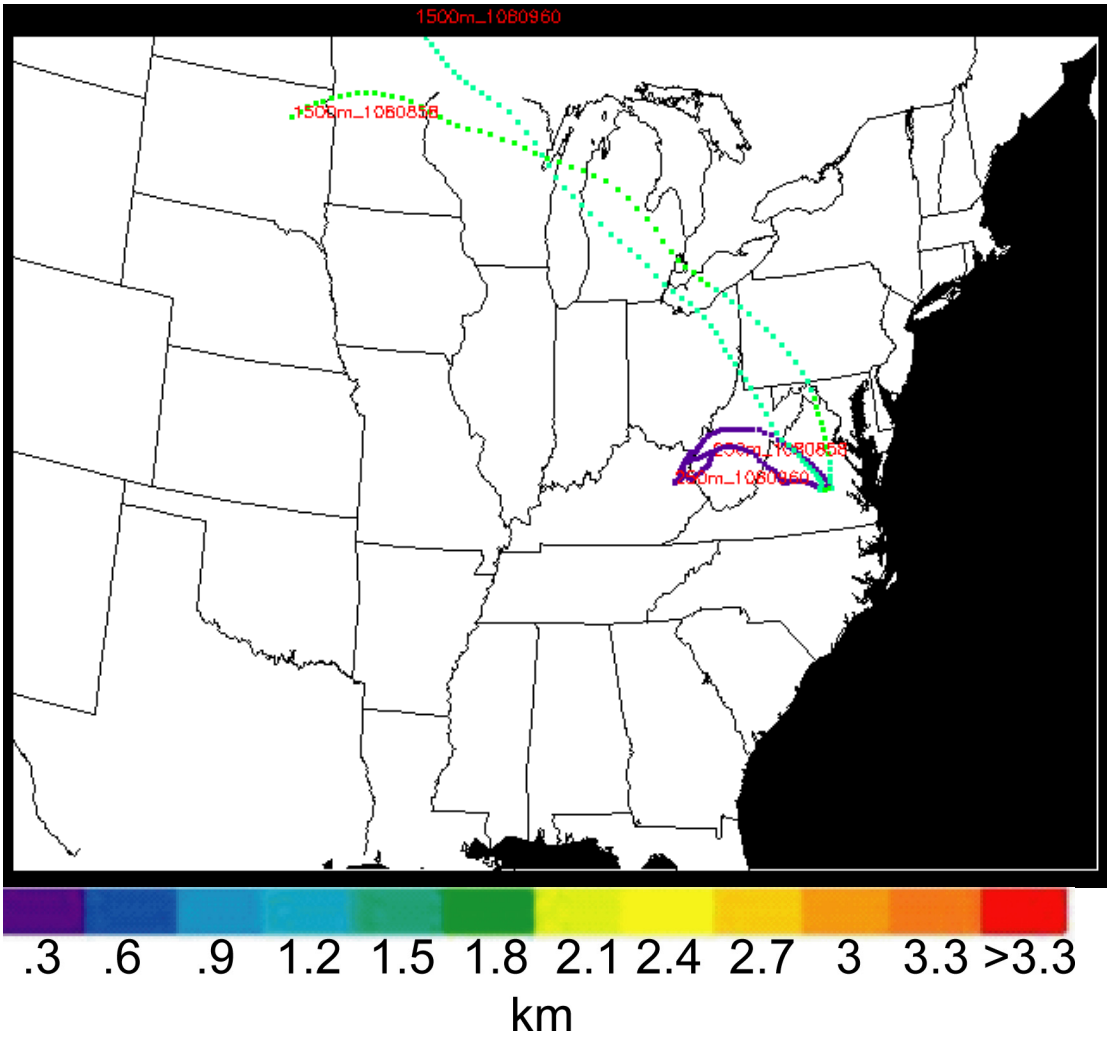

Appendix III.8. August 2001 FCI morning 72 h backward trajectories

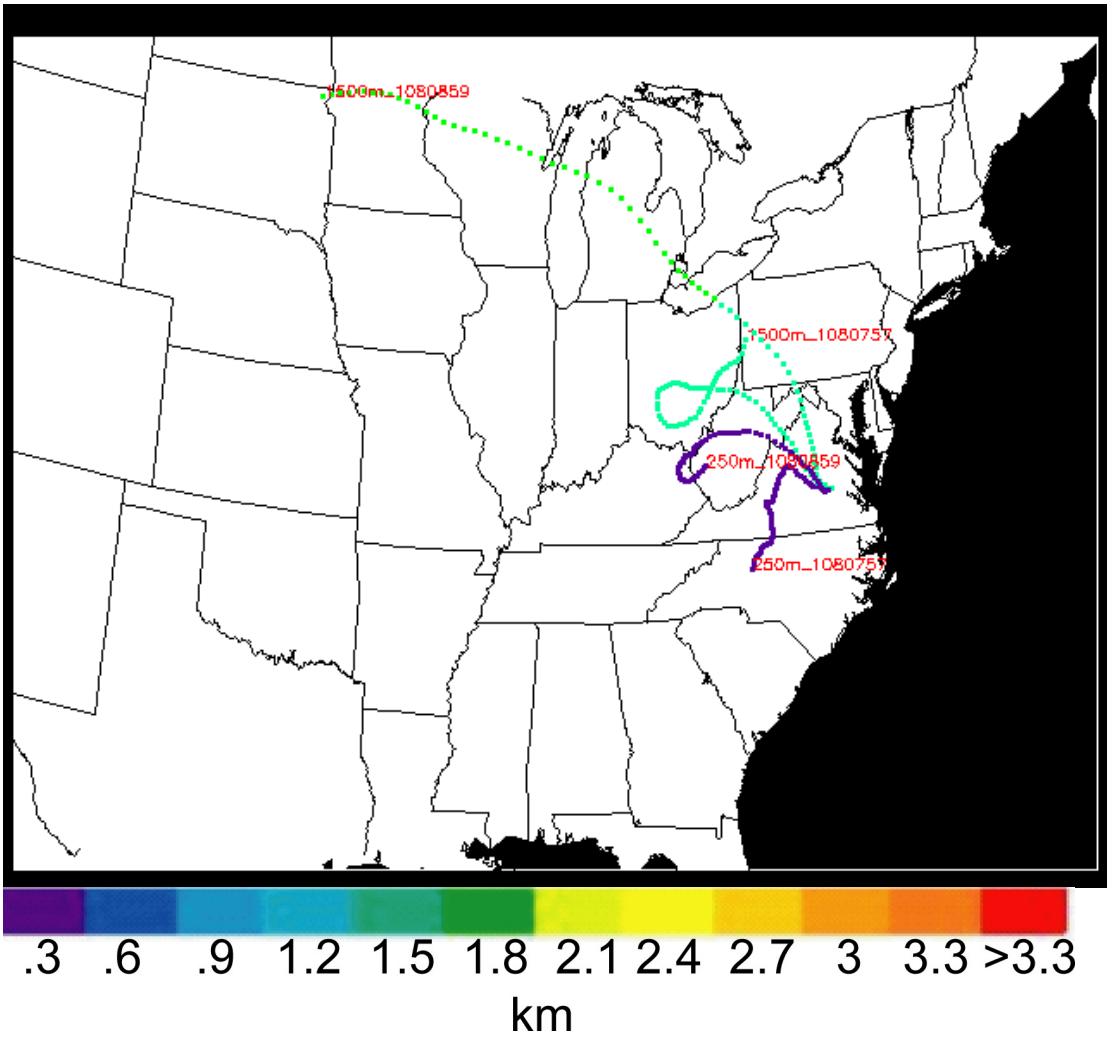

Appendix III.9. August 2001 FCI afternoon 72 h backward trajectories

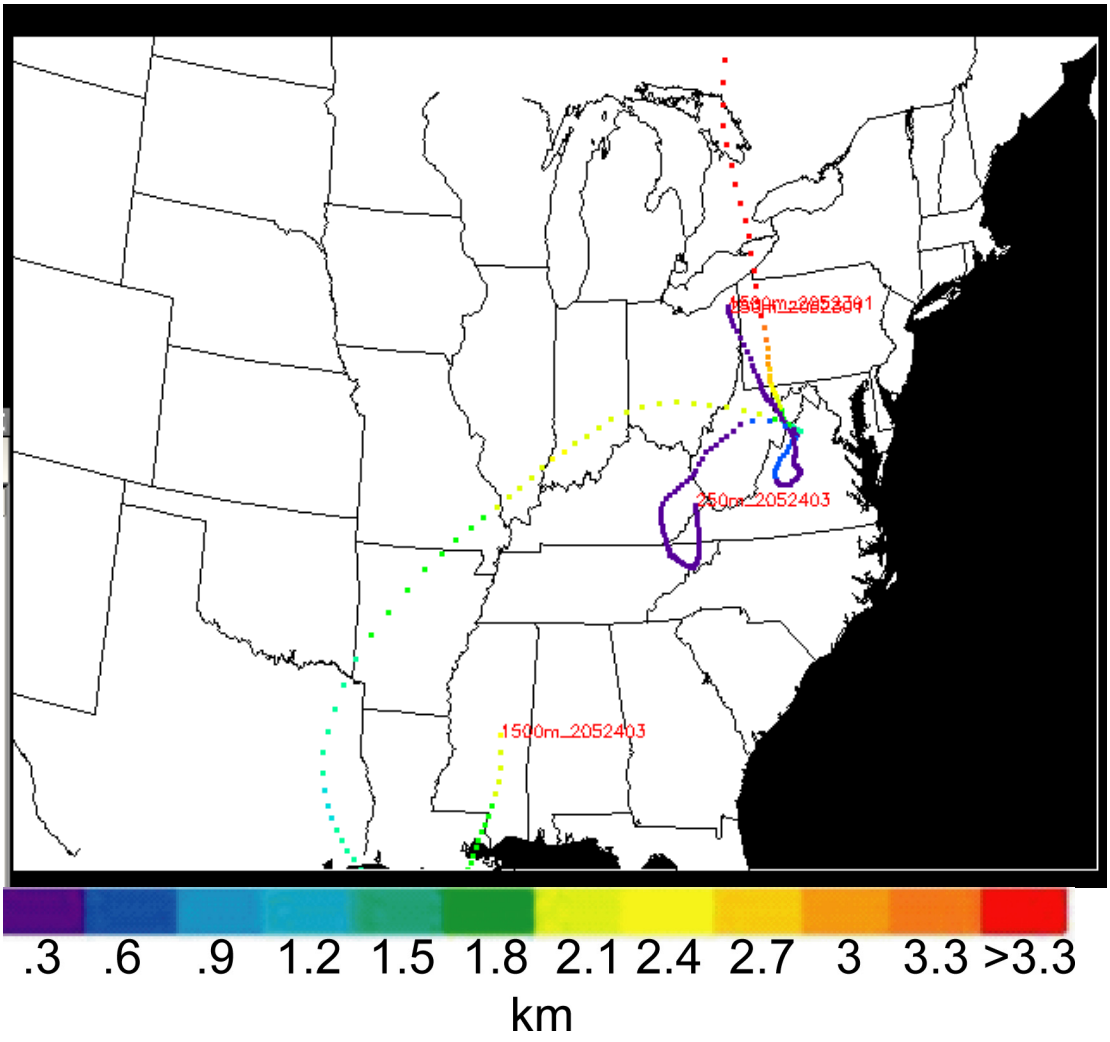

Appendix III.10. May 2002 W45 72 h backward trajectories

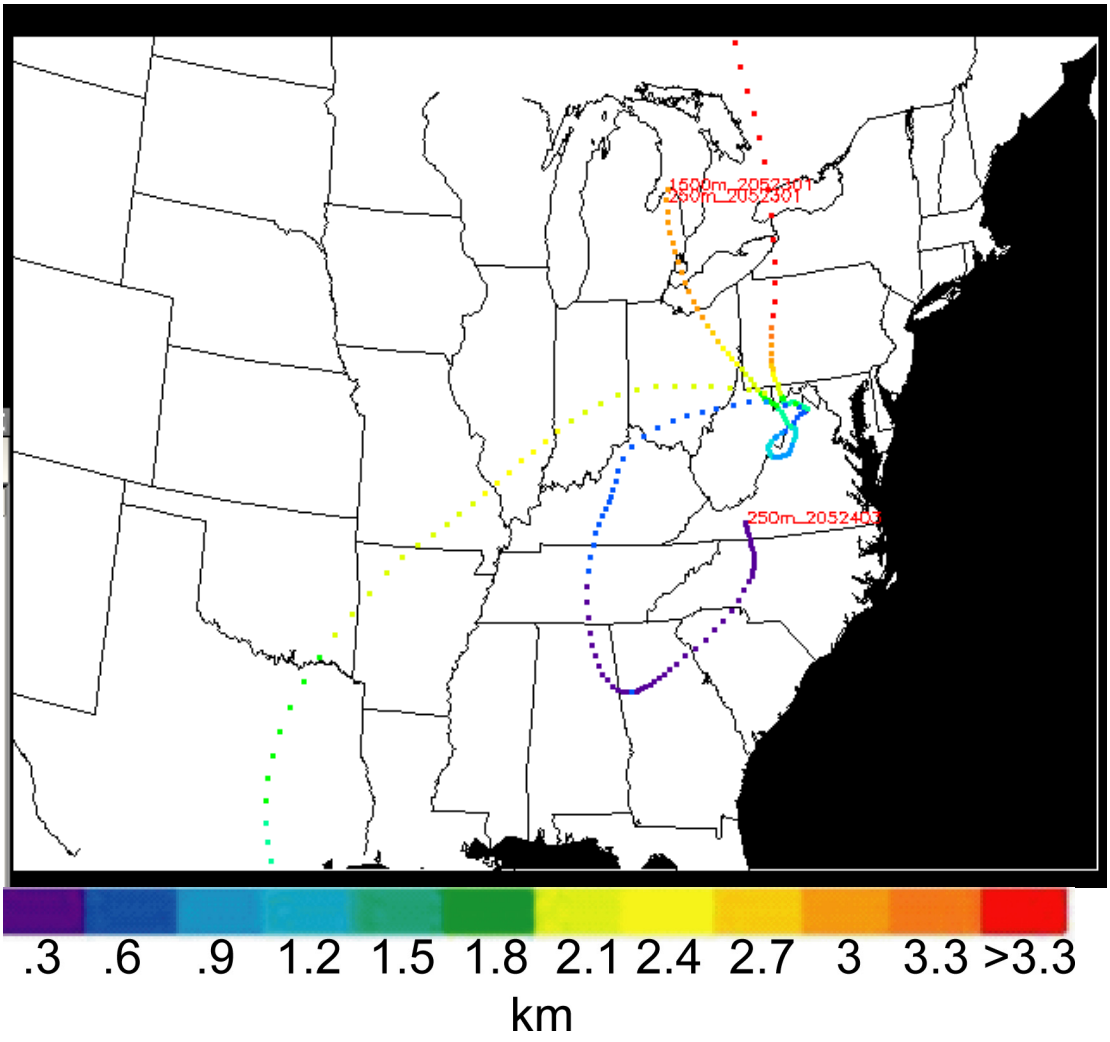

Appendix III.11. May 2002 OKV 72 h backward trajectories

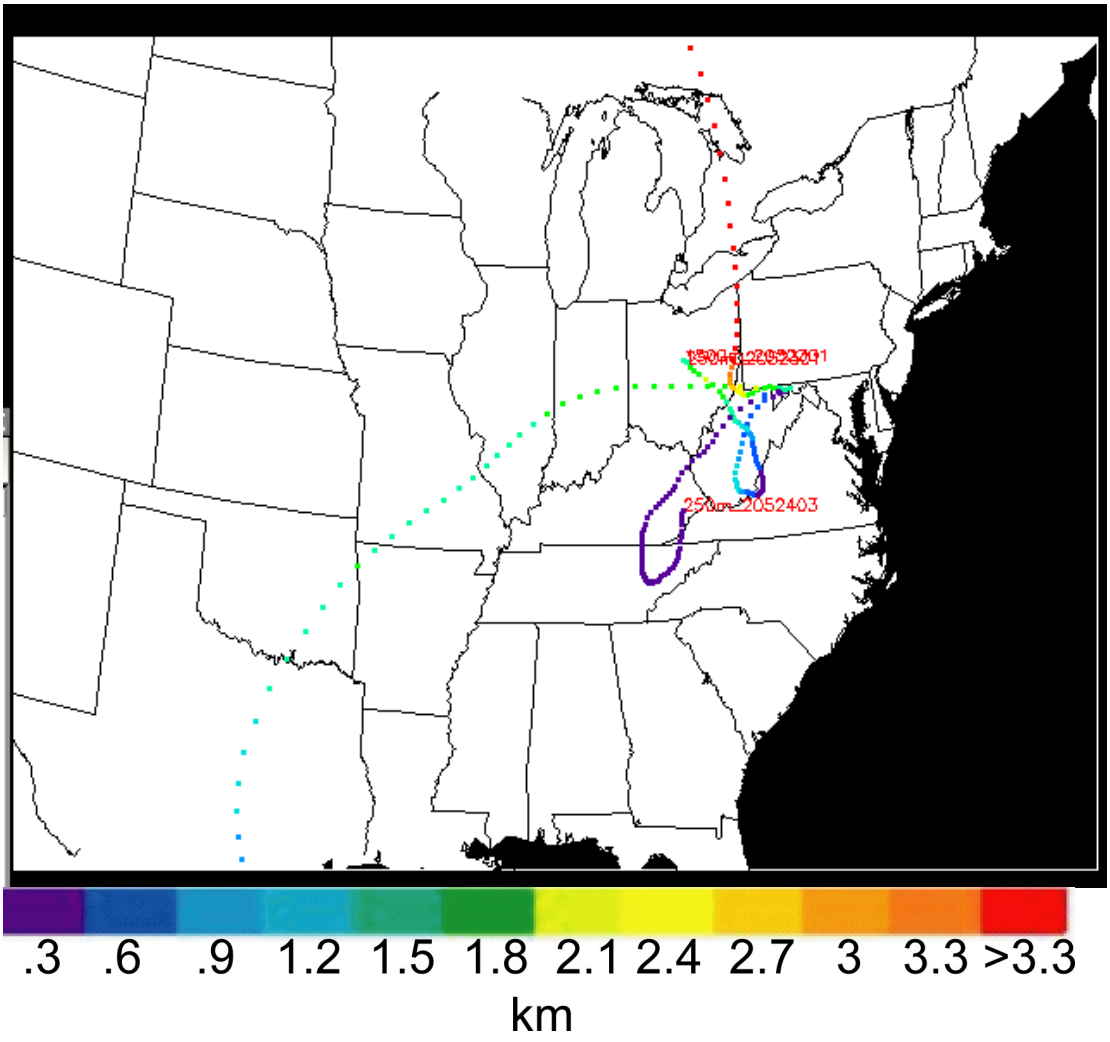

Appendix III.12. May 2002 CBE 72 h backward trajectories

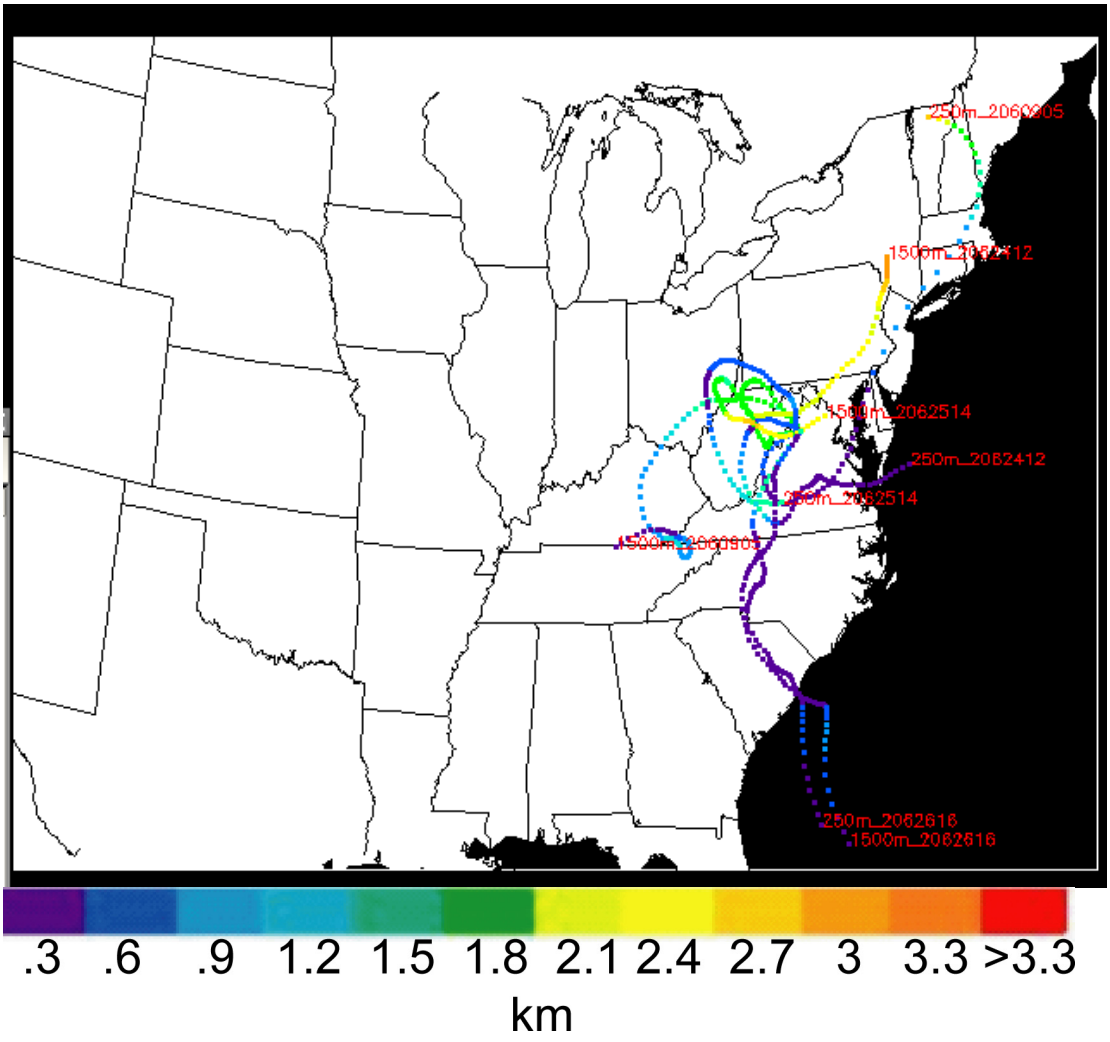

Appendix III.13. June 2002 W45 72 h backward trajectories

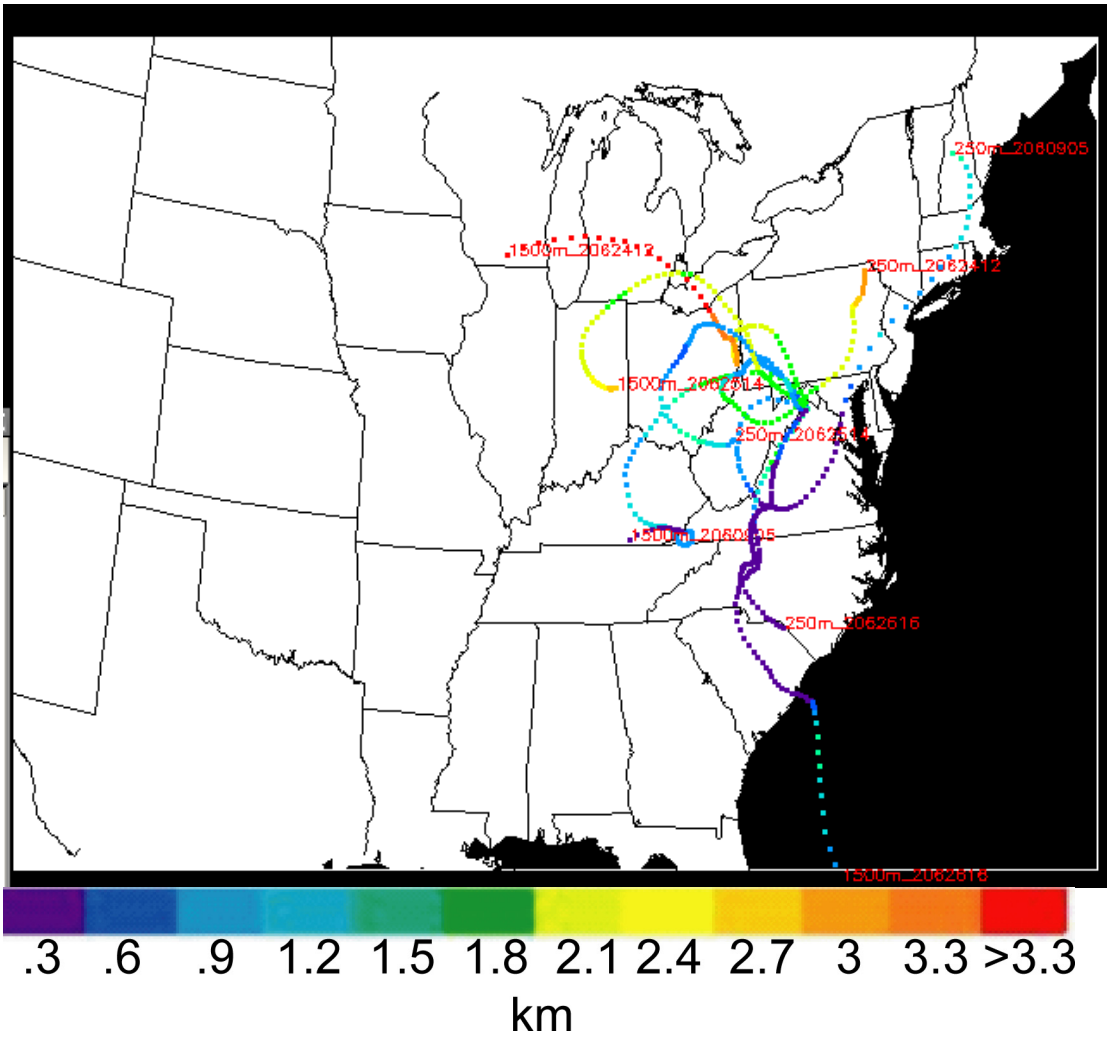

Appendix III.14. June 2002 OKV 72 h backward trajectories

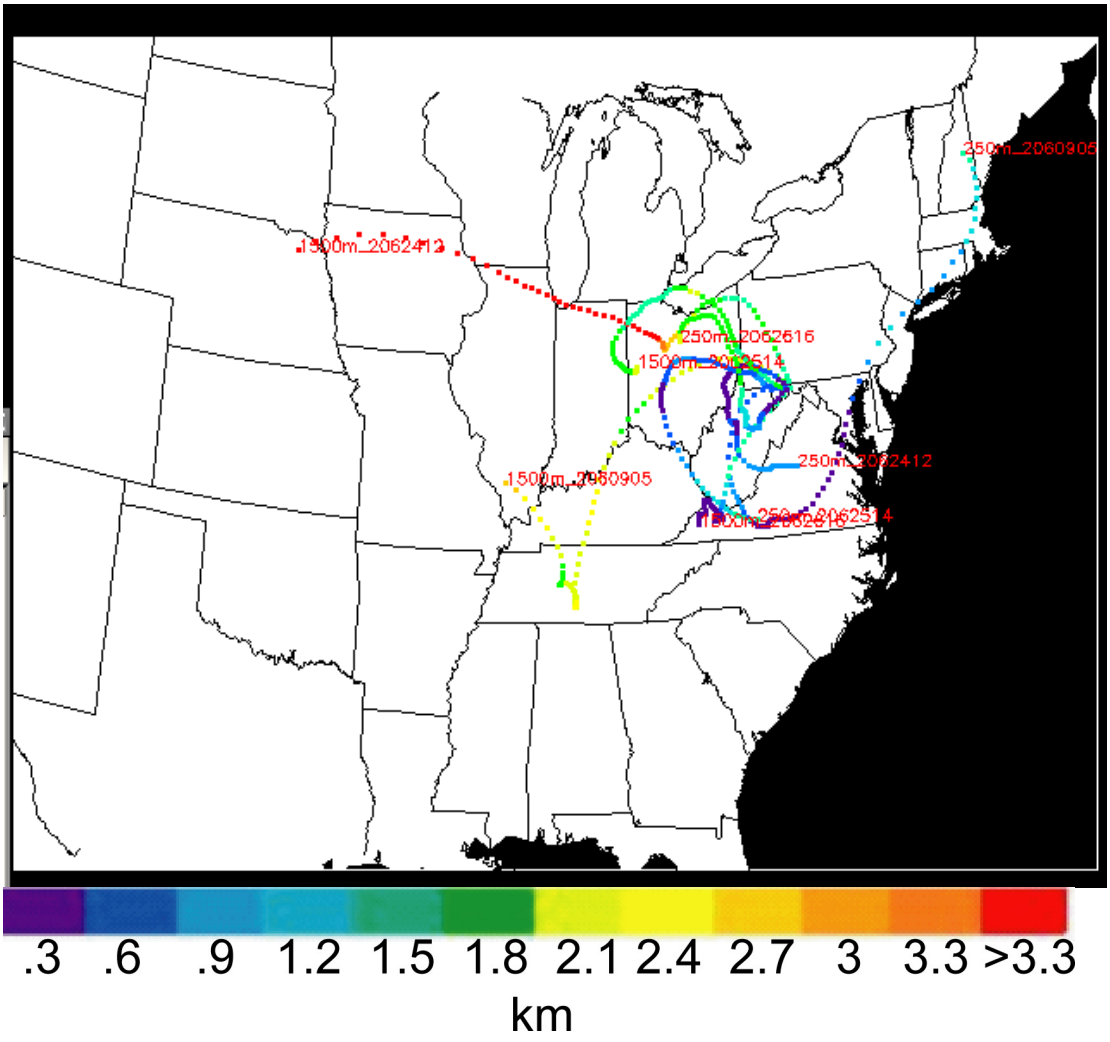

Appendix III.15. June 2002 CBE 72 h backward trajectories

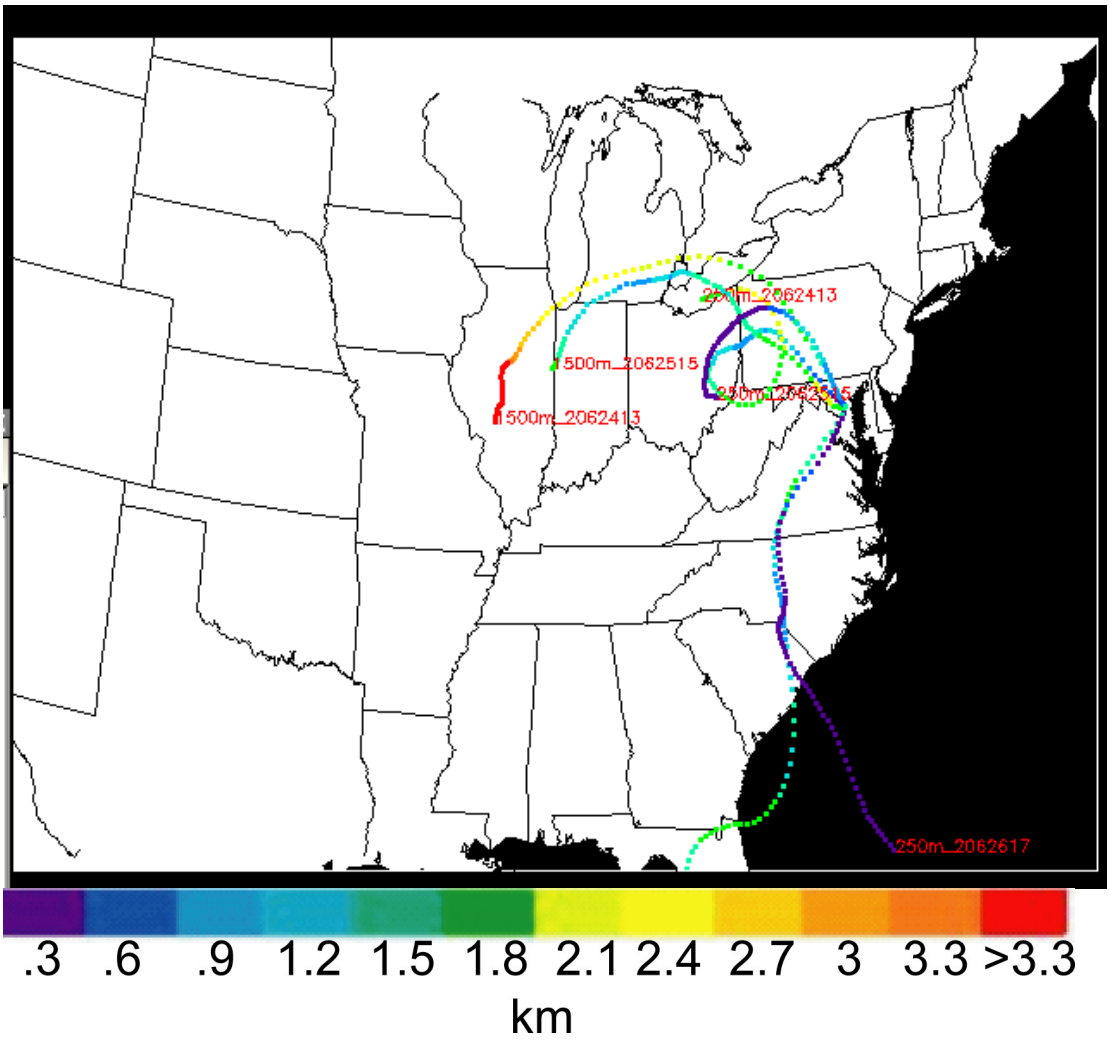

Appendix III.16. June 2002 FME 72 h backward trajectories

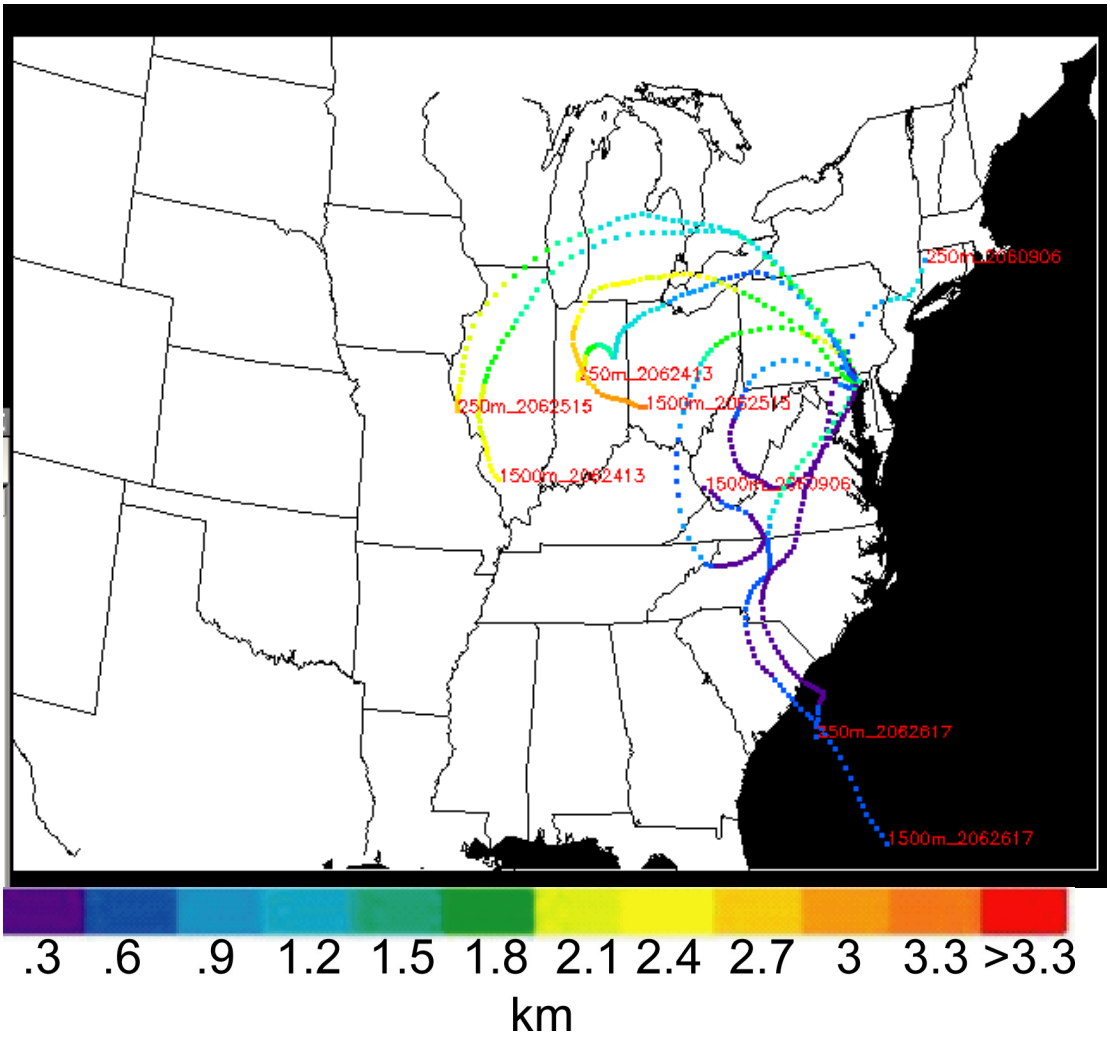

Appendix III.17. June 2002 0W3 72 h backward trajectories

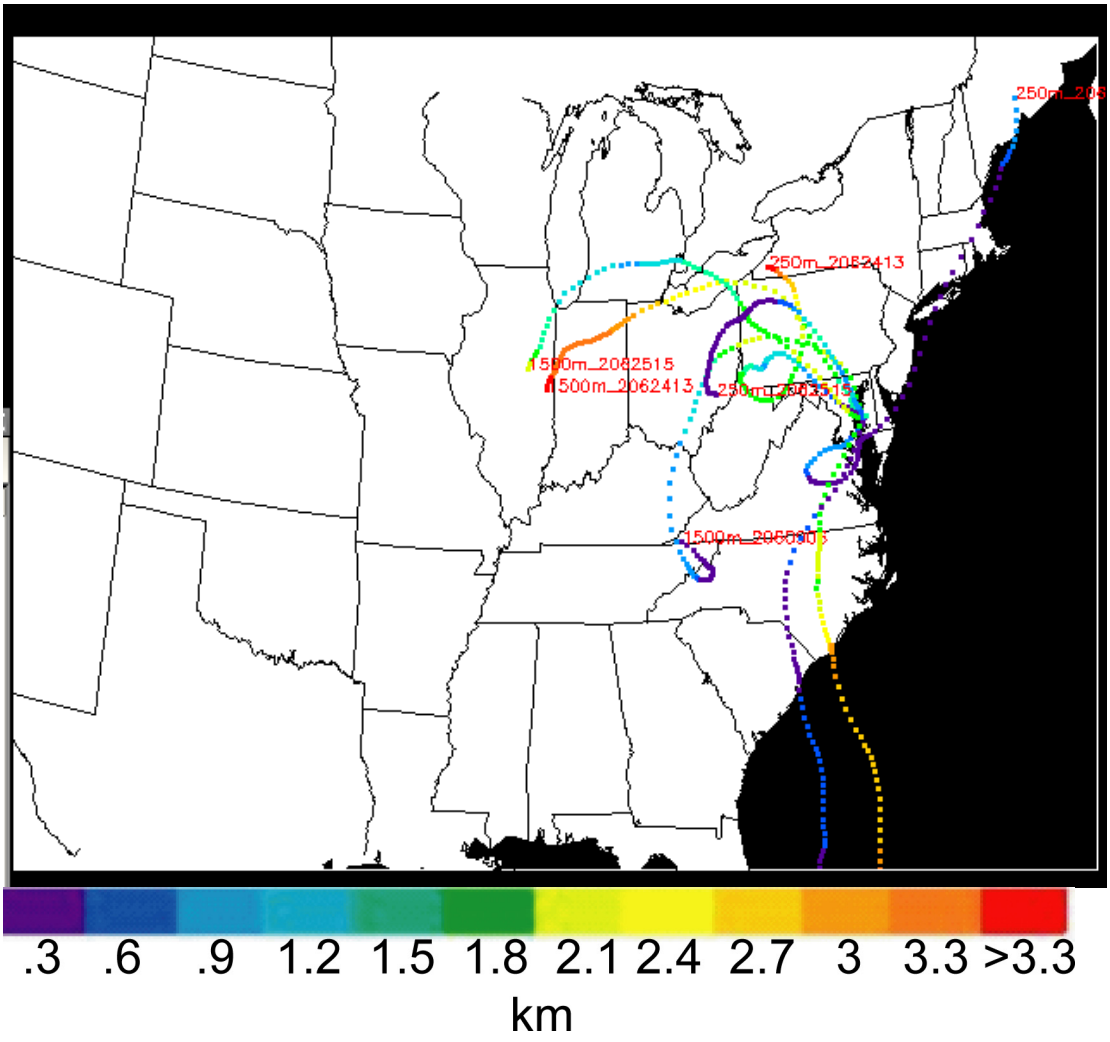

Appendix III.18. June 2002 ESN 72 h backward trajectories

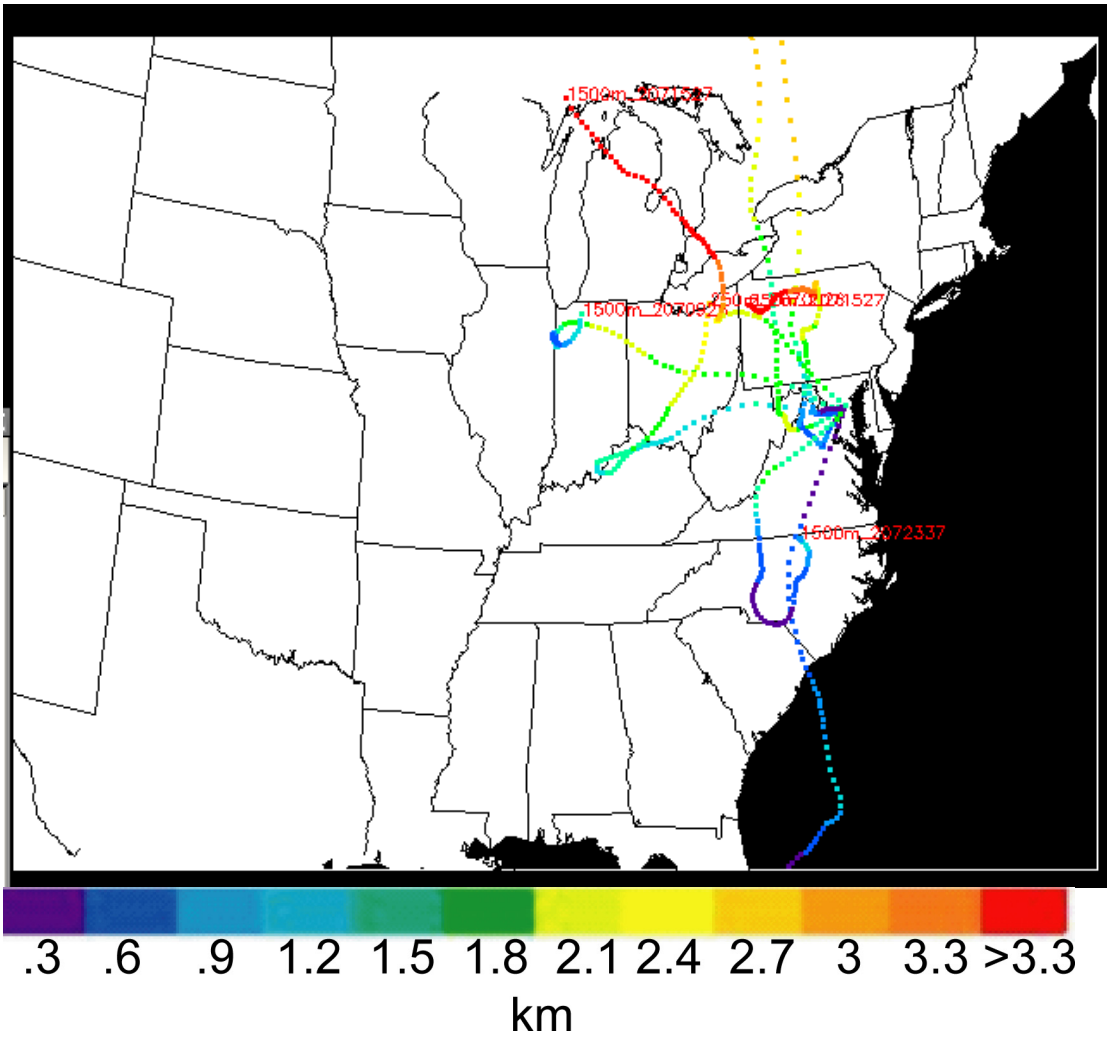

Appendix III.19. July 2002 FME 72 h backward trajectories

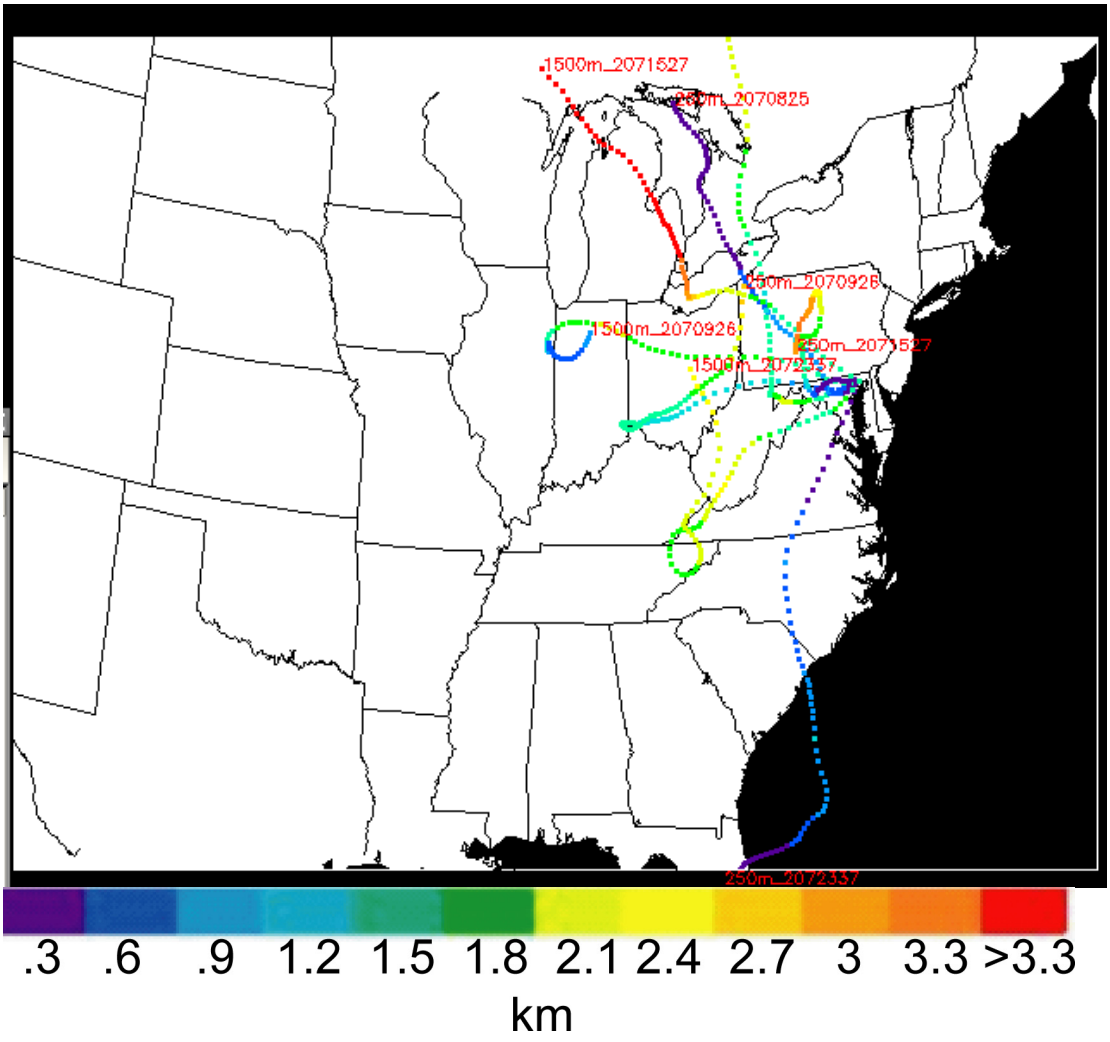

Appendix III.20. July 2002 0W3 72 h backward trajectories

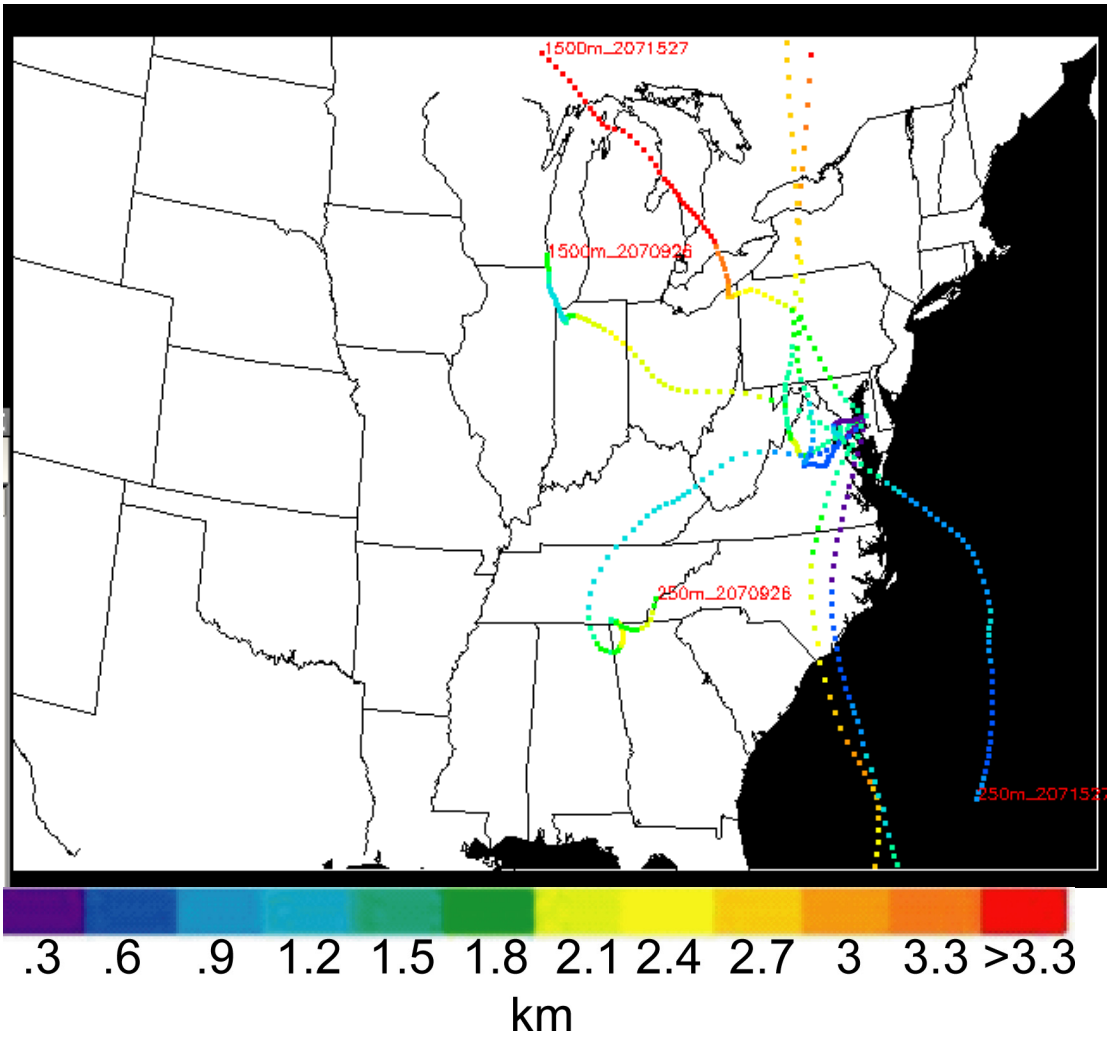

Appendix III.21. July 2002 ESN 72 h backward trajectories

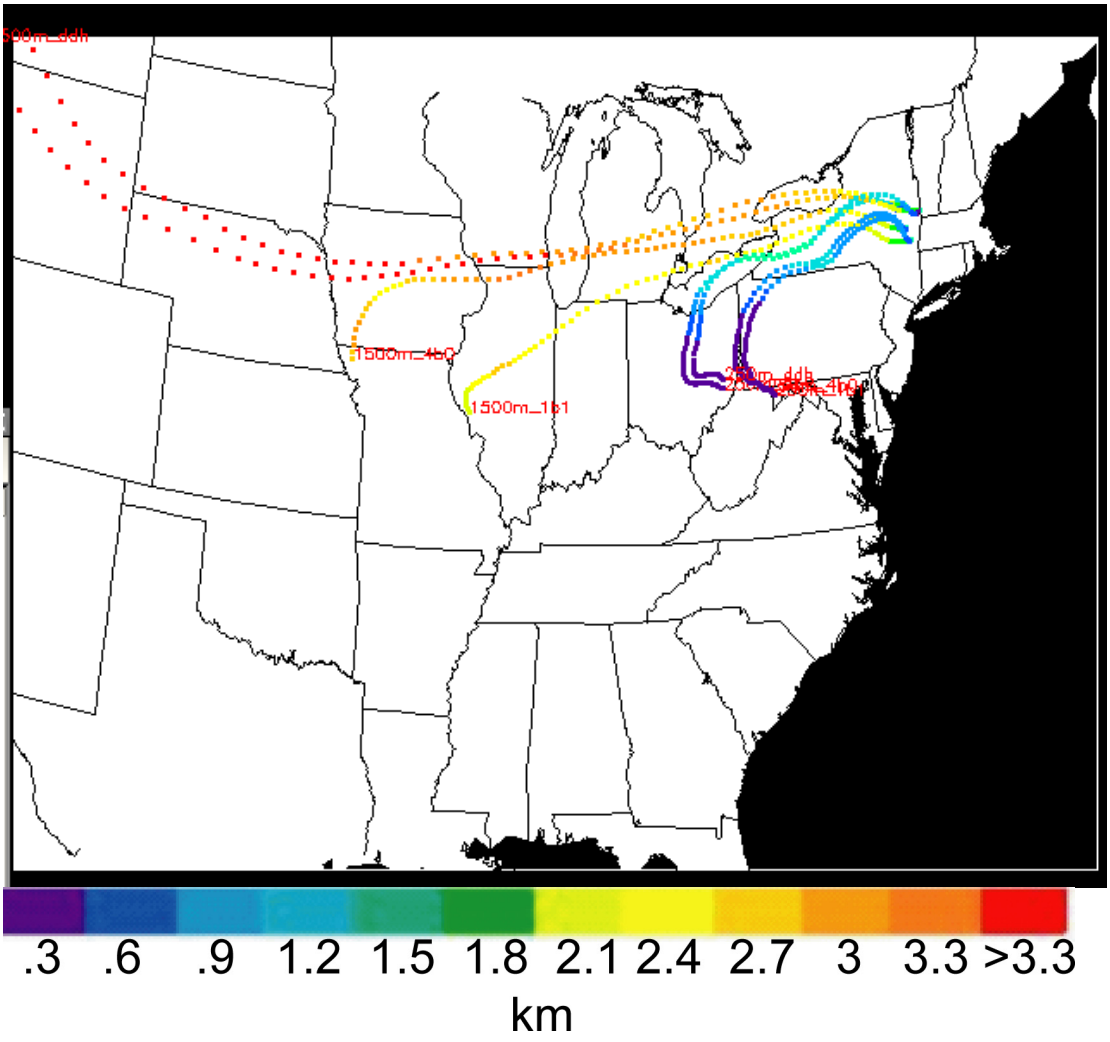

Appendix III.22. 12 August 2002 Northeast morning 72 h backward trajectories

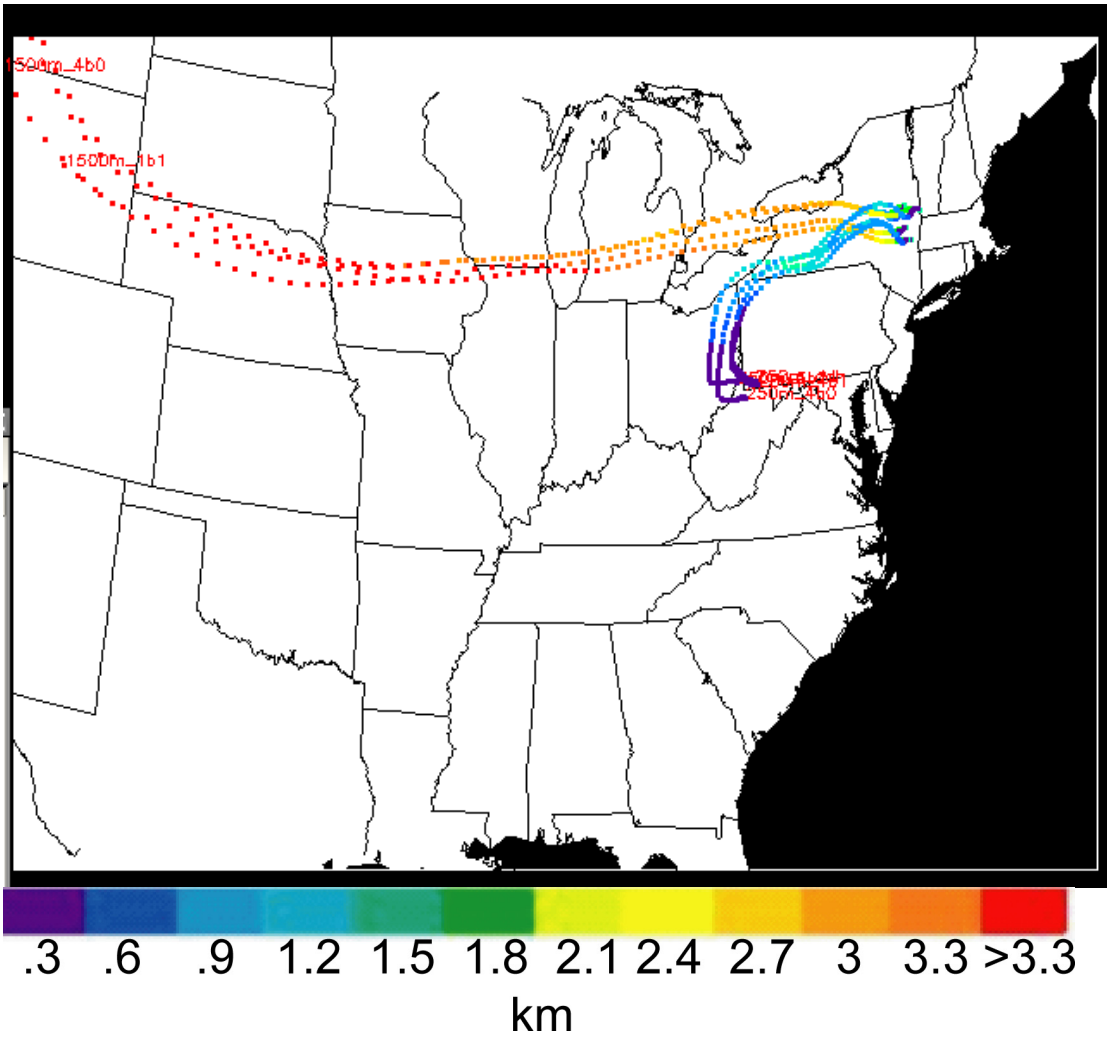

Appendix III.23. 12 August 2002 Northeast afternoon 72 h backward trajectories

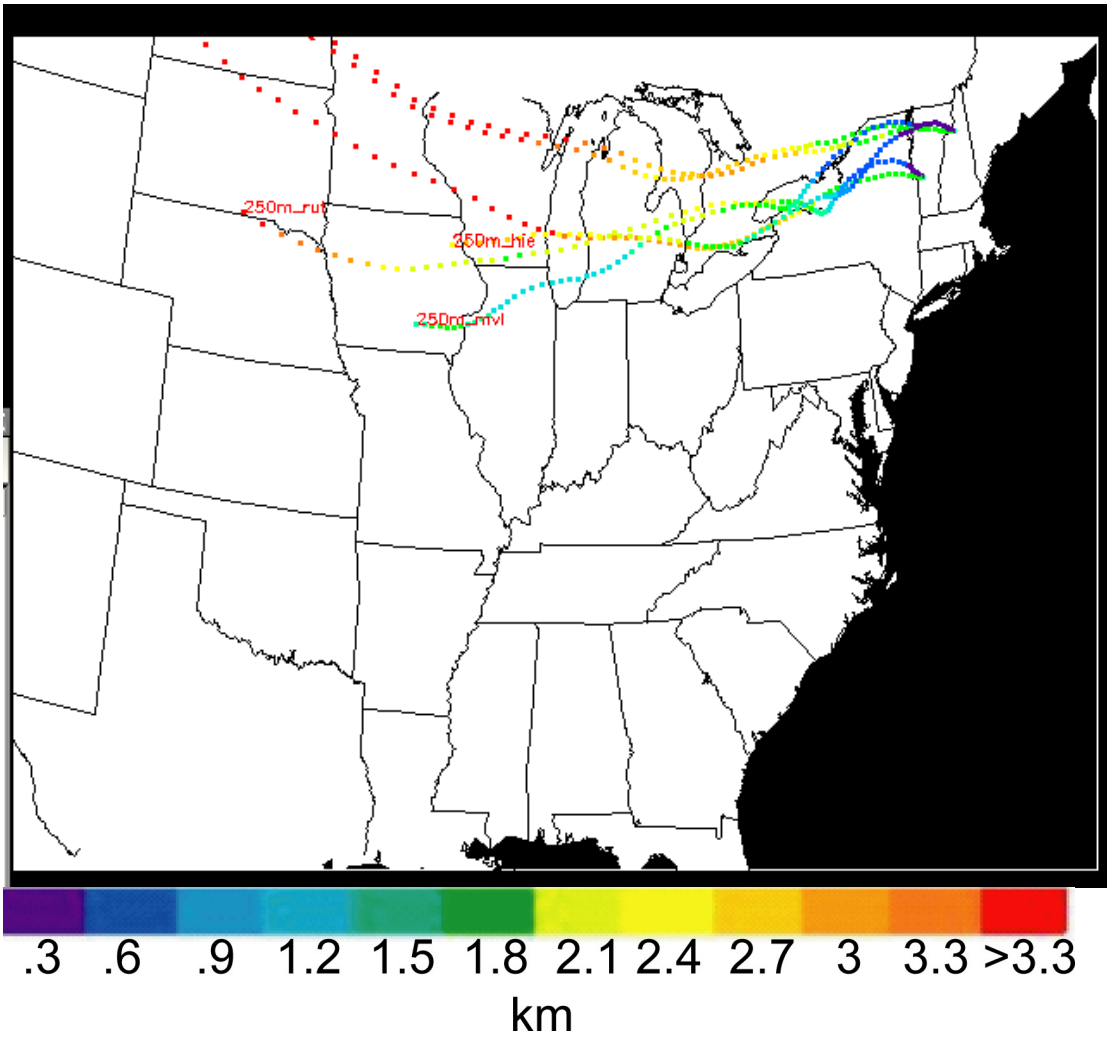

Appendix III.24. 13 August 2002 Northeast morning 72 h backward trajectories

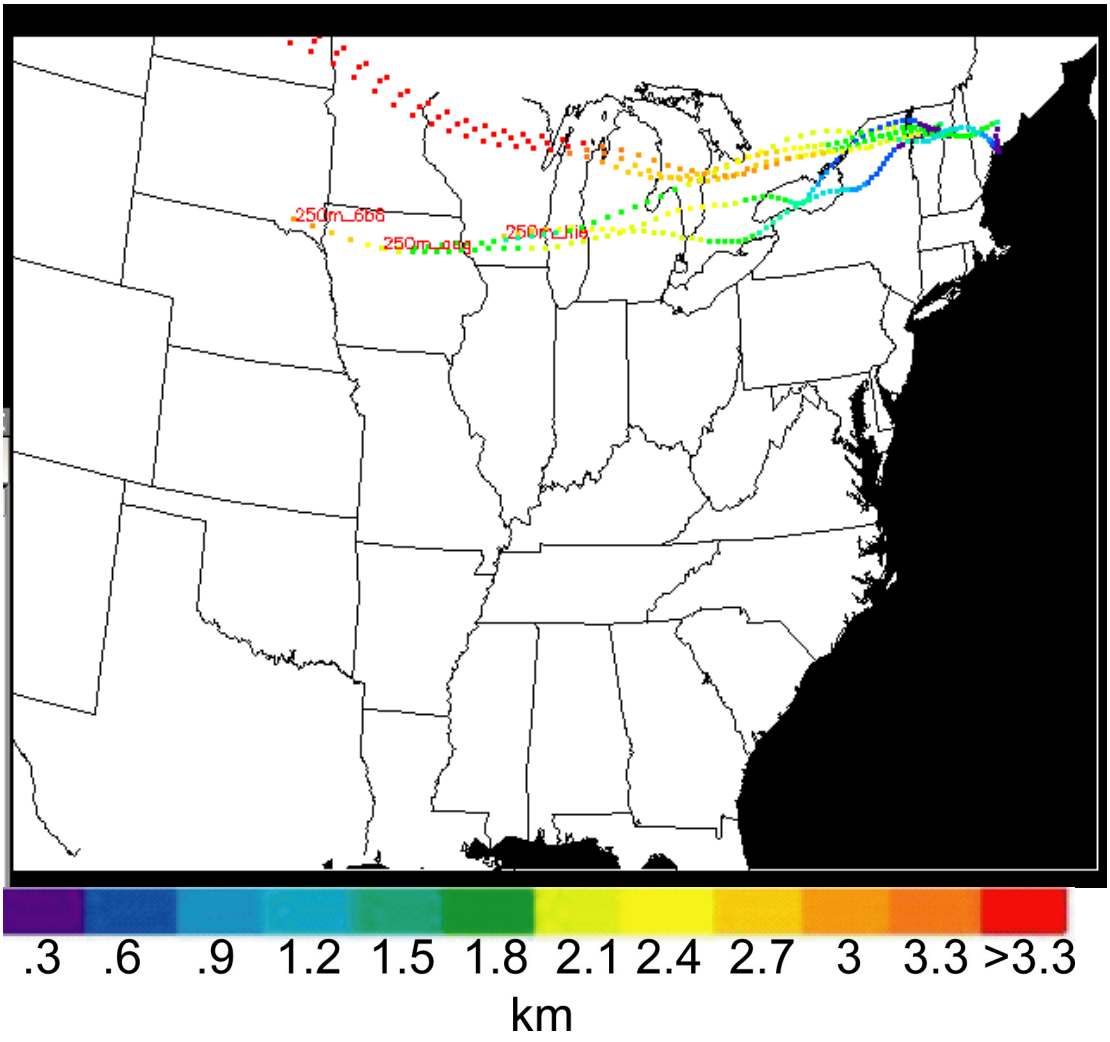

Appendix III.25. 13 August 2002 Northeast afternoon 72 h backward trajectories

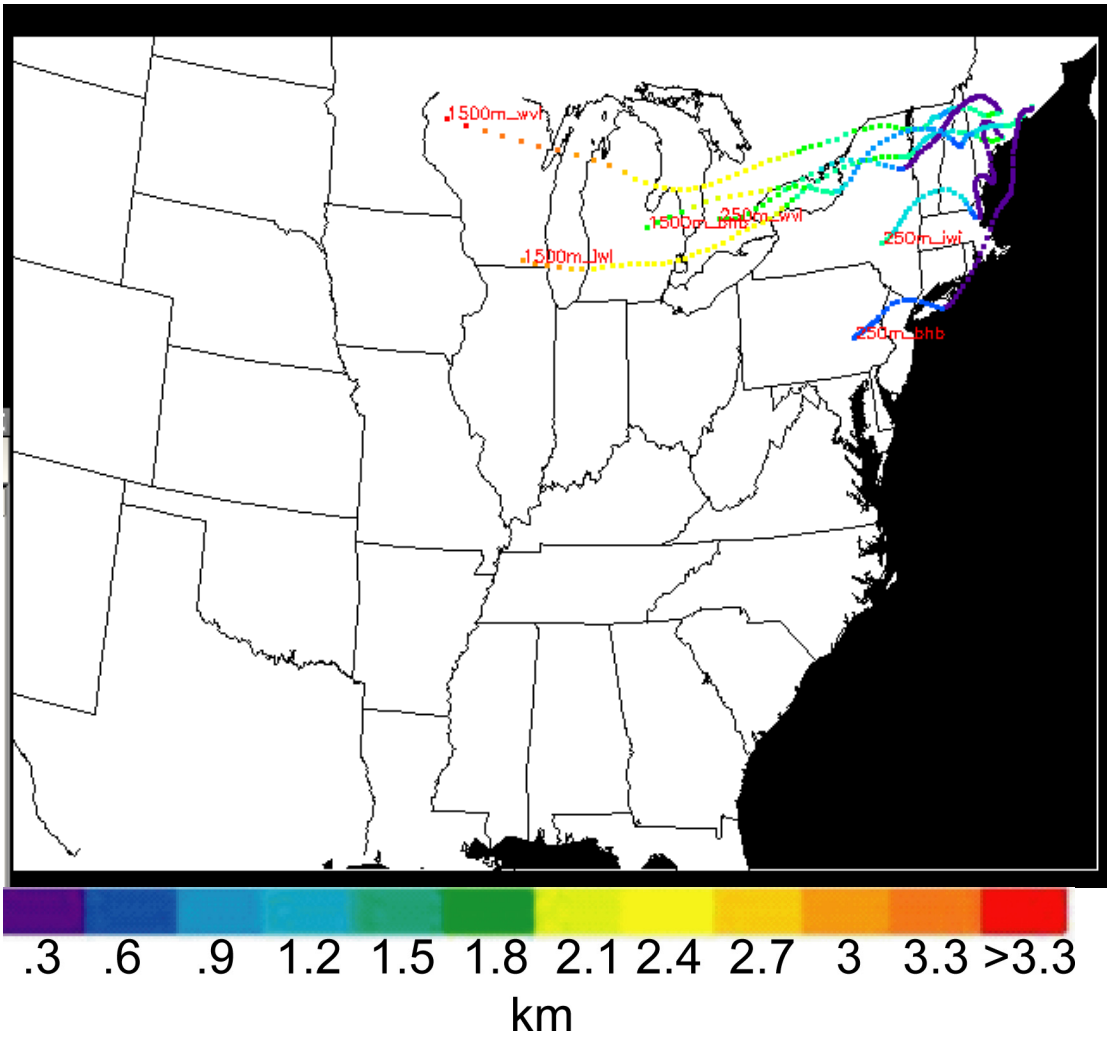

Appendix III.26. 14 August 2002 Northeast morning 72 h backward trajectories

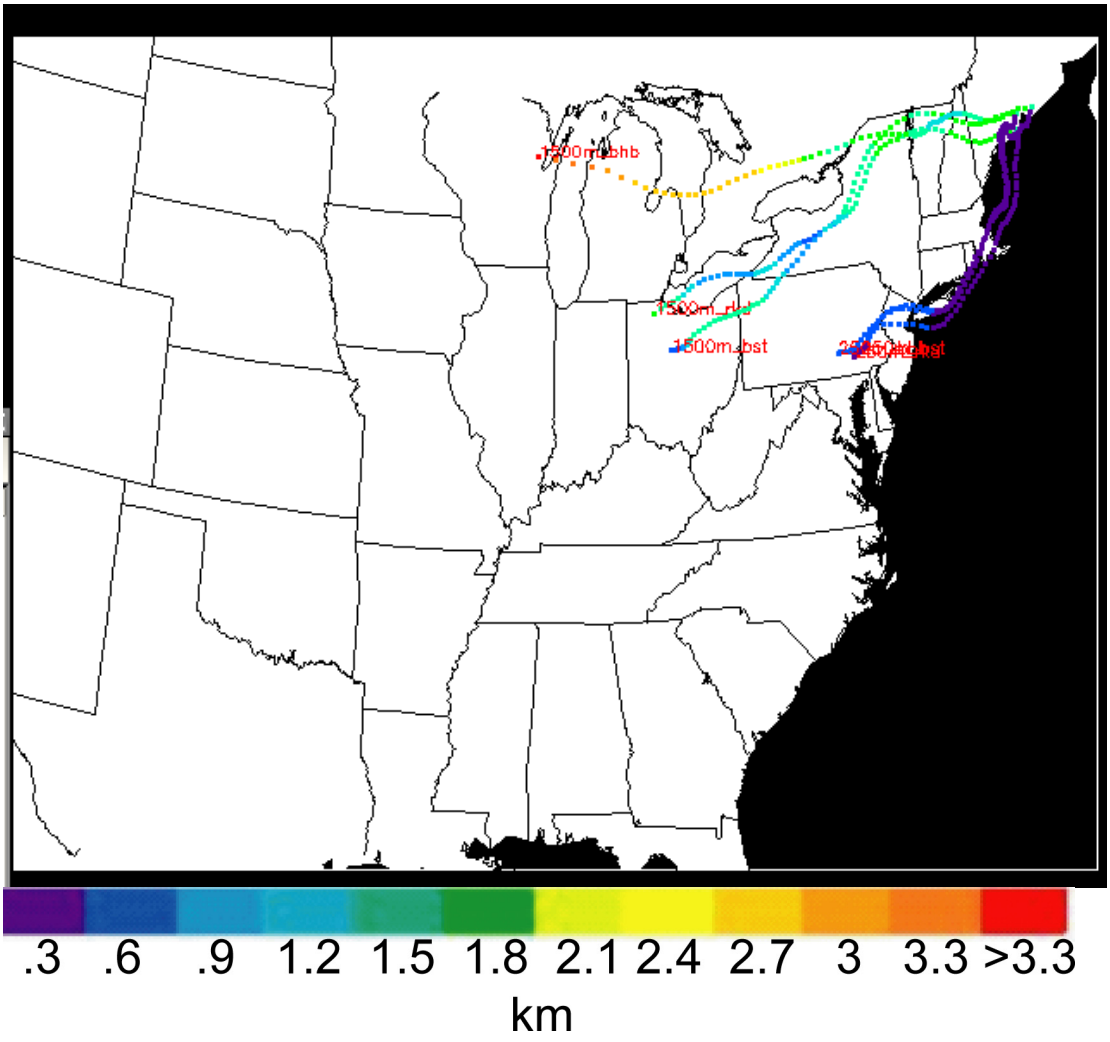

Appendix III.27. 14 August 2002 Northeast afternoon 72 h backward trajectories

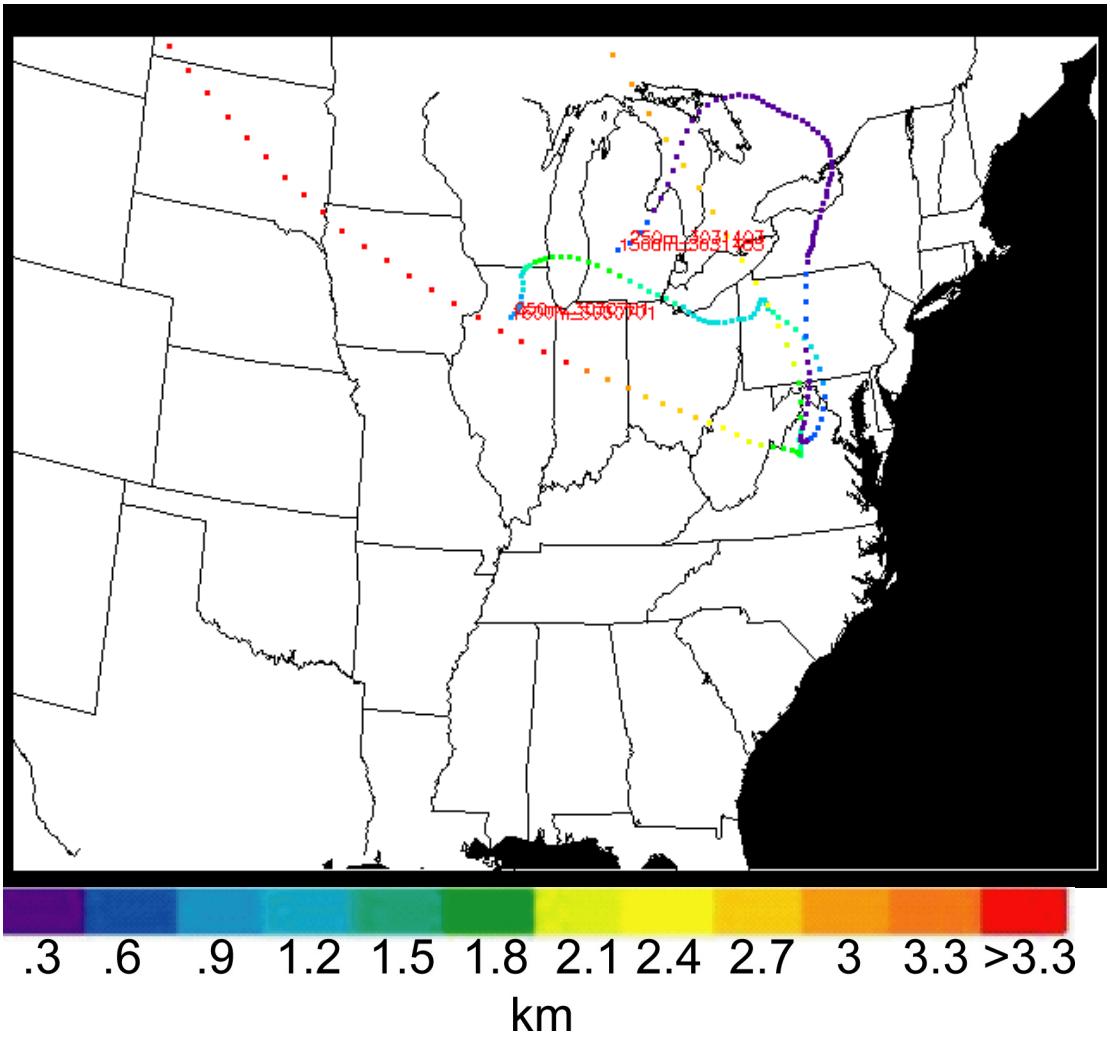

Appendix III.28. March 2003 W45 72 h backward trajectories

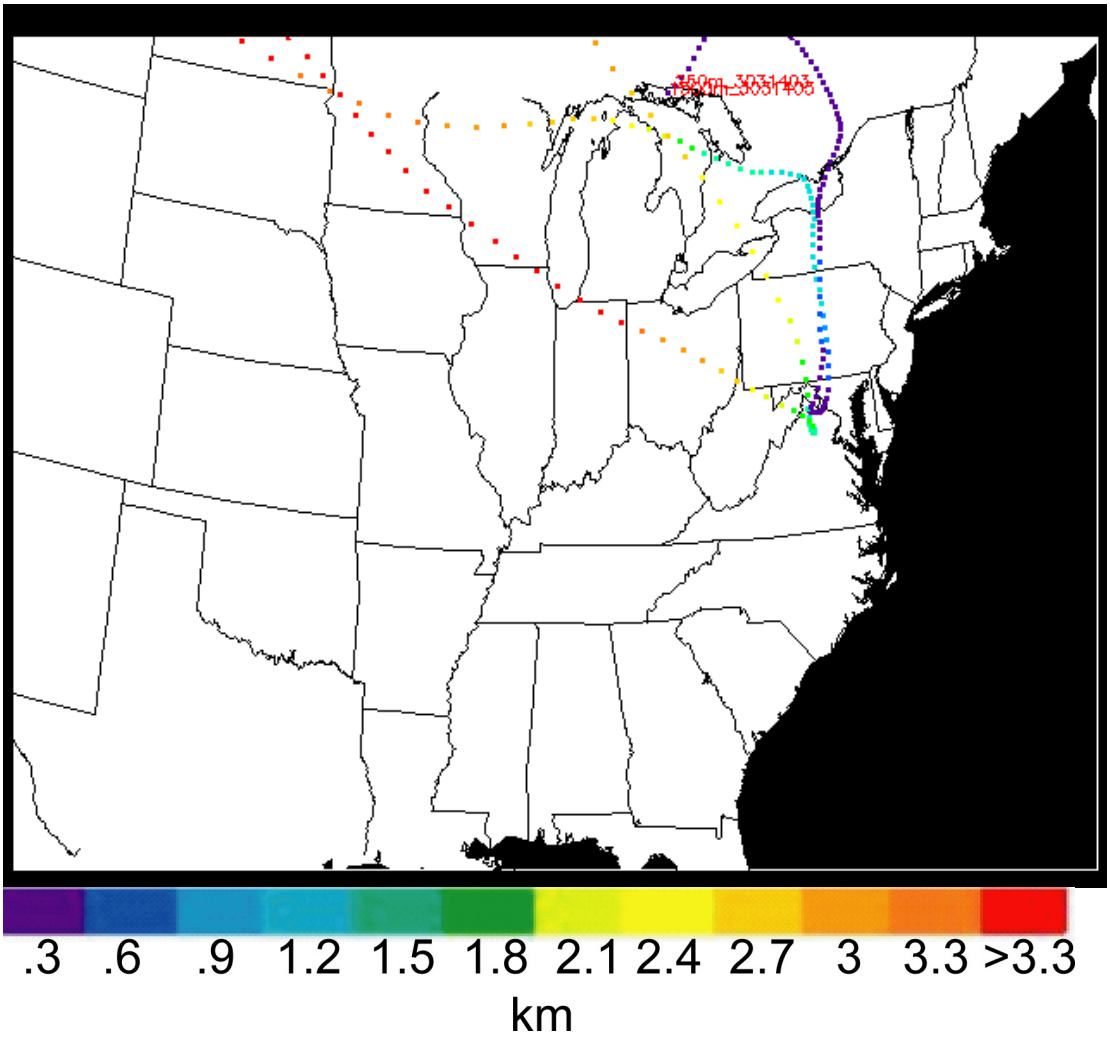

Appendix III.29. March 2003 OKV 72 h backward trajectories

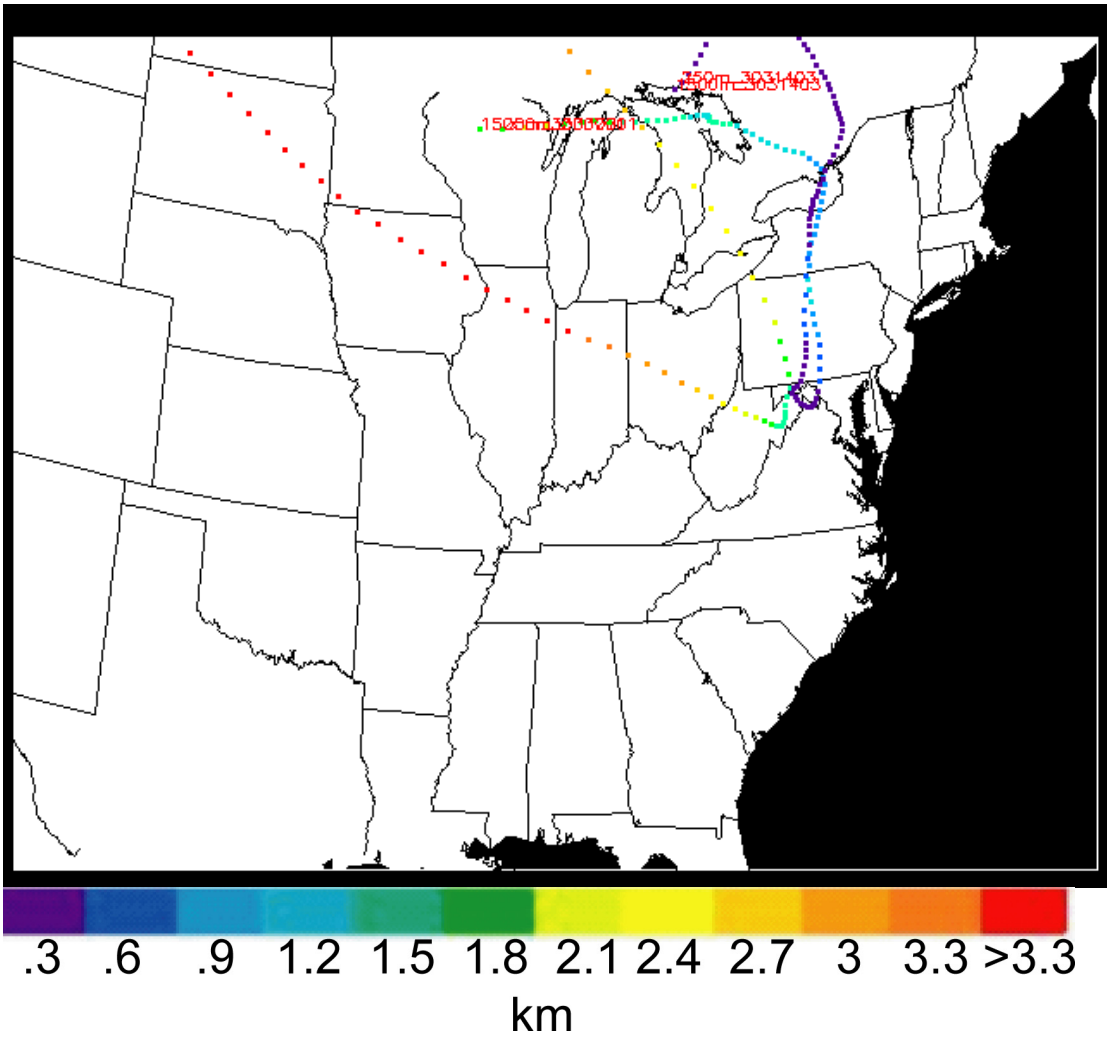

Appendix III.30. March 2003 CBE 72 h backward trajectories

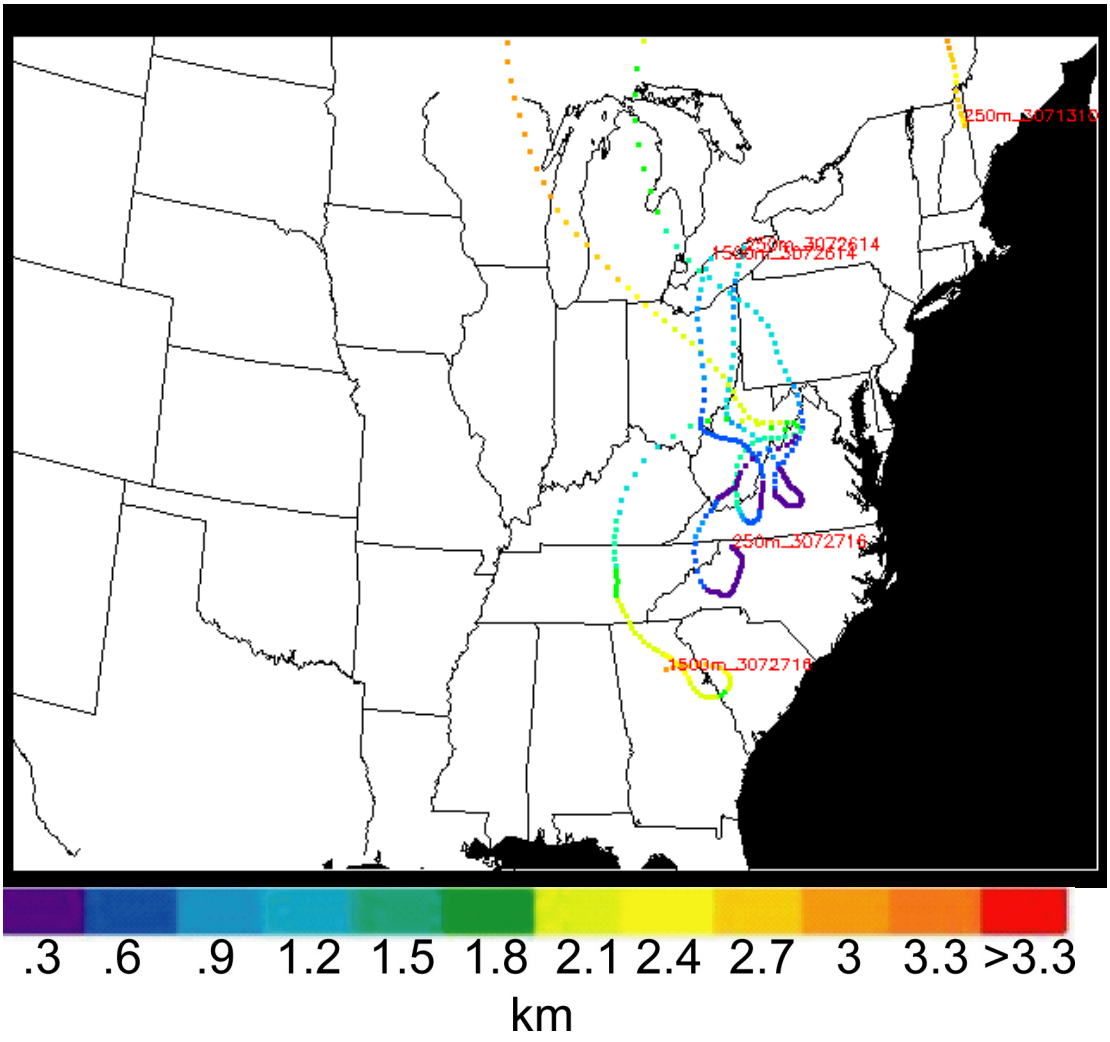

Appendix III.31. July 2003 W45 72 h backward trajectories

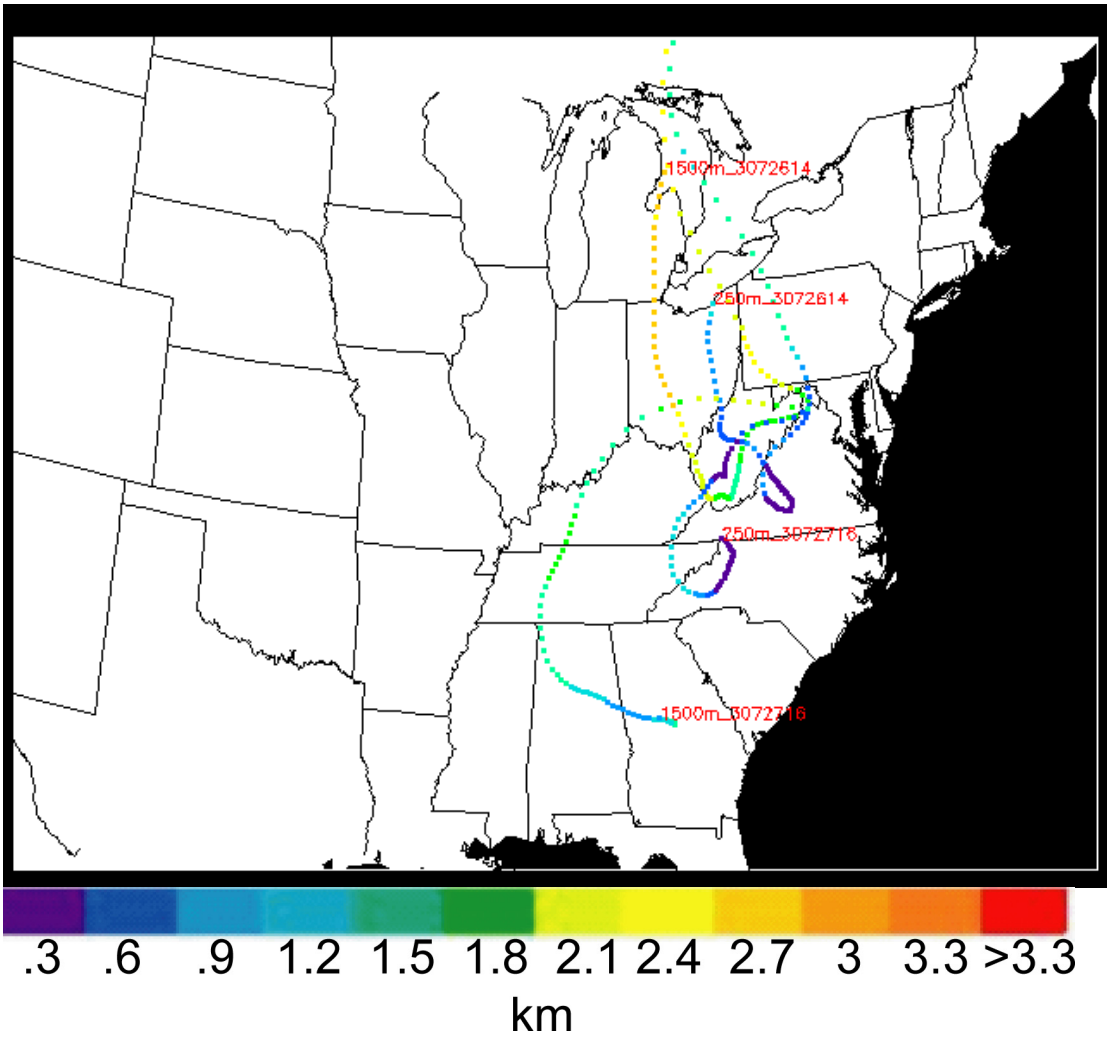

Appendix III.32. July 2003 OKV 72 h backward trajectories

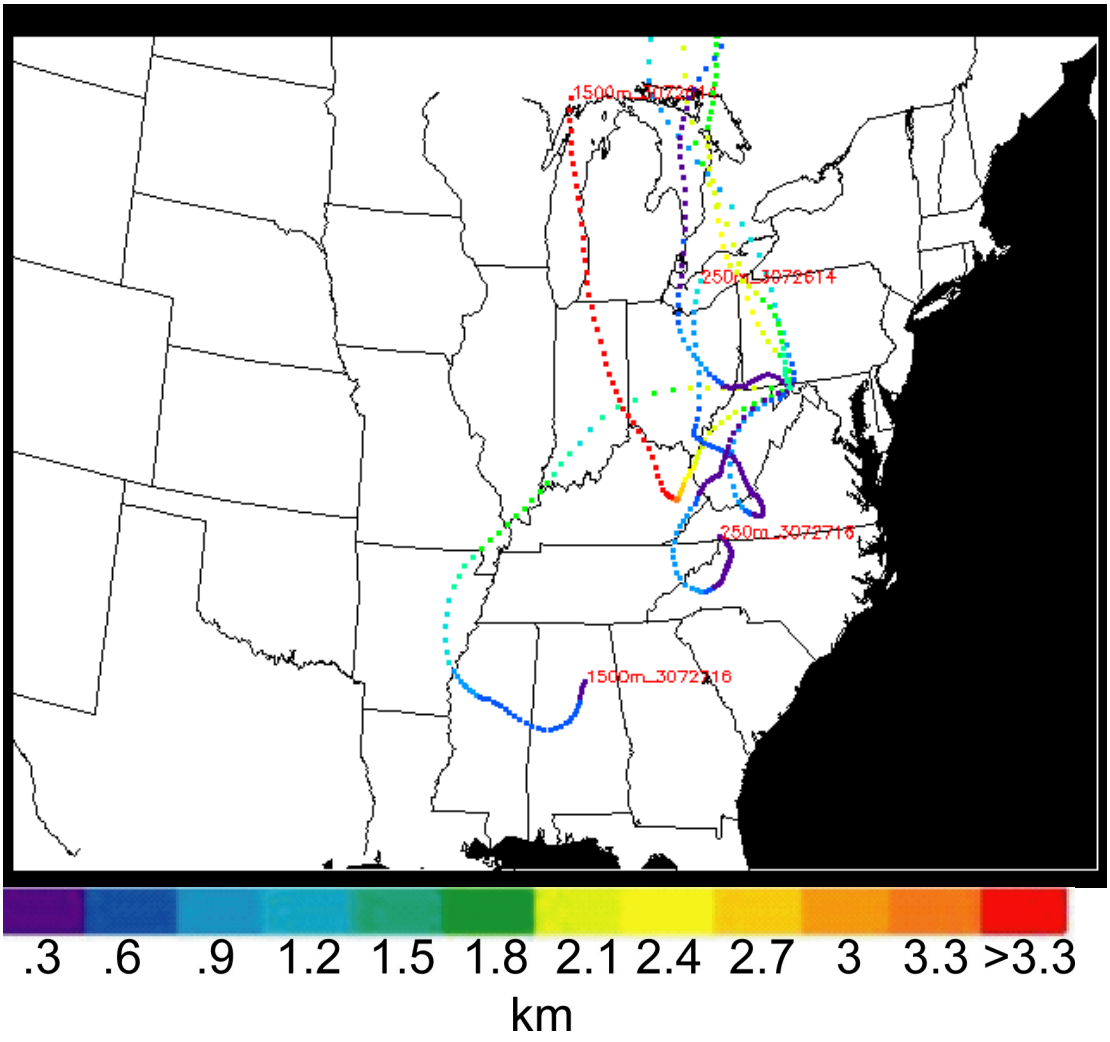

Appendix III.33. July 2003 CBE 72 h backward trajectories

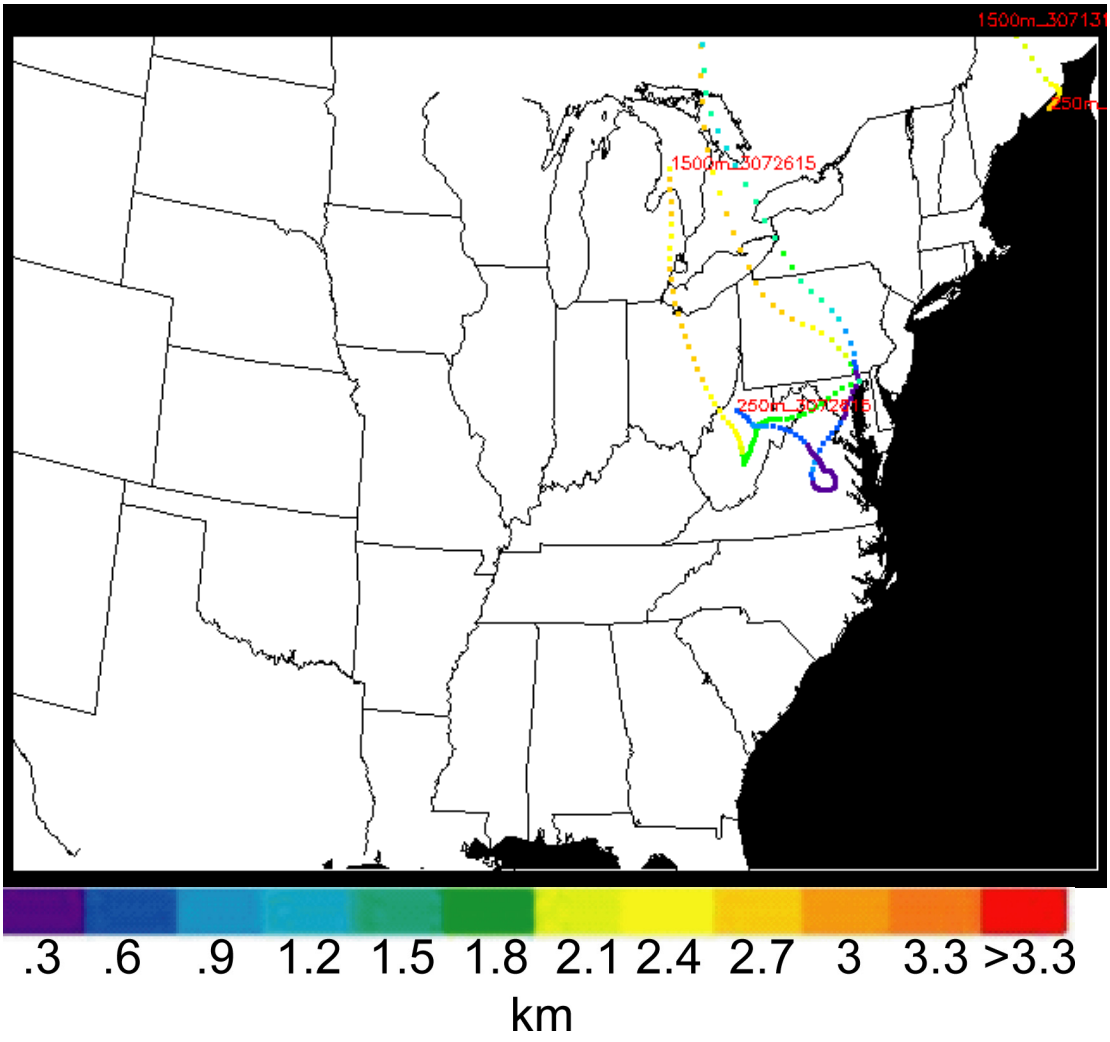

Appendix III.34. July 2003 0W3 72 h backward trajectories

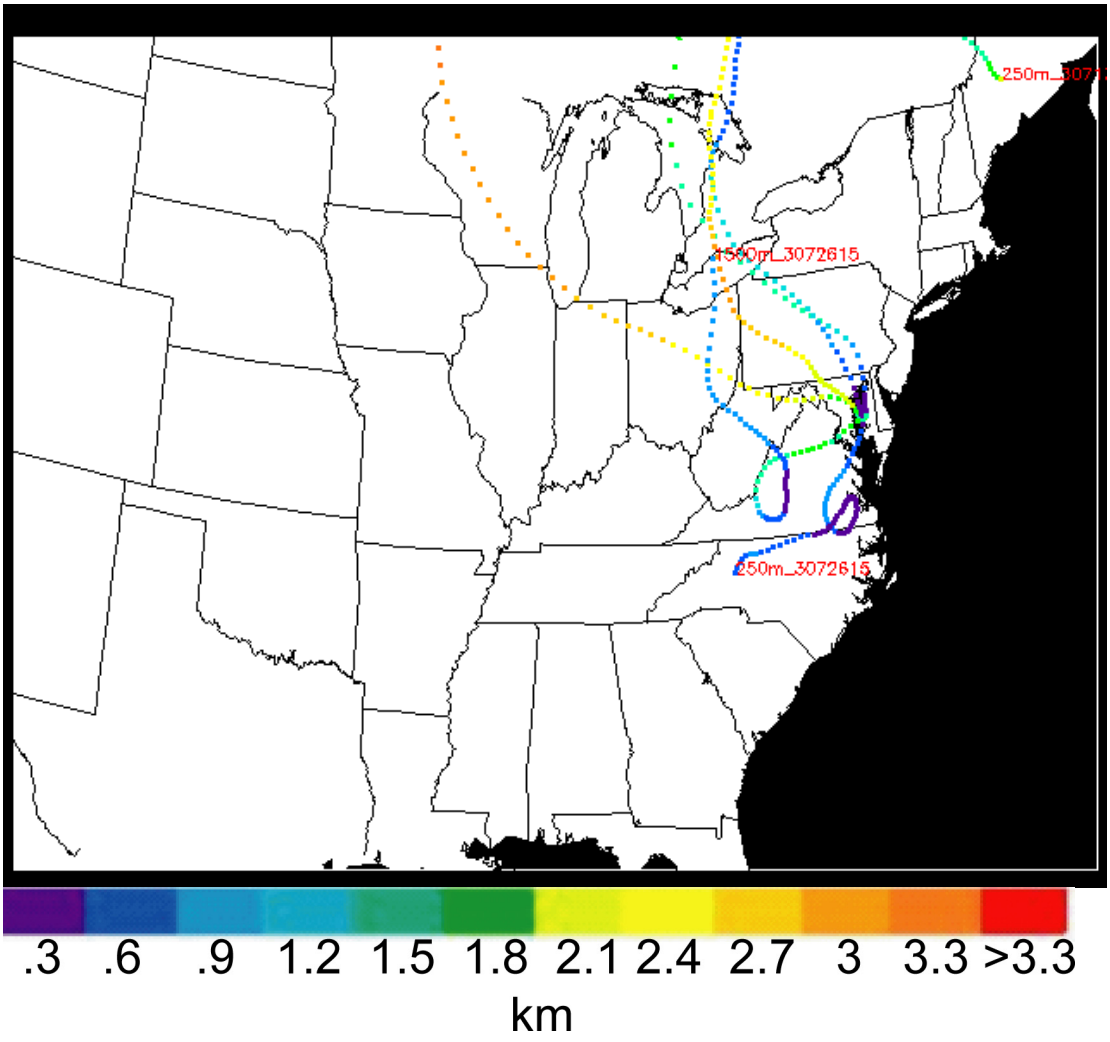

Appendix III.35. July 2003 ESN 72 h backward trajectories

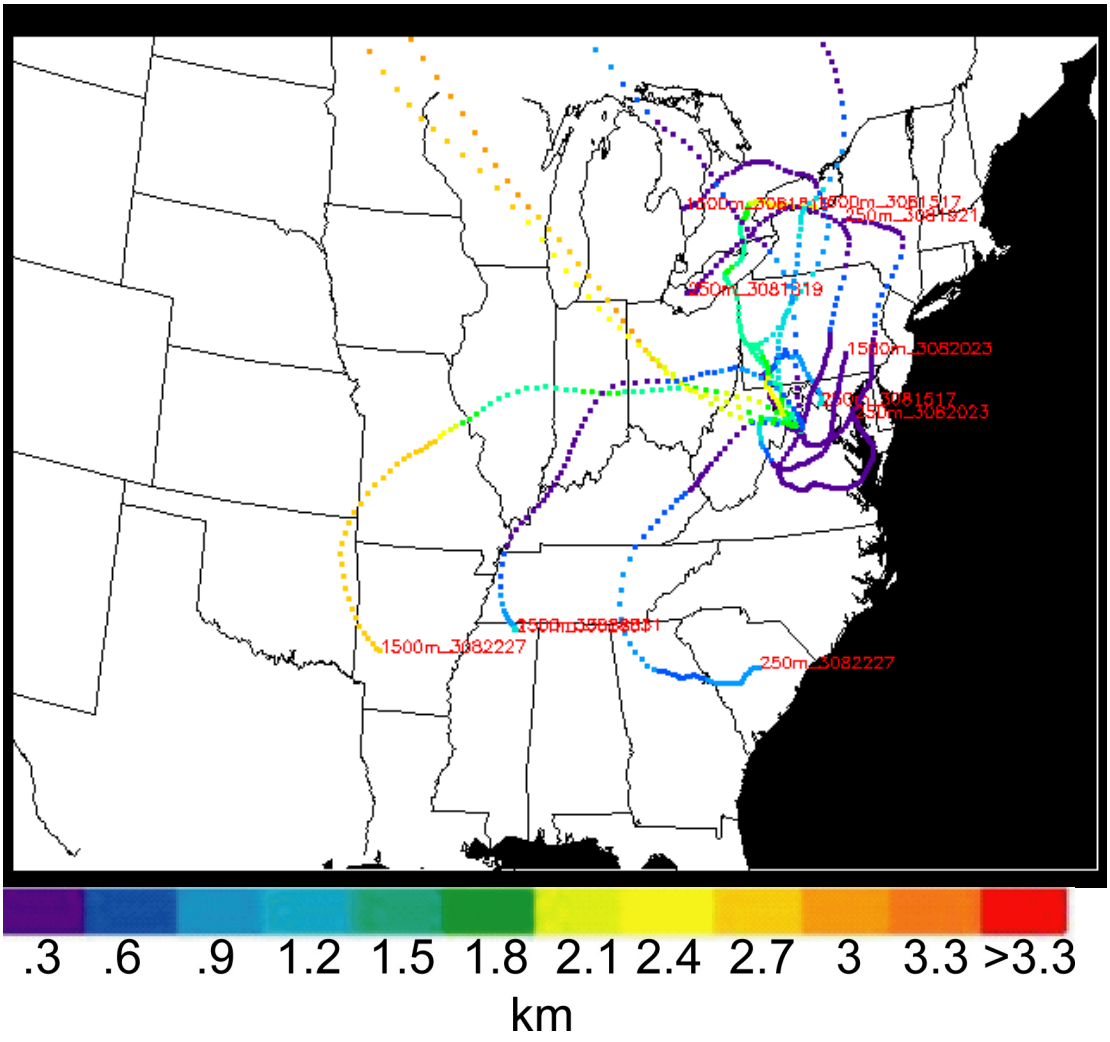

Appendix III.36. August 2003 W45 72 h backward trajectories

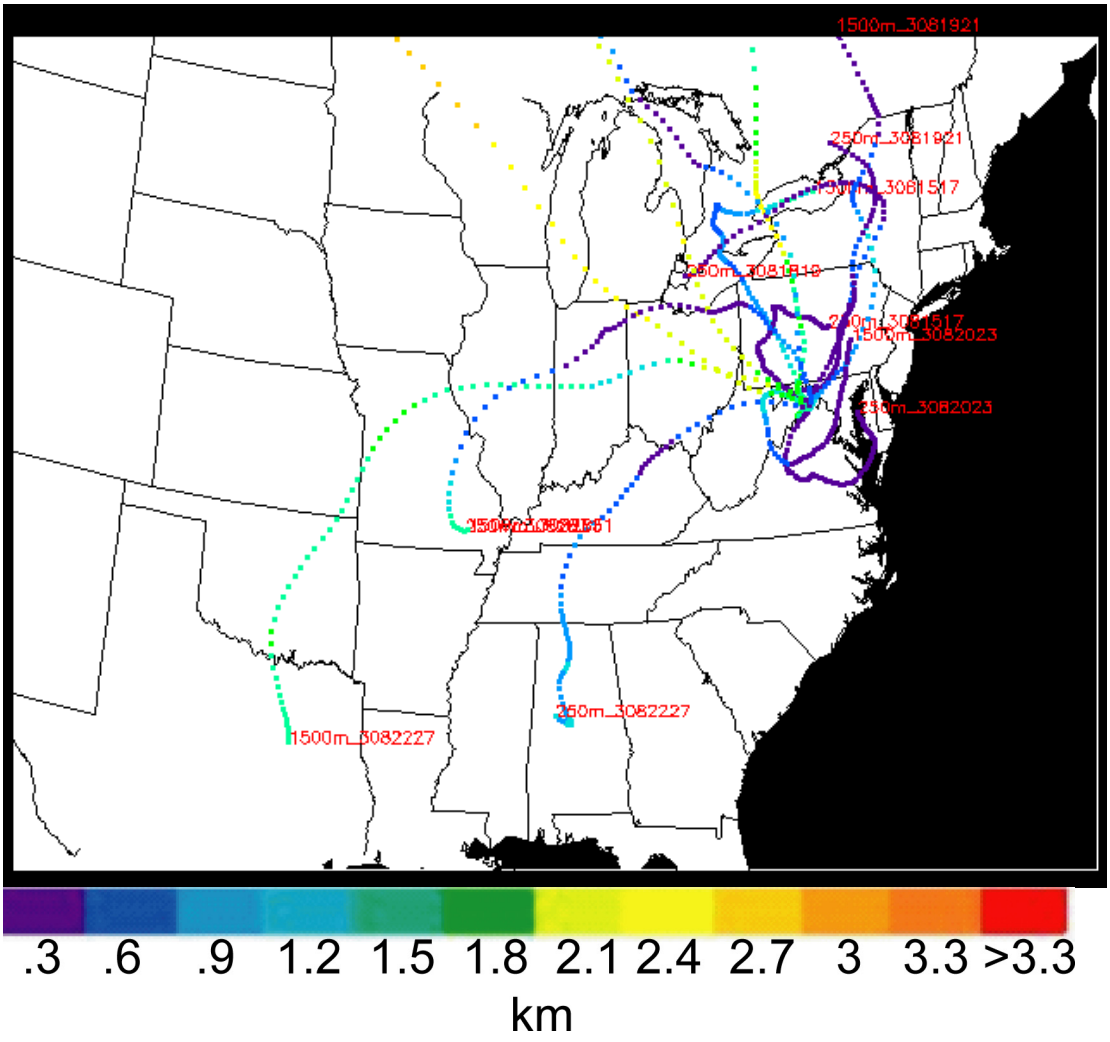

Appendix III.37. August 2003 OKV 72 h backward trajectories

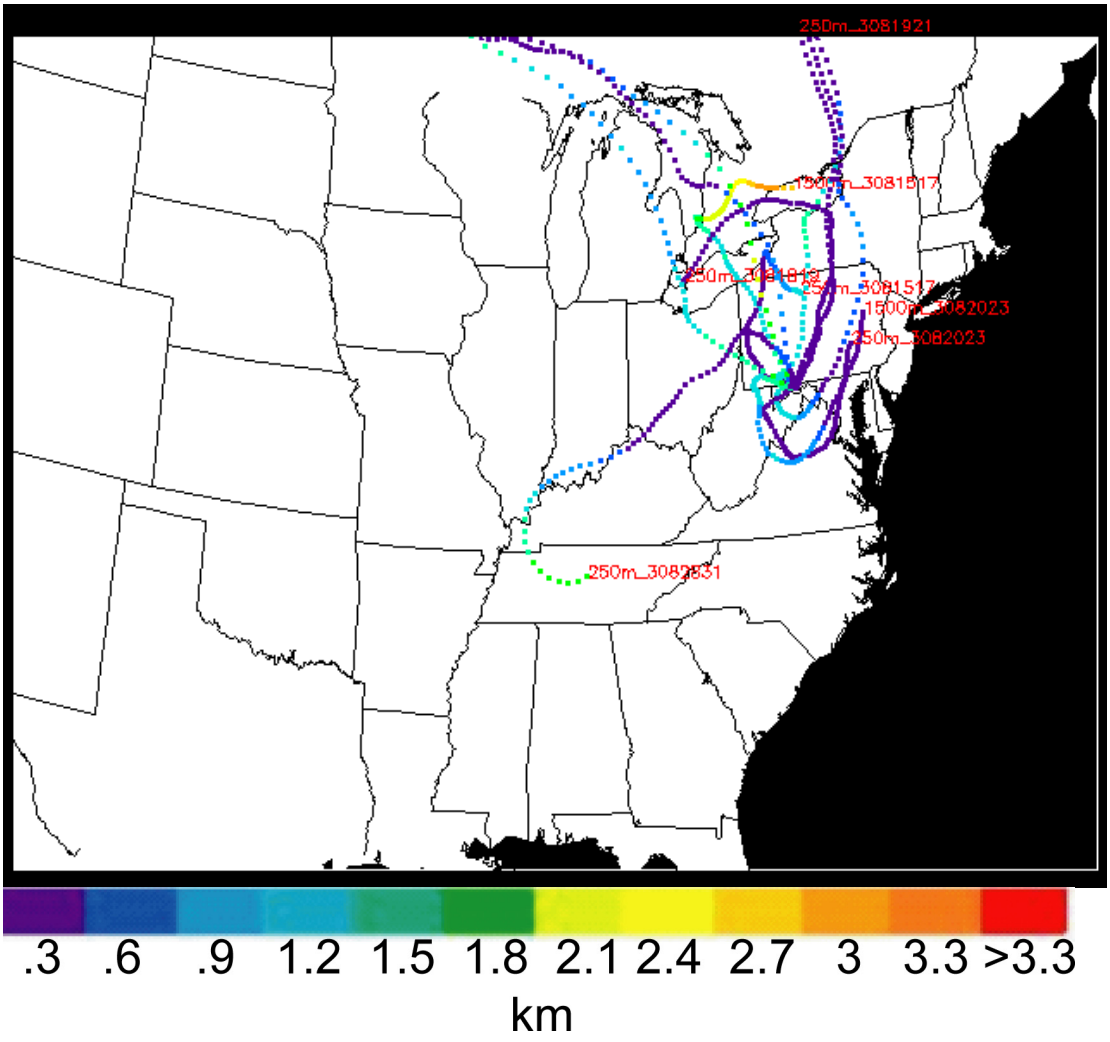

Appendix III.38. August 2003 CBE 72 h backward trajectories

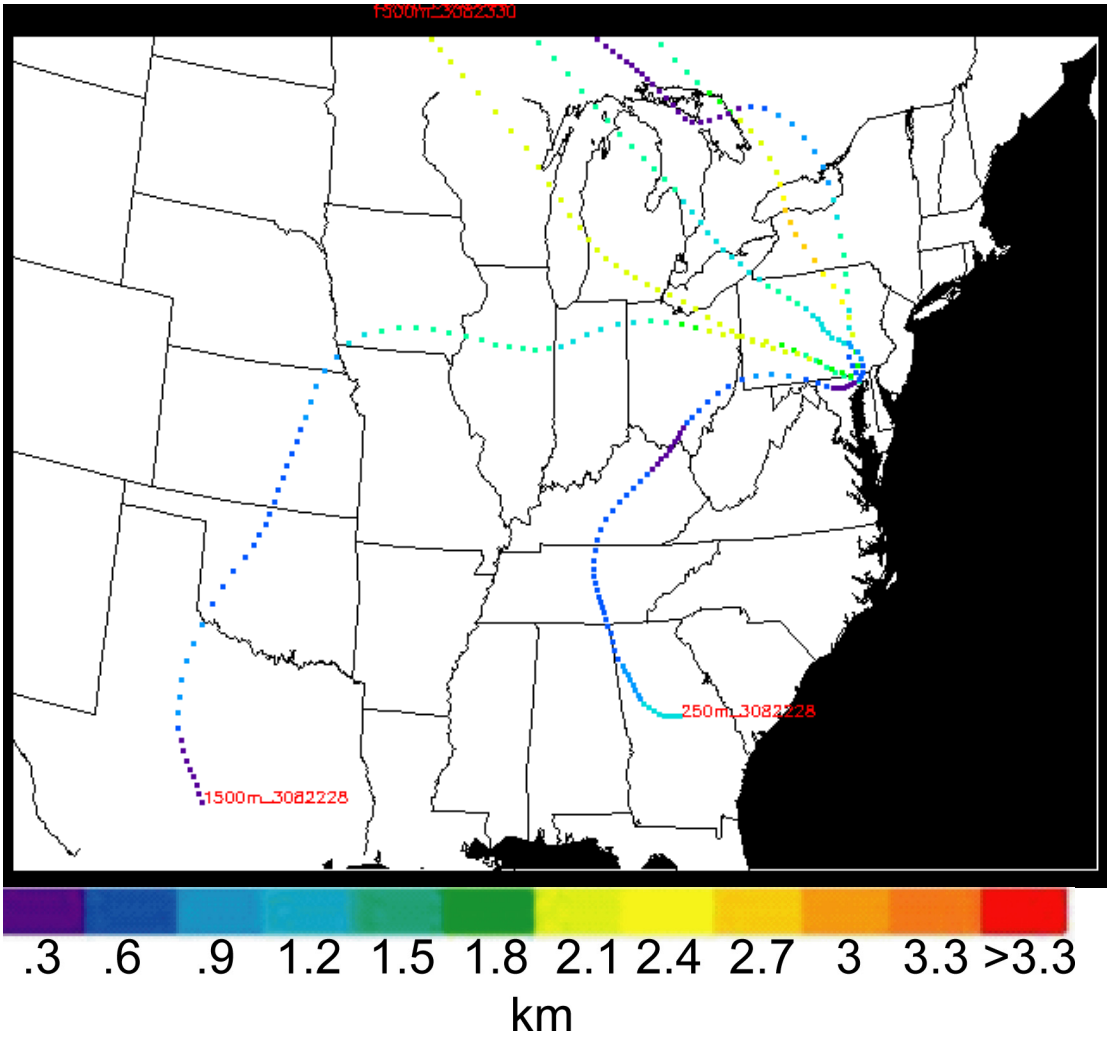

Appendix III.39. August 2003 0W3 72 h backward trajectories

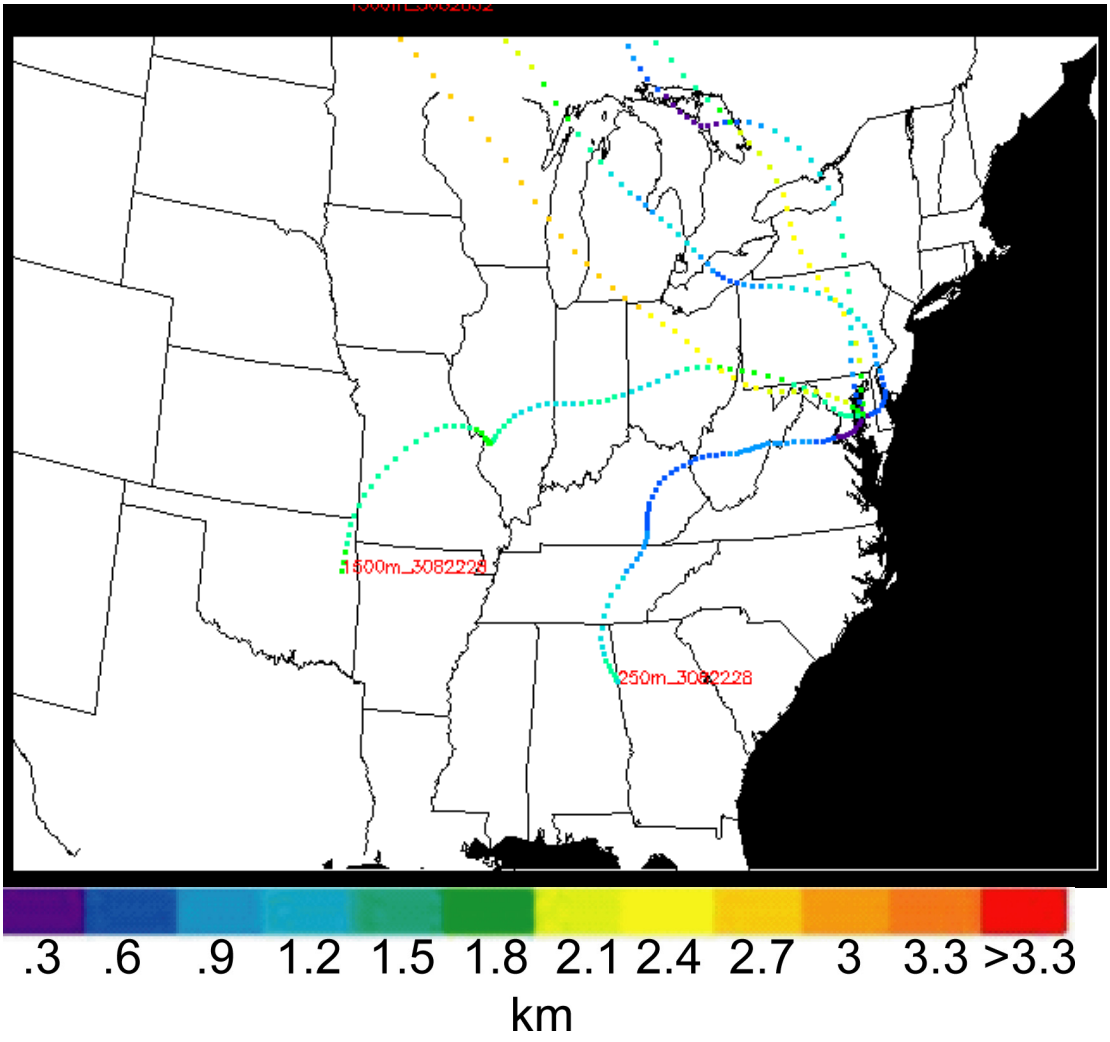

Appendix III.40. August 2003 ESN 72 h backward trajectories

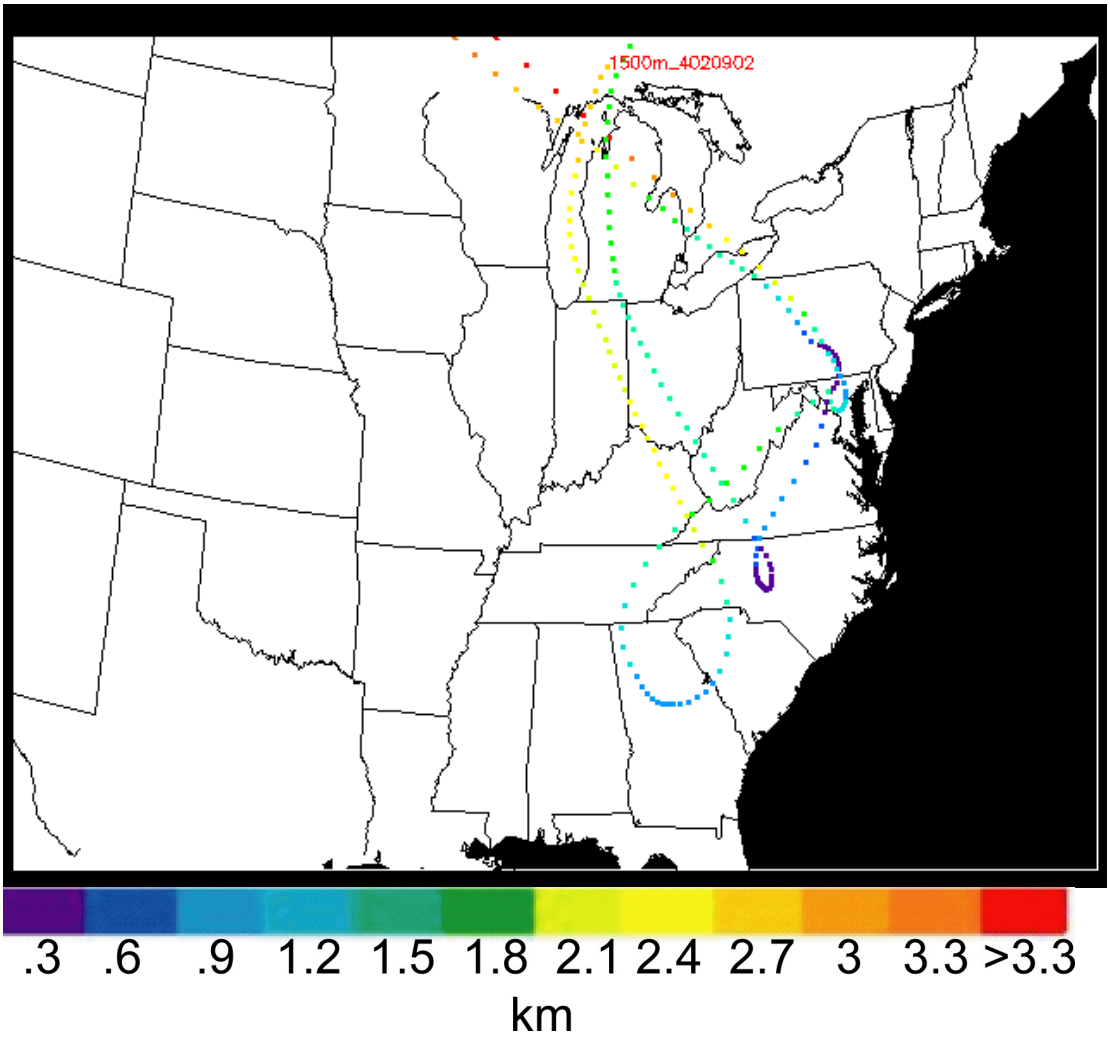

Appendix III.41. February 2004 FDK 72 h backward trajectories

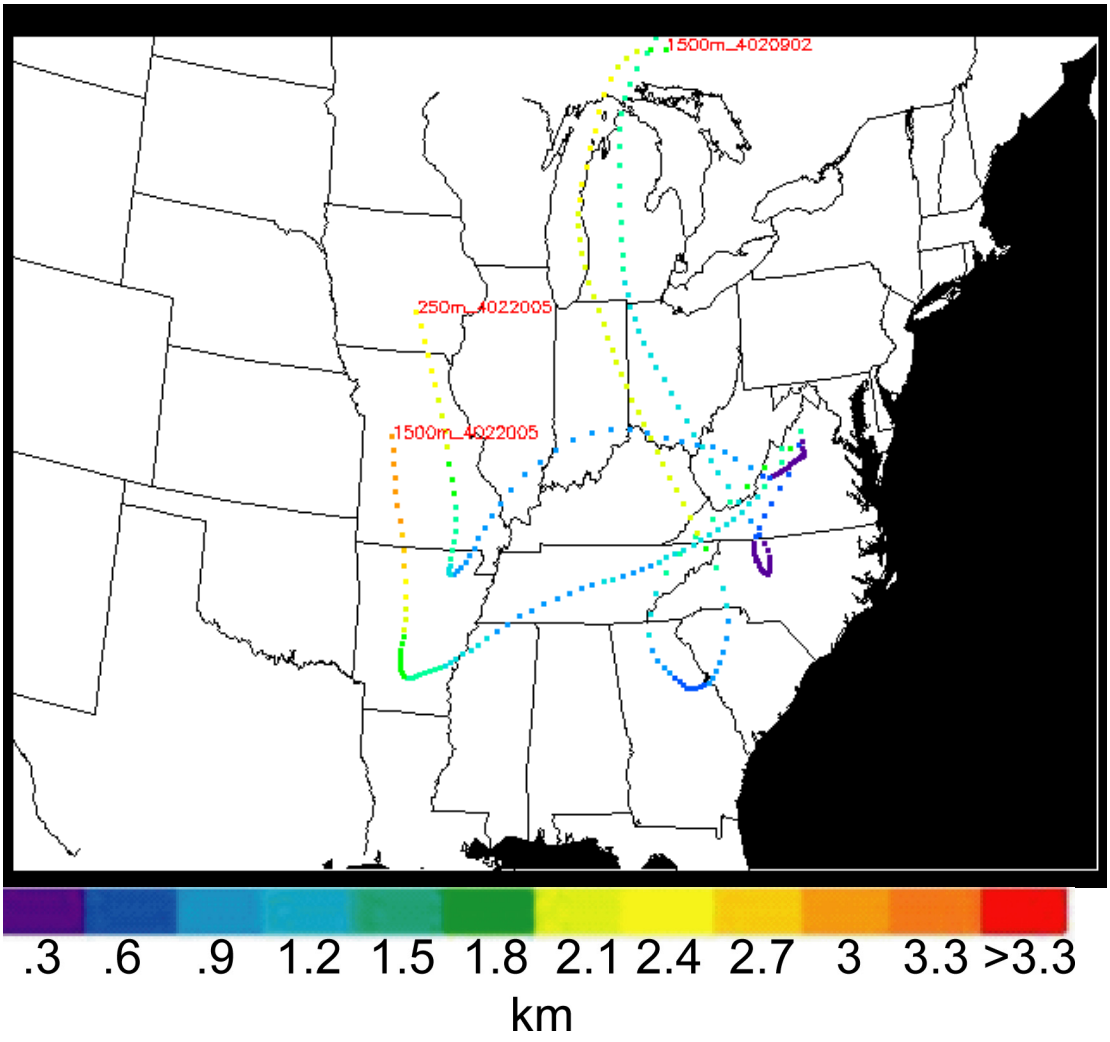

Appendix III.42. February 2004 W45 72 h backward trajectories

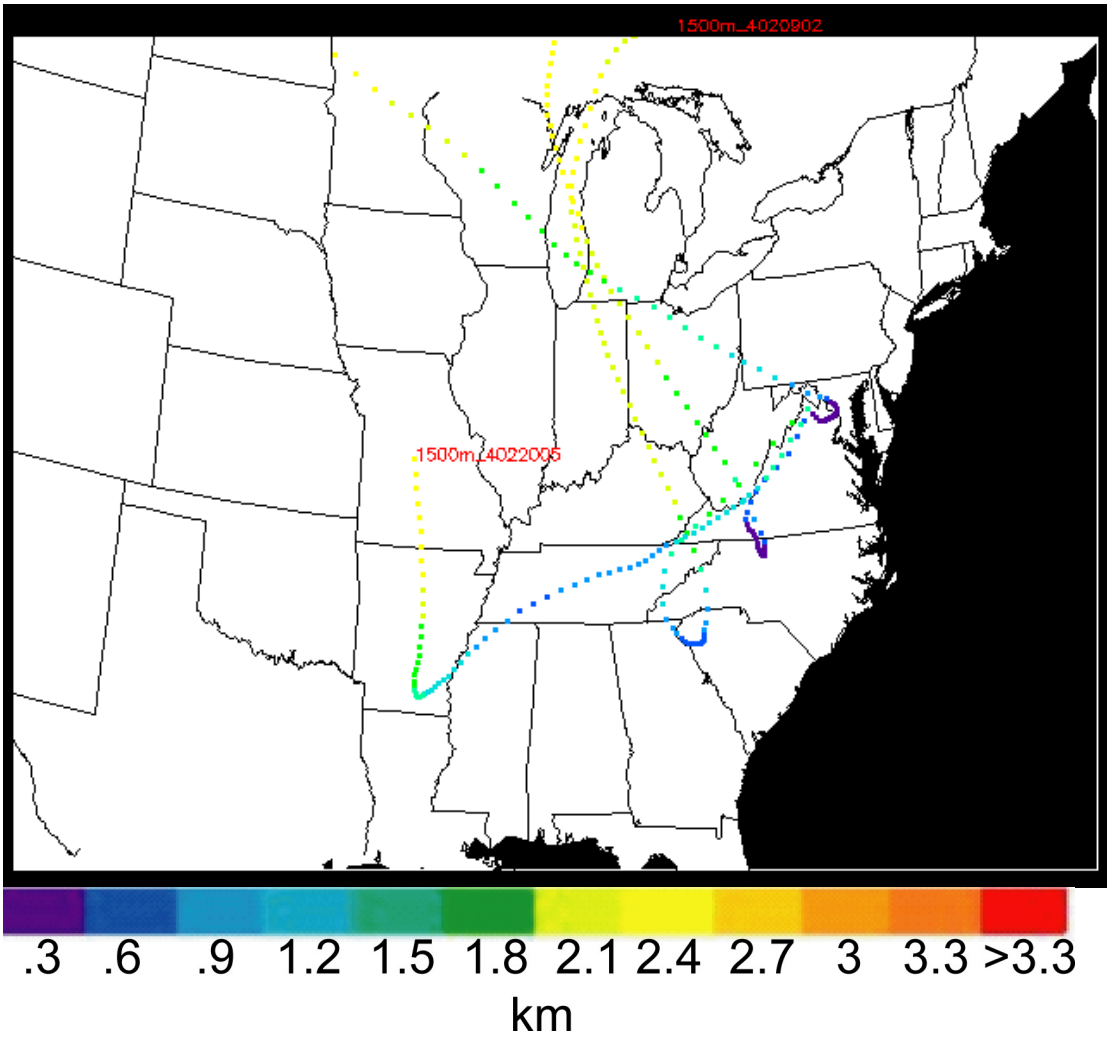

Appendix III.43. February 2004 OKV 72 h backward trajectories

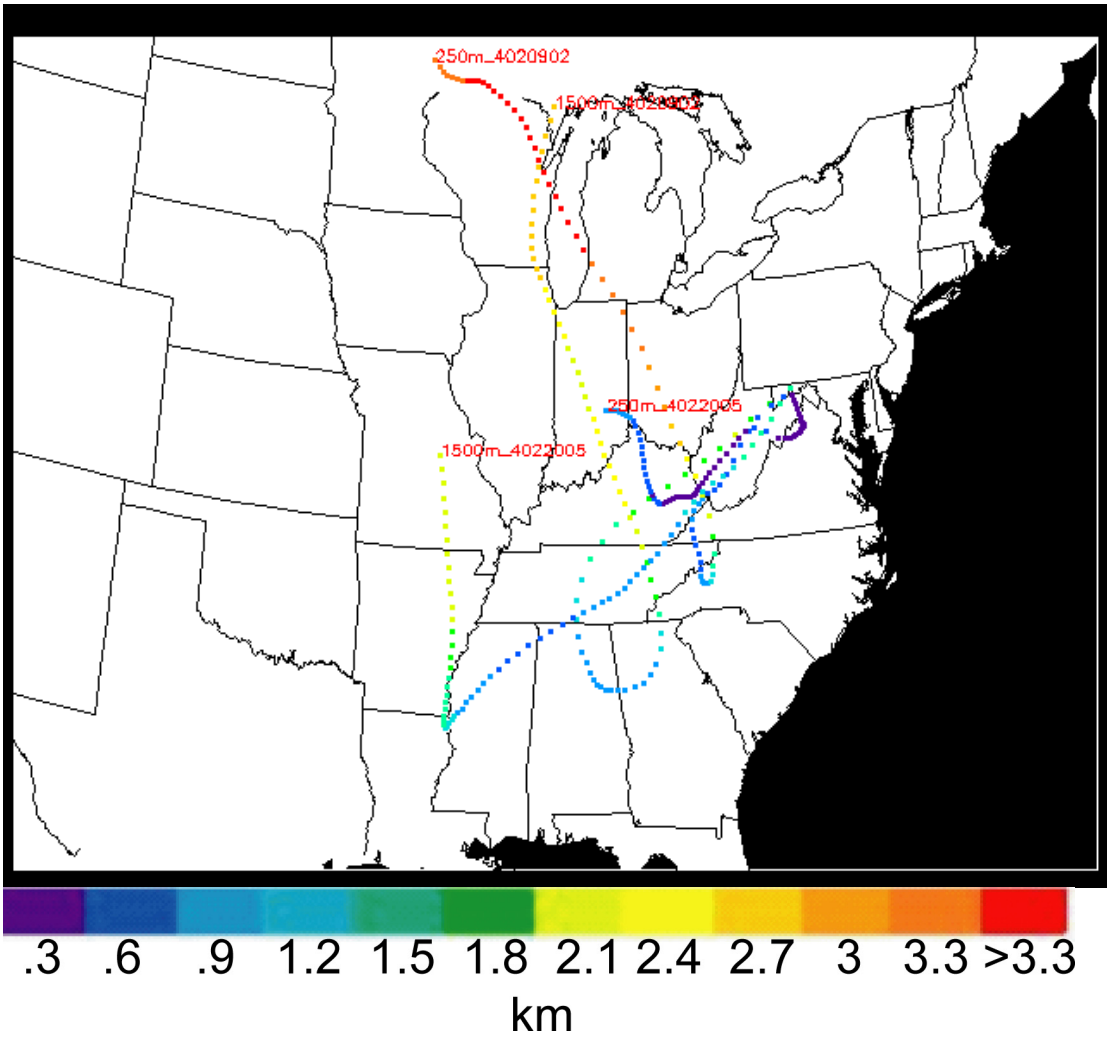

Appendix III.44. February 2004 CBE 72 h backward trajectories

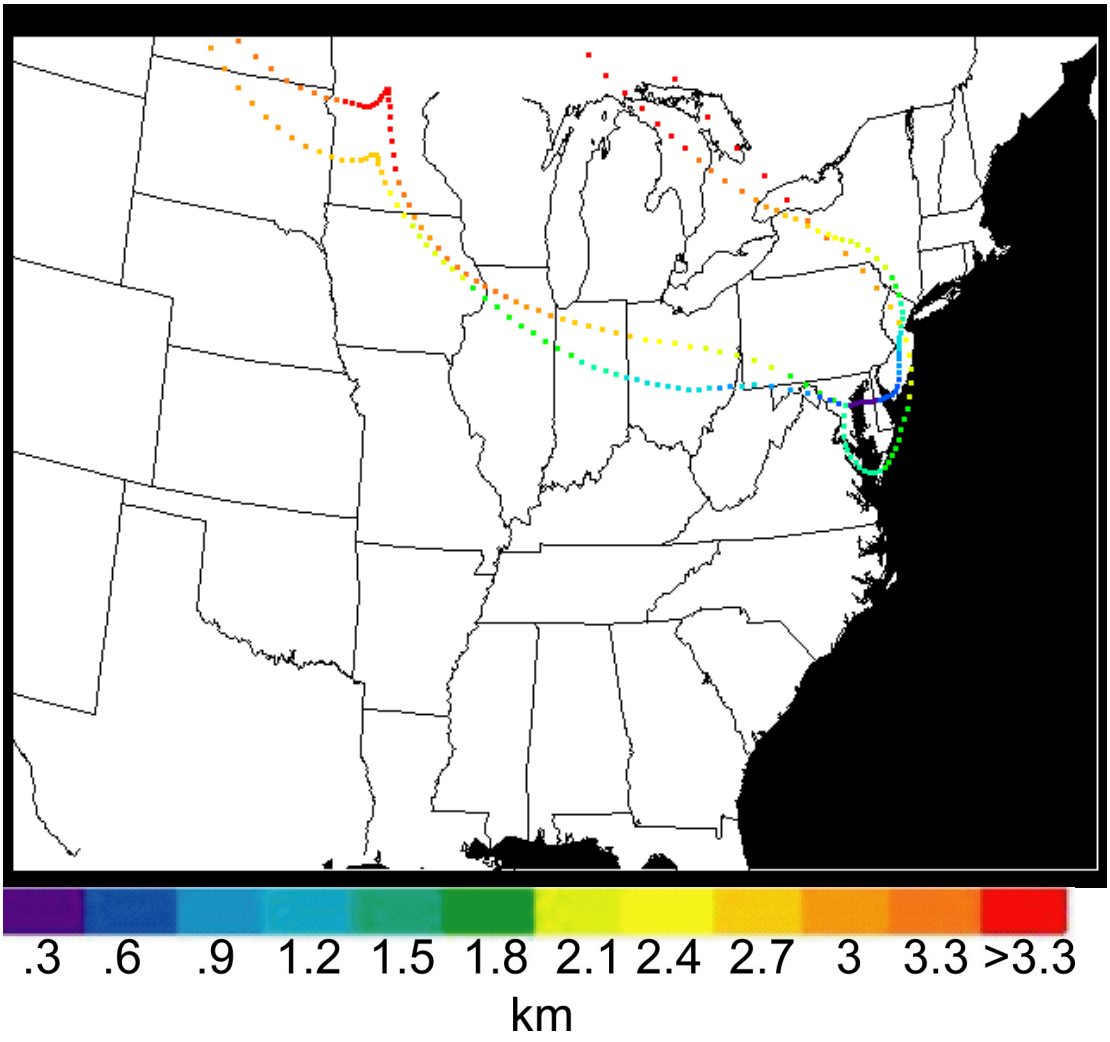

Appendix III.45. February 2004 FME 72 h backward trajectories

Appendix IV

Appendix IV.1. Monthly average AERONET ω_{0550} values and monthly median, extinction weighted, column averaged ω_{0550} aircraft in-situ values (see also Figure 53). The "minus" and "plus" represent the uncertainty. The AERONET uncertainty is estimated from that reported by Dubovik *et al.* (2001). The aircraft uncertainty represents the variability of the 1st and 3rd quartiles about the median values. See Figure 53 for symbology.

	Jun 01	Jul 01	Aug 01	May 02	Jun 02	Jul 02	Aug 02	Jul 03	Aug 03	Feb 04
AERONET	0.97	0.96	0.97	0.96	0.96	0.96	0.95	0.94	0.95	0.95
minus	0.02	0.02	0.02	0.02	0.02	0.02	0.02	0.02	0.02	0.02
plus	0.02	0.02	0.02	0.02	0.02	0.02	0.02	0.02	0.02	0.02
W45	0.91			0.83	0.88			0.87	0.90	0.71
minus	0.03			0.03	0.02			0.02	0.05	0.01
plus	0.02			0.03	0.03			0.02	0.03	0.01
OKV	0.94			0.89	0.94			0.83	0.88	0.80
minus	0.01			0.01	0.02			0.06	0.05	0.03
plus	0.01			0.01	0.01			0.06	0.05	0.03
CBE	0.88			0.86	0.93			0.87	0.86	0.81
minus	0.09			0.03	0.03			0.05	0.08	0.08
plus	0.05			0.03	0.02			0.05	0.02	0.03
0W3	0.93				0.94	0.92		0.82	0.87	
minus	0.01				0.00	0.02		0.02	0.03	
plus	0.01				0.00	0.02		0.02	0.04	
ESN	0.95				0.95	0.93		0.89	0.87	
minus	0.01				0.00	0.02		0.01	0.04	
plus	0.01				0.00	0.02		0.02	0.04	
FME	0.94	0.86			0.93	0.95				0.79
minus	0.02	0.04			0.05	0.03				0.16
plus	0.02	0.04			0.03	0.02				0.00
FCIm			0.92							
minus			0.01							
plus			0.01							
FCIa			0.97							
minus			0.00							
plus			0.00							
NEm							0.94			
minus							0.05			
plus							0.02			
NEa							0.95			
minus							0.02			
plus							0.01			

Appendix IV.2. Monthly average AERONET AOD values and monthly median, AOD aircraft in-situ values (see also Figure 54). The "minus" and "plus" represent the uncertainty. The AERONET uncertainty is estimated from that reported by Dubovik *et al*. (2001). The aircraft uncertainty represents the variability of the 1st and 3rd quartiles about the median values. See Figure 54 for symbology.

	Jun 01	Jul 01	Aug 01	May 02	Jun 02	Jul 02	Aug 02	Jul 03	Aug 03	Feb 04
AERONET	0.39	0.14	0.50	0.16	0.37	0.45	0.35	0.26	0.43	0.06
minus	0.03	0.03	0.03	0.03	0.03	0.03	0.03	0.03	0.03	0.03
plus	0.03	0.03	0.03	0.03	0.03	0.03	0.03	0.03	0.03	0.03
W45	0.38			0.10	0.17			0.25	0.41	0.07
minus	0.18			0.02	0.06			0.08	0.16	0.01
plus	0.20			0.02	0.10			0.06	0.20	0.01
OKV	0.55			0.10	0.23			0.11	0.33	0.10
minus	0.14			0.03	0.08			0.05	0.19	0.03
plus	0.08			0.02	0.13			0.09	0.19	0.03
CBE	0.33			0.12	0.34			0.20	0.27	0.13
minus	0.14			0.06	0.09			0.11	0.17	0.01
plus	0.20			0.05	0.22			0.09	0.20	0.01
0W3	0.45				0.62	0.44		0.11	0.37	
minus	0.13				0.08	0.16		0.06	0.20	
plus	0.13				0.08	0.82		0.06	0.12	
ESN	0.43				0.38	0.99		0.13	0.27	
minus	0.12				0.05	0.69		0.00	0.16	
plus	0.12				0.05	0.90		0.04	0.21	
FME	0.33	0.07			0.41	0.34				0.07
minus	0.08	0.04			0.21	0.17				0.02
plus	0.07	0.06			0.11	0.22				0.02
FCIm			0.54							
minus			0.07							
plus			0.07							
FCIa			0.87							
minus			0.01							
plus			0.01							
NEm							0.32			
minus							0.08			
plus							0.16			
NEa							0.34			
minus							0.11			
plus							0.21			
FDK										0.05
minus										0.00
plus										0.03

Bibliography

Akimoto, H., Global air quality and pollution, *Science, 302*, 1716-1719, 2003.

Anderson, T.L., D.S. Covert, S.F. Marshall, M.L. Laucks, R.J. Charlson, A.P. Waggoner, J.A. Ogren, R. Caldow, R.L. Holm, F.R. Quant, G.J. Sem, A. Wiedensohler, N.A. Ahlquist, and T.S. Bates, Performance characteristics of a high-sensitivity, three-wavelength, total scatter/backscatter nephelometer, *J. Atmos. Oceanic Technol.*, *13*, 967-986, 1996.

Anderson, T.L., D.S. Covert, J.D. Wheeler, J.M. Harris, K.D. Perry, B.E. Trost, and D.J. Jaffe, Aerosol backscatter fraction and single scattering albedo: measured values and uncertainties at a coastal station in the Pacific NW, *J. Geophys. Res.*, *104*, 26,793-26,807, 1999.

Anderson, T.L., and J.A. Ogren, Determining aerosol radiative properties using the TSI 3563 Integrating Nephelometer, *Aerosol Sci. Technol.*, *29*, 57-69, 1998.

Anderson, T.L., S.J. Masonis, D.S. Covert, N.C. Ahlquist, S.G. Howell, A.D. Clarke, and C.S. McNaughton, Variability of aerosol optical properties derived form in-situ aircraft measurements during ACE-Asia, *J. Geophys. Res.*, *108*(D23), 8647, 10.1029/2002JD003247, 2003.

Andreae, M.O., and P.J. Crutzen, Atmospheric aerosols: Biogeochemical sources and role in atmospheric chemistry. *Science*, 276, 1052-1058, 1997.

Andreae, M.O., and P. Merlet, Emission of trace gases and aerosols from biomass burning, *Global Biogeochem. Cycles*, *15*, 955-966, 2001.

Banta, R.M., C.J. Senff, A.B. White, M. Trainer, R.T. McNider, R. J. Valente, S.D. Mayor, R.J. Alvarez, R.M. Hardesty, D. Parrish, and F.C. Fehsenfeld. Daytime buildup and nighttime transport of urban ozone in the boundary layer during a stagnation episode. *J. Geophys. Res.*, *103,* 22,519-22,544, 1998.

Baumann, K., E.J. Williams, W.M. Angevine, J.M. Roberts, R.B. Norton, G.J. Frost, F.C. Fehsenfeld, S.R. Springston, S.B. Bertman, and B. Hartsell. Ozone production and transport near Nashville, Tennessee: Results from the 1994 study at New Hendersonville. *J. Geophys. Res., 105,* 9137-9153, 2000.

Benjamin, S.G., J.M. Brown, K.J. Brundage, B.E. Schwartz, T.G. Smirnova, and T.L. Smith. The operational RUC-2. Preprints*, 16th Conference on Weather Analysis and Forecasting,* Phoenix, AZ, Amer. Meteor. Soc*.,* 249-252, 1998.

Bergstrom, R.W., P.B. Russell, and P. Hignett. Wavelength dependence of the absorption of black carbon particles: Predictions and results from the TARFOX experiment and implications for the aerosol single scattering albedo, *J. Atmos. Sciences*, *59,* 567-577, 2002.

Berkowitz, C.M., and W.J. Shaw. Airborne measurements of boundary layer chemistry during the southern oxidant study: A case study, *J. Geophys. Res., 102*(D11), 12,795-12,804, 1997.

Bodhaine, B.A., Aerosol absorption measurements at Barrow, Mauna Loa, and the South Pole, *J. Geophys. Res.*, *100*, 8967-8975, 1995.

Bohren, C.F., Multiple scattering of light and some of its observable consequences, *Am. J. Phys.*, *55*(6), 524-533, 1987.

Bond, T.C., T.L. Anderson, and D. Campbell, Calibration and intercomparison of filter-based measurements of visible light absorption by aerosols, *Aerosol Sci. Technol.*, *30*, 582-600, 1999.

Bundke, U., et al, Aerosol optical properties during the Lindenberg Aerosol Characterization Experiment (LACE 98), *J. Geophys. Res. 107,* 10.1029/2000JD000188, 2002.

Chang, H., and T. Charalampopolous, Determination of the wavelength dependence of refractive indices of flame soot, *Proc. Roy. Soc. London*., *430,* 577-591, 1990.

Charlock, T. *et al.*, CERES/SARB Surface properties, Surface and Radiation Budget working group web page, http://snowdog.larc.nasa.gov/pub/surf/pages/explan.html, 2002.

Charlson, R.J., J. Langner, H. Rodhe, C.B. Leovy, and S.G. Warren, Perturbation of the northern-hemisphere radiative balance by backscattering from anthropogenic sulfate aerosols, *TellusA*, *43*, 152-163, 1991.

Chen, L.W.A., B.G. Doddridge, R.R. Dickerson, J.C. Chow, P.K. Mueller, J. Quinn, and W.A. Butler. Seasonal variations in elemental carbon aerosol, carbon monoxide, and sulfur dioxide: Implications for sources. *Geophys. Res. Lett., 28,* 1711-1714, 2001.

Chen, L.W.A. Urban fine particulate matter: Chemical composition and possible origins. *Ph.D. Dissertation*, Department of Chemical Physics, University of Maryland, 2002.

Chin, M., D.J. Jacob, J.W. Munger, D.D. Parrish, and B.G. Doddridge. Relationship of ozone and carbon monoxide over North America. *J. Geophys. Res., 99(D7),* 14,565-14,573, 1994.

Chung, S.H., and J.H. Seinfeld. Global distribution and climate forcing of arbonaceous aerosols. *J. Geophys. Res., 107(D19):* art. no. 4407, 2002.

Civerolo, K.L., H. Mao, and S.T. Rao. The airshed for ozone and fine particulate pollution in the eastern United States. *Pure Appl. Geophys., 160*, 81-105, 2003.

Crutzen, P.J. Ozone production rates in an oxygen-hydrogen-nitrogen oxide atmosphere. *J. Geophys. Res., 76*(30), 7311, 1971.

Crutzen, P.J., and M.O. Andreae, Biomass burning in the tropics – impact on atmospheric chemistry and biogeochemical cycles, *Science*, *250*, 1669-1678, 1990.

Crutzen, P.J., L.E. Heidt, J.P. Krasnec, W.H. Pollock, and W. Seiler, Biomass burning as a source of atmospheric gases CO, H_2, N_2O, NO, CH_3CL and COS, *Nature*, *282*, 253-256, 1979.

Daum, P.H., L.I. Kleinman, L. Newman, W.T. Luke, J. Weinstein-Lloyd, C.M. Berkowitz, and K.M. Busness. Chemical and physical properties of plumes of anthropogenic pollutants transported over the North Atlantic during the North Atlantic Regional Experiment. *J. Geophys. Res., 101*(D22), 29,029-29,042, 1996.

Delmas, R., On the emission of carbon, nitrogen and sulfur in the atmosphere during bushfires in intertropical savannah zones, *Geophys. Res. Lett.*, *9*, 761-764, 1982.

Dickerson, R.R., and A.C. Delany, Modification of a commercial gas filter correlation CO detector for increased sensitivity, *J. Atmos. Oceanic Technol.*, *5*(3), 424-431, 1988.

Dickerson, R.R., B.G. Doddridge, P. Kelley, and K.P. Rhoads, Large-scale pollution of the atmosphere over the remote Atlantic Ocean: Evidence from Bermuda, *J. Geophys. Res.*, *100*(D5), 8945-8952, 1995.

Dickerson, R.R., S. Kondragunta, G. Stenchickov, K.L. Civerolo, B.G. Doddridge, and B.N. Holben. The impact of aerosols on solar ultraviolet radiation and photochemical smog. *Science, 278*, 827-830, 1997.

Doddridge, B.G., P.C. Novelli, and R.M. Rosson, WMO meeting of experts on global carbon monoxide measurements, *Rapporteur's Report of the Working Session on Measurement Techniques and Standards*, pp. 8-11, 1995.

Draxler, R.R., and G.D. Rolph. HYSPLIT (HYbrid Single-Particle Lagrangian Integrated Trajectory) Model access via NOAA ARL READY website (http://www.arl.noaa.gov/ready/hysplit4.html). NOAA Air Resources Laboratory, Silver Spring, MD, 2003.

Dubovik, O., B. Holben, Y. Kaufman, M. Yamaxoe, A. Smirnov, D. Tanre, I. Slutsker, Single-scattering albedo of smoke retrieved from the sky radiance and solar transmittance measured from the ground, *J. Geophys. Res. 103,* 31,903-31,923, 1998.

Dubovik, O., B.N. Holben, T.F. Eck, A. Smirnov, Y.J. Kaufman, M.D. King, D. Tanre, and I. Slutsker. Variability of absorption and optical properties of key aerosol types observed in worldwide locations. *J. Atmos. Sciences*, *59,* 590-608, 2001.

Dubovik, O., A. Smirnov, B.N. Holben, M.D. King, Y.J. Kaufman, T.F. Eck, and I. Slutsker, Accuracy assessments of aerosol optical properties retrieved from Aerosol Robotic Network (AERONET) sun and sky radiance measurements, *J. Geophys. Res.*, *105*, 9791-9806, 2000.

Eck, T., B. Holben, J. Reid, O. Dubovik, A. Smirnov, N. O'Neill, I Slutsker, S. Kinne, Wavelength dependence of the optical depth of biomass burning, urban, and desert dust aerosols. *J. Geophys. Res. 104*, 31,333-31,349, 1999.

Eck, T.F., B.N. Holben, I. Slutsker, and A. Setzer, Measurements of irradiance attenuation and estimation of aerosol single scattering albedo for biomass burning aerosols in Amazonia, *J. Geophys. Res.*, *103*, 31,865-31,878, 1998.

Evans, L.F., I.A. Weeks, A.J. Eccleston, and D.R. Packham, Photochemical ozone in smoke from prescribed burning of forests, *Environ. Sci. Technol.*, *11*, 896-900, 1977.

Fast J.D., R.A. Zaveri, R.X. Bian, E.G. Chapman, and R.C. Easter. Effect of regional-scale transport on oxidants in the vicinity of philadelphia during the 1999 NE-OPS field campaign. *J. Geophys. Res*., *107*(D16), 10.1029/2001JD000980, 2002.

Ferrare, R.A., R.S. Fraser, and Y. Kaufman, Satellite measurement of large-scale air-pollution: measurements of forest fire smoke, *J. Geophy. Res*., *95*(D7), 9911-9925, 1990.

Fieberg, M., A Petzold, U. Wandinger, M. Wendisch, C. Kiemle, A. Stifter, M. Ebert, T. Rother, U. Leiterer, Optical Closure for an aerosol column: Method, accuracy, and inferable properties applied to a biomass-burning aerosol and its radiative forcing. *J. Geophys. Res. 107*, web correction, 2003.

Fiore A.M., D.J. Jacob, J.A. Logan, and J.H. Yin, Long-term trends in ground level ozone over the contiguous United States, 1980-1995, *J. Geophys. Res*., *103*(D1), 1471-1480, 1998.

Gent J.F., E.W. Triche, T.R. Holford, K. Belanger, M.B. Bracken, W.S. Beckett, and B.P. Leaderer, Association of low-level ozone and fine particles with respiratory symptoms in children with asthma, *J. Amer. Med. Assoc.*, *290*(14), 1859-1867, 2003.

Green, R. and Robbins, J., ERBE-like inversion to instantaneous TOA flux, *Clouds and the Earth's Radiant Energy System (CERES) Algorithm Theoretical Basis Document 03*, 37 pages, 1997.

Hartley, W.S., P.V. Hobbs, J.L. Ross, P.B. Russell, and J.M. Livingston. Properties of aerosols aloft relevant to direct radiative forcing off the Mid-Atlantic coast of the United States. *J. Geophys. Res.*, *105*(D8), 9859-9885, 2000.

Hansen, J., and L. Travis, Light-scattering in planetary atmospheres, *Space Sci. Rev.*, *16*, 527-610, 1974.

Haywood, J., and O. Boucher. Estimates of the direct and indirect radiative forcing due to tropospheric aerosols: A review. *Geophys. Rev.*, *38*(4), 513-543, 2000.

Hegg, D.A., J. Livingston, P.V. Hobbs, T. Novakov, and P. Russell. Chemical apportionment of aerosol column optical depth off the Mid-Atlantic coast of the United States. *J. Geophys. Res.*, *102*(D21), 25,293-25,303, 1997.

Hobbs, P.V., J.S. Reid, R.A. Kotchenruther, R.J. Ferek, and R. Weiss, Direct radiative forcing by smoke from biomass burning, *Science*, *275*, 1776-1778, 1997.

Hoffman, M.R., and J.G. Calvert. Chemical transformation modules for Eulerian acid deposition models, volume 2, the aqueous-phase chemistry. EPA/600/3-85/017, 1985.

Holben, B., et al, AERONET – a federeated instrument network and data archive for aerosol characterization, *Remote Sens. Env.*, *66*, 1-16, 1998.

Interagency Monitoring of Protected Visual Environments (IMPROVE), Spatial and Seasonal Patterns and Temporal Variability of Haze and its Constituents in the Unite States: Report III, ISSN: 0737-5352-47, 2000.

IPCC: Climate Change 2001: The Scientific Basis, Contribution of Working Group 1 to the Third Assessment Report of the Inter-governmental Panel on Climate Change [Houghton *et al.* (eds.)], Cambridge University Press, Cambridge, United Kingdom and New York, NY, USA, 881pp, 2001.

Jacobson, M.Z. A physically-based treatment of elemental carbon optics: Implications for global direct forcing of aerosols. *Geophys. Res. Lett.*, *27*(2), 217-220, 2000.

Jacobson, M.Z. Strong radiative heating due to the mixing state of black carbon in atmospheric aerosols. *Nature*, *409*, 695-697, 2001.

Jin, Z., Radiative transfer modeling of ocean surface albedo for CERES SARB. *23rd CERES team meeting,* http://www-cagex.larc.nasa.gov/jin/Papers/Jin23CERES.pdf, 2001.

Karoly, D.J., K. Braganza, P.A. Stott, J.M. Arblaster, G.A. Meehl, A.J. Broccoli, and K.W. Dixon, Detection of a human influence on North American climate, *Science, 302*, 1200-1203, 2003.

Kato, S., M. Bergin, T. Ackerman, T. Charlock, E. Clothiaux, R. Ferrare, R. Halthore, N. Laulainen, G. Mace, J. Michalsky, D. Turner, A comparison of the aerosol thickness derived from ground-based and airborne measurements, *J. Geophys. Res*., *105*(D11), 14,701-14,717, 2000.

Kaufman, Y. J. et al: Smoke, Clouds, and Radiation-Brazil (SCAR-B) Experiment. *J. Geophys. Res. 103*(D24), 31,783-31,808, 1998.

Kaufman, Y. J., R. Fraser, R. Ferrare, Satellite Measurements of Large-Scale Pollution: Methods*, J. Geophys. Res*. *95*, 9895-9909, 1990.

Kleinman, L.I., P.H. Daum, D.G. Imre, J.H. Lee, Y.N. Lee, L.J. Nunnermacker, S.R. Springston, J. Weinstein-Lloyd, and L. Newman. Ozone production in the New York City urban plume. *J. Geophys. Res*., *105*(D11), 14,495-14,511, 2000.

Lesins, G., P. Chylek, and U. Lohmann. A study of internal and external mixing scenarios and its effect on aerosol optical properties and direct radiative forcing. *J. Geophys. Res.*, *107*(D10), art. no. 4094, 2002.

Li, Z., 1998, Influence of absorbing aerosols on the inference of solar surface radiation budget and cloud absorption, *J. Climate*, *11*, 5-17, 1998.

Li, Z., and L. Kou, 1998, Atmospheric direct radiative forcing by smoke aerosols determined from satellite and surfase measurements, *Tellus (B)*, *50*, 543-554, 1998.

Liepert, B.G, J. Feichter, U. Lohmann, and E. Roeckner, Can aerosols spin down the water cycle in a warmer and moister world?, *Geophys. Res. Lett., 31*, 10.1029/2003GL019060, 2004.

Luke, W.T., Evaluation of a commercial pulsed fluorescence detector for the measurement of low-level SO_2 concentrations during the Gas-Phase Sulfur Intercomparison Experiment, *J. Geophys. Res.*, *102*(D13), 16,255-16,265, 1997.

Luke, W.T., T.B. Watson, K.J. Olszyna, R.L. Gunter, R.T. McMillen, D.L. Wellman, and S.W. Wilkison. A comparison of airborne and surface trace gas measurements during the Southern Oxidants Study (SOS). *J. Geophys. Res*., *103*(D17), 22317-22337, 1998.

Malm, W.C. Characteristics and origins of haze in the continental United States. *Earth-Science Review, 33*, 1-36, 1992.

Malm, W.C., B.A. Schichtel, R.B. Ames, and K.A. Gebhart, A 10-year spatial and temporal trend of sulfate across the United States, *J. Geophys. Res., 107*(D22), 10.1029/2002JD002107, 2002.

Malm, W.C., J. F. Sisler, D. Huffman, R. A. Eldred, and T. A. Cahill, Spatial and seasonal trends in particle concentration and optical extinction in the United States, *J. Geophys. Res., 99*(D1), 1347-1370, 1994.

Malm, W.C., B.A. Schichtel, M.L. Pitchford, L.L. Ashbaugh, and R.A. Eldred, Trends in speciated fine particle concentration in the United States, *J. Geophys. Res., 109*, 10.1029/2003JD003739, 2004.

Martins, J.V., P. Artaxo, C. Liousse, J.S. Reid, P.V. Hobbs, and Y.J. Kaufman, Effects of black carbon content, particle size, and mixing on light absorption by aerosols from biomass burning in Brazil, *J. Geophys. Res.*, *103*, 32,041-32,050, 1998.

Marufu, L.T., B.F. Taubman, B. Bloomer, C.A. Piety, B.G. Doddridge, and R.R. Dickerson, The 2003 North American electrical blackout: An accidental experiment in atmospheric chemistry, *Geophys. Res. Lett*., *31*, 10.1029/2004GL019771, 2004.

Maryland Department of Environment, http://www.mde.state.md.us/Air/air_quality/ozone_forecast.asp, 2003.

McClellan, R.O., Setting ambient air quality standards for particulate matter, *Toxicology*, *181*, 329-347, 2002.

McKeen, S.A., G. Wotawa, D.D. Parrish, J.S. Holloway, M.P. Buhr, G. Hubler, F.C. Fehsenfel, and J.F. Meagher, Ozone production from Canadian wildfires during June and July of 1995, *J. Geophys. Res.*, *107*, art. no. 4192, 2002.

Menon, S., J. Hansen, L. Nazarenko, and Y.F. Luo. Climate effects of black carbon aerosols in China and India. *Science*, *297*(5590), 2250-2253, 2002.

Mishchenko, M. I., L. D. Travis, and A. A. Lacis, *Scattering, Absorption, and Emission of Light by Small Particles*, Cambridge University Press, Cambridge. 2002.

Novakov, T., D.A. Hegg, and P.V. Hobbs, Airborne measurements of carbonaceous aerosols on the East Coast of the United States, *J. Geophys. Res.*, *102*(D25), 30,023-30,030, 1997.

Novelli, P.C., V.S. Connors, H.G. Reichle, Jr., B.E. Anderson, C.A.M. Brenninkmeijer, E.G. Brunke, B.G. Doddridge, V.W.J.H. Kirchoff, K.S. Lam, K.A. Masarie, T. Matsou, D.D. Parrish, H.E. Scheel, and L.P. Steele, An internally constistent set of globally distributed atmospheric carbon monoxide mixing ratios developed using results from an intercomparison of measurements, *J. Geophys. Res.*, *103*, 19,285-19,293, 1998.

Pagnotti, V. A mesoscale meteorological feature associated with high ozone concentrations in the northeastern United States. *J. Air Pollut. Control Assoc*., *37,* 720-722, 1987.

Parish, T.R., A.R. Rodi, and R.D. Clark. A case study of the summertime Great Plains low level jet. *Mon. Wea. Rev.*, *116*, 94-105, 1988.

Park, R.J., G.L. Stenchikov, K.E. Pickering, R.R. Dickerson, D.J. Allen, and S. Kondragunta, Regional air pollution and its radiative forcing: Studies with a single-column chemical and radiation transport model, *J. Geophys. Res.*, *106*(D22), 28,751-28,770, 2001.

Penner, J.E., R.E. Dickinson, and C.A. O'Neill, Effects of aerosol from biomass burning on the global radiation budget, *Science*, *256*, 1432-1434, 1992.

Ramanathan, V., P.J. Crutzen, J.T. Kiehl, and D. Rosenfeld, Aerosols, climate, and the hydrological cycle, *Science*, *294*, 2119-2123, 2001.

Ramanathan, V. et al, Indian Ocean Experiment: An integrated analysis of the climate forcing and effects of the great Indo-Asian haze, *J. Geophys. Res. 106,* 28,371-28,398, 2001.

Rao, S.T., J.Y. Ku, S. Berman, K. Zhang, and H. Mao. Summertime characteristics of the atmospheric boundary layer and relationships to ozone levels over the eastern United States. *Pure Appl. Geophys.*, *160*, 21-55, 2003.

Reid, J.S., P.V. Hobbs, R.J. Ferek, D.R. Blake, J.V. Martins, J.V. Dunlap, and C. Liousse, Physical, chemical, and optical properties of regional hazes dominated by smoke in Brazil, *J. Geophys. Res.*, *103*, 32,059-32,080, 1998(a).

Reid, J.S., T.F. Eck, S.A. Christopher, P.V. Hobbs, and B. Holben, Use of the Ångstrom exponent to estimate the variability of optical and physical properties of aging smoke particles in Brazil, *J. Geophys. Res.*, *104*, 27,473-27,489, 1999.

Reid, J.S., P. Hobbs, C. Liousse, J Martins, R. Weiss, T. Eck, Comparisons of techniques for measuring shortwave absorption and black carbon content of aerosols from biomass burning in Brazil, *J. Geophys. Res. 103*, 32,031-32,040, 1998(b).

Remer, L.A., S. Gasso, D.A. Hegg, Y.J. Kaufmann, and B.N. Holben. Urban/industrial aerosol: Ground based Sun/sky radiometer and airborne in-situ measurements. *J. Geophys. Res*, *102,* 16,849-16,859, 1997.

Remer, L.A., Y.J. Kaufman, B.N. Holben, A.M. Thompson, and D. McNamara, Biomass burning aerosol size distribution and modeled optical properties, *J. Geophys. Res.*, *103*, 31,879-31,891, 1998.

Ricchiazzi, P., S. Yang, D Gautier, and D. Sowle, SBDART: a research and teaching software tool for plane-parallel radiative transfer in the Earth's atmosphere, *Bull. Amer. Met. Soc.*, *79*, 2101- 2114, 1998.

Rosen, H., T. Novakov, and B. Bodhaine, Soot in the Arctic, *Atmos. Environ.*, *15*, 1371-1374, 1981.

Ross, J.L., P. Hobbs, B. Holben, Radiative Characteristics of regional hazes dominated by smoke from biomass burning in Brazil: Closure tests and direct radiative forcing, *J.Geophys. Res. 103,* 31,925-31,941, 1998.

Russell, P.B., J. Livingston, P. Hignett, S. Kinne, J. Wong, A. chien, R. Bergstrom, P. Durkee, P. Hobbs, Aerosol-induced radiative flux changes off the United States Mid-Atlantic Coast: Comparison of values calculated from sunphotometer and in-situ data with those measured by airborne pyranometer. *J. Geophys. Res. 104,* 2289-2307, 1999(a).

Russell, P.B., P. Hobbs, L. Stowe, Aerosol properties and radiative affects in the United States East Coast haze plume: an overview of the Tropospheric Aerosol Radiative Forcing Observational Experiment (TARFOX), *J. Geophys. Res. 104*, 2213-2222, 1999(b).

Ryan, W.F., B.G. Doddridge, R.R. Dickerson, R.M. Morales, K.A. Hallock, P.T. Roberts, D.L. Blumenthal, J.A Anderson, and K.L. Civerolo, Pollutant transport during a regional O_3 episode in the Mid-Atlantic states, *J. Air & Waste Manage. Assoc., 48*, 786-797, 1998.

Seaman, N.L., and S.A. Michelson. Mesoscale meteorological structure of a high-ozone episode during the 1995 NARSTO-Northeast study. *J. Appl. Met.*, *39*(3), 384-398, 2000.

Sekiguchi, M., T. Nakajima, K. Suzuki, K. Kawamoto, A. Higurashi, D. Rosenfeld, I. Sano, and S. Mukai, A study of the direct and indirect effects of aerosols using global satellite data sets of aerosol and cloud parameters, *J. Geophys. Res., 108*(D22), 10.1029/2002JD003359, 2003.

Sistla, G., W. Hao, J.Y. Ku, G. Kallos, K. Zhang, H. Mao, and S. T. Rao, An operational evaluation of two regional-scale ozone air quality modeling systems over the eastern United States, *Bull. Amer. Meteor. Soc.*, *82*(5), 945-964, 2001.

Solomon P., E. Cowling, G. Hidy, and C. Furiness, Comparison of scientific findings from major ozone field studies in North America and Europe, *Atmos. Environ.*, *34* (12-14), 1885-1920, 2000.

Stehr, J.W., R.R. Dickerson, K.A. Hallock-Waters, B.G. Doddridge, and D. Kirk. Observations of NO_y, CO, and SO_2 and the origin of reactive nitrogen in the eastern United States. *J. Geophys. Res.*, *105*(D3), 3553-3563, 2000.

Stephens, G., Remote Sensing of the Lower Atmosphere, Oxford University Press, New York, 1994.

Stith, J.L., F.R. Lawrence, and P.V. Hobbs, Particle emissions and the production of ozone and nitrogen-oxides from the burning of forest slash, *Atmos. Environ.*, *15*, 73-82, 1981.

Szekeres, D., Traffic counts data, Pennsylvania Department of Transportation (PDOT), Bureau of Planning and Research, 2004.

Taubman, B.F., L.T. Marufu, C.A. Piety, B.G. Doddridge, J.W. Stehr, and R.R. Dickerson, Airborne characterization of the chemical, optical, and meteorological properties, and origins of a combined ozone/haze episode over the eastern U.S., *J. Atmos. Sci.*, *61*(14), 1781-1793, 2004(a).

Taubman, B.F., L.T. Marufu, B.L. Vant-Hull, C.A. Piety, B.G. Doddridge, R.R. Dickerson, and Z. Li, Smoke over haze: Aircraft observations of chemical and optical properties and the effects on heating rates and stability, *J. Geophys. Res.*, *109*(D2), 10.1029/2003JD003898, 2004(b).

United States Environmental Protection Agency, *Personal Communication*, 2003.

United States Environmental Protection Agency, *EPA Acid Rain Program 2002 Progress Report*, EPA-430-R-03-011, November 2003(a).

United States Environmental Protection Agency, *Latest Findings on National Air Quality 2002 Status and Trends*, EPA 454/K-03-001, August 2003(b).

Vant-Hull, B.L., Z. Li, B.F. Taubman, R. Levy, L.T. Marufu, B.G. Doddridge, and R.R. Dickerson, Smoke over haze: Comparison of satellite, surface and in-situ measurements of aerosol optical properties and radiative forcing of forest fire smoke over the eastern U.S., *J. Geophys. Res.,* In Press, 2004.

Vermote, E., E. Vermuelen, Atmospheric correction algorithm: Spectral reflectances (MOD09). NASA Algorithm Theoretical Basis Document, http://modis.gsfc.nasa.gov/data/atbd/atbd_mod08.pdf, 1999.

Vukovitch, F.M. Regional scale boundary layer ozone variations in the eastern United States and their association with meteorological variations. *Atmos. Environ., 29,* 2259-2273, 1995.

Vukovich, F.M., and J. Sherwell. Comparison of fine particles and the relationship between particle variation and meteorology at an urban site and a remote site in the eastern United States. *J. Air Waste Manage. Assoc.*, *52* (5), 573-584, 2002.

Wong, J., and Z. Li, Retrieval of optical depth for heavy smoke aerosol plumes: uncertainties and sensitivities to the optical properties, *J. Atmos. Sci*., *59*, 250-261, 2002.

Zelenka, M.P., 1997: An analysis of the meteorological parameters affecting ambient concentrations of acid aerosols in Uniontown, Pennsylvania. *Atmos. Environ., 31* (6), 869-878, 1997.

Zhang, J., S.T. Rao, and S.M. Daggupaty. Meteorological processes and ozone exceedances in the northeastern United States during the 12-16 July 1995 episode. *J. Appl. Met.*, *37*, 776-789, 1998.

Zhang, J., and S.T. Rao. The role of vertical mixing in the temporal evolution of ground-level ozone concentrations. *J. Appl. Met.*, *38*, 1674-1691, 1999.